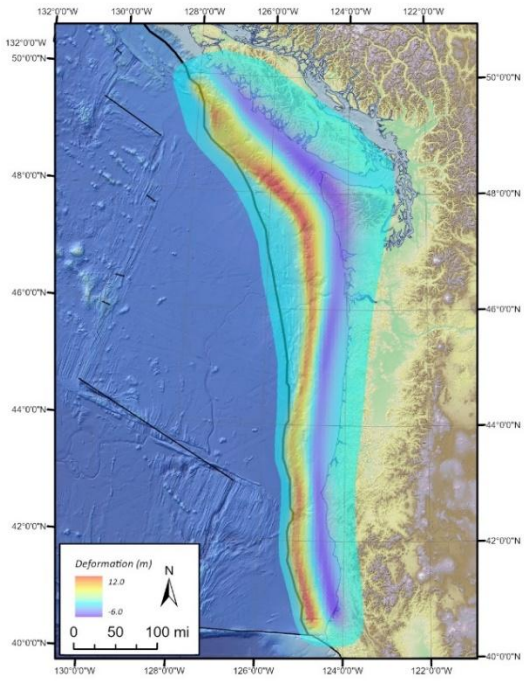
State of Oregon
Oregon Department of Geology and Mineral Industries
Ruarri J. Day-Stirrat, State Geologist

SPECIAL PAPER SP-56

MODELING 2,475-YEAR RECURRENCE INTERVAL PROBABILISTIC TSUNAMI HAZARD FOR THE CENTRAL TO NORTHERN OREGON COAST

by Jonathan C. Allan[1], Y. Joseph Zhang[2], Hong Kie Thio[3], Fletcher E. O'Brien[4], and George R. Priest[2]



2026

[1]Oregon Department of Geology and Mineral Industries, Coastal Field Office, P.O. Box 1033, Newport, OR 97365
[2]Virginia Institute of Marine Science, College of William & Mary, Center for Coastal Resource Management, 1375 Greate Road, Gloucester Point, VA 23062
[3]AECOM Technical Services, One California Plaza, 300 S. Grand Ave, Los Angeles, CA 90071
[4]Oregon Department of Geology and Mineral Industries, 800 NE Oregon Street, Suite 965, Portland, OR 97232

DISCLAIMER

This product is for informational purposes and may not have been prepared for or be suitable for legal, engineering, or surveying purposes. Users of this information should review or consult the primary data and information sources to ascertain the usability of the information. This publication cannot substitute for site-specific investigations by qualified practitioners. Site-specific data may give results that differ from the results shown in the publication.

WHAT'S IN THIS REPORT?

This study evaluates new 2,475-yr probabilistic tsunami modeling undertaken for three Oregon Coast counties: Clatsop, Tillamook, and Lincoln Counties. The objective of this modeling is to update the American Society of Civil Engineers (ASCE) tsunami design zone maps originally developed for Oregon in 2016. Improvements to these data will help guide future design of potential new vertical evacuation refuges on the Oregon Coast.

Cover photo: Cascadia Subduction Zone deformation model depicting >10 m of vertical seafloor uplift offshore the Oregon coast.



Expires: 11/30/2026

Oregon Department of Geology and Mineral Industries Special Paper SP-56
Published in conformance with ORS 516.030

DOGAMI Administrative Offices
800 NE Oregon Street, Suite 965
Portland, OR 97232
Telephone (971) 673-1555
https://www.oregon.gov/DOGAMI/

TABLE OF CONTENTS

Executive Summary **1**

1.0 Introduction **1**

1.1 Study Motivation 7

2.0 Background On PTHA Approaches And CSZ Source Characterization **9**

2.1 Previous PTHA Modeling 9
2.2 CSZ Sources 11
2.3 ASCE7-28 PTHA Update 21

3.0 Oregon Coast High-Resolution Tsunami Modeling **26**

3.1 Model DEM Development 27
3.2 SCHISM Model Parameters 29
3.3 Tsunami 2,475-yr Source Models 29
3.4 Model Runs 31
3.5 Simulation Outputs 36

4.0 Results **37**

4.1 Offshore Design Wave and Inundation Comparisons 38
4.2 Final Scenarios Used to Produce New 2,475-year Inundation Zones 55
4.3 Coseismic Responses 55
4.4 Revised Central to Northern Oregon Coast 2,475-yr Inundation Maps 61

5.0 Discussion **84**

6.0 Conclusion **90**

7.0 Acknowledgments **91**

8.0 References **92**

9.0 Appendix A: Report On Benchmark Results From SCHISM **97**

9.1 Introduction 97
9.2 Model Description 97
9.3 Benchmark Results 100
9.4 Lessons Learned 122
9.5 Acknowledgements 122
9.6 References 122

10.0 Appendix B: Procedures Used To Produce The Updated GIS **125**

10.1 Approach Used to Generate the Oregon Coast TDZ 125
10.2 NOAA-NCEI Tsunami Model Bathymetry/Topography Source DEM for Oregon 126
10.3 Process to Generate the Overwash Inundation Depth Points 127
10.4 Process to Generate the Runup Elevation Points 127

LIST OF FIGURES

Figure 1-1. Location map of the central to northern Oregon Coast showing key place names and offshore point locations 3
Figure 1-2. Updated CSZ logic tree 4
Figure 2-1. Earthquake rupture types used in developing a PTHA for Cascadia 12
Figure 2-2. End-member models of seafloor uplift that most commonly trigger tsunami 13
Figure 2-3. Examples of whole-margin deep and shallow buried models 15
Figure 2-4. Map showing the primary dip direction rupture boundaries 16

Figure 2-5. Examples of whole-margin splay-fault rupture models 18
Figure 2-6. Example Triangular Irregular Network (TIN) of the CSZ megathrust 22
Figure 2-7. Comparison of ASCE7-22 (red) and proposed new ASCE7-28 (blue) tsunami amplitudes for a 2,475-yr Cascadia event striking the PNW coast. 25
Figure 2-8. Latest 2,475-yr tsunami amplitudes calculated for the PNW coast. 26
Figure 3-1. Example of the approach used to validate horizontal model grid resolution in northern Clatsop County 28
Figure 3-2. Disaggregated 2,475-yr CSZ source model validation 30
Figure 3-3. Example 2,475-yr CSZ source model showing the calculated deformation and slip. 31
Figure 3-4. Seven 2,475-yr CSZ deformation models evaluated in this study 34
Figure 3-5. Profiles of different 2,475-yr earthquake deformation models used in the Cascadia tsunami simulations 35
Figure 3-6. Various terms used to define a tsunami wave form. 37
Figure 4-1. Comparison of simulated tsunami amplitudes and moving averages for the 2,475-year tsunami design wave and various source models offshore Clatsop County. 39
Figure 4-2. Two models of 2,475-yr tsunami inundation affecting Seaside and the Clatsop Plains 40
Figure 4-3. Comparison of simulated tsunami amplitudes and moving averages for the 2,475-year tsunami design wave and three adjusted source models for Clatsop County. 42
Figure 4-4. Change in tsunami inundation at Seaside due to scaling the Run02f scenario by 10%. 43
Figure 4-5. Time series of tsunami waves produced by Run02c and Run02g for select water depths along a transect offshore at Seaside. 44
Figure 4-6. Comparison of model flow depths at A) Seaside and B) Cannon Beach, Clatsop County 45
Figure 4-7. Plot showing simulated tsunami amplitudes for various model runs offshore Tillamook County and calculated moving averages determined for the 2,475-yr tsunami design wave and the various source simulations. 47
Figure 4-8. Two scenarios of 2,475-yr tsunami inundation affecting Rockaway Beach and the city of Tillamook, Tillamook County 48
Figure 4-9. Comparison of model flow depths at Rockaway Beach and Tierra Del Mar, Tillamook County 49
Figure 4-10. Plot showing simulated tsunami amplitudes for various model runs offshore Lincoln Countyand calculated moving averages determined for the 2,475-yr tsunami design wave and various source simulations. 51
Figure 4-11. Comparison of simulated tsunami amplitudes and moving averages for the 2,475-year tsunami design wave and three adjusted source models. 52
Figure 4-12. Two scenarios of 2,475-yr tsunami inundation affecting Lincoln City, Siletz Bay, Waldport, Alsea Bay, Lincoln County 53
Figure 4-13. Comparison of model flow depths at Gleneden Beach State Park, South Beach State Park, and Hatfield Marine Science Center, Lincoln County 54
Figure 4-14. Estimates of the 2,475-yr probabilistic subsidence, along with subsidence estimates determined for the various deformation models. 56
Figure 4-15. Estimates of coastal subsidence determined for the Run02c and Run02g Clatsop County simulations 58
Figure 4-16. Estimates of coastal subsidence determined for the Run01c and Run01i Tillamook County simulations 59
Figure 4-17. Estimates of coastal subsidence determined for the Run01c and Run02d Lincoln County simulations 60
Figure 4-18. Change in the 2,475-yr tsunami design zone proposed for Astoria, Clatsop C. 62
Figure 4-19. Change in the 2,475-yr tsunami design zone proposed for Warrenton, Clatsop Co. 63

Figure 4-20. Change in the 2,475-yr tsunami design zone proposed for Seaside and Gearhart, Clatsop County 64
Figure 4-21. Change in the 2,475-yr tsunami design zone proposed for Cannon Beach, Clatsop Co. 65
Figure 4-22. Change in the 2,475-yr tsunami design zone proposed for Arch Cape, Clatsop Co. 66
Figure 4-23. Change in the 2,475-yr tsunami design zone proposed for Manzanita, Nehalem, and Wheeler, Tillamook County 67
Figure 4-24. Change in the 2,475-yr tsunami design zone proposed for Rockaway Beach, Tillamook County. 68
Figure 4-25. Change in the 2,475-yr tsunami design zone proposed for Garibaldi and Bay City, Tillamook County. 69
Figure 4-26. Change in the 2,475-yr tsunami design zone proposed for Tillamook, Tillamook County. 70
Figure 4-27. Change in the 2,475-yr tsunami design zone proposed for Netarts Bay, Tillamook County. 71
Figure 4-28. Change in the 2,475-yr tsunami design zone proposed for Pacific City, Tillamook County. 72
Figure 4-29. Change in the 2,475-yr tsunami design zone proposed for Lincoln City, Lincoln County. 73
Figure 4-30. Change in the 2,475-yr tsunami design zone proposed for Lincoln Beach and Gleneden Beach, Lincoln County. 74
Figure 4-31. Change in the 2,475-yr tsunami design zone proposed for Depoe Bay, Lincoln County. 75
Figure 4-32. Change in the 2,475-yr tsunami design zone proposed for Newport, Lincoln County. 76
Figure 4-33. Change in the 2,475-yr tsunami design zone proposed for Seal Rock, Lincoln County. 77
Figure 4-34. Change in the 2,475-yr tsunami design zone proposed for Bayshore and Waldport, Lincoln County. 78
Figure 4-35. Change in the 2,475-yr tsunami design zone proposed for Yachats, Lincoln County 79
Figure 4-36. ECDF plots of tsunami runup elevations determined for Clatsop, Tillamook, and Lincoln Counties. 81
Figure 4-37. ECDF plots of tsunami flow depths along barrier spits backed by estuaries in Tillamook and Lincoln Counties. 83
Figure 5-1. Profiles of 2,475-yr earthquake vertical deformation, slip, and geometry models used in the latest CSZ tsunami simulations, compared with the original DOGAMI XXL scenarios developed by Witter and others (2011) 85
Figure 5-2. Comparison of the downdip limits of coseismic slip 86
Figure 5-3. Comparison of original DOGAMI XL2 (shallow), XL3 (deep buried), and Gao_AexpBDUpSU rupture models in Clatsop County, compared to the new 2,475-yr rupture models. 88
Figure 5-4. Map of Cascadia showing the seismogenic zone and the 350°C and 450°C isotherms on the plate boundary 89
Figure 9-1. Inundation algorithm in SCHISM. 99
Figure 9-2. Domain sketch for BP1. 100
Figure 9-3. Comparison of surface profiles at various times for the non-breaking wave, case A (H/d = 0.0185) of BP1. 101
Figure 9-4. Comparison of elevation time series at two locations for BP1.. 103
Figure 9-5. Convergence test for case A of BP1 at a time near the maximum runup and rundown 104
Figure 9-6. Schematics of the composite beach and locations of gauges used in BP2. 105
Figure 9-7. Comparison of elevation time history at 8 stations for case A of BP2.. 106
Figure 9-8. Comparison of surface profiles for case A of BP4. 107
Figure 9-9. Comparison of surface profiles for breaking-wave case C (H/d = 0.3) of BP4. 108
Figure 9-10. Runups as a function of the incident wave height for BP4. 108
Figure 9-11. Comparison of elevation time series for case A (L45 = 2.40 m) of BP5. 109
Figure 9-12. Comparison of elevation time series for case B (L45 = 0.98 m) of BP5. 110

Figure 9-13. Comparison of elevation time series for case C (L45 = 0.64 m) of BP5. 111
Figure 9-14. Comparison of elevation time series at 4 gauges for 3 cases of BP6 112
Figure 9-15. Nodes in the unstructured grid used in BP6. 112
Figure 9-16. Comparison of runups around the conical island for the 3 cases of BP6. 114
Figure 9-17. Comparison of runups around the conical island for the 3 cases of BP6, in spatial form. 115
Figure 9-18. Comparison of elevations at 3 gauges in front of the valley. 116
Figure 9-19. Inundation sequence near the narrow valley in BP7. 117
Figure 9-20. (a) Bathymetry as embedded in DEMs used in BP9; (b) unstructured grid and (c) zoom-in around the Okushiri Island. 117
Figure 9-21. Comparison of elevations at 2 tide gauges in BP9. 118
Figure 9-22. (a) Comparison of runups around the island in BP9. (b) Model predicted runups around the island. 119
Figure 9-23. Arrival of 2 waves at Aonae in BP9. 121
Figure 10-1. Example maps comparing the unmodified “raw” TDZ to the smoothed TDZ. 125

LIST OF TABLES

Table 3-1. Clatsop 2,475-yr disaggregated CSZ tsunami scenarios. 32
Table 3-2. Tillamook 2,475-yr disaggregated CSZ tsunami scenarios. 32
Table 3-3. Lincoln 2,475-yr disaggregated CSZ tsunami scenarios. 33
Table 4-1. CSZ scenarios adopted for the creation of the final 2,475-yr tsunami design zone in Clatsop, Tillamook, and Lincoln Counties. 55
Table 4-2. Change in probabilistic 2,475-yr tsunami inundation zone area for the central to northern Oregon Coast, relative to the existing ASCE7-22 tsunami design zone. 61
Table 9-1. BP1 model errors for surface profiles at t = [35, 40, 45, 50, 55, 60, 65], with respect to the analytical solution for H/d = 0.0185, as simulated by SELFE and SCHISM. 102
Table 9-2. BP1 model errors at two stations (x = 9.95 and x = 0.25) with respect to the analytical solution for H/d = 0.0185, as simulated by SELFE and SCHISM. 103
Table 9-3. BP4 model errors with respect to the lab experiment data a) surface profile for Case A, H/d = 0.0185 as simulated by SELFE and SCHISM. 107
Table 9-4. Error statistics for the 3 cases of BP6. 113
Table 9-5. Error statistics for runups for the 3 cases of BP6. 115
Table 9-6. Runup errors from SCHISM and SELFE (the latter from NTHMP 2012 report) for BP9. 120

GEOGRAPHIC INFORMATION SYSTEM (GIS) DATA

See the digital publication folder for files.
Geodatabase is Esri® ArcGIS Pro version 3.5 format. Metadata is embedded in the geodatabase and is also provided as a separate .xml format file.

PTHA_Clatsop_Run02c.gdb

Vector layers:

Run02c_Inundation (polygon)
Run02c_Points_Main (point)
Run02c_Points_Max_MF_Min_Depth (point)

Raster layers:

Run02c_Raster_Max_MF
Run02c_Raster_Flow_Depth
Run02c_Raster_Elev_NAVD88
Run02c_Raster_Elev_MHW
Run02c_Raster_Max_Vel_Ms
Run02c_Raster_Init_D_MHW
Run02c_Raster_Post_D_MHW

PTHA_Clatsop_Run02g.gdb

Vector layers:

Run02g_Inundation (polygon)
Run02g_Points_Main (point)
Run02g_Points_Max_MF_Min_Depth (point)

Raster layers:

Run02g_Raster_Flow_Depth
Run02g_Raster_Elev_NAVD88
Run02g_Raster_Elev_MHW
Run02g_Raster_Max_Vel_Ms
Run02g_Raster_Init_D_MHW
Run02g_Raster_Post_D_MHW
Run02g_Raster_Max_MF

PTHA_Tillamook_Run01c.gdb

Vector layers:

Run01c_Inundation (polygon)
Run01c_Points_Main (point)
Run01c_Points_Max_MF_Min_Depth (point)

Raster layers:

Run01c_Raster_Flow_Depth
Run01c_Raster_Elev_NAVD88
Run01c_Raster_Elev_MHW

Run01c_Raster_Max_Vel_Ms
Run01c_Raster_Init_D_MHW
Run01c_Raster_Post_D_MHW
Run01c_Raster_Max_MF

PTHA_Tillamook_Run01i.gdb

Vector layers:

Run01i_Inundation (polygon)
Run01i_Points_Main (point)
Run01i_Points_Max_MF_Min_Depth (point)

Raster layers:

Run01i_Raster_Flow_Depth
Run01i_Raster_Elev_NAVD88
Run01i_Raster_Elev_MHW
Run01i_Raster_Max_Vel_Ms
Run01i_Raster_Init_D_MHW
Run01i_Raster_Post_D_MHW
Run01i_Raster_Max_MF

PTHA_Lincoln_Run01c.gdb

Vector layers:

Run01c_Inundation (Polygon)
Run01c_Points_Main (Point)
Run01c_Points_Max_MF_Min_Depth (Point)

Raster layers:

Run01c_Raster_Flow_Depth
Run01c_Raster_Elev_NAVD88
Run01c_Raster_Max_Vel_Ms
Run01c_Raster_Elev_MHW
Run01c_Raster_Init_D_MHW
Run01c_Raster_Post_D_MHW
Run01c_Raster_Max_MF

PTHA_Lincoln_Run02d.gdb

Vector layers:

Run02d_Inundation (Polygon)
Run02d_Points_Main (Point)
Run02d_Points_Max_MF_Min_Depth (Point)

Raster layers:

Run02d_Raster_Flow_Depth
Run02d_Raster_Elev_NAVD88
Run02d_Raster_Max_Vel_Ms
Run02d_Raster_Elev_MHW
Run02d_Raster_Init_D_MHW

Run02d_Raster_Post_D_MHW
Run02d_Raster_Max_MF

UNITS OF MEASUREMENT

The intended audience for this report is scientists, public safety agencies, and decision makers at the community, county, tribal, state, and federal levels. Therefore, we selected SI (International System) Metric units as the primary units. A conversion table for U. S. Customary units is included for easier conversion where needed.

U.S. Customary Units to SI (International System) Metric

	Original Units	Conversion Equation	To Obtain
length:	inch (in)	in × 25.4	millimeter (mm)
—	inch (in)	in × 2.54	centimeter (cm)
—	mile (mi)	mi × 1.609	kilometer (km)
area:	square mile (mi^2)	mi^2 × 2.590	square kilometer (km^2)
—	acre (ac)	ac x 0.004	square kilometer (km^2)
volume:	cubic ft (ft^3)	ft^3 × 0.028	cubic meter (m^3)
seismic moment:	dyne-centimeters (dyn cm)	$\mathrm{dyn\ cm} \times 10^7$	Newton-meters (Nm)

EXECUTIVE SUMMARY

The objective of this study has been to produce updated 2,475-yr average return period (ARP) probabilistic tsunami hazard analysis (PTHA) maps for the central to northern Oregon Coast, including Clatsop County, Tillamook County, and Lincoln County. The new maps incorporate improved Cascadia earthquake rupture models developed in the past five years, improved bathymetric and topographic digital elevation models produced by NOAA's National Center for Environmental Information (NCEI), and high-resolution tsunami inundation modeling.

We modeled seven disaggregated Cascadia subduction zone (CSZ) deformation models that were scaled to meet the minimum requirements of a 2,475-yr earthquake rupture. Calculated earthquake moment magnitudes (M_W) ranged from 9.02 to 9.22, with maximum slip offshore of the northern Oregon Coast ranging from 38–42 m. The rupture scenarios evaluated in this study included:

- A full-margin deep rupture with a downdip limit constrained to the 1 cm/yr locking contour
- Two different full-margin shallow buried ruptures with downdip extents located halfway between the fully locked zone from thermal modeling and the 1 cm/yr locking contour
- A full-margin 100% trench breaching rupture with a downdip extent constrained to the 1 cm/yr locking contour
- A full-margin splay fault rupture with a downdip extent constrained to the 1 cm/yr locking contour
- A segment C deep buried rupture with a downdip extent constrained to the 1 cm/yr locking contour

In total, some 26 tsunami simulations were performed, including a reevaluation of rupture scenarios (XL2 shallow buried and XL3 deep buried rupture models) originally produced by DOGAMI between 2010 and 2013. From the simulated results, the authors produced new GIS data showing tsunami inundation zones for a 2,475-yr ARP tsunami that span multiple scenarios, rasters that depict the simulated flow depths and maximum water levels as well as rasters of tsunami-generated currents and momentum flux, and other derivative products. Combined, these data are intended for use and adoption by the ASCE Tsunami Loads Committee to replace the existing ASCE7-22 Tsunami Design Zone (TDZ) and geodatabases produced for Oregon in 2016. With the modeling now complete, the timeline for adoption of the new maps by the full ASCE committee is 2028. Once adopted, the new 2,475-yr ARP tsunami hazard maps and geodatabase will automatically become part of the Oregon Building Codes 2019 Oregon Structural Specialty Code (OSSC) and will be accessible through the ASCE tsunami hazard tool.

1.0 INTRODUCTION

The Oregon Department of Geology and Mineral Industries (DOGAMI) is responsible for the production of technical maps and products that address tsunami hazards in the State of Oregon. This report introduces new probabilistic tsunami hazard modeling and mapping undertaken for Clatsop, Tillamook, and Lincoln Counties on the northern to central Oregon Coast (**Figure 1-1**). Specifically, the objective of this study is to update the existing 2,475-year average return period (ARP) Tsunami Design Zone (TDZ) maps adopted in 2016 for the Oregon Coast by the American Society of Civil Engineers (ASCE) 7-16 Standards and Commentary process (ASCE, 2017). The TDZ has a 2% probability of being exceeded in a 50-year period and is used by engineers when designing Risk Category III and IV buildings located in the tsunami hazard zone. Such buildings may include large buildings having an occupancy greater than 300 people, schools,

fire stations, designated emergency preparedness centers, hospitals, and vertical evacuation structures (VES). As a result, the ASCE TDZ is a different product than the tsunami inundation and evacuation maps developed by DOGAMI between 2010 and 2013 (e.g., Witter and others, 2011; Priest and others, 2013). Priest and Allan (2019) expressed several concerns with the original ASCE 7-16 tsunami maps. These concerns included 1) the very coarse 60-m grids used in the tsunami modeling and 2) the exclusion of splay faulting and DOGAMI source models (e.g., Witter and others, 2011) from the Cascadia earthquake source models. These concerns are the impetus for this latest tsunami modeling effort.

To address known gaps in the original ASCE7-16 modeling, a joint U.S. Geological Survey (USGS) and National Tsunami Hazard Mitigation Program (NTHMP) workshop was held in May 2022 at the USGS Powell Center in Fort Collins, Colorado. The workshop brought together scientific experts in paleoseismology, Cascadia geophysics, earthquake fault mechanics, geology, and hydrodynamic modeling (Patton and others, 2022). The goal of the workshop was to produce a new earthquake/tsunami logic tree (**Figure 1-2**) for performing updated probabilistic tsunami hazard analysis (PTHA) for Cascadia. Despite the presence of a few gaps in the final logic tree, the overarching goal of the workshop was achieved.

Following the Cascadia Powell Center workshop, DOGAMI contracted with technical experts at the University of Victoria, Canada, to help construct new Cascadia deformation and slip model sources guided by the updated logic tree. To facilitate that process, a Cascadia Sources Working Group (CSWG) was established to provide technical guidance on those components of the earthquake/tsunami logic tree (**Figure 1-2**) not finalized at the 2022 USGS/NTHMP Powell Center meeting. With input from the CSWG, Sypus and Wang (2024) eventually constructed 3,502 geometrically unique CSZ source scenarios using best available science.

Having completed the suite of CSZ source scenarios, Dr. Hong Kie Thio of AECOM led the actual PTHA and modeling, completing the process in early 2025. The results of Thio (2026) included the production of revised offshore tsunami hazard curves defined for discrete point locations located in deep (≥ ~100 m) water offshore of the U.S. Pacific Northwest Coast (PNW; **Figure 1-1**).

The final phase in the PTHA modeling was the detailed inundation modeling derived from the disaggregated Cascadia source scenarios that approximate a 2,475-year ARP earthquake and tsunami; these scenarios are described in this report. The DOGAMI 2,475-yr tsunami modeling and inundation maps were developed using updated, higher-resolution bathymetric and topographic grids and have been vetted by DOGAMI staff and a Technical Advisory Committee. DOGAMI is providing the results of our inundation modeling and inundation maps to the ASCE7 Tsunami Loads and Effects Subcommittee for integration into a proposed Version 2028-1.0 update of the ASCE Tsunami Design Geodatabase. The upgraded TDZ maps and geodatabase will improve the implementation of the Oregon Building Code (OBC).

Figure 1-1. Location map of the central to northern Oregon Coast showing key place names and offshore point locations (colored circles) used to define probabilistic tsunami hazard curves. Green and black circles with pink borders highlight those points that overlap across model domains. Inset map depicts plate convergence rates (mm/year) defined by Scholz (2014).

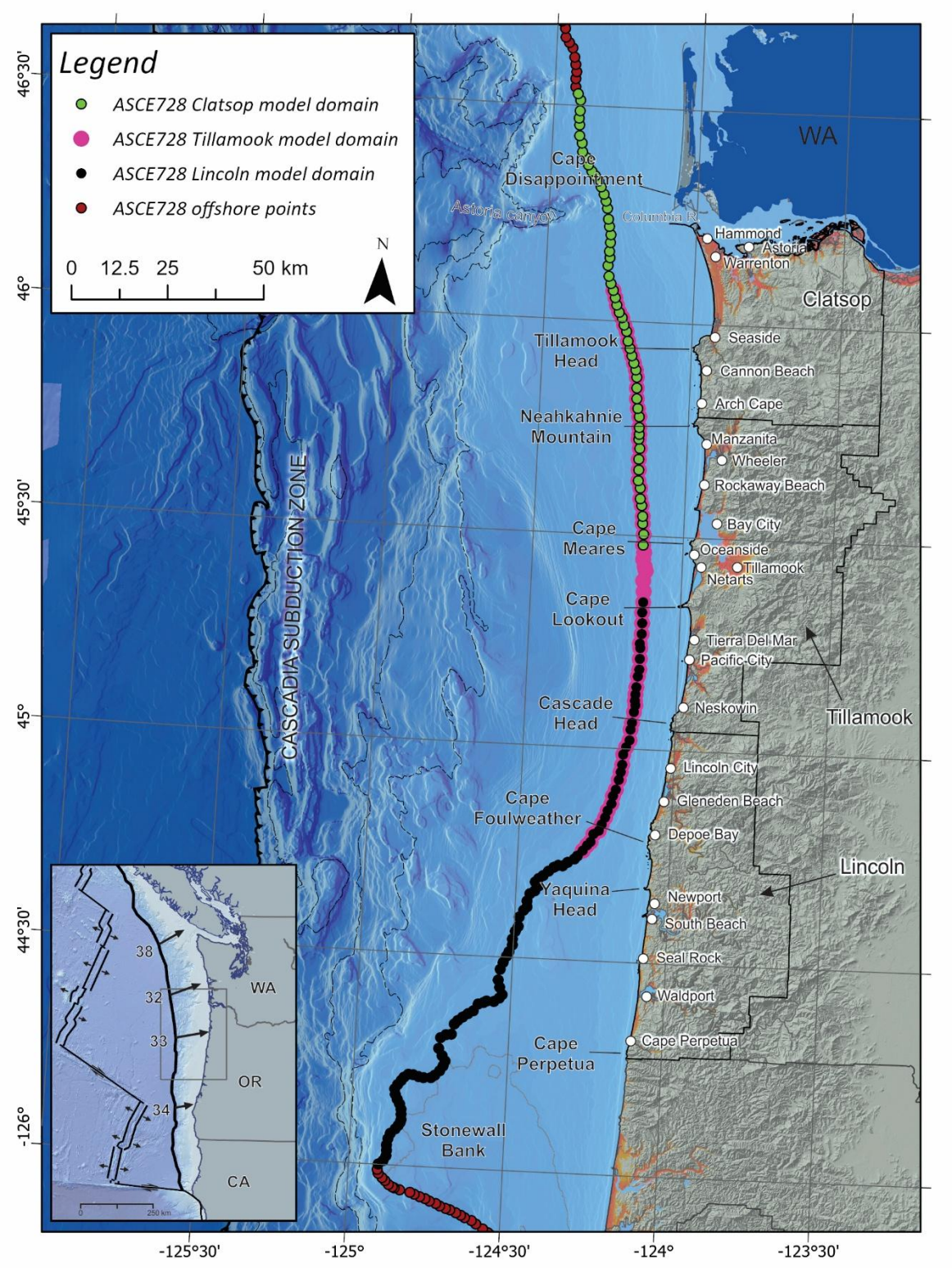


Figure 1-2. Updated CSZ logic tree (modified from Sypus and Wang, 2024). Click here to view a PDF of this figure accessible by screen reader.

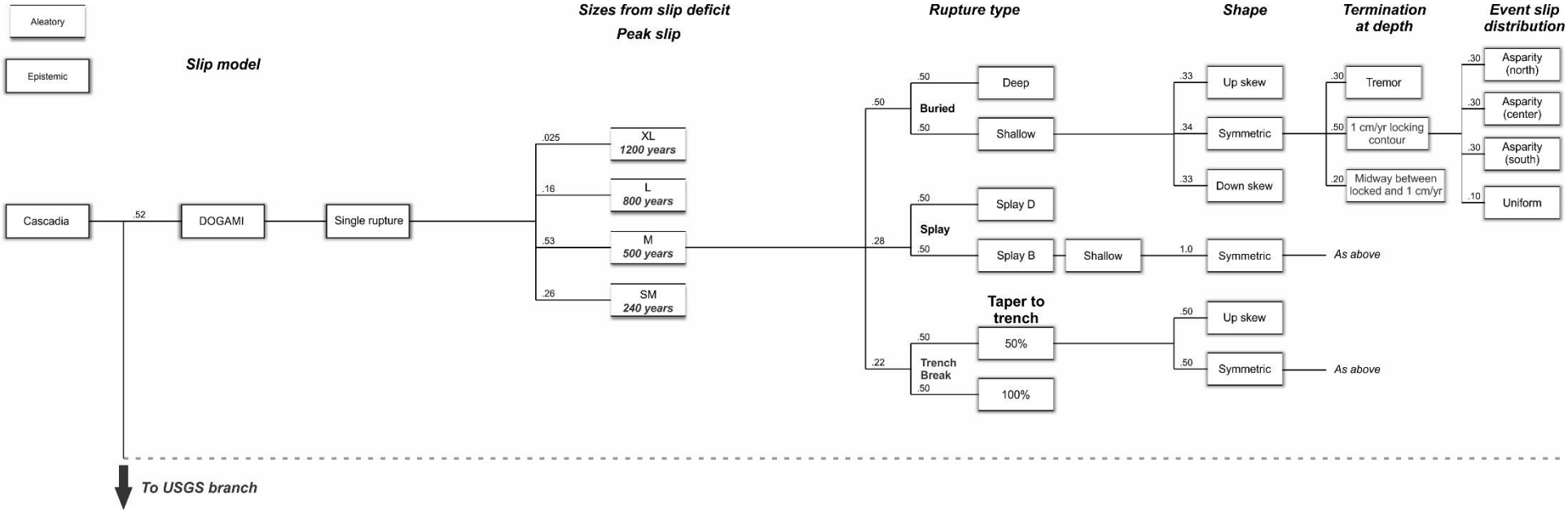


Figure 1-2 (cont.). Updated CSZ logic tree, USGS branch (modified from Sypus and Wang, 2024). Click here to view a PDF of this figure accessible by screen reader.

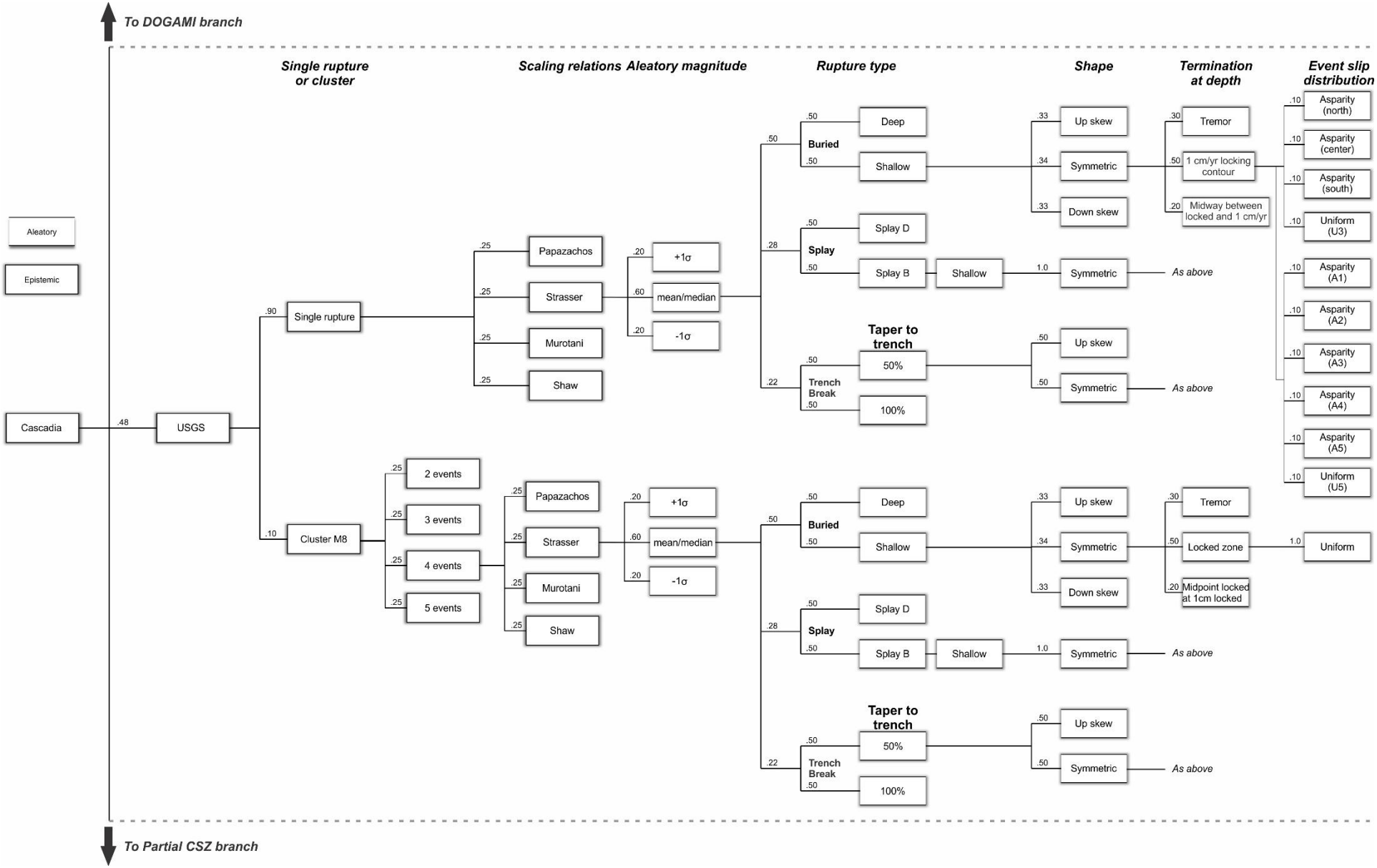
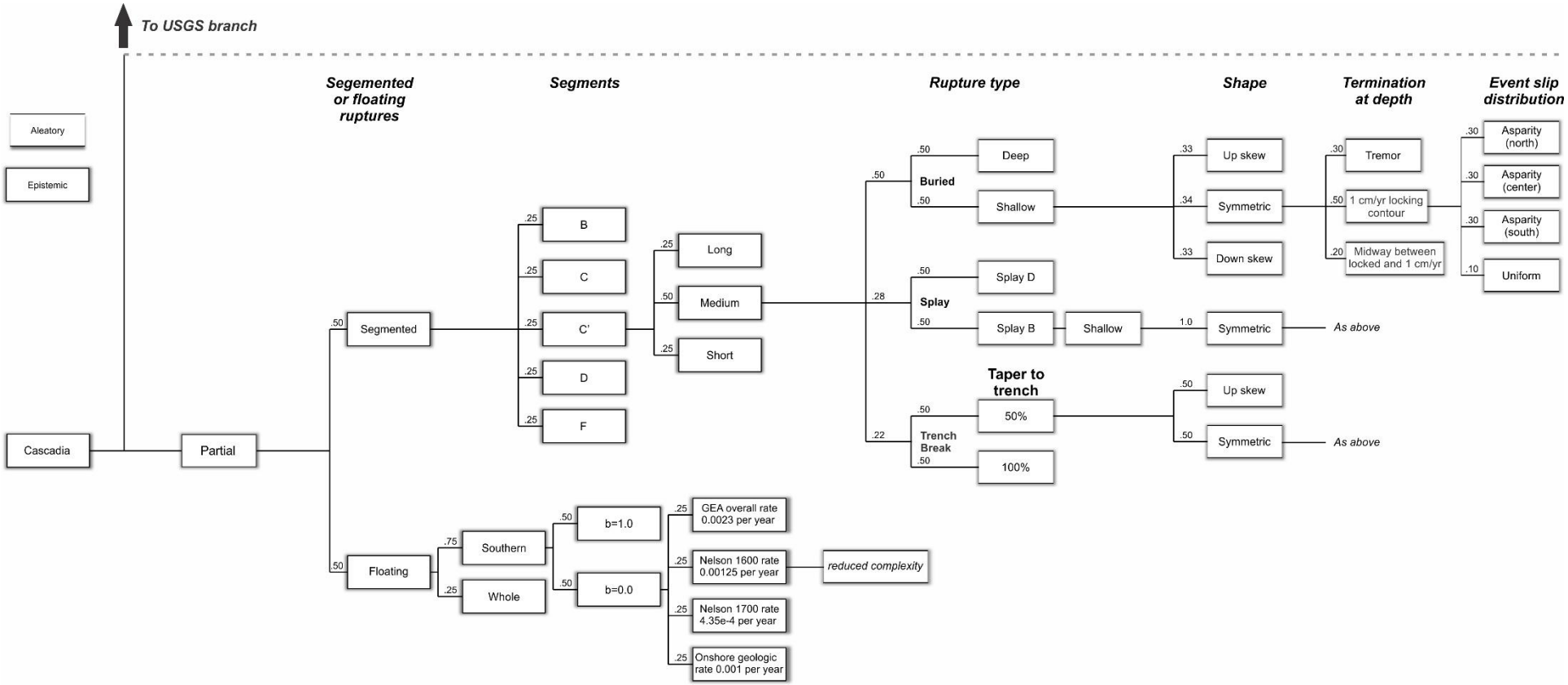


Figure 1-2 (cont.). Updated CSZ logic tree, partial rupture branch (modified from Sypus and Wang, 2024). Click here to view a PDF of this figure accessible by screen reader.



This document provides background information on the new Cascadia earthquake sources, detailed tsunami inundation modeling undertaken by DOGAMI, an evaluation of those scenarios that meet the needs of the ASCE Tsunami Loads Committee and updated TDZ, and ancillary modeling products created by DOGAMI. As described in Wilson and others (2021), three broad areas of investigation characterize the overall PTHA process: source generation, tsunami propagation in deep water using Green's functions, and detailed tsunami inundation modeling. The following steps defined by Wilson and others (2021) describe the entire PTHA process adopted here:

- Source generation
    1. Identification and characterization of the earthquake sources, including both distant and local tsunami sources
    2. Definition of earthquake recurrence models
    3. Production of scenario events that represent the full integration over earthquake magnitudes, rupture locations, and sources for every logic tree branch
- Green's function propagation
    4. Computation of the fundamental Green's functions for every scenario combination as defined in the updated earthquake logic tree (i.e., **Figure 1-2**)
    5. Computation of nearshore (~100–200 m water depths) probabilistic tsunami amplitudes and hazard curves for discrete offshore points along the coast
- Tsunami inundation modeling
    6. Identification of the dominant sources affecting the return period of interest, accomplished through source disaggregation
    7. Computation of probabilistic tsunami inundation hazard areas associated with the return period(s) of interest, achieved by matching the nearshore tsunami amplitudes of step 6 against the design amplitudes determined in Step 5 and then simulating inundation from the best matching source

Section 1.1 of this report provides background information on the existing ASCE 7-22 Standards and Commentary section, production of the original ASCE TDZ maps, and motivation for the DOGAMI update of the TDZ for Oregon. **Section 2.1** introduces previous PTHA studies completed for the U.S. West Coast. **Section 2.2** presents the various CSZ earthquake source models used in the updated tsunami inundation modeling, while **Section 2.3** introduces the PTHA framework developed by co-PI Theo. **Section 3.0** summarizes the numerical model used by DOGAMI to produce new 2,475-yr tsunami hazard maps, along with the CSZ scenarios and their characteristics. **Section 4.0** presents and discusses the model results, review process for the PTHA method, and the overall approach used to evaluate the suite of disaggregated 2,475-yr ARP Cascadia sources. **Section 4.4** presents the final tsunami modeling results and related mapping products developed for the ASCE Tsunami Design Geodatabase (proposed Version 2028-1.0). It also includes maps comparing the areal extent of inundation from this study with the previous ASCE 7-22 TDZ and geodatabase. **Section 5.0** discusses future considerations for needed updates to the overall CSZ logic tree and modeling approach.

1.1 Study Motivation

Tsunami hazards pose significant risk to Oregon Coast communities, especially megathrust earthquakes occurring on the CSZ where it intersects the surface ~50–100 km offshore of the coast. Geologic data indicates that there is a 15–22% chance of a full margin megathrust earthquake occurring in the next 50

years (Goldfinger and others, 2017; Wirth and others, 2025) and a 30–43% chance of a partial rupture affecting the Oregon Coast south of Cape Blanco (Goldfinger and others, 2012; Wirth and others, 2025). Such an earthquake would trigger a catastrophic tsunami that would reach the coast in minutes, with most communities inundated in 24–33 minutes (Allan and O'Brien, 2025). Allan and O'Brien estimate ~4,550 (M1 scenario) to ~14,000 (XXL1 scenario) residents killed, and potentially another ~11,000 (M1) to ~31,700 (XXL1) visitors killed.

Efforts to mitigate this public safety risk in Oregon have largely centered on the dissemination of evacuation brochures, installation of tsunami hazard signage, and considerable education and outreach. However, in several communities where high ground is far away, successful evacuation from the inundation zone presents significant challenges and large numbers of people are likely to be killed. For these locations, construction of vertical evacuation structures (VES) may be the only option for reducing loss of life. Furthermore, disaster resilience in coastal communities requires that certain critical and essential facilities provide structural resilience to collapse (Chock and others, 2016) and remain available for assistance with post-disaster recovery. However, in both situations care must be taken to design such structures so that 1) they survive the earthquake shaking; 2) they withstand the hydrodynamic forces associated with the tsunami, including surviving potential impact forces from debris striking the structure and; 3) they are not overtopped by the tsunami. Although ~18,500 people were killed in the 2011 Tōhoku Japan tsunami (National Police Agency of Japan, 2020), 5,428 people successfully evacuated into VES and designated multi-story buildings (Fraser and others, 2012). The success of VES in Japan is a testament to their recognition and understanding of the tsunami risk and engineering design.

In 2011, the ASCE established the Tsunami Loads and Effects Subcommittee (TLESC) to develop a new chapter in the ASCE 7-16 Standards and Commentary (2017) focusing on the impacts of tsunami on structures (Wilson and others, 2021). That effort included the development of new TDZ maps that were developed for the U.S. West Coast, Alaska, and Hawaii. The tsunami modeling was undertaken through a collaboration between AECOM (Thio and others, 2017), who performed the offshore deepwater modeling and PTHA, and the National Oceanic Atmospheric Administration (NOAA) Pacific Marine Environmental Lab (PMEL), who completed the actual inundation modeling of the TDZ (Wei and others, 2017). The ASCE TDZ was generated by first matching tsunami simulations from disaggregated sources to a probabilistically based offshore tsunami amplitude or "design wave" determined for multiple point locations along the 100-m bathymetric contour (Wilson and others, 2021). Once the "wiggle matching" was deemed to have fallen within an acceptable range, PMEL modelers performed the final tsunami inundation modeling using 60-m resolution digital elevation model (DEM) grids.

In 2018, the International Building Code adopted the ASCE 7-16 standards and TDZ maps. In January 2022, the Oregon Building Codes Division officially adopted these ASCE 7-16 standards and TDZ maps as an interim amendment to the 2019 Oregon Structural Specialty Code (OSSC). According to ORS 455.447, any Risk Category III and IV buildings (defined in Table 1604.5 of the Oregon Structural Specialty Code) located within the TDZ must be designed and constructed to resist the tsunami loads and effects of the maximum considered tsunami. These requirements are implemented through OSSC Section 1615, which references Chapter 6 of ASCE 7. For ASCE 7 Chapter 6 purposes, the maximum considered tsunami (MCT) is taken as having a 2% probability of being exceeded in a 50-year period or a 2,475-year mean recurrence interval.

2.0 BACKGROUND ON PTHA APPROACHES AND CSZ SOURCE CHARACTERIZATION

This section briefly examines the need for PTHA as well as past studies that have implemented PTHA tsunami modeling for the U.S. West Coast. This is followed by a brief description of recently developed CSZ sources produced by Sypus and Wang (2024) for the region. Finally, the authors summarize the approach developed by co-PI Theo to produce the latest update to the CSZ PTHA adopted by the ASCE, including the development of updated hazard curves for offshore points of interest (POIs) along the PNW coast.

2.1 Previous PTHA Modeling

An acceptable approach for defining tsunami inundation scenarios is to evaluate the historical and geologic record of past tsunamis, from which a conservative event is selected, typically the 'maximum considered' or 'worst credible,' which may then be simulated and used to delineate tsunami evacuation maps (Mori and others, 2018). The written and instrumental records for Oregon are too short to offer much practical information on 2,475-year exceedance events, but geological data are available. The geological record is typically derived from the paleotsunami history recorded in coastal marshes, estuaries, and lakes (e.g., Nelson and others, 2021; Staisch and others, 2024), and from offshore coring of submarine turbidites (e.g., Goldfinger and others, 2017). Integral to this process is an understanding of the geological-geophysical data associated with subduction zones and earthquake rupture characteristics (e.g., Flück and others, 1997; Wang and others, 2003; Hyndman, 2013; Watt and Brothers, 2021; Sypus and Wang, 2024; Wang, 2025). Deterministic scenarios of the desired size can then be developed and modeled (e.g., Witter and others, 2011; Priest and others, 2013). Subsequently, tsunami inundation zones and maps, flow depths, flow velocities, and momentum flux may be defined from these scenarios for eventual use in outreach, risk assessments, engineering design and other situations. However, this approach assumes the completeness of the geological record, which in fact may be limited in quality, duration, accuracy, and scope (Goda and others, 2024). To address these limitations, scientists have increasingly turned to probabilistic modeling to better account for uncertainties in earthquake rupture processes, tsunami generation, recurrence, propagation, and inundation of coastal areas (Mori and others, 2018; Behrens and others, 2021). Rather than dealing with a few deterministic scenarios spanning a limited spectrum of possibilities, PTHA considers hundreds to thousands of combinations of plausible earthquake rupture sequences and their associated tsunami hazards.

Pioneering research undertaken by Geist and Parson (2006) demonstrated the relative benefits of using PTHA for evaluating tsunami hazards. They compared tsunami hazard curves derived from empirical tide-gage measurements with those generated from a limited number of stochastic tsunami simulations. Overall, they showed that stochastic simulations can mitigate the limitations of a sparse empirical record by recovering the kinds of high-amplitude tsunami scenarios that were absent from available observations. They applied this approach to Cascadia by evaluating ~100 synthetic slip distributions around an M9 CSZ event to produce an initial PTHA for the PNW.

TPSWG (2006) developed a pilot probabilistic tsunami hazard assessment for Seaside, Oregon. They evaluated both locally generated CSZ earthquakes and distant earthquake sources from subduction zones around the Pacific Basin. TPSWG characterized these distant sources using a range of plausible tsunamigenic earthquake magnitudes, with average recurrence rates assigned according to Gutenberg-Richter relationships (TPSWG, 2006). For Cascadia, TPSWG (2006) performed a Monte Carlo simulation

using a random sample of earthquake interevent times, drawn from a specified probability distribution of ~MW 9 earthquakes. These data were then compared to the paleotsunami interevent time history. TPSWG then generated numerical tsunami simulations to calculate hazard curves for every grid cell, from which exceedance wave heights for the 1% and 0.2% annual probabilities were interpolated. These data were then contoured and mapped in GIS, resulting in probabilistic tsunami inundation maps for Seaside, both for characteristic CSZ earthquakes and for distant sources. TPSWG (2006) compared their probabilistic hazard assessment with the deterministic tsunami inundation modeling of Priest and others (1997). They found that their PTHA produced higher maximum wave heights for Cascadia earthquakes, largely because it incorporated distributed-slip earthquake source models, compared with uniform slip models used by Priest and others (1997).

A subsequent improvement in PTHA methodology came from Thio and others (2010), who implemented a two-step process to evaluate a PTHA for California that incorporated epistemic uncertainty by using earthquake logic trees. The first step reflected the computation of probabilistic tsunami wave heights along the 100-m bathymetric contour using several thousand scenarios. Aleatory uncertainties were included in their computations by applying a standard deviation to the probabilistic wave heights and tidal elevations. Epistemic uncertainties were accounted for in their earthquake rupture models by varying the segmentation type, amount of slip, down-dip limits, and recurrence, all of which were characterized in an earthquake logic tree. Like Geist and Parson (1996) and TPSWG (2006), Thio and others (2010) used Gutenburg-Richter models to constrain earthquake magnitudes and recurrence. Tsunami propagation in the offshore domain was modeled using Green's functions to resolve the deepwater tsunami wave forms for the suite of scenarios. Hazard curves were then developed for discrete offshore points, from which design wave amplitudes corresponding to specific ARPs (e.g., 975-yr, 2,475-yr) were determined. These results were subsequently used to identify the disaggregated earthquake sources associated with each return period. Finally, fully nonlinear tsunami simulations were performed to produce inundation maps for the specified return periods.

Separately, Gonzales and others (2013) extended the TPSWG (2006) methodology in a PTHA for Crescent City, northern California. Their work reflected an update on previous PTHA studies undertaken in California, improving CSZ sources and the quantification of tidal uncertainty as well as including the 2011 Japan distant tsunami source. Each source was effectively modeled five times to account for different tidal elevations. In contrast to Thio and others (2010), the full suite of inundation models was simulated. This enabled hazard curves to be created for each grid point on land, similar to the approach used by the TPSWG (2006).

Thio and others (2017) expanded on their 2010 approach by applying their methodology across the five U.S. West Coast states, defining the 2,475-year exceedance tsunami event for use in coastal engineering design of critical facilities (i.e., ASCE7-16). The final 2,475-year inundation simulations used 60-m model grids (Thio and others, 2017; Wei and others, 2017), an update to the 120-m grids they used previously (Thio and others, 2010). However, Priest and Allan (2019) questioned several aspects of the methodology. Most notably, they argued that the calculated seismic slip values used to define the 2,475-year event were about twice those of the deterministic scenarios developed by Witter and others (2011), making them difficult to justify within the constraints of Cascadia slip budgets inferred from the 10,000-year paleoseismic record. They further questioned the use of global earthquake scaling relationships to estimate Cascadia earthquake size and slip, arguing that these relationships may not adequately reflect Cascadia-specific geologic constraints. The resulting 2,475-yr tsunami amplitudes equaled or exceeded the most extreme L1 scenario of Witter and others (2013), which at the time was considered to approximate a 3,333-year ARP event based on the geologic record. Other concerns included the grid

resolutions used, which appear to inaccurately simulate tsunami propagation effects around key bathymetric features, such as banks and canyons.

Advancing PTHA toward fully stochastic earthquake source characterization, Melgar and others (2019) used a stochastic approach to evaluate differences between homogenous (simple) and heterogeneous (non-uniform) slip models. Their approach, which used simplified subduction zone geometry and earthquake magnitudes between 7 and 9, found that the homogenous slip models produced lower tsunami energies than heterogeneous models. Furthermore, the homogenous slip models were found to underpredict peak tsunami amplitudes, especially for larger-magnitude earthquakes. However, the use of stochastic slip models in PTHA remains an active area of research and was not adopted for use in the updated CSZ logic tree and revised offshore CSZ hazard curves described further below.

A successful PTHA therefore requires characterization of a range of plausible earthquake sources and incorporation of both aleatory uncertainty (randomness of the physical system) and epistemic uncertainty (limited knowledge of earthquake geophysics). Mori and others (2018) describe three main approaches that may be taken to develop a PTHA: 1) evaluating the historical record or assessing a generally limited number of sources based on expert geologic opinion (e.g., Geist and Parson, 2006; Tsunami Pilot Study Working Group [TPSWG], 2006); 2) developing a logic tree that describes a suite of possible combinations of slip scenarios (full-margin, partial, and floating ruptures), slip distributions, and down-dip extents (e.g., Priest and others, 2009; Thio and others, 2010; Thio and others, 2017; Witter and others, 2013); and 3) generating a suite of synthetic slip distributions that cover many thousands of random combinations (e.g., Melgar, 2021; Small and others, 2025). As noted above, sole reliance on the historical or paleotsunami record could result in underestimating the size of subduction earthquakes and is increasingly less favored as an approach. Furthermore, Mori and others (2018) observe that because knowledge of subduction zones have evolved rapidly in recent years, this necessitates the development of more complex logic trees to account for the increased information on faults (e.g., **Figure 1-2**), which is resulting in the production of many more tsunami models. Such complexities are best accounted for using a PTHA.

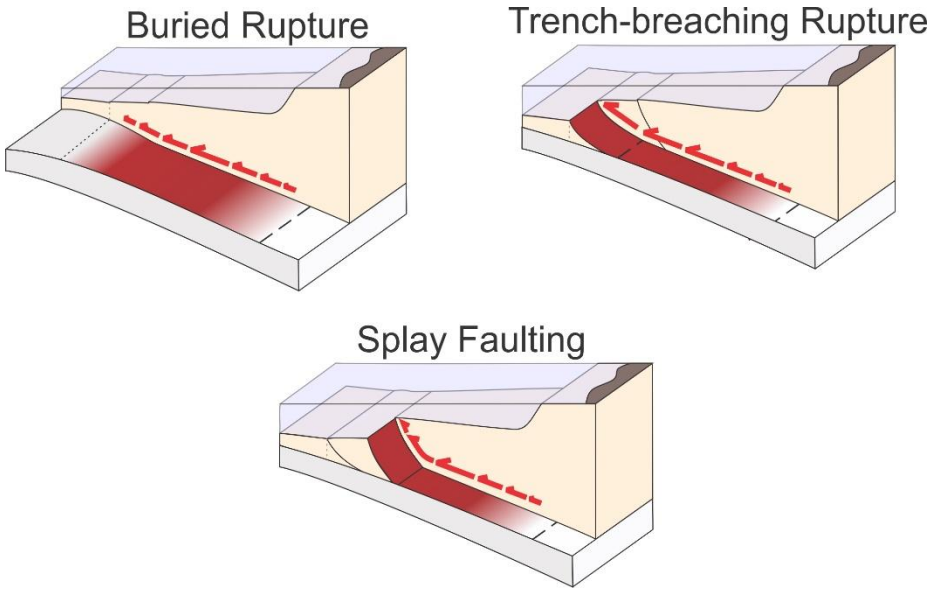
2.2 CSZ Sources

A major undertaking over the past several years has been a reevaluation of the seismic sources used in the PTHA modeling originally performed in ASCE7-16 for Cascadia. To facilitate this process, a joint NTHMP-USGS workshop was convened in May 2022 at the USGS Powell Center facility in Fort Collins, Colorado. An outcome of that meeting was the development of a revised earthquake logic tree for Cascadia that considers earthquake sources developed by the USGS through the NSHM update process, a branch that included the DOGAMI "T-shirt" models, and a third branch that captured partial rupture models (Peterson and others, 2024). However, the revised CSZ logic tree was incomplete since some of the branch details were unable to be fully specified, while many of the branches and parameters were missing assigned weights, needed for the PTHA. To complete the CSZ logic tree (i.e., **Figure 1-2**), DOGAMI contracted with Dr. Kelin Wang at the University of Victoria, Canada, to help build the new CSZ deformation and slip model sources based on the updated CSZ logic tree. Further details describing the overall approach used to produce the new deformation and slip models can be found in the report by Sypus and Wang (2024).

The CSZ source models developed by Sypus and Wang (2024) are broadly based on three potential CSZ rupture types that reflect buried, splay, and trench-breaching scenarios (**Figure 2-1**). Other epistemic uncertainties characterized in **Figure 1-2** are reflected by variations in choice of slip model branches (e.g.,

DOGAMI slip deficit models and USGS scaling relations), along-strike extent (full-margin, clustered, segmented, and floating ruptures), three downdip extents (halfway between the locked zone and 1 cm/yr locking contour, 1 cm/yr locking contour, and top of the tremor zone), and in localization of peak slip. Aleatory uncertainty was also included and is controlled by various distribution functions. The following sections briefly describe how each of the components of the earthquake source models were developed.

Figure 2-1. Earthquake rupture types used in developing a PTHA for Cascadia (Sypus and Wang, 2024).



2.2.1 Revised Megathrust Geometry

The initial focus of Sypus and Wang (2024) was the development of an updated megathrust geometry. This was informed by recently acquired CASIE21 seismic imaging data provided by Carbotte and others (2024), hypocenter locations of low frequency earthquakes (LFE), legacy seismic imaging data from southern Cascadia, and intraslab earthquake hypocenter locations. The CASIE21 data included top of crust (TOC) picks as well as picks of the décollement, which separate sections of subducted and accreted sediment. They first created contours to fit the TOC picks. They then modified the geometry by fitting the décollement picks identified by interpreting margin-normal profiles. Accordingly, the megathrust geometry reflects the TOC in certain places and décollement in others.

Subsequently, Sypus and Wang (20204) used LFE data collected in northern Washington and southern Oregon to help constrain the downdip extent of the megathrust model. Between latitude ~42°N and 47°N (Oregon and southern Washington), they relied on legacy controlled-source seismic data, intraslab earthquake data, and past models of the megathrust geometry (e.g., McCrory and others, 2012). The final megathrust geometry is considerably smoother when compared with the more detailed interpretation of Carbotte and others (2024), although the degree of smoothing remains within the range of depth uncertainties associated with interpretation of the seismic imaging data (Sypus and Wang, 2024). Although smoother, Sypus and Wang argued that the final megathrust model reflects a necessary compromise because a more detailed model could influence tsunami modeling in unrealistic ways.

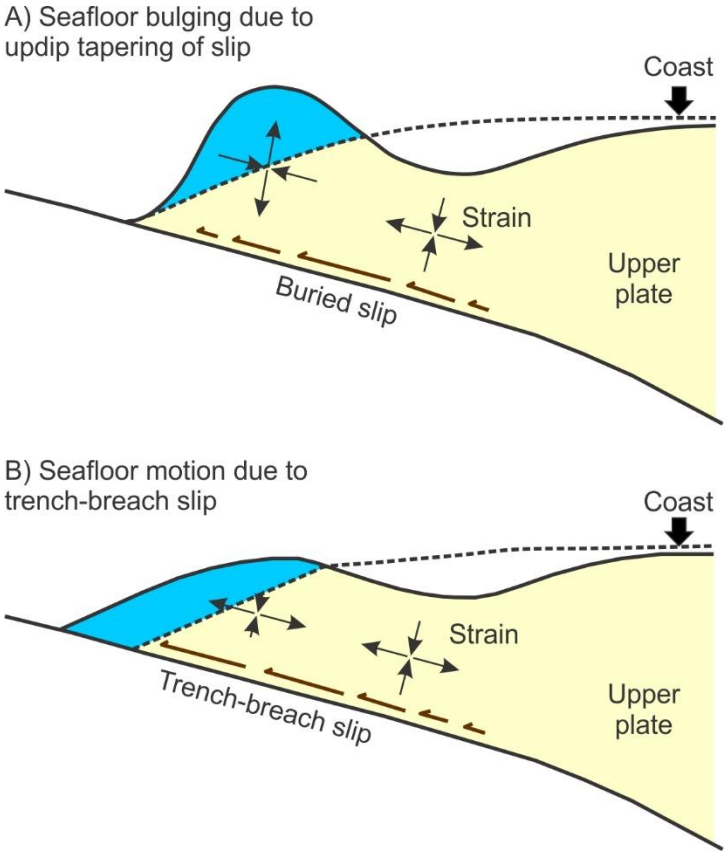
To account for the bathymetric variation of the sea floor above and along the subduction zone, Sypus and Wang (2024) adjusted the dip of the shallowest part of the megathrust model so that the fault depth in a flat-surface model is similar to the actual fault depth below the seafloor. This step is necessary since the deformation models use the point source dislocation model solution of Okada (1985) in a uniform

elastic half-space with a flat upper surface (Sypus and Wang, 2024). Such an adjustment is especially critical for trench-breaching scenarios but is less important for deep buried ruptures, since the latter remain buried under 2–4 km of sediment even after dip adjustment. According to Sypus and Wang (2024), the adjustment modifies the fault dip to approximately the sum of the seafloor slope angle (α) and the actual near-trench fault dip (β). This produces more vertical seafloor deformation near the trench, which is needed in the flat-surface Okada model to compensate for the absence of a seaward movement of the seafloor in the updip direction. Sypus and Wang (2024) note the adjustment results in very accurate results for both buried and trench-breaching rupture scenarios.

2.2.2 Megathrust Tsunami Sources

After establishing the megathrust geometry, the earthquake rupture scenarios used to generate tsunami sources were defined. Wang and others (2024) note that most earthquakes that trigger tsunamis are the product of two end-member scenarios: buried and trench-breaching ruptures. In the buried scenario, the updip decrease in fault slip results in a shortening of the upper plate, which correspondingly produces seafloor uplift (blue shaded region in **Figure 2-2A**). Conversely, in the trench-breaching scenario, slip on a shallow megathrust produces a seaward-directed motion of the sloping sea floor in the updip direction (blue shaded region in **Figure 2-2B**), reduced bulging, and correspondingly less sea floor uplift.

Figure 2-2. End-member models of seafloor uplift that most commonly trigger tsunami: A) buried slip, and B) trench-breach slip (modified from Wang and others, 2024).



2.2.2.1 Buried Rupture Models

The buried rupture models developed by Sypus and Wang (2024) is based on a bell-shaped function proposed by Wang and He (2008), which was found to agree well with slip distributions of real earthquakes. The underlying basis for the model is that coseismic slip decreases updip on the megathrust, due to velocity strengthening behavior of the weakly coupled portion of the seaward part of the megathrust. Accordingly, for this region the slip tapers to zero as it approaches the deformation front; justification for this approach is discussed further in Priest and others (2010). The basic bell shape function is:

$$s(x') = s_o \delta(x')[1 + sin(\pi[\delta(x')]^b)] \qquad (1)$$

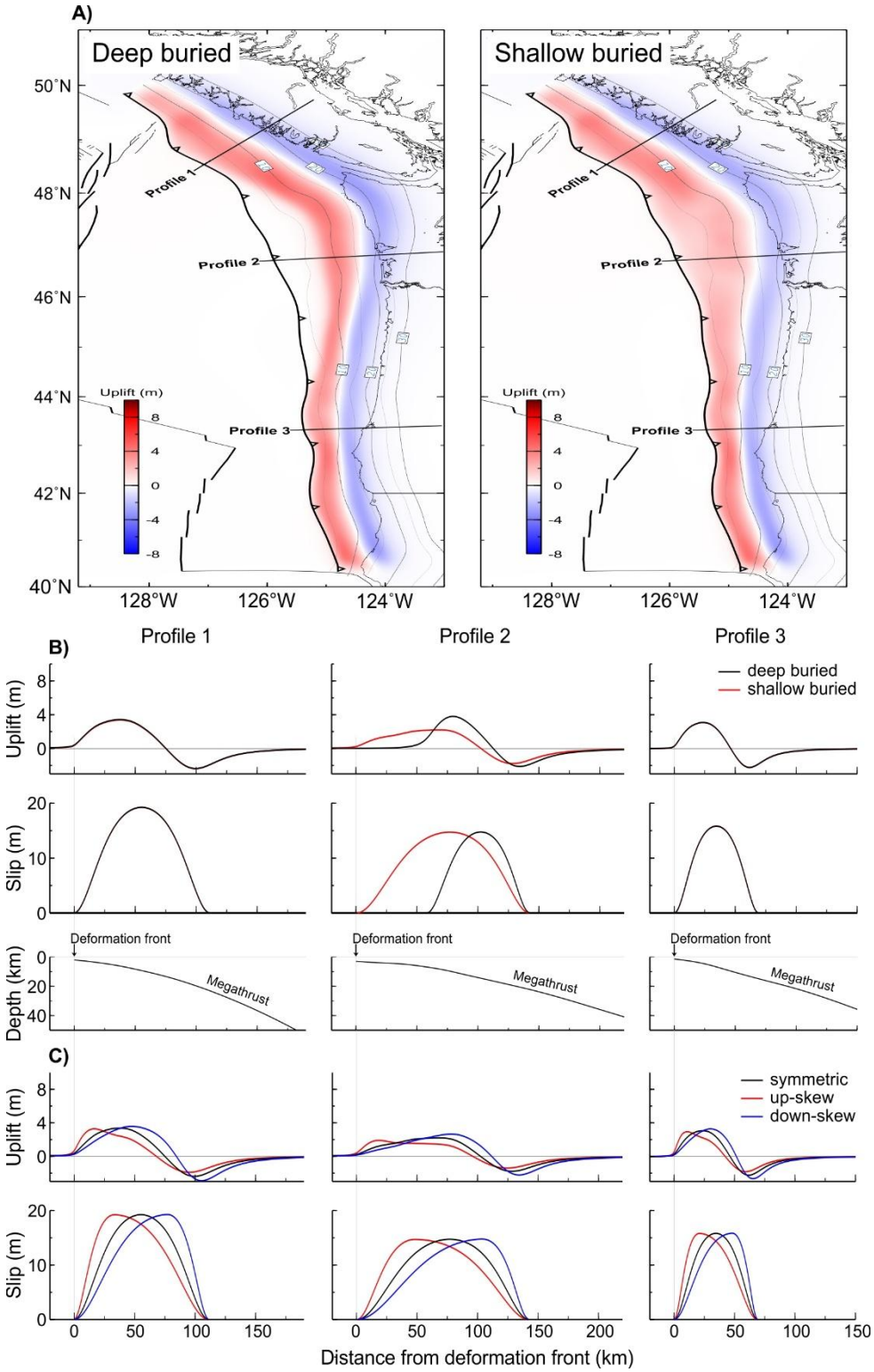
where $x' = x/W$ is the downdip distance x from the upper edge of the rupture zone, normalized by the downdip width W, s_o = peak slip, b is a broadness parameter that ranges from 0 to 0.3, and $\delta(x')$ is defined by:

$$\delta(x') = \begin{cases} \frac{6x'^2}{q^3}\left(\frac{q}{2} - \frac{x'}{3}\right) & 0 \le x' \le q \\ \frac{6(1-x')^2}{(1-q)^3}\left(\frac{1-q}{2} - \frac{1-x'}{3}\right) & q \le x' \le 1 \end{cases} \qquad (2)$$

where q is a skewness parameter ranging from 0 to 1. The skewness parameter causes the bell shape to be skewed in either the updip or downdip directions and is a particularly important parameter. In tsunami modeling, skewness strongly influences the shape of the deformed seafloor and thus the generation of the tsunami, its propagation, and eventual runup (Carvajal and others, 2022). The inclusion of Eq. 2 in Eq. 1 was to introduce the broadness term. Hence, if b = 0, Eq. 1 reduces to Eq. 2, which gives a slip distribution characterized by a narrow peak.

The buried (B) rupture models reflect two types (**Figure 2-3**): deep (D) and shallow (S). In general, the width of slip in the deep buried model is narrower between ~44°N and 48°N when compared with the shallow model (compare left and right plots **Figure 2-3A**). This produces greater uplift over the narrow section that is closer to shore (see profile 2 in **Figure 2-3B**), a function of greater horizontal shortening of the upper plate due to the fault slip decreasing rapidly in the updip direction. As a result, the buried rupture model is expected to produce a larger tsunami between ~44°N and 48°N. Variations in skewness further affect the shape and characteristics of the tsunami and reflect three types: symmetric (Sym, q = 0.5), up-skew (UpS, q = 0.3), and down-skew (DnS, q = 0.7) models. Up-skewed slip produces larger uplift close to the deformation front, while down-skewed slip has the opposite effect and leads to greater coastal subsidence (**Figure 2-3C**).

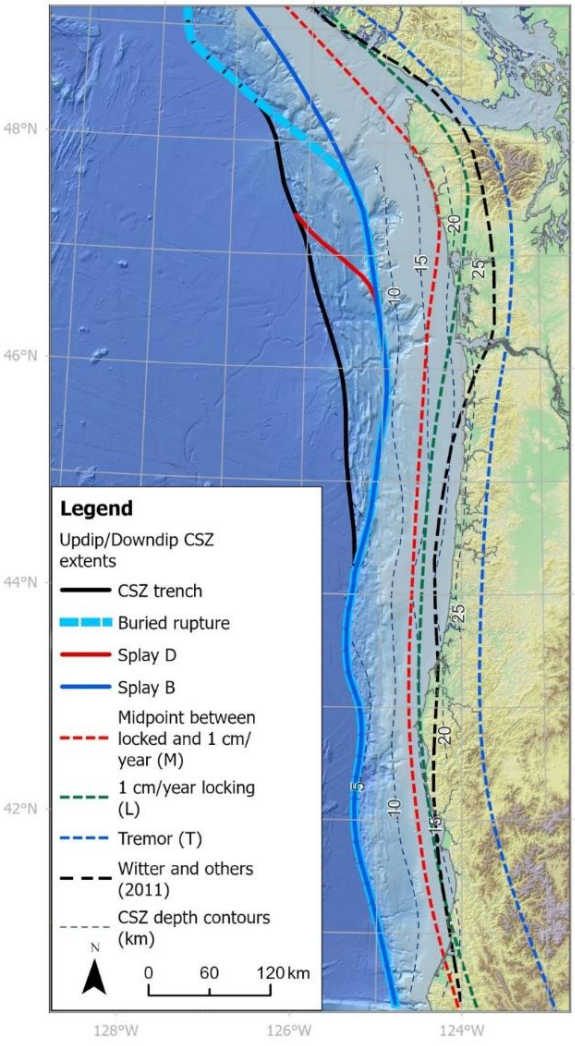
Figure 2-3. Examples of whole-margin deep and shallow buried models. A) surface vertical deformation caused by deep (left) and shallow (right) buried ruptures. B) Surface deformation, fault slip, and fault geometry at profiles 1 –3 for a buried rupture scenario assuming a symmetric slip distribution. C) Surface deformation, fault slip, and fault geometry at profiles 1 to 3 for a shallow buried scenario, assuming up-skew, symmetric, and down-skew slip distributions (modified from Sypus and Wang, 2024).



Downdip limits of the deformation models reflect three rupture extent models (**Figure 2-4**) defined by the USGS NSHM (Peterson and others, 2014):

- Halfway between the fully locked zone and 1 cm/yr locking contour, defined as "M" in the Sypus and Wang (2024) deformation models. This rupture depth limit reflects the **shallowest** part of the rupture zone. An alternate description of this downdip limit is that it reflects the midpoint between a thermal model (e.g., Flück and others, 1997) and the 1 cm/yr locking contour.
- The 1 cm/year locking contour, defined as "L" in the Sypus and Wang (2024) deformation models. This is the region where both plates are considered to be fully coupled or locked (Wang and others, 2003).
- The top of the tremor zone, defined as "T" in the Sypus and Wang (2024) deformation models, and represents the **deepest** extent to which potential ruptures may extend.

Figure 2-4. Map showing the primary dip direction rupture boundaries used by Sypus and Wang (2024). The four updip boundaries include the deformation front (black), deep buried rupture termination (cyan dash), Splay D (solid red) and Splay B (solid blue). The down-dip boundaries are based on the USGS Seismic Hazard Program (Peterson and others, 2014) and include: midpoint between the fully locked zone and the 1 cm/yr locking contour (M, red dash), 1 cm/yr locking contour (L, green dash), and top of tremor zone (T, purple dash). Included is the downdip extent used by Witter and others (2011, black dash), along with depth contours to the down-going slab.



Varying these parameters affects the deformation wavelength, which widens due to a deeper limit as one progress from the shallowest rupture scenario (i.e., midpoint between the fully locked zone and the 1 cm/yr locking contour) downdip to the top of the tremor zone (deepest) limit (Sypus and Wang, 2024). Sypus and Wang (2024) assigned 500 years of slip deficit to the apex of the bell-shaped distribution in all the models; the exception to this are the asperity models. Because seafloor deformation is proportional to fault slip, the results can thus be easily scaled to obtain deformation due to other slip values.

2.2.2.2 Splay Models

Inundation modeling undertaken by Priest and others (2010) and Witter and others (2013) included the possibility that rupture of the Cascadia plate interface may be partitioned on to a splay fault. Such a rupture is directed upward along the splay producing significantly greater seafloor uplift (**Figure 2-1**), which correspondingly produces a larger tsunami wave (Gao and others, 2018). Priest and others (2010) describe the presence of a potential megasplay[1] fault along central Cascadia between ~45°N to 47°N based on a few discrete seismic image profiles. Interpretation of those data revealed the approximate dip of the megasplay fault to be ~30°. Because there was some evidence for seafloor offset, Priest and others (2010) argued that this suggested the splay may have undergone recent movement and hence, warranted its inclusion in new inundation modeling being developed for Oregon.

As part of the updated suite of Cascadia resources, the CSWG discussed the inclusion of splay models and subsequently decided on two splay models: Splay D and Splay B. Those discussions included considerable input from Dr. Harold Tobin and students from the University of Washington, who have been actively researching the presence of splay faults along the CSZ (e.g., Ledeczi and others, 2024; Lucas and others, 2025). Lucas and others (2025) evaluated the CASIE21 seismic imaging data and found little to no evidence for an active megasplay in northern Oregon/southern Washington of the scale suggested by Witter and others (2011). Although evidence for splay faults was observed in several seismic imaging profiles across the CSZ, most of the splay faults were found to be buried beneath thick sediment layers, with little to no evidence for late Quaternary activity. Compelling evidence for a limited Quaternary surface rupture of a splay fault was observed offshore Grays Harbor (line PD08 in Lucas and others [2025]), ~20 km west of the previously hypothesized Witter and others (2011) megasplay.

Splay D reflects a more spatially limited model when compared with the Witter and others (2011) splay model and was guided by the CASIE21 imaging data and interpreted picks provided by Lucas and others (2025). The northernmost extent of the Splay D model occurs ~47°N, where it merges with the deformation front (**Figure 2-5A**, right).

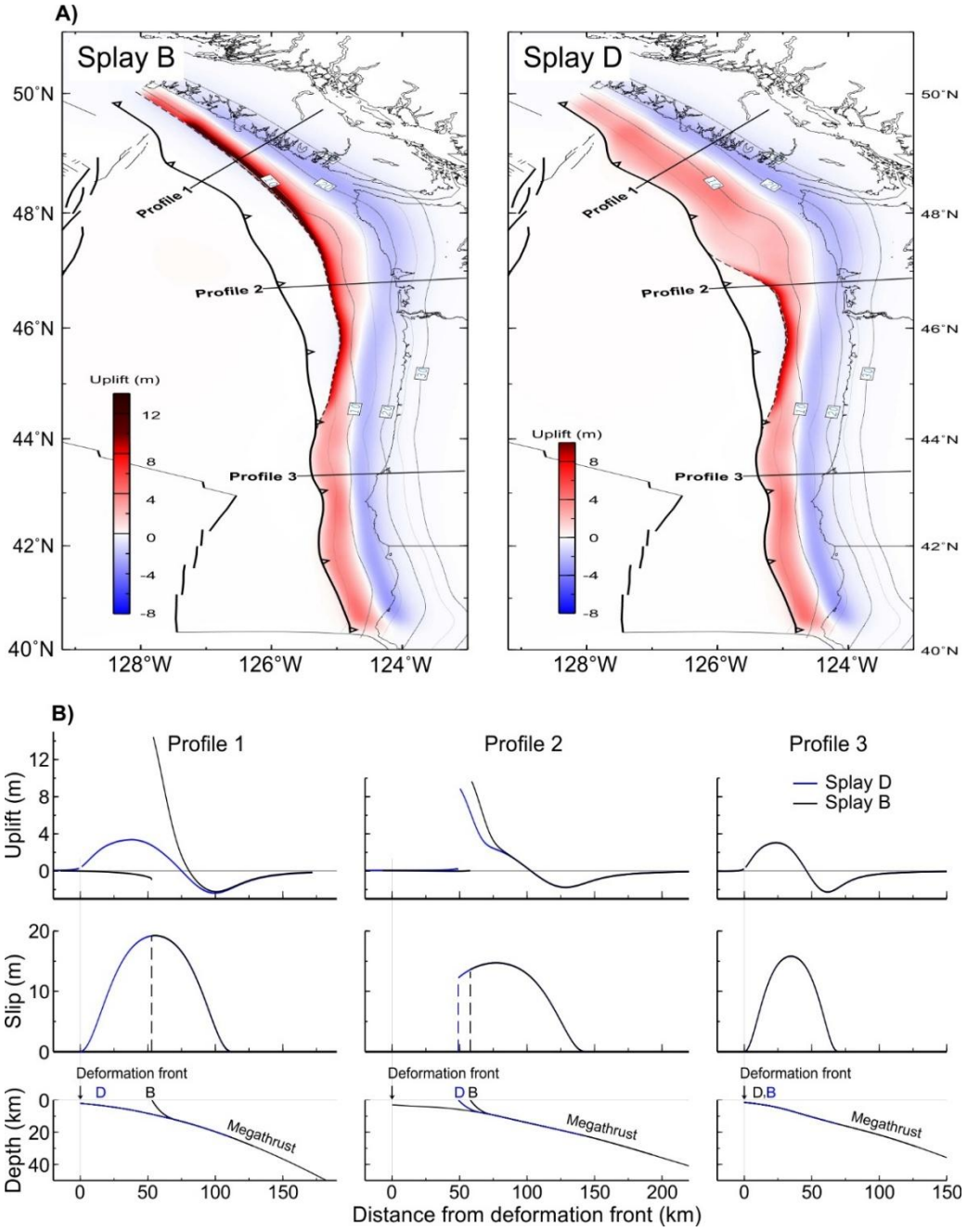
Splay B (**Figure 2-5A**, left) is broadly similar to the megasplay model of Witter and others (2011). It was retained in response to a request by the Washington Department of Natural Resources (WA DNR), who modified the original DOGAMI L1 megasplay by extending the deformation model up along Vancouver Island. This was necessary to account for the effects of CSZ ruptures and tsunami propagation into Puget Sound.

Both splay models were characterized with a dip of 45°, which was a compromise based on the latest CASIE21 results. Final construction of the models involved careful placement of zero-depth control points and additional control points, which help connect the megathrust to a more steeply dipping thrust fault (i.e., splay) that breaks the seafloor (Sypus and Wang, 2024). Each model is characterized by having considerable uplift near the fault trace (**Figure 2-5B**) due to slip along a more steeply dipping fault

[1] A megasplay is defined by Lucas and others (2025) as a persistent, large, out-of-sequence thrust fault or fault system within the accretionary wedge of a subduction zone that merges with the main megathrust fault at depth while also branching up to the seafloor.

compared to the low angle megathrust. In northern Cascadia and offshore Vancouver Island, Splay B produces significantly greater uplift, which can be expected to produce a larger tsunami. In the region of ~44.5°N to 47°N (profile 2 in **Figure 2-5B**), both splay models produce similar deformation, while in southern Cascadia the splay models effectively become buried ruptures due to the lack of evidence for splay faulting in southern Cascadia, consistent with Witter and others (2011).

Figure 2-5. Examples of whole-margin splay-fault rupture models. A) Surface vertical deformation of Splay B (left) and Splay D (right) and select profile locations. B) Surface deformation, fault slip, and fault geometry for representative splay model scenarios for profiles 1–3 (modified from Sypus and Wang, 2024).



Finally, of the two splay models, the CSWG originally placed greater weight on Splay D, while Splay B was given a low weight due to the absence of strong evidence to support the concept of a megasplay in Cascadia. Unfortunately, due to the many iterations performed to update the CSZ logic tree, this distinction was omitted in the final version of the logic tree developed by Thio (2026). Accordingly, the Splay B and D weights should be reevaluated in a future update.

2.2.2.3 Trench-Breaching Ruptures

Tsunami simulations of trench-breaching rupture scenarios have previously been undertaken by Gao and others (2018) for Cascadia. This type of rupture reflects slip in the updip direction that extends to the deformation front along the frontal thrust and is based on the devastating 2011 Mw 9.0 Tōhoku, Japan, earthquake. From a purely tsunamigenic standpoint, the trench-breaching rupture consists of two components: 1) a "rigid-body" translation in the updip direction that is controlled by the seafloor slope and fault dip (**Figure 2-2B**) and 2) the elastic deformation that contributes to seafloor uplift or subsidence. Gao and others (2018) noted that evidence for this type of rupture scenario is not persuasive in Cascadia, in part because much of the trench is buried by large amounts of sediment. Furthermore, evaluation of seismic image data revealed no recent (e.g., 1700) evidence for a large trench-breaching seismic rupture. Nevertheless, they argued that the absence of evidence for trench-breaching in Cascadia did not preclude the possibility of such an event having occurred in the past or potentially happening in the future. Gao and others (2018) performed tsunami modeling based on two trench-breaching scenarios and observed that this type of rupture model did not appear to produce large tsunamis in Cascadia. They suggested that this was probably because the continental slope along Cascadia is not steep and where it is steep, it is not as broad as in the Japan trench, minimizing the rigid-body translation component of tsunamigenesis.

Given uncertainties in whether such a rupture could have occurred in Cascadia, the CSWG adopted two trench-breaching scenarios where slip at the seafloor trace is assumed to be either 50% or 100% of the peak slip (**Figure 1-2**), consistent with the approach of Gao and others (2018). In building the trench-breaching models used in this PTHA, Sypus and Wang (2024) noted that such ruptures were assumed to occur primarily in areas characterized as having seaward-vergent frontal thrusts close to the deformation front, along with mixed zones of seaward and landward vergence. These zones were informed by the CSWG, particularly in response to CASIE21 data and recent research undertaken by Watt and Brothers (2021). Where there is no evidence for seaward-vergent frontal thrusts offshore Washington State, the deformation instead reflects a shallow buried rupture response.

Like Gao and others (2018), the slip distribution in the downdip half of the rupture zone is modeled in the same manner as a buried rupture (**Section 2.2.2.1**), represented by the downdip half of the bell-shaped slip function. For the updip portion, the slip is modelled using a segment of a sine function that allows the slip to decrease smoothly from the peak value in the middle of the rupture to a specified value at the seafloor trace of the frontal thrust (see Figure 12 in Gao and others, 2018). The adjustment of the shallow megathrust geometry modeled by Gao and others (2018) produces deformation that approximates horizontal and vertical seafloor motion expected for a seafloor-breaching rupture along the megathrust. Additional details describing these modifications is described in **Section 3.2** of Sypus and Wang (2024). Finally, Sypus and Wang (2024) note the geological unlikelihood of a single frontal thrust over large distances along strike in a single earthquake. Thus, the trench-breaching scenario reflects a potential worst-case scenario in which numerous secondary faults in the frontal area undergo trench-breaching slip at the same time in the presence of thick trench sediment.

2.2.3 CSZ Logic Tree Scenarios

The revised CSZ logic tree presented in **Figure 1-2** consists of four broad rupture categories: whole-margin, segment, clusters, and floating. The whole-margin scenarios are divided into two branches, distinguished by the DOGAMI and USGS branches. Sypus and Wang (2024) note that the newly built DOGAMI whole-margin deformation models are not the same as those constructed by Witter and others (2011). They point out that Witter and others (2011) modeled the slip magnitude to decrease in a stepwise fashion southward along strike to allow for the more frequent partial megathrust ruptures that characterize southern Cascadia (e.g., Goldfinger and others, 2017). However, CSWG decided not to implement the stepwise decrease in slip in the new whole-margin deformation models because the segmented and partial rupture branches of the logic tree deal with these geophysical differences directly. As a result, Sypus and Wang (2024) note further that their revised whole-margin rupture scenarios would be expected to produce larger tsunami waves in southern Cascadia when compared with those of Witter and others (2011).

The revised DOGAMI scenarios developed by Sypus and Wang (2024) also have significantly different downdip extent of coseismic ruptures than those of Witter and others (2011). Downdip termination of the Witter and others (2011) ruptures was defined by geothermal data and geological stress patterns in the upper plate (Priest and others, 2009). The terminus of the Witter and others (2011) ruptures are at the black dash line shown in **Figure 2-4**. As seen in the figure, their downdip extent lies just landward of the 1 cm/year locking scenario (green dash) of Sypus and Wang (2024) in central and southern Oregon. However, in northern Oregon and southwest Washington the Witter and others (2011) rupture extent lies significantly further landward when compared with those of the USGS NSHM. As will be shown in **Section 3.3**, the broader rupture of Witter and others produces a smaller deformation (and hence a smaller tsunami amplitude) when compared to the Sypus and Wang (2024) fully locked scenario for a given slip deficit release and slip distribution. The reason for this is that the coseismic uplift and subsidence of Witter and others (2011) is basically spread over a much wider area (particularly in northern Oregon), including greater deformation in shallow water. Conversely, the Sypus and Wang (2024) 1 cm/year locking tsunami associated with the latest models shifts the deformation further seaward, with the trough of the coseismic subsidence now concentrated offshore the coast, which produces a more asymmetric tsunami (effectively a steep, narrow tsunami wave). These differences are explored further in **Section 3.3** and in **Section 5.0**.

In its present form, the DOGAMI portion of the logic tree (**Figure 1-2**) yields 144 potential scenarios, which may be scaled to reflect the SM (240 years of accumulated peak slip), L (800 years), and XL (1200 years) scenarios defined by Witter and others (2011). Thus, the DOGAMI branch of the revised CSZ logic tree reflects 576 possible combinations.

Deformation models constructed for the USGS full margin scenarios reflect 360 built scenarios, which scale to 2,880 possible combinations. The substantial increase in USGS rupture scenarios in **Figure 1-2** is indicative of the influence of the use of four global scaling relations (Strasser, Murotani, Shaw, and Papazachos adopted by Thio and others [2017]), efforts to account for aleatory uncertainty in the scaling relations (±1σ), and multiple asperity type models (n = 3, n = 5, and two uniform asperity models [U3 and U5]). Aside from the addition of the uniform and five asperity models, the USGS branch is broadly consistent with previous PTHA modeling undertaken by Thio and others (2017) and Thio (2019).

The segmented suite of rupture scenarios in the revised CSZ logic tree (**Figure 1-2**) is based on Goldfinger and others (2017) and includes two additional segmentation boundaries that extend the boundaries north and south of the primary segment by an additional 50 km. The purpose here is to simply account for uncertainties in the segment boundary locations. Sypus and Wang (2024) excluded the "E"

segment since it was similar to "D" in Goldfinger and others (2017). The segmented scenarios were designed such that the southern segments (e.g., "D") rupture more frequently with smaller slip as proposed by Goldfinger and others (2017). The segment models include all the same scenarios as described above for the DOGAMI models (i.e., rupture type, skewness, downdip extents, and asperities). Within this grouping, Sypus and Wang (2024) constructed 2,160 deformation models. Unfortunately, due to time constraints, the CSWG were unable to resolve the relative weights that should be assigned to the partial rupture portions. Accordingly, the partial rupture weights should be reevaluated in a future update to the CSZ logic tree.

The cluster suite of ruptures is from the USGS NSHM and has a wide range of along-strike rupture lengths and downdip termination locations (see Figure 6.1 in Sypus and Wang, 2024). The cluster scenarios are broadly similar to the other models but exclude the asperity scenarios. The total number of cluster models is 756 rupture scenarios, which scales to 6,048 possible combinations due to the influence of the four global scaling relations (Strasser, Murotani, Shaw, and Papazachos adopted by Thio and others [2017]) and efforts to account for the uncertainty in the scaling relations (±1σ).

Floating rupture scenarios developed by Sypus and Wang (2024) are also based on the USGS NSHM. Here the location of the rupture's start point is not fixed but is allowed to vary within a specified range. The CSWG settled on 100 km by 40 km elliptical slip patches, with peak slip in the center, which decreased away toward the edges. The same size rupture patches were then allowed to occur in different locations along Cascadia under different scenarios (Sypus and Wang, 2024). Floating ruptures reflect the smallest number of deformation models, accounting for ~80 scenarios. Combining all possible combinations and scaling across branches, the revised CSZ logic tree accounts for some 11,744 potential earthquake sources.

2.3 ASCE7-28 PTHA Update

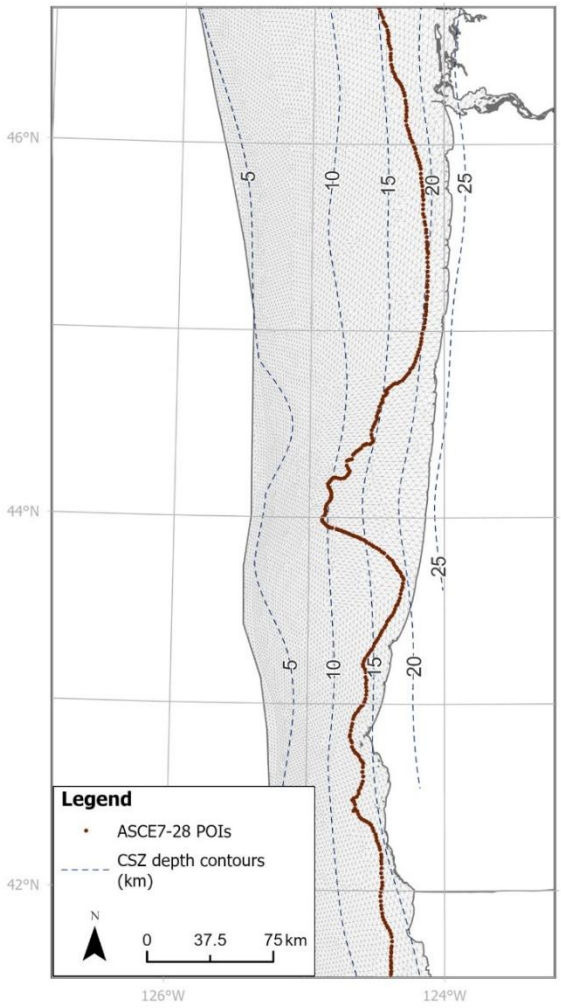
In deepwater, tsunamis are typically characterized as shallow-water waves due to their very small amplitudes and long wavelengths when compared to the ocean depths (Gusman and others, 2024). Accordingly, linearized shallow-water equations that utilize Green's Functions may be used to characterize the tsunami wave form and its propagation in deepwater (Loomis, 1979; Satake, 1985; Xu, 2007; Thio and others, 2017; Gusman and others, 2024). As the tsunami travels into very shallow water, the tsunami wave slows down and its height increases. These changes become increasingly important and complex due to nonlinear effects that begin to occur as the tsunami interacts with complex bathymetric and coastal geomorphology. For these situations, sophisticated numerical models that utilize nonlinear shallow water equations are used to account for such complexities.

Since the initial generation of a tsunami wave form is related to the elastic deformation of the sea floor in the source area, and deformation and slip are linearly related, the surface waveform can be computed for any point of interest (POI) in deepwater using Green's functions (Gusman and others, 2024). This means one can precalculate the tsunami amplitudes for many POIs (e.g., along the 100 m bathymetric contour offshore the coast), for different slip combinations governed by the input sources. This approach allows for the efficient synthesization of many slip distributions by summing the individual subfault tsunami waveforms weighted by their slip, which can then be used in a PTHA (Thio and others, 2017). It also avoids the need to run many thousand high-resolution tsunami models on to land, which is computationally time consuming and expensive to run.

Miranda and others (2014) describe one approach to precompute a Green's functions database for source areas of interest. The first step involves defining the source areas that may be displaced by a seismic source and dividing that area into "subfaults" with known strike, dip, rake, and unit slip. An

example source area developed by Sypus and Wang (2024) for the CSZ is provided in **Figure 2-6**. Once the source area is defined, the region may be further subdivided into unit water sources or rectangular prisms of water of unit height 1 m. The length and width of the unit water sources should be small enough to capture sufficient detail of the initial displaced area and large enough to be used as initial displacement in the shallow-water model code (Miranda and others, 2014). Thio (2019) used subfaults with dimensions of 30 km (along strike) × 15 km (in dip direction) when performing PTHA modeling in California, which were further refined to 1 km × 1 km patches to capture the curvature of the subduction interface. The response at the water surface to vertical displacement within each subfault is thus expressed as linear combinations of the calculated Green's functions among the various subfaults, which can be scaled for any given slip magnitude and deformation. The final step is specifying the POIs along a coast where the Green's functions tsunami waveforms are calculated according to the unit prisms (Miranda and others, 2014).

Figure 2-6. Example Triangular Irregular Network (TIN) of the CSZ megathrust showing areas of higher resolution near the deformation front relative to areas of coarser resolution in the east. Blue dash lines denote the depth contours. Brown circles define the offshore PTHA points of interest (POIs) where the probabilistic hazard curves are calculated.



An alternative approach to that of Miranda and others (2014) is to implement a reciprocal Green's function approach. This is accomplished by putting a unit source (corresponding to a 1 m sea surface uplift) in a single POI in deepwater offshore the coast and propagating the resulting tsunami to all points within the model. It is this latter approach that has been adopted by Thio (2026) as part of the ASCE7-28 update.

The Sypus and Wang (2024) catalog of seismic sources therefore forms the basis of the updated Cascadia PTHA, together with the circum-Pacific model developed under the auspices of the USGS Powell Center workshops on tsunami sources (Patton and others, 2025). The procedures for the circum-Pacific sources are generally similar in character to the ones previously used as part of the original ASCE 7-16 PTHA modeling. The Cascadia catalog of tsunami sources produced by Sypus and Wang (2024) contains 3,502 unique sources that cover the rupture geometries originally developed at the May 2022 Powell Center workshop (Patton and others, 2022). These sources were subsequently refined by Sypus and Wang (2024) and guided by an ad hoc steering committee (CSWG) comprised of a dozen scientists via a series of mini workshops. The Cascadia logic tree thus contains many branches that have similar geometries but differ in terms of magnitude/slip to capture the magnitude/slip uncertainties. These scenarios can then be simply scaled up from the original base scenarios, which is fully consistent with the linear approximation (in tsunami propagation and surface deformation) used in the offshore hazard.

2.3.1 Aleatory Uncertainty

Aleatory uncertainty is the random nature of physical processes resulting in ambiguity in the character of future events. In previous PTHA modeling, aleatory uncertainty is typically resolved with distribution functions as opposed to using single mean or median values (Thio and others, 2017). As a result, the probability of an event being within a certain range is given by the area under the probability distribution function. In the original development of the probabilistic tsunami hazard methodology, Thio and others (2010) described three main contributors to aleatory uncertainty: modeling error (σ_A), uncertainty in dip (σ_D), and uncertainty in random slip distributions (σ_S). Other potential areas of uncertainty were also noted including tidal uncertainty and uncertainty associated with magnitude scaling relations. In the latest PTHA performed by Thio (2026), some of these variabilities are now included using numerical sampling over the variability as outlined in the following sections.

2.3.2 Modeling Error (σA)

Modeling error is the product of both the numerical implementation and the resolution and shortcomings of the bathymetric grid (i.e., types of instruments used, age of surveys, and instrument accuracy). Other factors, such as the characterization of the rupture sources, are especially important. The latter may also include landslide-triggered sources, though these are not included in the latest PTHA modeling, since these are not well-developed for the PNW region. Quantification of σ_A has previously been achieved by simulating several well-constrained earthquakes that produced tsunami data using coarse and fine grids (Thio and others, 2010). Not surprisingly, the fine grids yielded smaller standard deviations compared with the coarse grid. Thio and others (2017) used the 2011 Tohoku Japan tsunami to better constrain σ_A, which was determined to be $\sigma_A = 0.35$ (log10 units) and has been used in the updated ASCE7-28 PTHA work.

2.3.3 Magnitude (σM)/Average Slip (σS)

The various earthquake rupture parameters (magnitude, rupture length, width, and average slip) are all related to each other, and empirical scaling relations have been developed to account for these correlations. The use of different regression models (**Figure 1-2**, USGS branch) constitutes an epistemic

uncertainty, but each of these models also contains variability (expressed by the standard deviation, σ) due to the scatter (misfit) of the data around the regression model. Magnitude scaling errors were based on the previous work of Strasser and others (2010), which were determined to be $\sigma_M = 0.286$. Since the average slip is a function of the moment magnitude, shear modulus, and rupture area, Thio and others (2017) sampled the magnitude area distribution at five points from $-2\sigma_M$ to $+2\sigma_M$. Over the last 15 years, several new relations specifically for subduction megathrust sources have been developed, and these (with their sigmas) are described in Thio (2026) and are included in **Figure 1-2**. The new models are based on detailed subduction zone geometries (e.g., Slab2.0 or detailed Cascadia geometries). Application of this adjustment factor only applies to the USGS branch of the logic tree (**Figure 1-2**), where earthquake scaling relations are used. Because of improvements to the geometry of the CSZ over the past decade, the latest PTHA modeling now assumes that the dip uncertainty is negligible and as result can be largely ignored.

2.3.4 Variable Slip

Previous PTHA work has relied on homogenous slip models to produce tsunami. However, some researchers have begun to question this approach given recent occurrences of large tsunami events. For example, Melgar and others (2019) compared homogenous and heterogenous synthetic slip models and demonstrated that the former may underestimate the heights of the tsunami produced. In addressing this issue, Thio and others (2017) noted that the Tohoku 2011 earthquake produced maximum slip that exceeded the average slip by at least a factor of 2. To address this uncertainty in ASCE7-16, Thio and others included variable slip rupture models, where one third of the rupture experienced twice the average slip (an asperity), while the remaining two-thirds experienced half the average slip. Thus, for Cascadia, the rupture length was divided into three segments, such that each segment was subject to the asperity rupture model. In the latest PTHA update, the same approach was applied to the DOGAMI branch (**Figure 1-2**), while the USGS whole-margin branch included both a three-segment and a five-segment asperity model (**Figure 1-2**, and discussed in **Section 2.2.3**).

2.3.5 Tidal Variability

While the offshore hazard in ASCE 7-16 included probabilistic treatment of tide-level variations, this factor is best left for the inundation modeling (which is typically performed at MHW). The effect of tides is not only significant in terms of wave amplitudes but also has a strong bearing on flow velocities, especially in estuaries, ports, and harbors. Accordingly, the latest PTHA modeling update does not include a tidal uncertainty factor.

2.3.6 Production of Hazard Curves

Application of Green's functions is only valid in deepwater, where the ratio of the water depth to wavelength is approximately >1/20, which limits its use to water depths >50 m (Shuto, 1991). In the original ASCE7-16 PTHA, Thio (2017) established POIs along the 100 m bathymetric contour, where the reciprocal Green's functions could be calculated. However, concerns were raised by Priest and Allan (2019) that for some locations this may be too shallow. Offshore POIs developed by Thio (2026) for the ASCE7-28 update are shown in **Figure 2-6**. For the most part, the locations of the POIs follow the 100-m bathymetric contour but were slightly relaxed to avoid areas of complex bathymetry that could give rise to spurious results in the linear approach. For these latter areas, such as offshore the mouth of Juan de Fuca (JdF) Strait in Washington State or Stonewall Bank offshore the central Oregon Coast, the offshore POIs were placed further seaward of the features in greater water depths (~200–500 m depths). The goal here is to minimize the potential for nonlinear interactions as much as possible around those features.

Thio (2026) used a reciprocal Green's function method to compute the tsunami propagation using the linear version of the AECOM tsunami propagation model. This approach consists of putting a unit source (corresponding to a 1-m sea surface uplift) in the single cell in which the offshore point is located and propagating the resulting tsunami to all points within the model. Reciprocity means that the Green's functions computed from the offshore POI to all the grid points are the same as the Green's functions from any of those grid points to the target offshore POI. Since the tsunami source database contains the uplift grids for all the scenarios, users can compute the response at the offshore POI by convolving the surface deformation from the Sypus and Wang (2024) catalog of tsunami sources with the Green's functions that are computed for the target offshore point.

For every scenario, Thio (2026) computes its effective recurrence time, which is the total weight of its particular logic tree branch multiplied by its actual recurrence rate. In the case of the DOGAMI logic tree branch, the recurrence rate is specified by the T-shirt sizes established by Witter and others (2011), while the recurrence for the USGS branch is specified from the scaling models. The hazard curve at every offshore point is then computed and the hazard at 2,475-year recurrence interval is determined through interpolation (**Figure 2-7**).

Figure 2-7 presents a comparison of the proposed new ASCE7-28 2,475-yr tsunami amplitude "design waves" calculated for the PNW coast of Oregon and Washington (Thio, 2026) and compared with the previous ASCE7-22 model results. Although the calculated standard deviations for both ASCE7-28 and ASCE7-22 are essentially the same (~1 m standard deviation), the latest PTHA results indicate much less along-coast short wavelength variability. In particular, large peaks in the ASCE7-22 2,475-yr amplitudes in northern Oregon and offshore of the Washington coast have been significantly reduced in ASCE7-28. On average, the proposed new ASCE7-28 tsunami amplitudes are ~1.3 m lower than the previous ASCE7-22 PTHA modeling.

Figure 2-7. Comparison of ASCE7-22 (red) and proposed new ASCE7-28 (blue) tsunami amplitudes for a 2,475-yr Cascadia event striking the PNW coast.

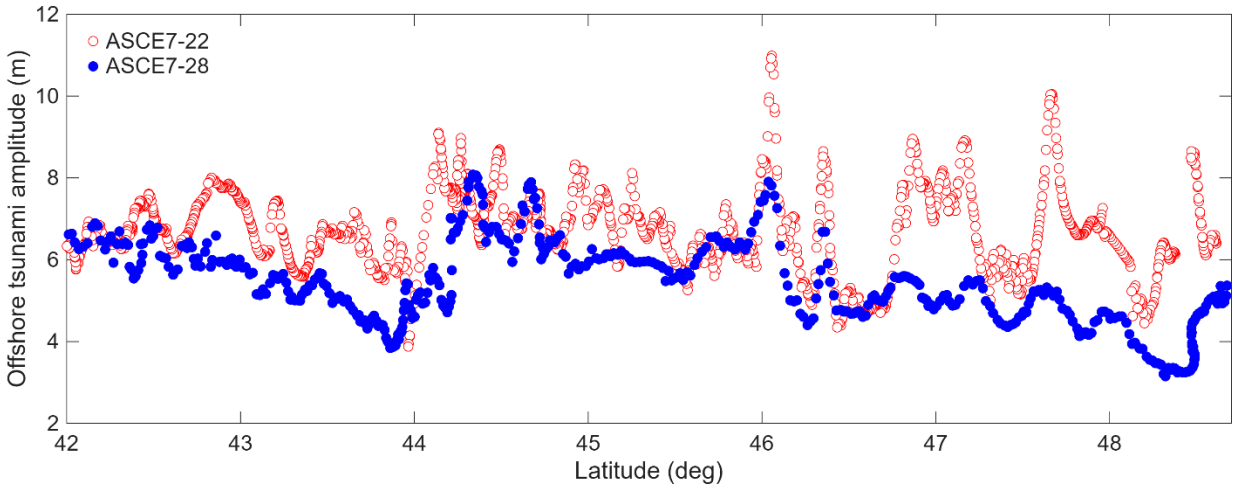
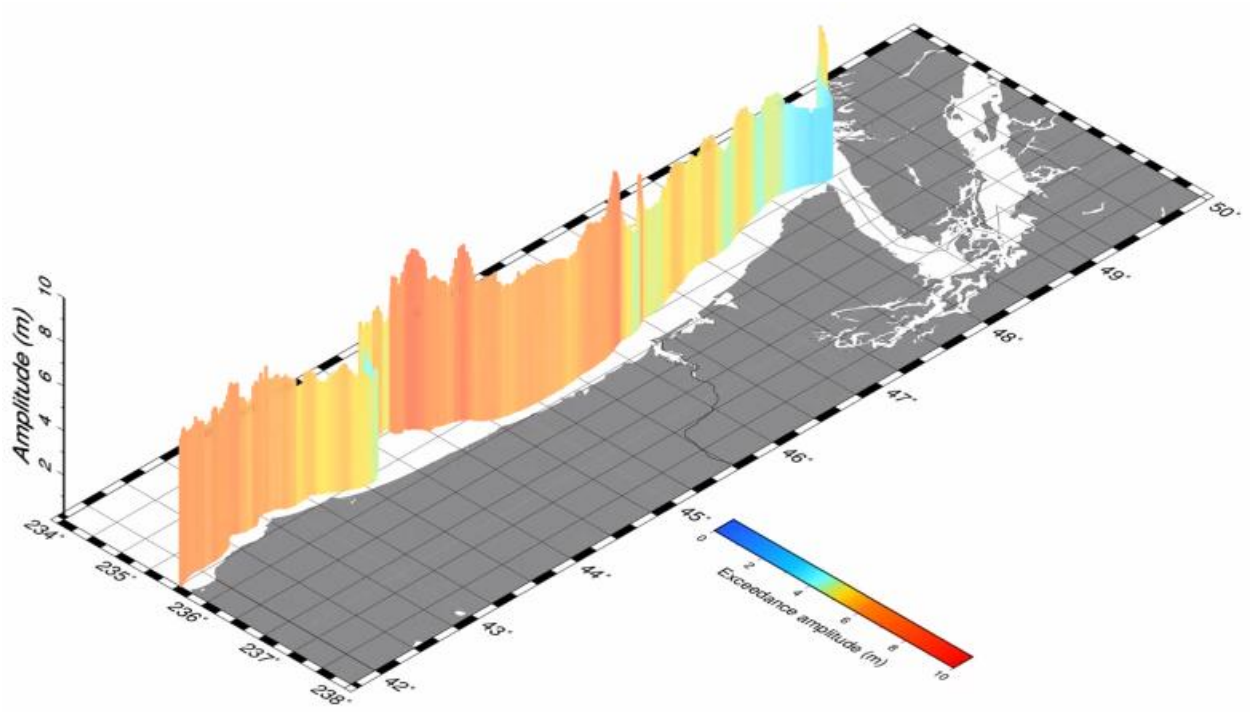


Figure 2-8 is a heat plot of the ASCE7-28 amplitudes visualized for PNW coast. In general, the latest 2,475-yr modeling indicates larger tsunami amplitudes in the vicinity of Stonewall Bank (~44.3°N, offshore Lincoln County) and offshore Seaside (~46°N) in Clatsop County (**Figure 1-1**). Lower amplitudes shown south of 44°N are probably due to the sheltering effect caused by Stonewall Bank. Amplitudes are generally lower along the Washington Coast compared with Oregon and reach their minima at the

entrance to Puget Sound. The latter is probably a function of the significantly deeper water depths that characterize the entrance to Puget Sound and the seaward shift of the POIs into deeper water.

Figure 2-8. Latest 2,475-yr tsunami amplitudes calculated for the PNW coast.



3.0 OREGON COAST HIGH-RESOLUTION TSUNAMI MODELING

Simulations of tsunami propagation and inundation used the hydrodynamic finite element model SCHISM (Semi-implicit Cross-scale Hydroscience Integrated System Model; Zhang and others, 2016a), which is derived from the model SELFE (Semi-implicit Eulerian-Lagrangian Finite Element model) (Zhang and Baptista, 2008a). Algorithms used to solve the Navier-Stokes equations in these models are computationally efficient and stable. SELFE passed all standard tsunami benchmark tests (Zhang and Baptista, 2008b) and closely reproduced observed inundation and flow depths of the 1964 Alaska tsunami in a trial at Cannon Beach (Zhang and others, 2011). SELFE (and SCHISM) have been used by the State of Oregon for modeling statewide tsunami inundation zones (e.g., Witter et al., 2013; Priest et al., 2013; Allan and O'Brien, 2020) and for maritime preparation (e.g., Allan and others, 2018). In 2016, SCHISM successfully passed a suite of standardized tsunami current benchmark tests (Zhang and others, 2016b; Lynett and others, 2017). For the purposes of this study, SCHISM was evaluated against a suite of standardized inundation benchmark tests established by the NTHMP and passed those tests (see **Appendix A**). Accordingly, SCHISM has met established standards for simulating both tsunami inundation and currents.

3.1 Model DEM Development

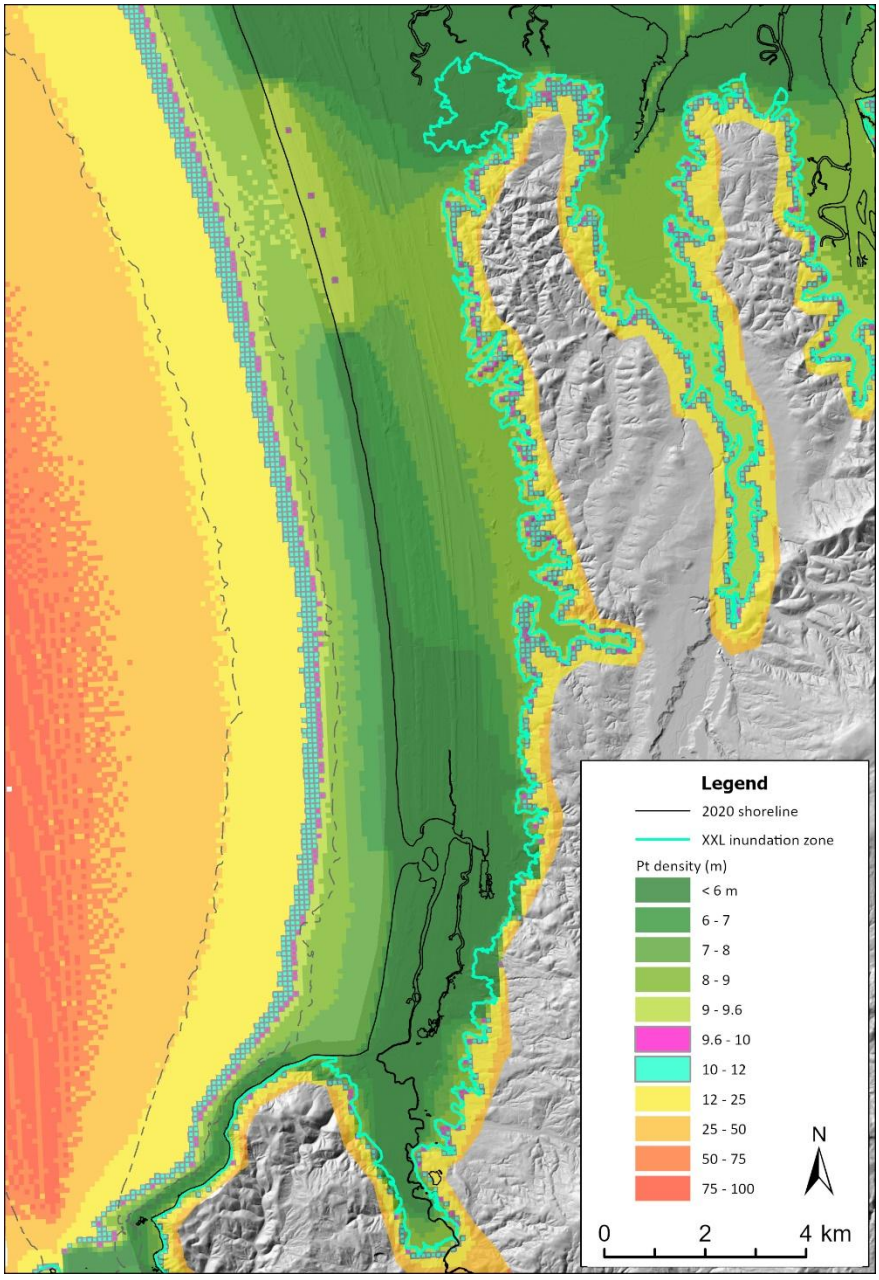
The unstructured finite element mesh used in the central to north coast modeling was constructed by first compiling digital elevation models (DEMs) covering the model domain and then retrieving elevations from the DEM at a series of points defining a triangulated irregular network. The DEM for the tsunami simulations was developed from a combined bathymetric/topographic seamless digital surface model created by NOAA's National Center for Environmental Information (NCEI). The DEMs comprise a variety of data sources, including NOAA bathymetric data, water-penetrating airborne lidar survey data, and channel survey data from the U.S. Army Corps of Engineers (Carignan and others, 2019; Carignan and others, 2021; Linn and others, 2024). In areas of dry land, NCEI supplemented the bathymetric data with 2008–2020 terrestrial lidar data collected by DOGAMI, NOAA, USGS, and USACE. The final DEM consists of 1/9 arc-second (~3 m) grid cells referenced to the North American Vertical Datum of 1988 (NAVD88).

We created three independent tsunami model domains spanning Clatsop, Tillamook, and Lincoln Counties (e.g., **Figure 1-1**). For each county, the authors developed a high-resolution model domain that extended 20 miles north and south of the northernmost and southernmost offshore points that span the county of interest. These are the same points that are used to compare model tsunami amplitudes with the new ASCE7-28 2,475-year tsunami design amplitudes for a 2,475-yr event. Furthermore, the high-resolution model domain is integrated within a much larger regional grid that extends southward into California, northward up into the Gulf of Alaska, and westward across the Pacific Ocean. The size of the unstructured grids is summarized as follows:

- Clatsop County contains ~12.4 million nodes and ~24.8 million triangular elements in the horizontal dimension.
- Tillamook County contains ~9 million nodes and ~18 million triangular elements in the horizontal dimension.
- Lincoln County contains ~9 million nodes and ~17.7 million triangular elements in the horizontal dimension.

In all three cases, the nominal horizontal resolution of the model DEMs is ~7 m on land and ≤10 m in the nearshore in water depths <11 m (**Figure 3-1**). The DEM was further refined by adding finer-resolution detail in areas adjacent to the Columbia River, Nehalem, Tillamook, and Yaquina jetties and along major levees where present. Where there are estuaries, the model DEM was extended well beyond the primary area of interest. For example, the model grid extends 55 km upriver of Tongue Point, Astoria, in the Columbia River estuary to Longview, WA. In other areas, the model DEM extended well beyond the XXL1 inundation boundary that characterize existing Oregon tsunami inundation maps (**Figure 3-1**).

Figure 3-1. Example of the approach used to validate horizontal model grid resolution in northern Clatsop County. ASCE requires that model grids have a resolution of 10 m or better in water depths <10 m. The authors used 100 m × 100 m polygon cells to calculate the number of grid points within each cell, from which an average point count was calculated for each polygon. Dashed black line immediately west of the shoreline denotes the 11-m bathymetric contour; the westernmost dash line is the 20 m contour.



3.2 SCHISM Model Parameters

Vertical components of seabed deformation response from the earthquake ruptures were used to set up the initial water surface for tsunami simulations as well as the initial velocity, assuming a short (10 s) initial constant acceleration of the seafloor. Only one layer was used in the vertical dimension, so the model is effectively 2D-depth–averaged. This depth-averaging is consistent with most existing tsunami inundation modeling efforts presently being implemented within the NTHMP (e.g., Allan and others, 2018). Each simulation was run for 24 hours, providing sufficient time for the tsunami to run its course. The simulation time step is 2 seconds for local CSZ sources; the data output was established at 40-second intervals. The model was fully parallelized with hybrid openMP[2] and MPI[3] and ran ~10 times faster[4] than real time on 1920 Intel® Ice Lake cores using the higher-resolution grid. CSZ simulations longer than 24 hours were not necessary as the tsunami decayed rapidly during the first 12 hours. The tsunami simulations were run at mean high water (MHW) based on the nearest tide gauge stations: Astoria (NOS #9439040), Clatsop County, MHW = 2.418 m; Garibaldi (NOS #9437540), Tillamook County, MHW = 2.320 m; and South Beach (NOS #9435380), Lincoln County, MHW = 2.331 m. The bottom drag coefficient (*Cd*), or friction, used in tsunami modeling was specified from Manning-*n*, which is known to be a function of land cover type. However, this study used a fixed Manning-*n* = 0.025, which is standard for ASCE purposes.

3.3 Tsunami 2,475-yr Source Models

Disaggregated source models corresponding to a suite of 2,475-yr CSZ events were provided by co-investigator, Thio. These were defined individually for each county being modeled. **Figure 3-2** (top plot) provides an example of the approach taken to evaluate a single scenario in which the calculated source model tsunami amplitudes (blue circles) are initially compared with the 2,475-yr ASCE7-28 tsunami design wave (red circles) defined along the 100 m bathymetric contour line. The lower plot of **Figure 3-2** provides various statistics: ratio, scaling, and correlation coefficient. The ratio (1.57) and scaling (1.4848) values are combined to yield a multiplier, which is used to scale the original Sypus and Wang (2024) source model in order for it to be consistent with a 2,475-yr ARP scenario. It is the final scaled model that is then used for modeling tsunami inundation. The correlation coefficient provided in **Figure 3-2** (bottom plot, R = 0.89) shows the degree of agreement between the design wave and the scaled model wave; perfect agreement would reflect a straight line at 1. Lastly, scenarios in the area of interest (defined by the dash box) must exceed the 80% threshold in the lower plot. This process was then repeated for all potential 2,475-yr CSZ events, which may be applicable to a particular section of coastline yielding potentially multiple scenarios that could be used for further inundation modeling testing.

[2] openMP: share memory parallelism (MP=multi-processing)
[3] MPI: message passing protocol (for distributed parallelism)
[4] 24/16=1.5 hours to finish one simulation day

Figure 3-2. Disaggregated 2,475-yr CSZ source model validation. Example is of a full margin, deep buried rupture scenario where the calculated source model tsunami amplitudes are compared with the 2,475-yr design wave. This approach is used to determine the initial best-fit multiplier (1.57 x 1.4848 = 2.3311) that is then applied to the source model used in the higher resolution inundation modeling.

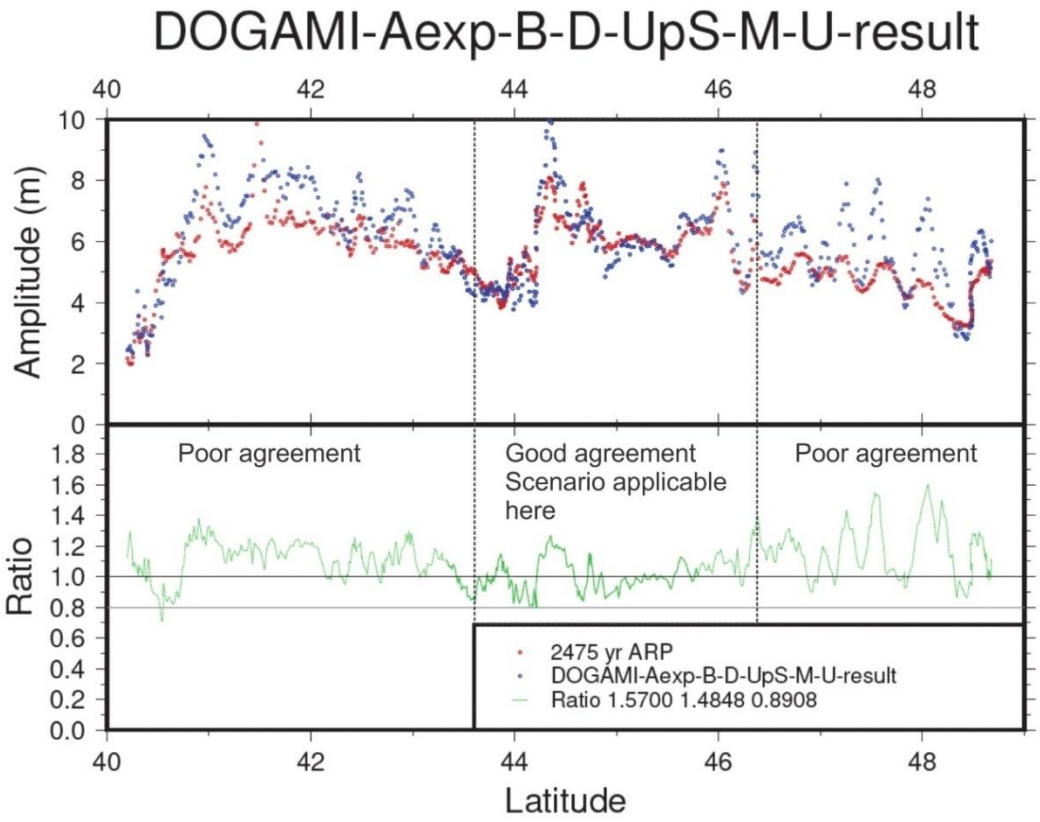
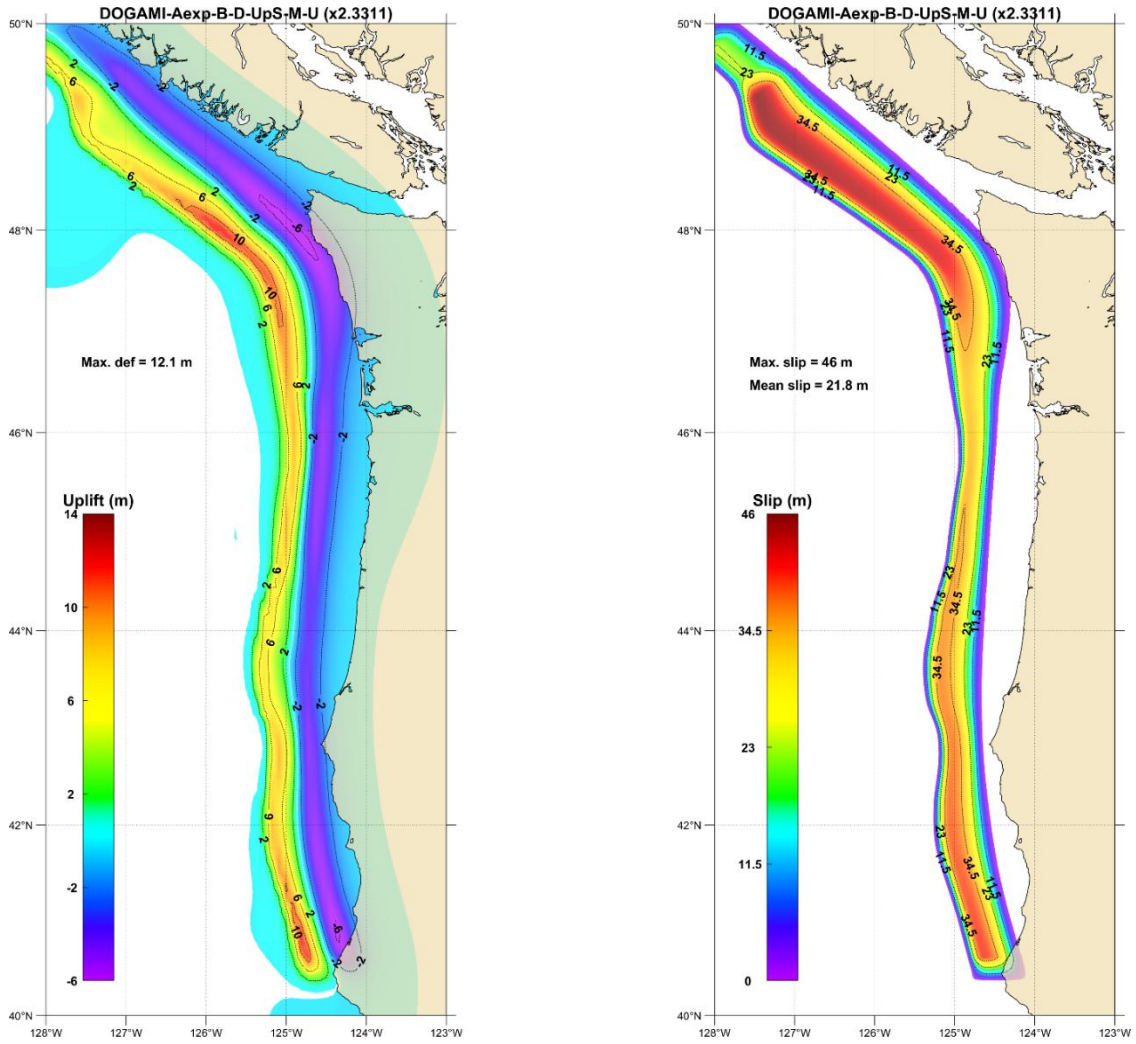


Figure 3-3 is an example 2,475-yr source model that has been scaled (× 2.3311) from the original Sypus and Wang (2024) deformation model. The example reflects a full margin deep buried rupture, with the slip skewed updip, while the downdip limit is halfway between the fully locked zone and 1 cm/yr locking contour (i.e., shallowest region). As a reminder, the original source model assumes 500 years of plate convergence, and the scaling factor (× 2.3311) is used to adjust the original rupture model to produce the equivalent 2,475-yr source model shown in **Figure 3-3**. The left panel defines the modeled vertical deformation, while the right panel indicates the calculated slip. In this example, the maximum deformation is determined to be 12.1 m, while the maximum slip is 46 m (mean slip is 21.8 m) across the entire rupture zone. However, the calculated deformation and slip immediately offshore of the central to northern Oregon Coast (i.e., where the source model is most directly applicable of a 2,475-yr ARP scenario) is closer to ~9.2 m of uplift, while the maximum slip is 34.9 m. If a plate convergence rate of ~0.035–0.040 m.yr^{-1} is assumed, this equates to ~870–1000-years of accumulated strain directly offshore of the central to northern Oregon Coast.

Figure 3-3. Example 2,475-yr CSZ source model showing the calculated deformation and slip.



3.4 Model Runs

Table 3-1, **Table 3-2**, and **Table** 3-3 provide a summary of the various source models and accompanying tsunami inundation model runs undertaken for Clatsop, Tillamook, and Lincoln Counties. The final column included in these three tables includes the "Run Name" adopted in the SCHISM modeling. Each table also includes additional notes that describe various secondary scaling adjustments applied to a few of the rupture models. The purpose of these adjustments was to undertake sensitivity testing on both the modeled offshore wave amplitudes and the accompanying tsunami inundation hazard zones to see if the authors could obtain a better match, while maintaining ASCE requirements at the TDZ.

Table 3-1. Clatsop 2,475-yr disaggregated CSZ tsunami scenarios.

Scenario	Multiplier	Seismic Moment (Mo) N.m	Magnitude (Mw)	Maximum Slip (m)	Description	Run Name
DOGAMI Aexp-B-D-UpS-L-U	2.5	0.369148×10^{23}	9.222	38.3	Full margin, deep buried, skewed updip, down-dip extent = lock zone, uniform slip distribution	Run02c
USGS A-B-D-UpS-M-U3	2.2768	0.268834×10^{23}	9.125	34.9	Full margin, deep buried, skewed updip, down-dip extent = midpoint, uniform slip distribution of 3-part asperity model	Run02d
USGS A-T100-S-UpS-M-A4	3.5068	0.213363×10^{23}	9.183	30.3	Full margin, 100% trench breach, skewed updip, down-dip extent = midpoint, uniform slip distribution of 5-part asperity model	Run02e
DOGAMI Aexp-B-D-UpS-M-U	2.3311	0.277686×10^{23}	9.141	35.7	Full margin, deep buried, skewed updip, down-dip extent = midpoint, uniform slip distribution	Run02f
DOGAMI Aexp-B-D-UpS-M-U	2.5642	0.277686×10^{23}	9.168	39.3	As described for Run02f. Deformation model scaled up 10%.	Run02g
DOGAMI Aexp-B-D-UpS-L-U	2.25	0.369148×10^{23}	9.213	34.5	As described for Run02c. Deformation model scaled down 10%.	Run02h
DOGAMI Aexp-B-D-UpS-L-U	2.325	0.369148×10^{23}	9.222	35.7	As described for Run02c. Deformation model scaled down 7%.	Run02i

Table 3-2. Tillamook 2,475-yr disaggregated CSZ tsunami scenarios.

Scenario	Multiplier	Seismic Moment (Mo) N.m	Magnitude (Mw)	Maximum Slip (m)	Description	Run Name
DOGAMI Aexp-B-D-UpS-L-U	2.5	0.369148×10^{23}	9.222	38.3	Full margin, deep buried, skewed updip, down-dip extent = lock zone, uniform slip distribution	Run01c
USGS A-B-D-UpS-M-U3	2.2768	0.268834×10^{23}	9.125	34.9	Full margin, deep buried, skewed updip, down-dip extent = midpoint, uniform slip distribution of 3-part asperity model	Run01d
USGS A-T100-S-UpS-M-A4	3.5068	0.213363×10^{23}	9.183	30.3	Full margin, 100% trench breach, shallow buried (offshore WA), skewed updip, down-dip extent = midpoint, uniform slip distribution of 5-part asperity model	Run01e

Scenario	Multiplier	Seismic Moment (Mo) N.m	Magnitude (Mw)	Maximum Slip (m)	Description	Run Name
DOGAMI Aexp-B-D-UpS-M-U	2.3311	0.277686×10^{23}	9.141	35.7	Full margin, deep buried, skewed updip, down-dip extent = midpoint, uniform slip distribution	Run01f
DOGAMI Aexp-B-D-UpS-M-U	2.5642	0.277686×10^{23}	9.168	39.3	As described for Run01f. Deformation model scaled up 10%.	Run01i

Table 3-3. Lincoln 2,475-yr disaggregated CSZ tsunami scenarios.

Scenario	Multiplier	Seismic Moment (Mo) N.m	Magnitude (Mw)	Maximum Slip (m)	Description	Run Name
DOGAMI Aexp-B-D-UpS-L-U	2.5	0.369148×10^{23}	9.222	38.3	Full margin, deep buried, skewed updip, down-dip extent = lock zone, uniform slip distribution	Run01a
DOGAMI Aexp-B-D-UpS-M-U	2. 5642	0.277686×10^{23}	9.168	39.3	As described for Tillamook Run01f. Deformation model scaled up 10%.	Run01b
DOGAMI Aexp-B-D-UpS-L-U	2.75	0.369148×10^{23}	9.271	42.2	As described for Run01a. Deformation model scaled up 10%.	Run01c
USGScluster 3b2-B-S-UpS-L-U	2.6083	0.139442×10^{23}	8.974	40.0	3b-2 cluster model, shallow buried, skewed updip, down-dip extent = lock zone, uniform slip distribution	Run02a
USGS A-Sb-S-Sym-L-A5	4.4838	0.170527×10^{23}	9.189	25.8	Full margin, extended splay fault, shallow, symmetric shape, down-dip extent = lock zone, 5-part asperity model	Run02b
Segmented Cs-B-D-UpS-L-U	2.7639	0.152212×10^{23}	9.016	42.4	Segment C rupture (short), deep buried, skewed updip, down-dip extent = lock zone, uniform slip distribution	Run02c*
Segmented Cs-B-D-UpS-L-U	2.7639	0.152212×10^{23}	9.016	42.4	As above. Modified model grid to address insufficient spatial coverage in a few discrete areas	Run02d

Note: Run02c* used in Lincoln County is not the same rupture model as that used in Clatsop County.

To calculate the moment magnitude (M_w), the seismic moment is scaled by the multiplier first to reflect the 2,475-yr scenario being evaluated and then converted to dyne-centimeters (Eq. 3). The moment magnitude (M_w) is then calculated using Eq. 4 (Hanks and Kanamori, 1979). The maximum slip is determined in Matlab for the CSZ rupture area directly offshore the three Oregon Coast counties.

Seven corresponding 2,475-year CSZ rupture scenarios were identified from the disaggregated sources and are shown in **Figure 3-4**. Five of the sources reflect margin wide ruptures (**Figure 3-4A–D**, **Figure 3-4G**), while two of the scenarios are a segmented (**Figure 3-4F**) or cluster type rupture (**Figure**

3-4E). Two of the buried models (DOGAMI Aexp-B-D-UpS-L-U [Figure 3-4A] and DOGAMI Aexp-B-D-UpS-M-U [Figure 3-4B]) differ only in terms of the downdip extent of the rupture zones (locked vs. midpoint [shallowest] extents). Two of the buried rupture scenarios (USGS A-B-D-UpS-M-U3 [Figure 3-4C] and DOGAMI Aexp-B-D-UpS-M-U [Figure 3-4B]) were found to be virtually indistinguishable from each other. One of the seven models is a trench-breaching scenario (Figure 3-4D), while the other reflects a splay fault model (Figure 3-4G). Included in Table 3-1, Table 3-2, and

Table 3-3 is a multiplier value used to scale the original deformation models developed by Sypus and Wang (2024) in order to meet the ASCE 2,475-year TDZ, the seismic moment (M_o) associated with the original (unscaled) rupture model, computed moment magnitude (M_w), and maximum slip.

$$M_{o\ revised} = (M_o * multiplier) * 10^7 \qquad (3)$$

$$M_w = \frac{2}{3} * log10(M_{o\ revised}) - 10.73 \qquad (4)$$

Figure 3-4. Seven 2,475-yr CSZ deformation models evaluated in this study and the counties where the models were found to apply. Calculated moment magnitudes are included in the figure. Model scenarios are described in more detail in Table 3-1, Table 3-2, and

Table 3-3.

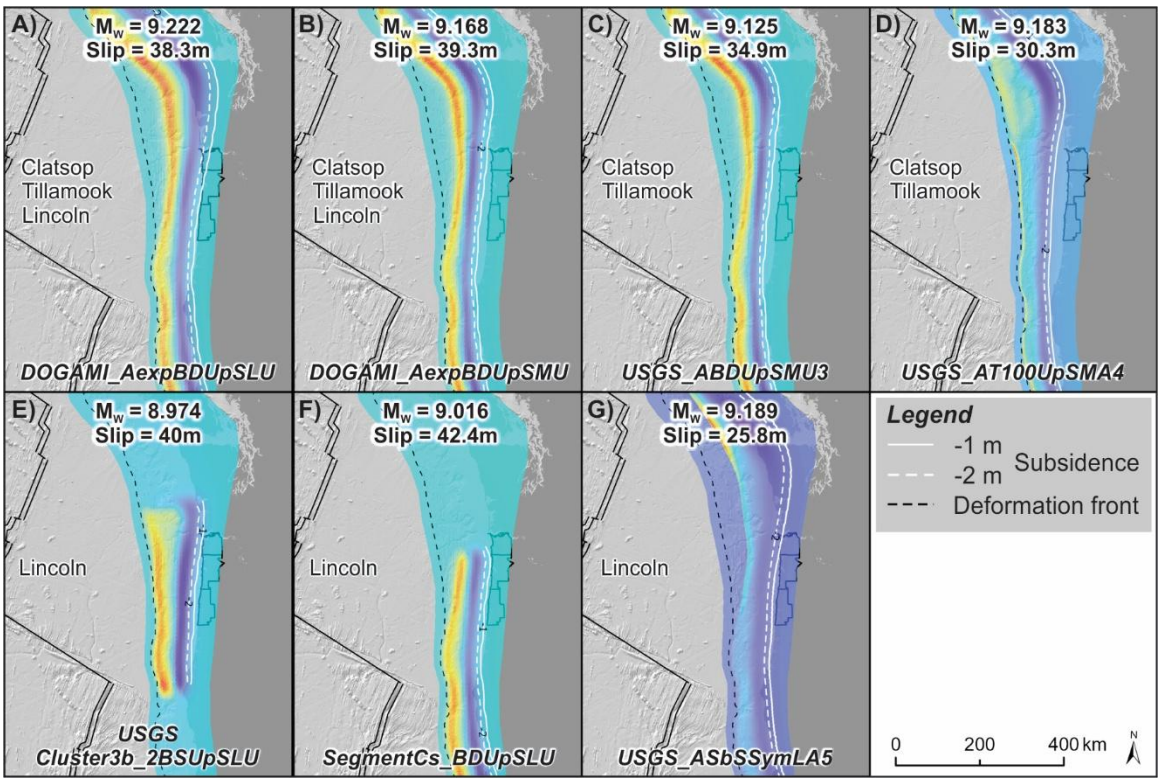
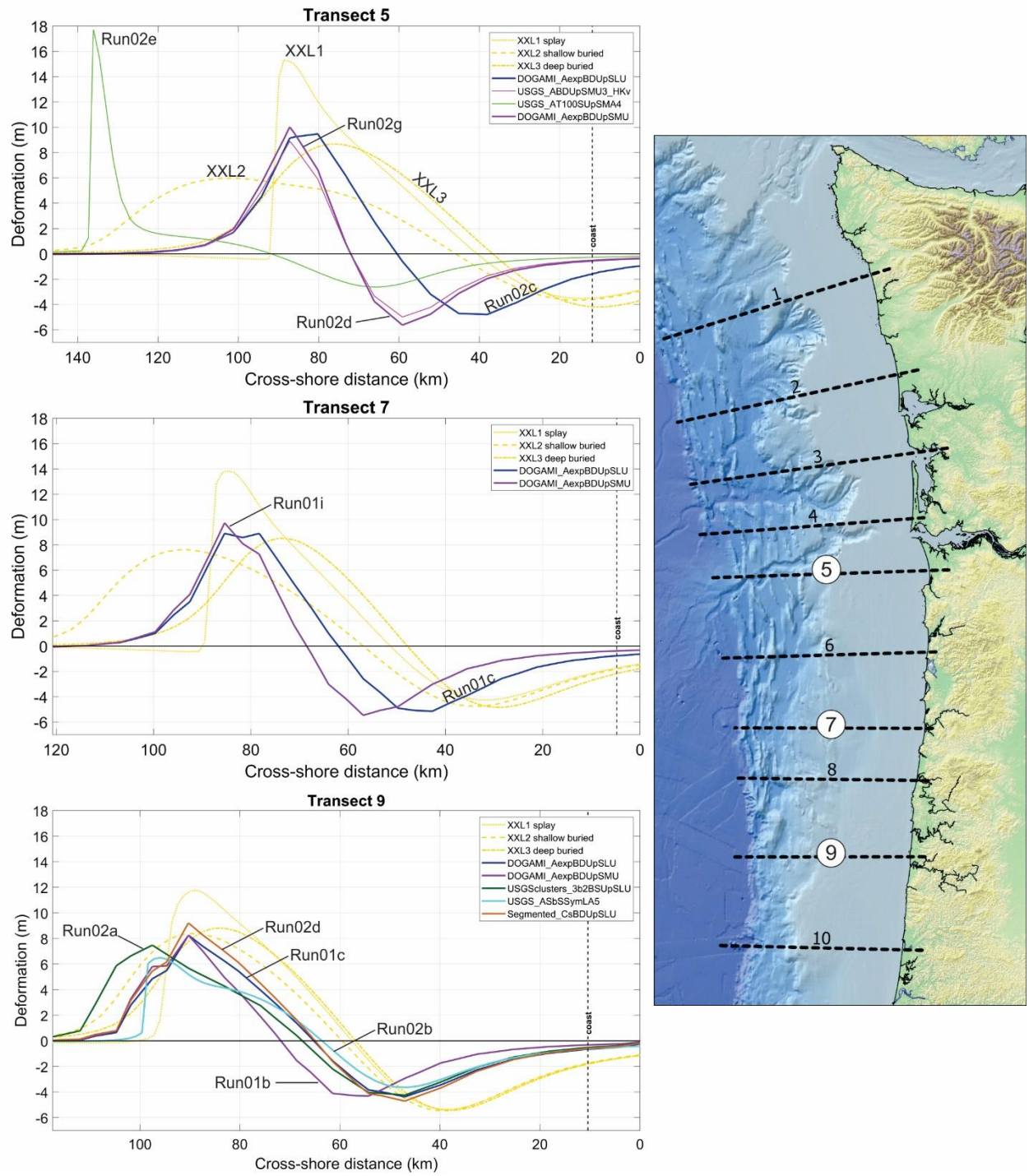


Figure 3-5 presents three cross sections of surface deformation derived from the suite of 2,475-yr source models. Transect 5 is located near Seaside and includes four rupture scenarios, while Transect 7 is located further south near Pacific City, Tillamook County, and includes two of the same scenarios evaluated for Clatsop County. Transect 9 is in Lincoln County and crosses the coast near Seal Rock. Lincoln County source models shown in Table 3-3 include the same two scenarios used in Tillamook and Clatsop,

along with three additional scenarios (**Figure 3-4A, B, E–G**). Included in each of the plots are the original XXL deformation models developed by Witter and others (2011). Although these latter scenarios reflect the most conservative scenarios developed by Witter and others, they remain useful when comparing the shape of the surface deformation and ultimately the tsunami that is generated.

Figure 3-5. Profiles of different 2,475-yr earthquake deformation models used in the Cascadia tsunami simulations, compared with the original DOGAMI XXL scenarios developed by Witter and others (2011).



At the coast, the newer deformation models produce lower subsidence when compared with the original DOGAMI XXL models (**Figure 3-5**). For example, in Clatsop County the original DOGAMI models result in very large subsidence (~3–4 m) immediately along the Clatsop coastline, while the newer buried models place the maximum subsidence much further offshore, some 40–60 km from the coast. At the coastline, this difference results in ~60% to 80% less subsidence when compared with the original DOGAMI models. In fact, this oceanward shift in the location of the peak of the subsidence is consistent along the length of the Oregon Coast. These differences are mainly the product of downdip extent constraints (e.g., halfway between the fully locked zone and 1 cm/yr locking contour [Run02g/Run01i] and the location of the locked zone [Run02c/Run1c]) adopted as part of the revised source models and is discussed further in **Section 5.0**. Additional factors that may also be affecting the widths of the updated CSZ source models include:

- the shape of the slip distributions (symmetric compared with updip skewed models)
- improved constraints provided by the paleoseismic record (e.g., Kemp and others, 2018; Behavar and others, 2025), particularly the amount of coseismic (subsidence) determined from the geologic data
- refinements in the overall approach used to construct the deformation models (i.e., Sypus and Wang, 2024)
- the geometry of the down-going plate captured by the CASIE21 seismic imaging data.

Other notable characteristics evident from **Figure 3-5** include a slight westward shift in the peak deformation in the buried rupture models, which have shifted westward by ~10–15 km. The combination of shifting the peak and trough of the deformation essentially produces greater asymmetry in the resulting tsunami (i.e., a shorter/steeper wave) when the deformation is translated to the ocean surface. **Figure 3-4** also highlights the deformation produced from a trench-breaching scenario. In this example, peak uplift reaches ~18 m but is confined to a much narrower area (Transect 5 in **Figure 3-5**). On land, the trench-breaching scenario produces the lowest subsidence on the northern Oregon Coast.

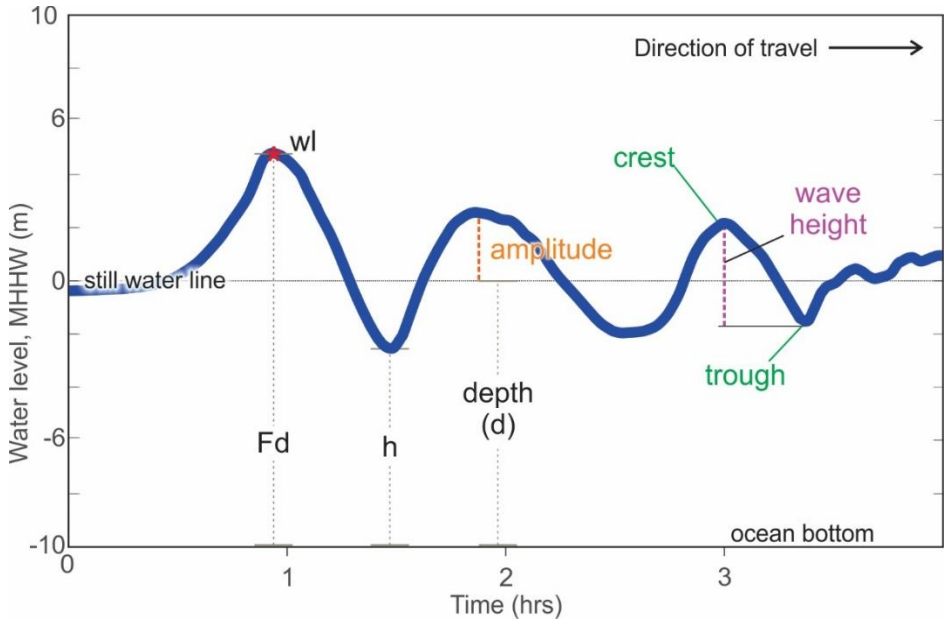
Finally, in Lincoln County (Transect 9 in **Figure 3-4**), several other scenarios are included that reflect a potential splay fault rupture, a shallow-buried cluster model, and a deep-buried segment C rupture. One of the deformation models has its downdip limit in the shallowest portion of the subduction zone (Run01b at Transect 9 in **Figure 3-5**), while the remaining source models have downdip limits confined to the 1 cm/year locked zone (Run01c, Run02b, and Run02d at Transect 9 in **Figure 3-5** and **Figure 3-4A**). This difference explains why the trough in the DOGAMI Aexp-B-D-UpS-M-U deformation model shown for Transect 9 in **Figure 3-4** is shifted further westward (i.e., in the updip direction) when compared with the other buried rupture models.

3.5 Simulation Outputs

For each simulation, the authors output a suite of key hydraulic parameters, including the maximum water level (defined for any given vertical datum), u and v velocities, flow depth (Fd), momentum flux, minimum depth below the tsunami wave trough (h; **Figure 3-6**), and time series information for predefined virtual water level stations, including the offshore POIs used to evaluate the tsunami simulations. For the purposes of this study, the maximum water level (wl) reflects the maximum value observed in any given model grid cell over the duration (time series) of the model simulation and is determined from wl = Fd – d (**Figure 3-6**). Depth (d) reflects the depth from the still water line (assuming a static water surface) to the seafloor; on land, d becomes the ground surface elevation. The momentum flux (mf) is defined by

$Fd*spd^2$, where spd is the tsunami current velocity defined from the orthogonal velocity components, $spd = \sqrt{(u^2 + v^2)}$.

Figure 3-6. Various terms used to define a tsunami wave form.



4.0 RESULTS

This section initially evaluates the tsunami modeling results relative to the offshore design wave for a 2,475-yr ARP event, followed by a discussion of the accompanying tsunami inundation generated from the simulations. The final inundation models that will be used to revise the existing ASCE7-22 tsunami zone are then presented, along with accompanying secondary datasets.

To meet the minimum ASCE tsunami modeling standards, the 2,475-yr tsunami design wave amplitudes are first derived from the PTHA for POIs offshore of the coast (e.g., along the 100 m bathymetric contour). These data are then compared with tsunami amplitudes derived from our SCHISM modeling produced from the equivalent disaggregated 2,475-yr CSZ sources. Two criteria are assessed to determine if a simulation can be said to have met the minimum standards established by the ASCE. These criteria include the following:

1. No more than 5% of the simulated points are allowed to fall below the minimum 80% threshold defined for the 2,475-yr tsunami design wave.
2. The mean of the simulated points determined for each scenario must meet or exceed 100% of the mean of the 2,475-yr tsunami design wave points.

When comparing the scenario simulations with the 2,475-yr tsunami design waves, an important point to note is that the design wave was originally developed using a coarse model grid (~900 m cell spacing) at the 100 m bathymetric contour, whereas our SCHISM model grid uses a much higher grid resolution (~140 m) in the same general area. As described in **Section 3.1**, the high-resolution model grid smoothly transitions toward even finer grid resolutions in the nearshore and on land, where point densities average ~5–10 m, whereas the original PTHA grid remains coarse. As a result, these differences in grid resolutions will have a bearing on the variability of the model amplitudes observed along the 100 m POIs.

4.1 Offshore Design Wave and Inundation Comparisons

4.1.1 Clatsop County

Figure 4-1A presents the 2,475-yr tsunami design wave for offshore Clatsop County as well as the simulated tsunami amplitudes that correspond to the scenarios (Run02c, 02d, 02e, and 02f) presented in **Table 3-1**. **Figure 4-1B** compares the moving average of the simulated amplitudes relative to the moving average of the 2,475-yr design waves. Thus, the upper plot of **Figure 4-1** addresses the requirements of the ASCE criteria 1 introduced previously, while the lower plot focuses on criteria 2. Included in **Figure 4-1** are estimates of the root mean square error (RMSE) calculated for each of the scenarios and compared to the design wave. These data provide a measure of the deviations between the model results and the 2,475-yr design-wave values. Based on these data, it is evident that Run02d and 02f have smaller RMSE values, while Run02c and 02e show larger differences. There are several factors that may influence the RMSE calculations. These include the following:

- Differences in the grid resolutions probably account for much of the variation observed
- It is unclear how the original PTHA modeling accounts for non-linear processes such as wave reflection at the coast, which may have been absorbed into the original PTHA hazard curve calculations
- When defining the offshore wave amplitudes for the design wave, it is presumed that the chosen peak wave amplitude coincides with the first wave peak. It is possible that secondary peaks may have been extracted in areas where strong reflection from the coast may occur.

As can be seen in **Figure 4-1**, three of the 2,475-yr CSZ scenarios modeled for Clatsop County meet both the 80% threshold as well as the mean test. Conversely, the trench-breach scenario (Run02e) fails both the 80% threshold test as well as the mean test since the moving mean of the simulations falls well below the mean of the 2,475-yr design wave. Based on these results the trench breach scenario was removed from further consideration. Additionally, the authors chose to discard the Run02d scenario from further consideration because Run02d (green line) and 02f (orange line) produced very comparable offshore amplitudes (**Figure 4-1A**) and inundation results (not shown). Instead, the authors focused on the slightly more conservative Run02f model.

Evident in **Figure 4-1** are a number of areas along the Clatsop Coast where the model amplitudes consistently exceed the 2,475-yr tsunami design wave, including between latitudes 45.6°N and 45.7°N (Rockaway Beach to Manzanita in Tillamook County), just north of Seaside, and offshore Cape Disappointment (~46.35°N) in Washington State. These peaks are indicative of a variety of effects characteristic of the higher resolution modeling, including:

- The reflection of tsunami waves away from the coast, especially around headlands (e.g., Cape Falcon, Tillamook Head and Cape Disappointment)
- The reflected waves travelling away from the coast interact with secondary waves travelling toward the coast
- Propagation of edge waves that travel either oblique to the coast or parallel to it (the edge waves interact with the tsunami reflected from the shore and can cause amplification of later arriving tsunami waves)
- The simulated amplitudes and 2,475-yr design amplitudes match best in areas associated with deep water (e.g., near Astoria Canyon offshore the mouth of the Columbia River). This is probably due to the POIs being close to very deep water, and the fact that there is little reflection of waves from the area surrounding the Columbia River estuary.

Figure 4-1. A) Plot showing simulated tsunami amplitudes for various model runs offshore Clatsop County. Solid black line with circles is the 2,475-yr tsunami design wave, while the red dashed line depicts the 80% threshold below which simulated amplitudes fail to meet the minimum threshold. B) Calculated moving averages determined for the 2,475-yr tsunami design wave and the various source simulations.

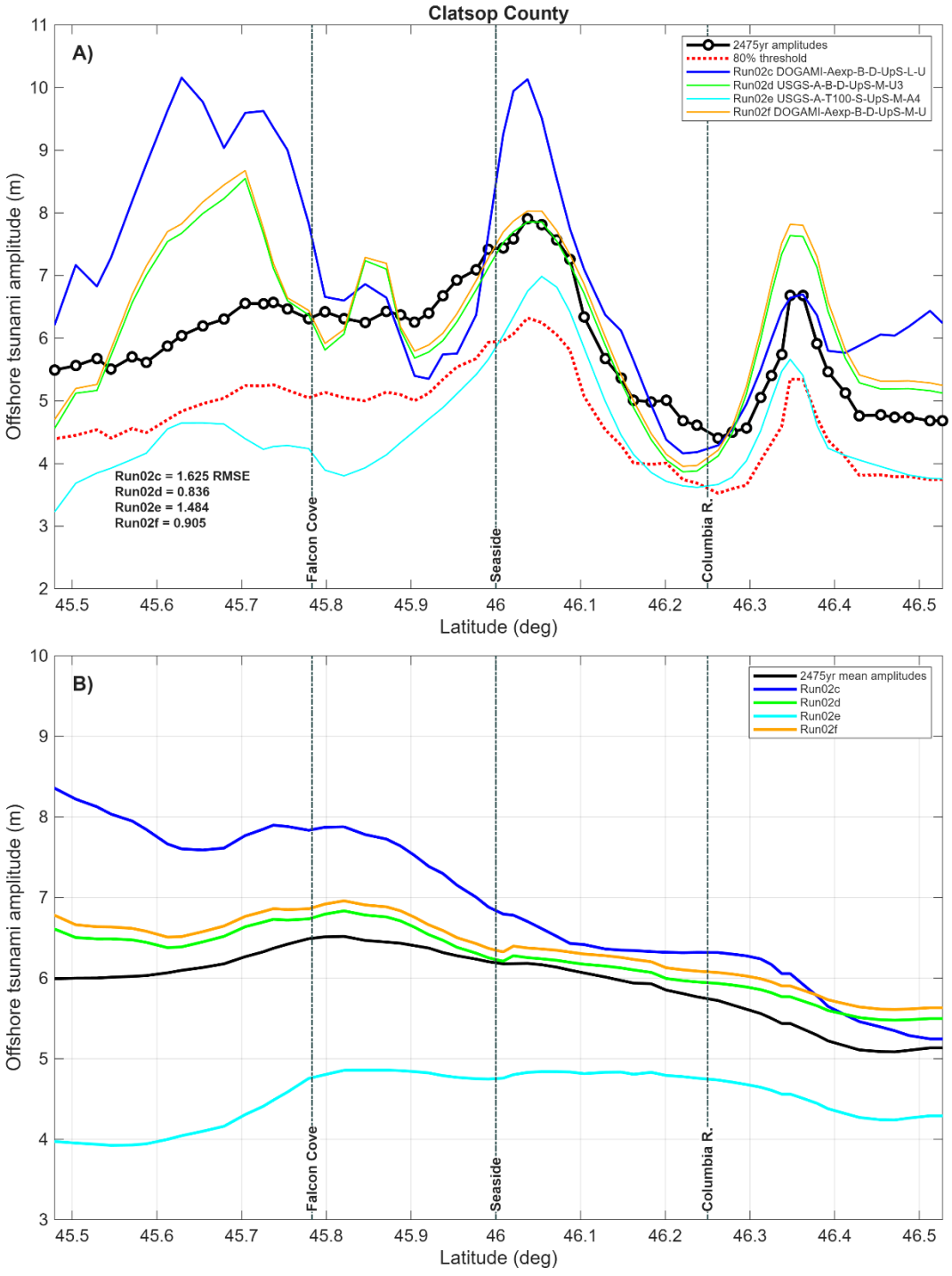
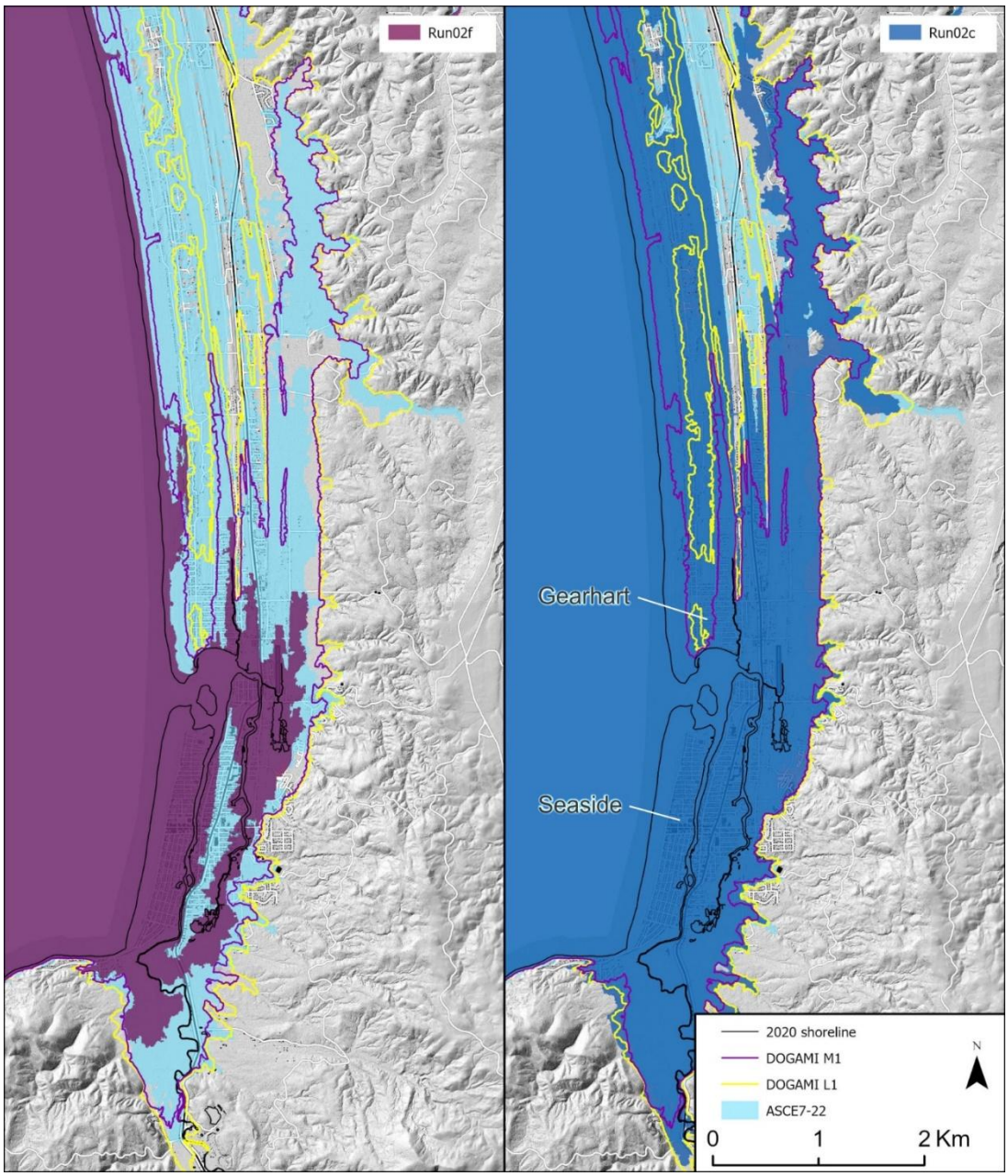


Figure 4-2 compares the inundation produced by the remaining two scenarios under consideration, Run02f (left) and Run02c (right), highlighting the very significant difference in flooding produced by two equivalent 2,475-yr CSZ scenarios. Included in the figure is the existing ASCE7-22 inundation zone (cyan polygon) along with the inundation produced by the DOGAMI M1 (purple line) and L1 (yellow line) scenarios. Although the original CSZ source models produced by Witter and others (2011) have changed (i.e., Sypus and Wang, 2024) and the tsunami simulations were run with zero bottom friction (Manning-n = 0), the original T-shirt size model scenarios remain a useful benchmark for assessing the degree of inundation produced by the latest model results.

Figure 4-2. Two models of 2,475-yr tsunami inundation affecting Seaside and the Clatsop Plains. Figure includes the original DOGAMI M1 and L1 scenarios and existing ASCE7-22 inundation zone for comparison.



Based on the data presented in **Figure 4-2**, it can be seen that Run02f underpredicts the degree of inundation, especially when compared to the average-sized DOGAMI M1 scenario (equivalent to ~500 years of plate convergence) and the L1 scenario (~800 years plate convergence). In contrast, apart from select areas along the central to northern Clatsop Plains where previous ASCE7-22 showed greater inundation, Run02c is generally more conservative than the previous ASCE7-22 modeling and is either comparable to the L1 scenario or exceeds it. Again, a major difference between these latest model runs and the previous ASCE7-22 modeling is the use of much higher resolution model grids (~5– 10 m on land compared with 60 m grids used for ASCE7-22) and improvements to the source models.

Because Run02f produced less peak slip when compared with Run02c (35.7 m compared with 38.3 m; **Table 3-1**) and significantly less inundation, the authors simulated three additional scenarios in which they adjusted the scaling of both Run02f and Run02c according to the following parameters:

- Run02g: Run02f scaled up by an additional 10%
- Run02h: Run02c scaled down by 10%
- Run02i: Run02c scaled down by 7%

As presented in **Table 3-1**, the scaling has a corresponding effect on the calculated peak slip and moment magnitude, which are modified slightly while remaining somewhat consistent among all the scenario estimates.

Figure 4-3 presents the revised offshore amplitudes for Run02g, 02h, and 02i overlaid against the original Run02c and Run02f scenarios. As can be seen in **Figure 4-3A**, the Run02g amplitudes are slightly larger when compared to the original Run02f, approaching levels that are in some areas comparable to Run02c. In contrast, the two scaled down versions of Run02c either violate the 80% threshold (e.g., Run02h) or fall below the 2,475-yr moving average threshold (both Run02h and Run02i). To that end, both Run02h and Run02i were not considered any further and the original Run02c model is retained as is.

Figure 4-3. A) Plot showing simulated tsunami amplitudes for three additional Clatsop County model runs in which the deformation and slip are modified. Solid black line with circles is the 2,475-yr tsunami design wave, while the red dashed line depicts the 80% threshold below which simulated amplitudes fail to meet the minimum threshold. B) Calculated moving averages determined for the 2,475-yr tsunami design wave and the adjusted sources.

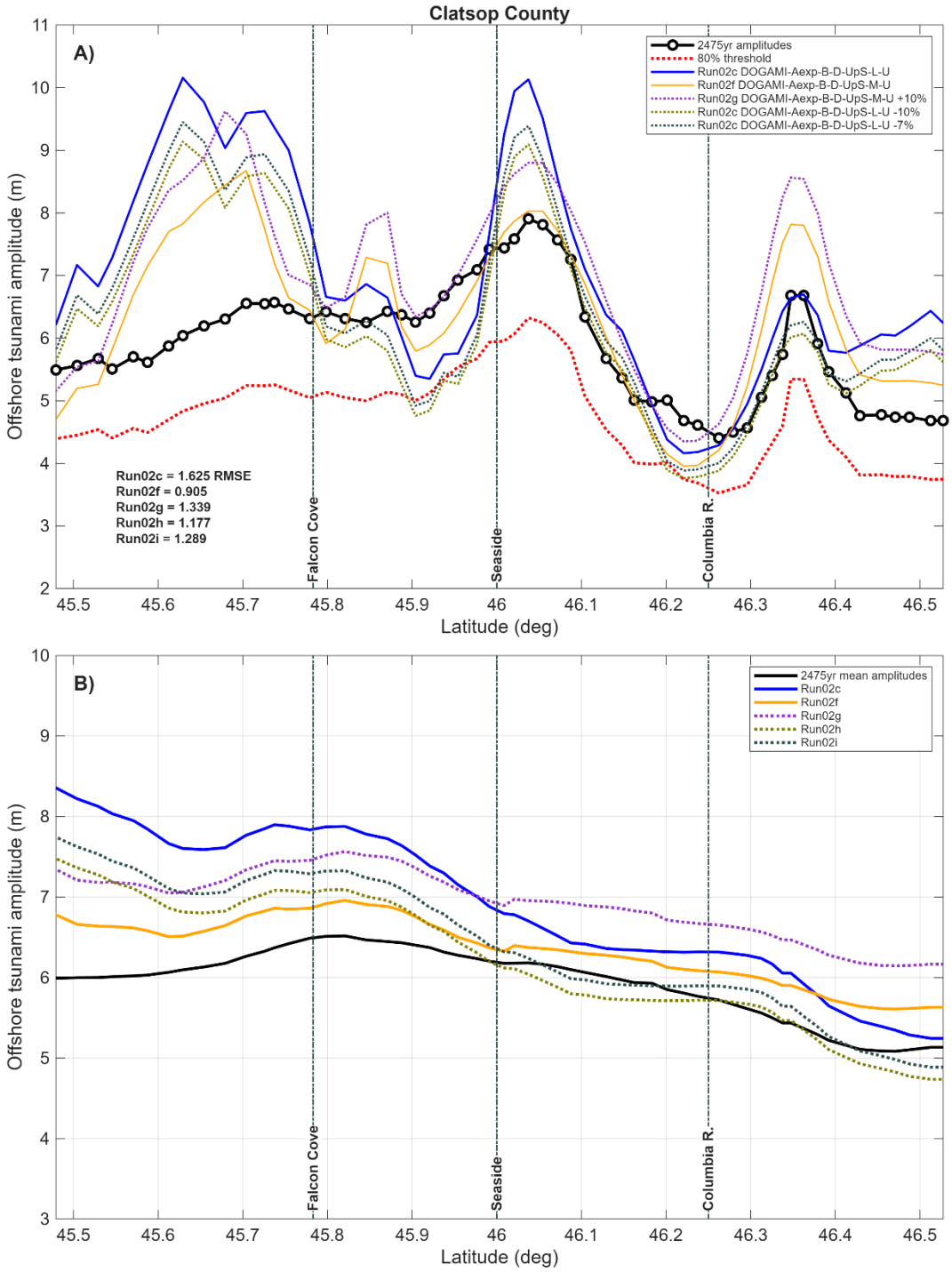
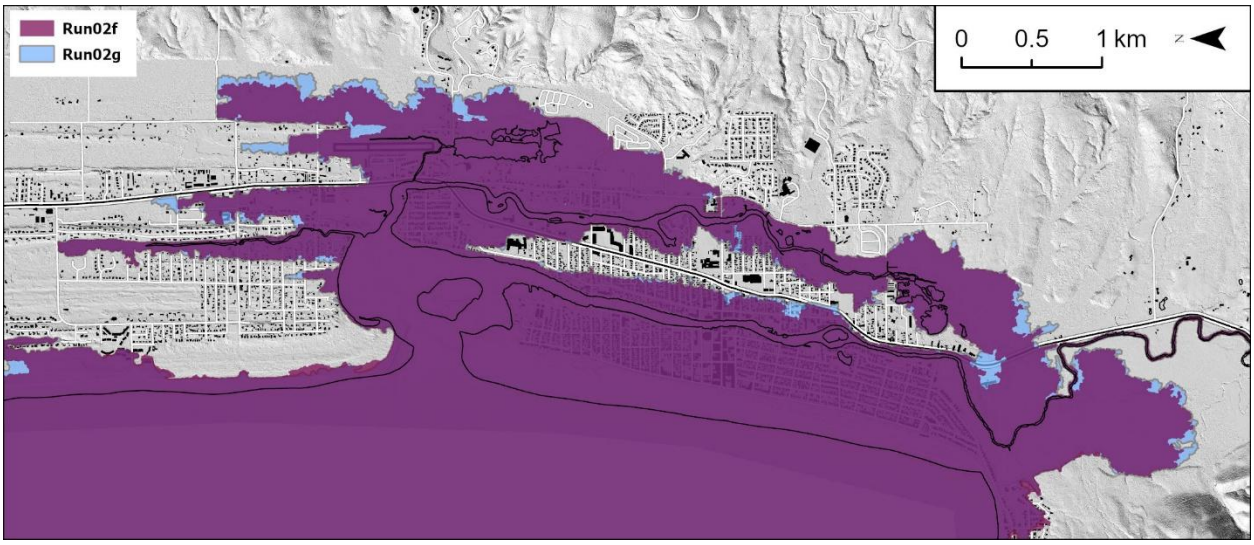


Figure 4-4 shows the change in inundation between the original Run02f and Run02g scenarios. Essentially, the 10% scaling associated with Run02g results in a nominal improvement in the inundation extent, despite the slight increase in maximum slip (**Table 3-1**). Nevertheless, inundation levels produced by Run02g were found to be either comparable to or exceeded Run02c in parts of southern Clatsop County (e.g., around Tillamook Head) and further south in Tillamook County. Based on those results, the Run02g simulation results are retained along with Run02c.

Figure 4-4. Change in tsunami inundation at Seaside due to scaling the Run02f scenario by 10%.

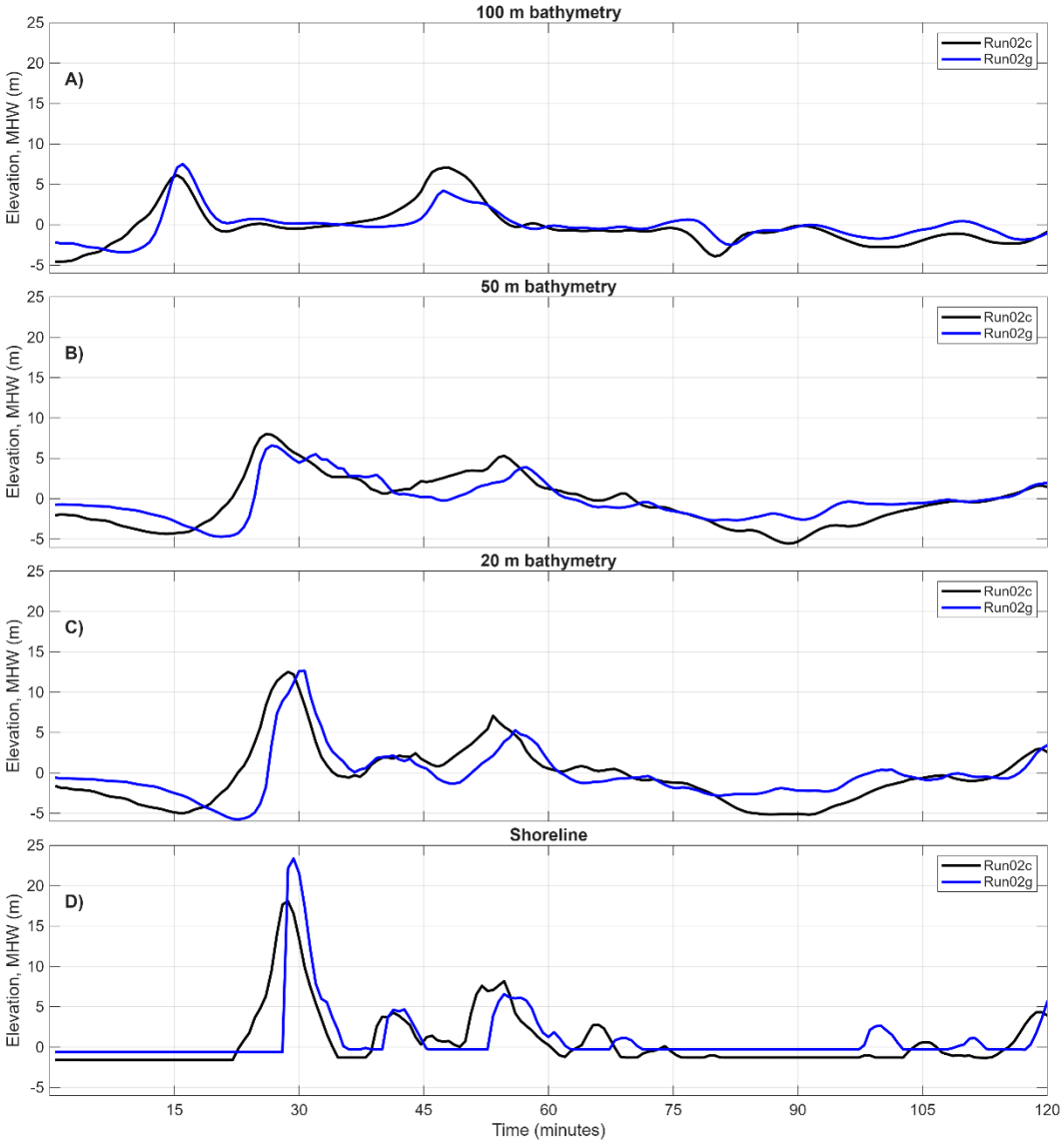


The difference in inundation extents produced by Run02c versus Run02g raises the question of whether the increased inundation in Run02c resulted partially from differences in the modeled subsidence or if RunO2c is simply producing a much larger tsunami. The only difference between these two scenarios is their downdip extents: the downdip extent of Run02c is at the 1 cm/yr locking zone, while the downdip extent for Run02g is located at a shallower depth. These differences directly influence the amount of deformation across the subduction zone, including the degree of subsidence that occurs on land (e.g., **Figure 3-5**). To further evaluate the potential role of subsidence, the authors reduced the on-land subsidence in Run02c by 0.5 m to make it more consistent with the subsidence observed in Run02g. However, this adjustment made little difference to the inundation observed, which suggests that subsidence is probably a small factor in the degree of inundation modeled by Run02c, and that the deformation (and tsunami wave asymmetry) is probably controlling the degree of inundation.

Figure 4-5 presents a time series of tsunami amplitudes for selected water depths along a transect in line with Seaside. As can be seen in the figure, the initial tsunami identified at ~17 minutes after the earthquake in Run02g is in fact larger when compared with the Run02c scenario. However, this situation is reversed at ~46 minutes after the earthquake (**Figure 4-5**), where Run02c is characterized by a very large secondary wave. Further evaluation of this scenario using an animation of Run02c indicates that the secondary wave peak is formed in response to the initial tsunami wave having reflected off the coast at Seaside, where it subsequently combines out in the inner shelf with edge waves travelling along the coast. **Figure 4-5** shows the asymmetry in the shape of the tsunami produced, which becomes more noticeable as the tsunami reaches shallower water depths (e.g., the -20 m bathymetry and at the coast). For example, Run02c is a broader wave when compared with the shorter, steeper shape of the Run02g tsunami. The abrupt arrival of the wave front at the coastline (**Figure 4-5D**) is simply because this station is on land.

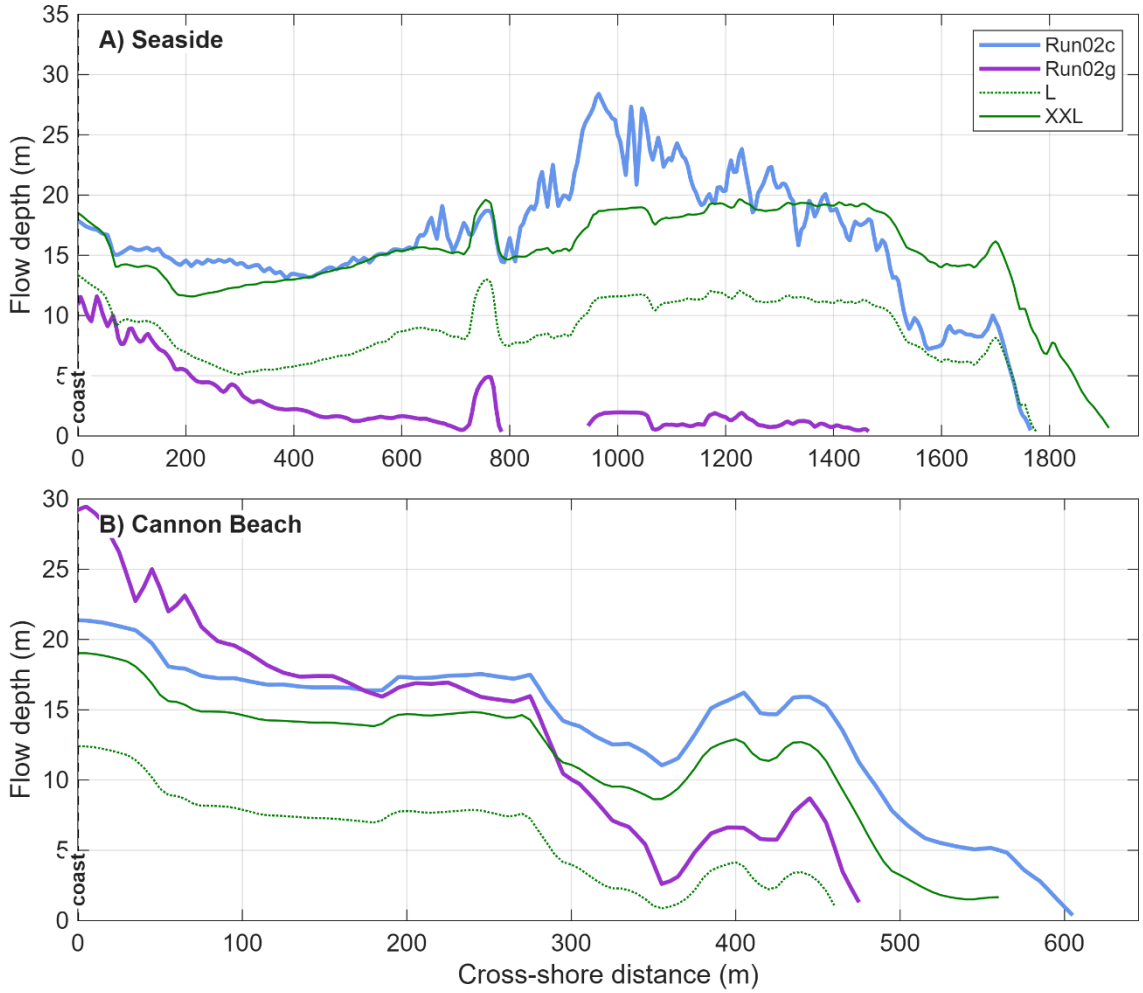
Again, however, the characteristics of the wave form at a single point, such as the provided example, do not give the complete answer. **Figure 3-5** highlighted differences in the deformation profiles for discrete sections of the coast. Since the initiation of the tsunami is related to deformation across the CSZ, the authors evaluated the volume of ocean water displaced by the two deformation models. In taking this approach, the authors find that the Run02c scenario moves ~39% more water when compared with the Run02g scenario. The difference in volume of water displaced at the initiation of the earthquake, combined with the asymmetry of the tsunami, directly translates to the magnitude of the Run02c tsunami and thus the amount of inundation observed on land.

Figure 4-5. Time series of tsunami waves produced by Run02c and Run02g for select water depths along a transect offshore at Seaside.



Besides differences in modeled inundation, the 2,475-yr scenario simulations reveal very significant differences in modeled flow depths. **Figure 4-6** shows the modeled flow depths defined for transects that cross the communities of Seaside and Cannon Beach. At Seaside, the modeled flow depths for Run02c are the largest observed with the peak flow depth reaching ~28 m, exceeding the DOGAMI XXL1 scenario by several meters in some locations. **Figure 4-6** indicates that the Run02c inundation at Seaside is about the same as the L1 scenario and is slightly smaller than the XXL1 scenario. In contrast, Run02g produces a 10 m high flow depth at the coast (**Figure 4-6**), which rapidly decreases landward of the coast. The fluctuations present in the Run02c flow depths are indicative of the piling up of tsunami surges within the Necanicum Estuary. At Cannon Beach, Run02g results in a larger flow depth at the open coast, reaching almost 30 m deep, while Run02c is ~8m lower when compared to Run02g. However, this result is reversed ~200 m from the beach, such that the Run02c scenario is now characterized by significantly deeper flow depths that are maintained across much of the inundation zone. Of note also, Run02c produces larger inundation at Cannon Beach when compared to the XXL1 scenario.

Figure 4-6. Comparison of model flow depths at A) Seaside and B) Cannon Beach, Clatsop County. Plot includes flow depths produced by the DOGAMI L1 and XXL1 scenarios.



4.1.2 Tillamook County

Figure 4-7A presents the 2,475-yr tsunami design wave for offshore Tillamook County as well as the simulated tsunami amplitudes that correspond to the evaluated scenarios (Run01c, 01d, 01f, and 01i) introduced in **Table 3-2**. Of note here, the scenarios presented in **Table 3-2** are the same as those previously evaluated for Clatsop County. **Figure 4-7B** compares the moving average of the simulated amplitudes relative to the moving average of the 2,475-yr design waves. As with the Clatsop County modeling, the authors include calculations of the RMSE for each of the scenarios. Based on these data, it is apparent that Run01d and 01f have smaller RMSE values, while Run01c and 01i show slightly larger differences. The authors excluded the trench-breaching scenario (Run01e) from **Figure 4-7** since it fails both ASCE modeling criteria, consistent with findings for Clatsop County.

As can be seen in **Figure 4-7**, two of the model runs (Run01d and 01f) fail both criteria 1 (more than 5% of the points fall below the 80% threshold) and criteria 2 (the model mean must meet or exceed the mean of the 2,475-yr PTHA). As with Clatsop County, the authors chose to discard Run01d from further consideration since it is very similar to Run01f. Furthermore, because Run01f was found to fail both initial tests, the authors scaled up the deformation model by a further 10% (Run01i in **Table 3-2** and **Figure 4-7**). As can be seen in **Figure 4-7**, Run01i now passes the 80% threshold test along the entire Tillamook coastline. In addition, except for a small section of shoreline between Sand Lake and Cape Lookout, Run01i meets the minimum requirements of the mean test. The authors chose not to scale the Run01i deformation model further, since the calculated maximum slip produced by Run01i and Run01c are broadly similar, and further scaling was deemed to be unnecessary given that Run01c is already meeting all ASCE requirements.

The along coast variability in modeled tsunami waves, defined by areas exhibiting both high and low amplitudes along the Tillamook County coastline (**Figure 4-7**), again demonstrate complex nonlinear effects that occur due to the shoaling of tsunami across the shallowing inner shelf, and their subsequent interaction with reflected waves from the coast and edge waves that develop on the shelf. Modeling indicates large peak amplitudes (~8–10 m) in northern Tillamook County (consistent with Clatsop modeling), offshore Netarts estuary, near Pacific City, and near the Siletz estuary in Lincoln County. Between the peaks are areas of much lower amplitudes that generally fall below the 2,475-yr design wave. In contrast, the 2,475-yr design waves exhibit relatively uniform tsunami amplitudes (~5.5–6.5 m) across much of the Tillamook coastline, before increasing in southern Clatsop County. Again, these variations are strongly dependent on the utilized high-resolution model grid, when compared with the grid used to define the original 2,475-yr design wave.

Figure 4-8 provides a comparison of the modeled inundation for Run01i and Run01c at Rockaway Beach in northern Tillamook County, and for Tillamook located at the head of Tillamook Bay. Unlike Seaside in Clatsop County where the difference in inundation between the same runs were substantial, inundation differences in Tillamook County are much smaller and in many parts of the open coast the two scenarios produce comparable inundation. Larger differences between the models become more apparent within the various coastal estuaries, such as Tillamook Bay (**Figure 4-8** right), particularly at the distal ends of the inundation zones. As can be seen in **Figure 4-8**, the latest modeling appears to indicate slightly less inundation when compared with the previous ASCE7-22 modeling. Conversely, both model runs are broadly consistent with the DOGAMI L1 inundation extent along the open coast but differ more significantly within the coastal estuaries. This latter change is to be expected since the latest modeling includes friction, while earlier DOGAMI modeling did not.

Figure 4-7. A) Plot showing simulated tsunami amplitudes for various model runs offshore Tillamook County. Solid black line with circles is the 2,475-yr tsunami design wave, while the red dashed line depicts the 80% threshold below which simulated amplitudes fail to meet the minimum threshold. B) Calculated moving averages determined for the 2,475-yr tsunami design wave and the various source simulations.

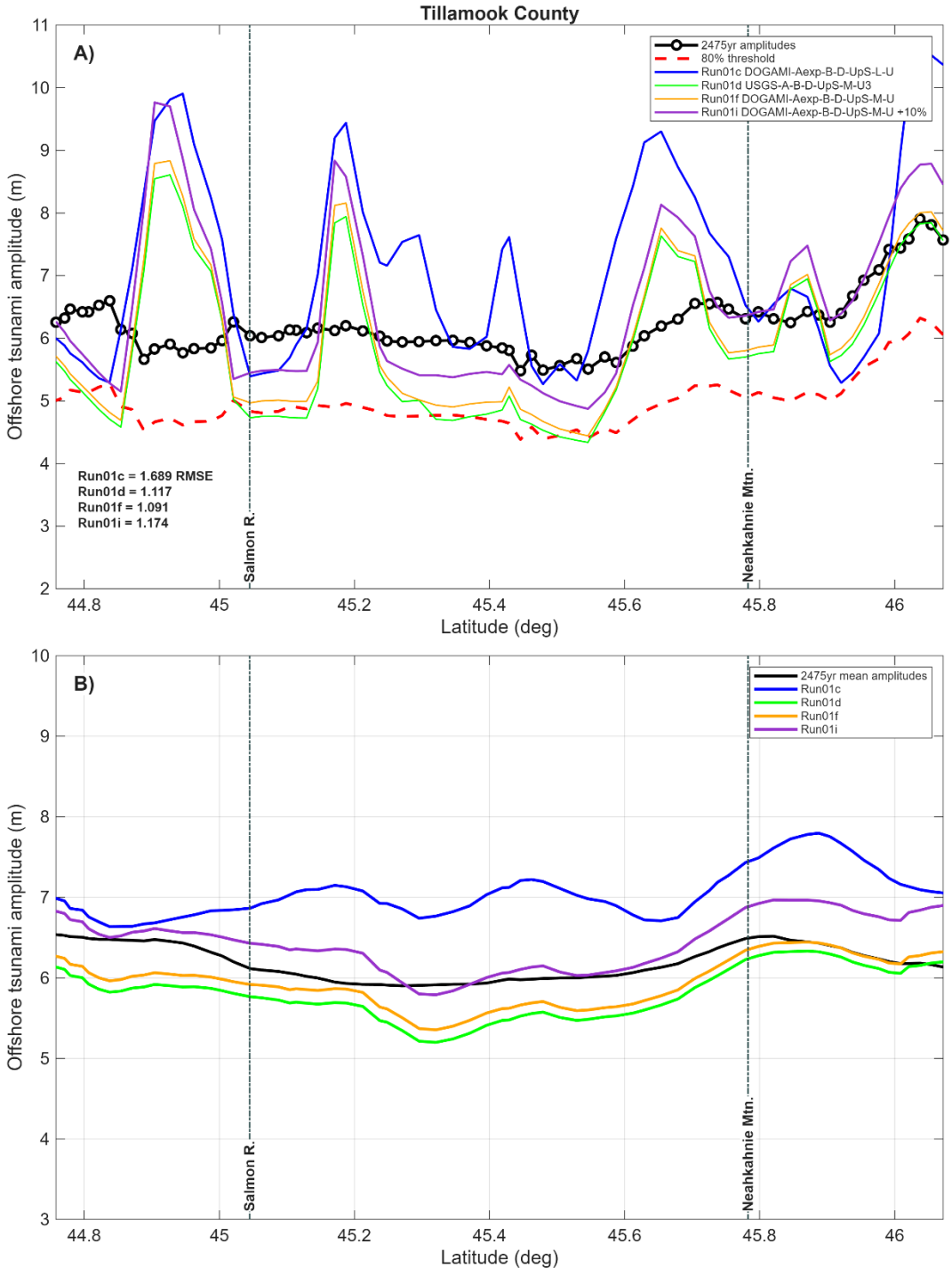


Figure 4-8. Two scenarios of 2,475-yr tsunami inundation affecting Rockaway Beach (left) and the city of Tillamook (right), Tillamook County. Figure includes the original DOGAMI L1 scenario and existing ASCE7-22 inundation zone for comparison.

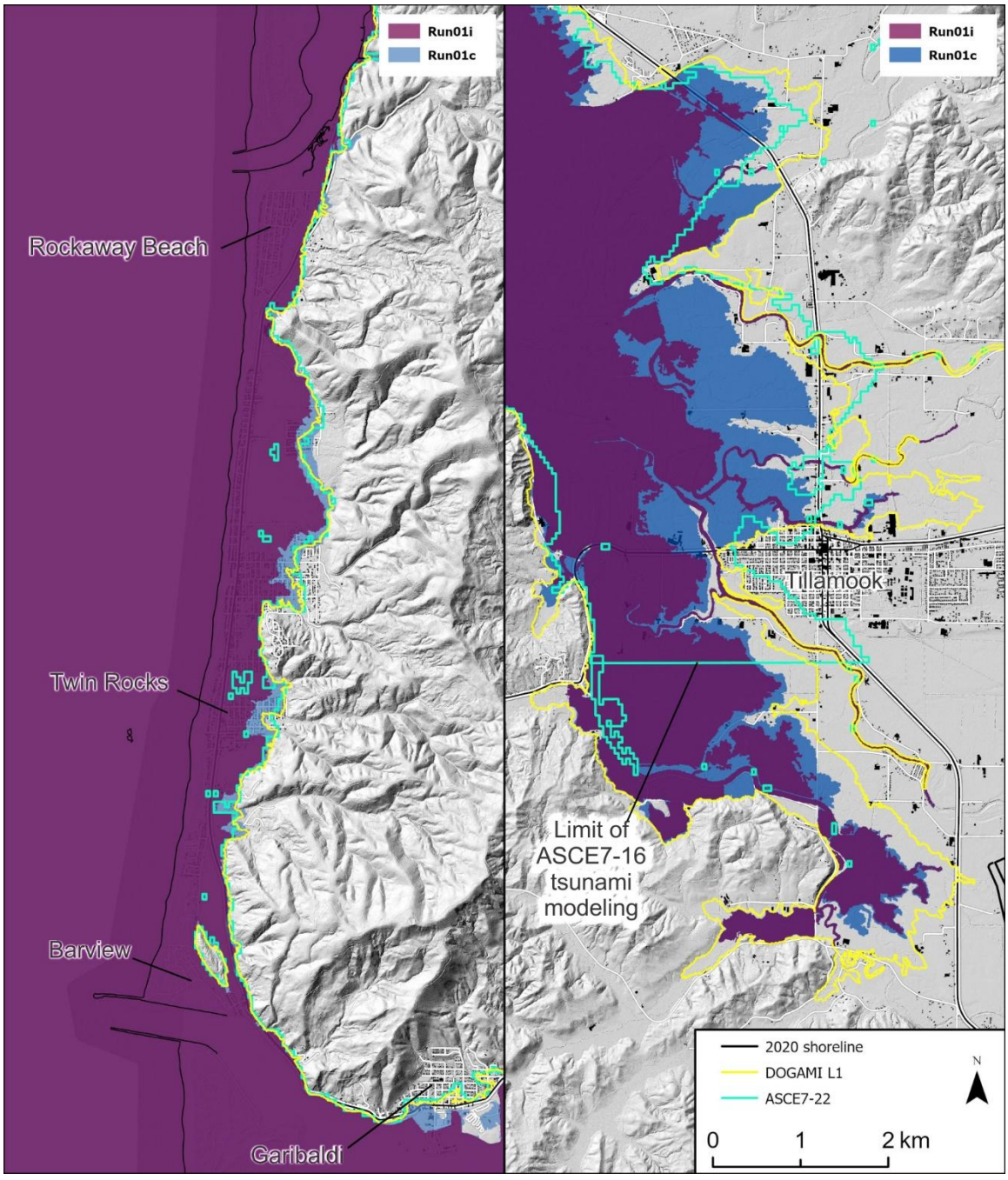
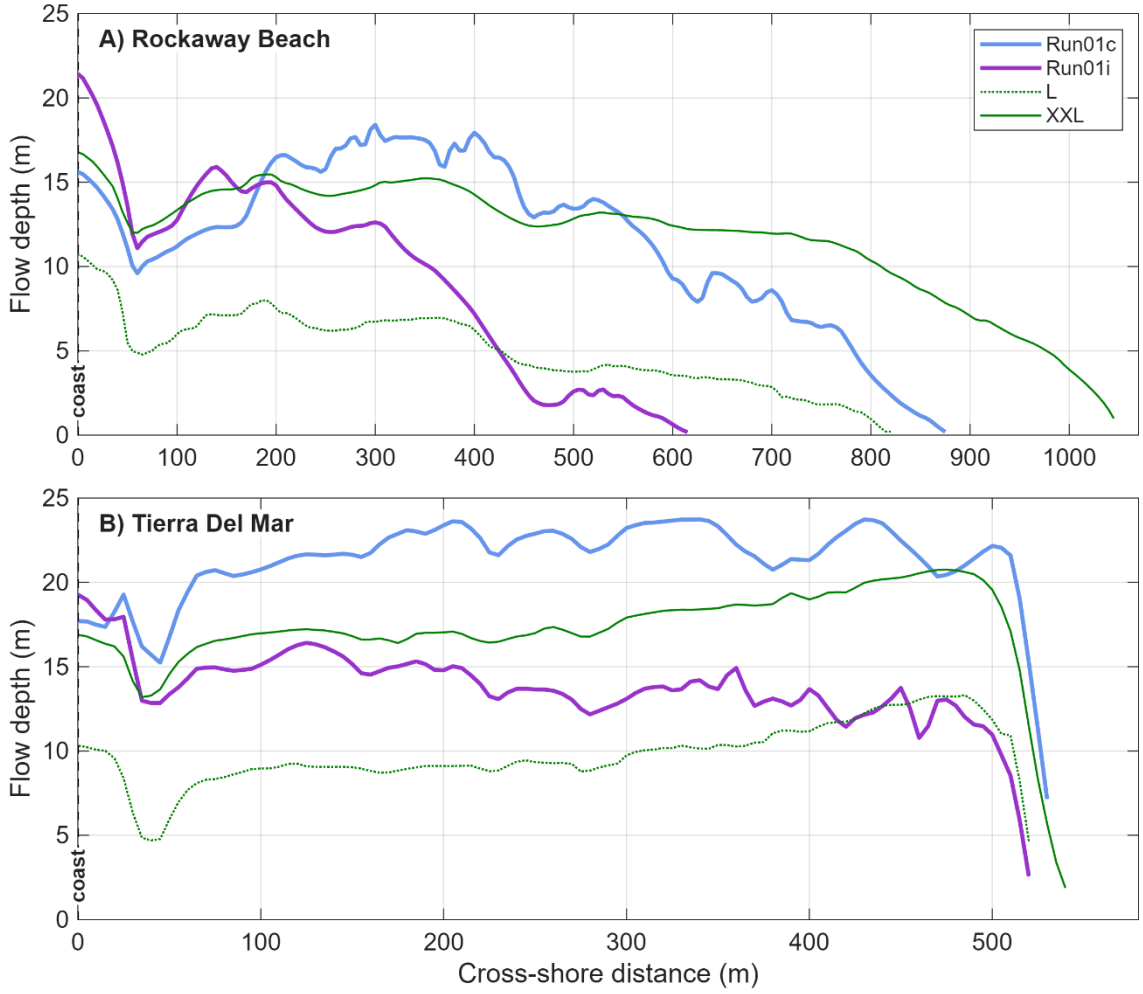


Figure 4-9 presents the modeled flow depths defined for transects that cross the communities of Rockaway Beach and Tierra Del Mar (**Figure 1-1**), respectively northern and southern Tillamook County. At Rockaway Beach, the modeled flow depths for Run01i are initially larger than both the Run01c and XXL flow depths; the peak Run01i flow depth reaches ~21.4 m at the coast. However, landward of the coast the modeled flow depths produced by the Run01i simulation rapidly decrease in height as the tsunami travels inland, reaching its inundation limit ~600 m from the beach. Conversely, Run01c produces a 15.5 m flow depth at the coast, where it then initially decreases in height as the tsunami crosses a tall foredune, before building to its peak of ~16–18 m. As can be seen in **Figure 4-9**, the Run01c flow depths are comparable to the DOGAMI XXL scenario but produce an inundation extent that is less than the XXL scenario. Model flow depths produced by the Run01c scenario at Tierra Del Mar are deeper when compared to Rockaway Beach but are maintained over a much shorter distance. This is because the community is backed by a marine terrace, which limits the degree of inundation occurring at this site.

Figure 4-9. Comparison of model flow depths at A) Rockaway Beach and B) Tierra Del Mar, Tillamook County. Plot includes flow depths produced by the DOGAMI L1 and XXL1 scenarios.



4.1.3 Lincoln County

Figure 4-10A presents the 2,475-yr tsunami design wave for offshore Lincoln County as well as the simulated tsunami amplitudes that correspond to the evaluated scenarios (Run01a, 01b, Run02a, 02b, and 02c) introduced in
Table 3-3. Of note here, two of the scenarios (Run01a and Run01b) are the same as those previously adopted for Clatsop County (Run02c and Run02g) and Tillamook County (Run01c and Run01i). As can be seen in **Figure 4-10** and
Table 3-3, the authors evaluated three additional CSZ 2,475-yr earthquake sources unique to the Lincoln County area. **Figure 4-10B** compares the moving average of the simulated amplitudes relative to the moving average of the 2,475-yr design waves. As with the previous modeling, the authors include calculations of the RMSE for each of the scenarios in **Figure 4-10A**.

Evident from **Figure 4-10**, Run01b and 02b have the smallest RMSE values, while Run01a and 02c produced the largest RMSE values. As with Clatsop County and Tillamook County, a major contributor to the RMSE values are the variations in the alongshore peaks (and troughs) in offshore tsunami amplitudes, characteristic of the inner shelf bathymetry and reflection of waves from the Lincoln County coastline. In particular, the authors note the very significant 2,475-yr scenario amplitudes in southern Lincoln County in line with the southern boundary of the county. These large amplitudes are the product of non-linear effects taking place offshore the coast on and around Stonewall Bank. At Stonewall Bank, refraction processes cause the tsunami to focus in across the bank, producing very large tsunami waves (seaward side), while diffraction processes and sheltering effects provided by the bank on its lee side results in much smaller tsunami (**Figure 4-10**). These effects are only nominally captured by the original PTHA and 2,475-yr tsunami design wave.

Based on the initial modeling, four of the five 2,475-yr scenarios were found to fail the 80% threshold test (criteria 1), with only Run02c exceeding this test (**Figure 4-10A**). The four models that fail all underestimate the tsunami amplitudes south of Cape Perpetua (i.e., south of ~44.2°N). This is the region in which Stonewall Bank is found to strongly influence tsunami amplitudes, due to sheltering effects. Run02b (USGS cluster source) also fails further north near ~44.65°N (offshore Newport). Only two of the models meet or exceed the moving mean test presented in **Figure 4-10B**, while the rest of the scenarios fail the test in several places. Based on these initial modeling results, the authors chose to discard the Run01b, 02a, and 02b scenarios, and focus on the Run01a and Run02c scenarios. Since Run01a was found to fail the 80% threshold test, the authors scaled this scenario 10% to produce a new Run01c scenario. In addition, the authors discovered a few areas in Lincoln County where the model grid did not extend sufficiently high enough and accordingly updated the model grid to correct for those problem areas. Hence, both Run01c and Run02d (formerly Run02c) were re-run on the updated model grid. The results of the updated modeling results showing the offshore amplitudes and moving means are presented in **Figure 4-11**. For reference, the authors include the original unscaled Run01a model to demonstrate the effect of the additional 10% scaling. As can be seen in **Figure 4-11**, the 10% scaling (Run01c, solid blue line) increases the overall amplitudes (~1 m) and moving means. Importantly, despite a few points south of ~44.2°N still falling below the 80% threshold test, the overwhelming majority (>95%) remain above and hence now meets the minimum ASCE criteria 2 threshold.

Figure 4-12 compares the modeled inundation for Run01c and Run02d at Lincoln City in northern Lincoln County, and for Waldport located in Alsea Bay. Because the inundation produced by these two scenarios shows little difference, the authors flipped the color order in **Figure 4-12** in order to highlight differences in a few discrete locations (typically up small valleys). **Figure 4-12** indicates a variety of responses that range from less to more inundation when compared with the previous ASCE7-22 modeling.

However, when compared with the DOGAMI L1 inundation zone, the latest modeling indicates generally greater inundation.

Figure 4-10. A) Plot showing simulated tsunami amplitudes for various model runs offshore Lincoln County. Solid black line with circles is the 2,475-yr tsunami design wave, while the red dashed line depicts the 80% threshold below which simulated amplitudes fail to meet the minimum threshold. B) Calculated moving averages determined for the 2,475-yr tsunami design wave and the various source simulations.

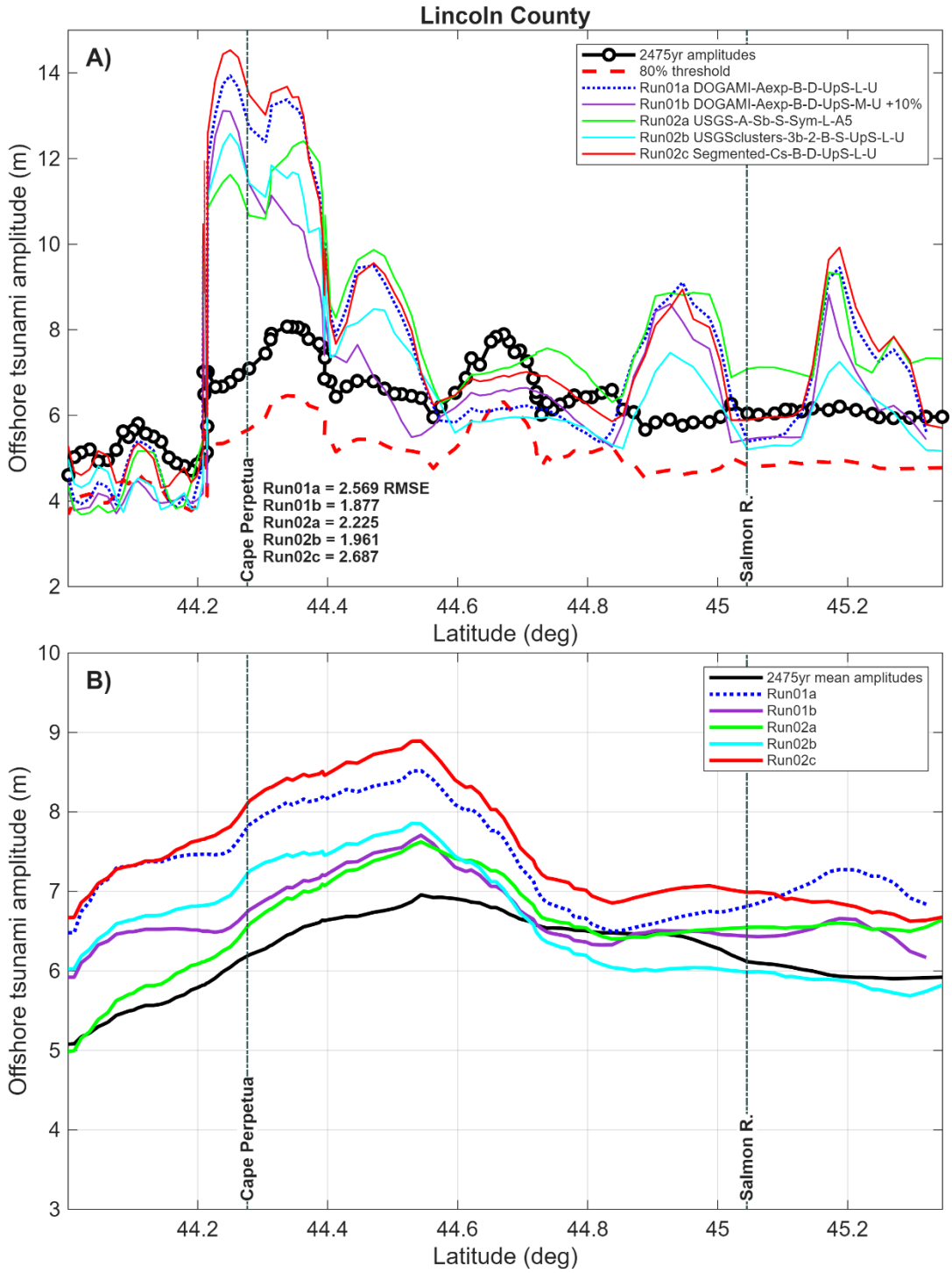


Figure 4-11. A) Plot showing simulated tsunami amplitudes for the final Lincoln County model runs in which the Run01a deformation and slip is increased by 10% (Run01c). Solid black line with circles is the 2,475-yr tsunami design wave, while the red dash line depicts the 80% threshold below which simulated amplitudes fail to meet the minimum threshold. B) Calculated moving averages determined for the 2,475-yr tsunami design wave and the adjusted sources.

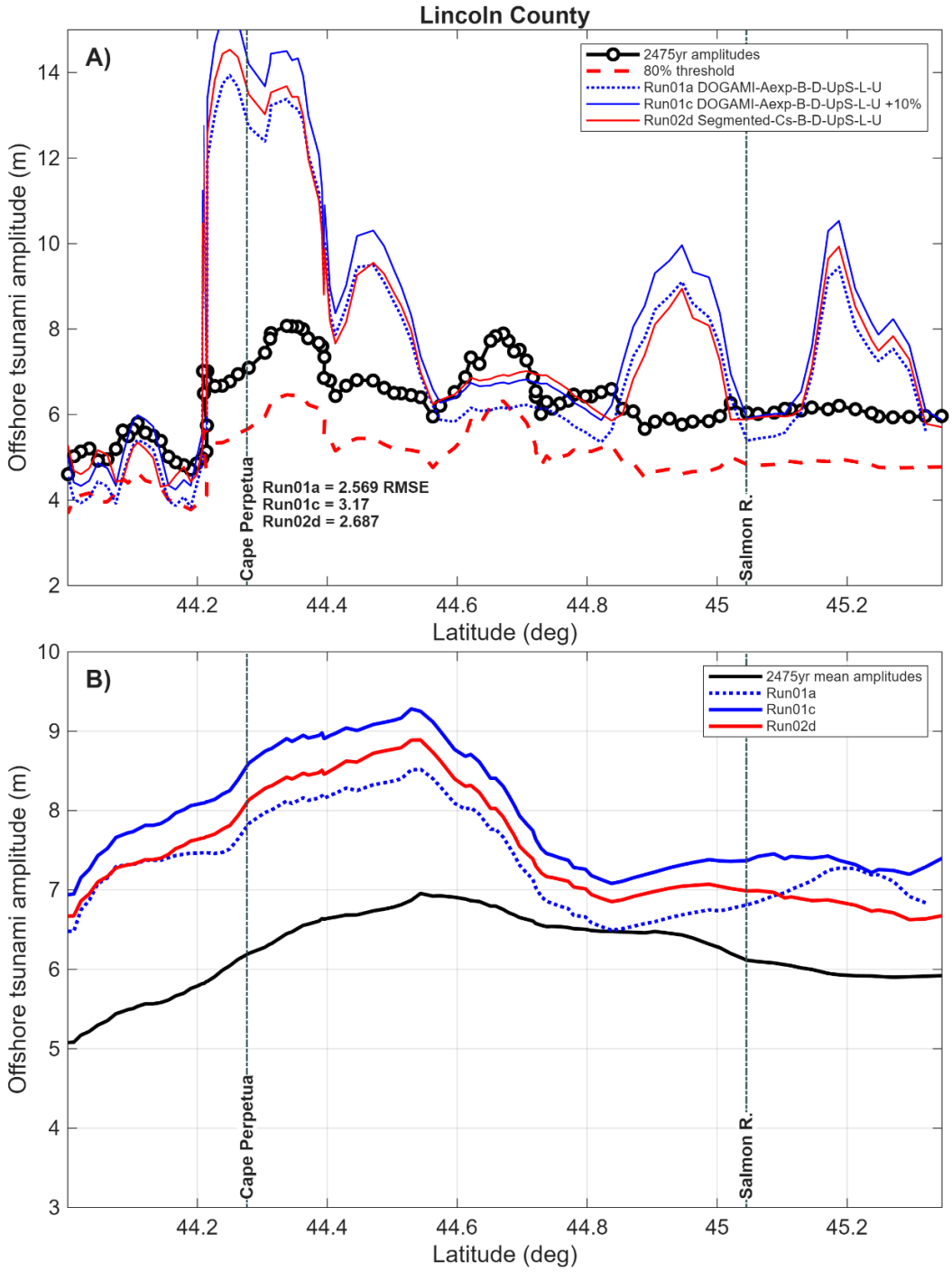


Figure 4-12. Two scenarios of 2,475-yr tsunami inundation affecting Lincoln City and Siletz Bay (left) and Waldport and Alsea Bay (right), Lincoln County. Figure includes the original DOGAMI L1 scenario and existing ASCE7-22 inundation zone for comparison.

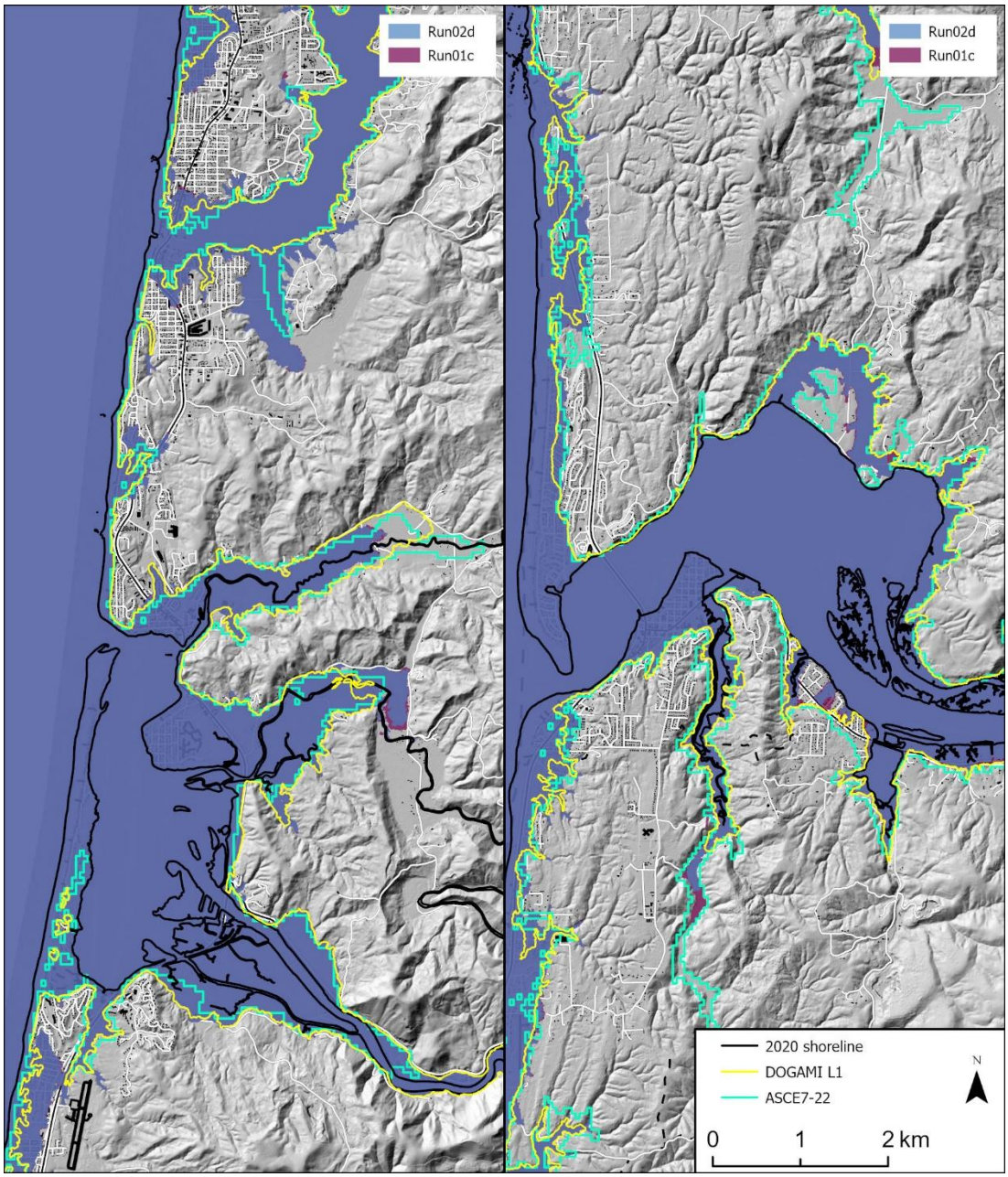
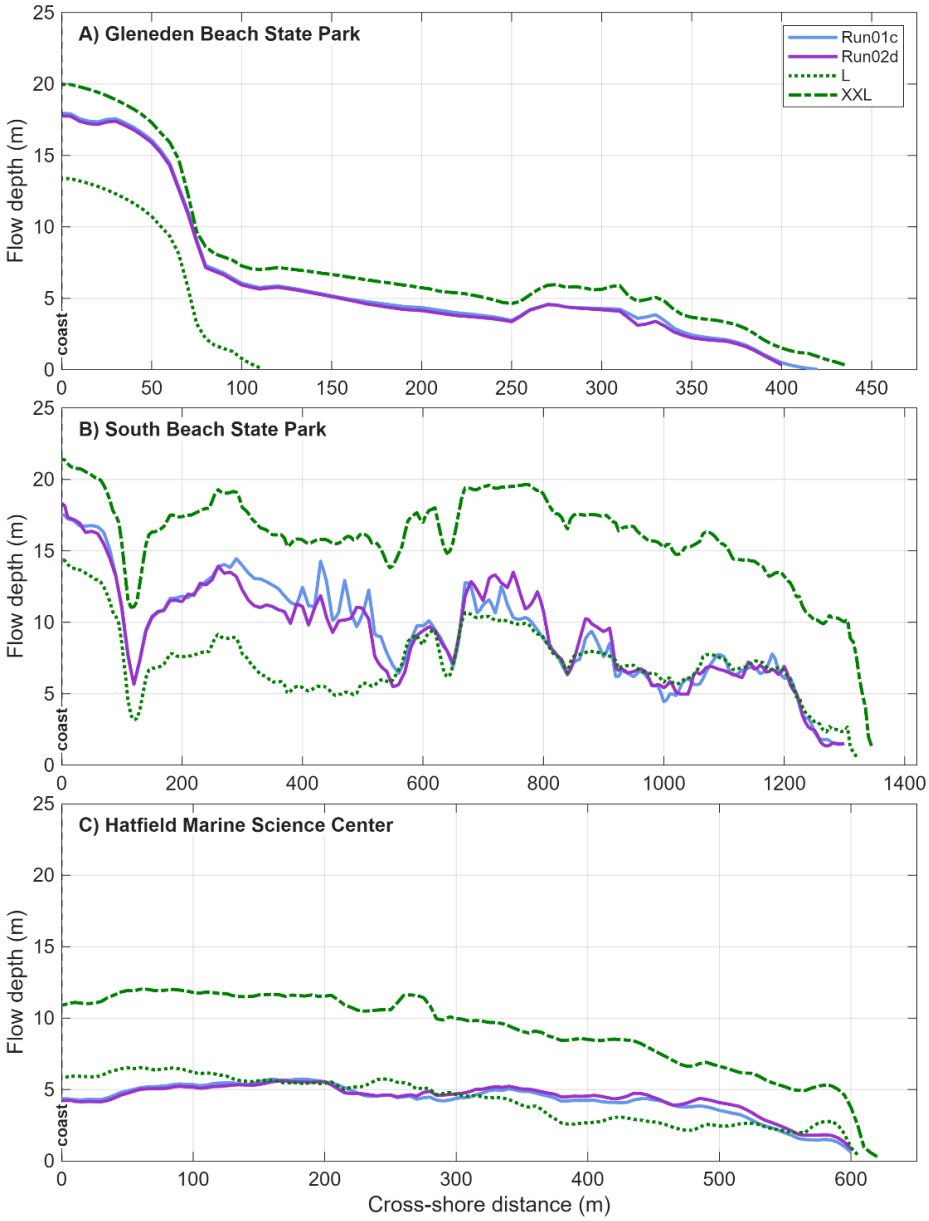


Figure 4-13 presents the simulated flow depths for three locations in Lincoln County: A) Gleneden Beach State Park, B) South Beach State Park, and C) the Hatfield Marine Science Center (HMSC) at Newport. The Gleneden Beach transect is located just south of Salishan Spit near Siletz Bay while the other two sites are in Newport. The authors included the HMSC site since this is a site where an existing vertical evacuation structure was built. Unlike the flow depths presented previously for Tillamook County and Clatsop County which demonstrated large differences between the model runs, the Lincoln County flow depths show generally close agreement. Aside from the Gleneden Beach transect, the latest modeling

indicates that the 2,475-yr flow depths are either slightly larger or comparable to the DOGAMI L1 flow depths and consistently fall below the XXL flow depths (**Figure 4-13**). As mentioned previously, the inundation extents between the Run01c and Run02d model runs fall close to each other and this is further reinforced in the termination of the inundation seen in all three flow depth plots for Lincoln County. Finally, **Figure 4-13C** indicates that the latest 2,475-yr model runs at HMSC fall well below the XXL flow depths. This is encouraging to see since the new Marine Science Institute vertical evacuation structure constructed at HMSC was designed based on the flow depths produced by the XXL scenario.

Figure 4-13. Comparison of model flow depths at A) Gleneden Beach State Park, B) South Beach State Park, and C) Hatfield Marine Science Center, Lincoln County. Plot includes flow depths produced by the DOGAMI L1 and XXL1 scenarios.



4.2 Final Scenarios Used to Produce New 2,475-year Inundation Zones

Table 4-1 presents the final suite of scenarios that were found to meet or exceed the offshore wave amplitude threshold tests as defined by the ASCE. The original Sypus and Wang (2024) deformation and slip models assume 500 years of plate convergence, which equates to an average event akin to the 1700 event. However, in order to match the ASCE 2,475-year offshore tsunami amplitudes, the deformation and slip models must be scaled using a multiplier (**Table 4-1**). **Table 4-1** also includes the calculated moment magnitude (Eq. 4) and the maximum slip, which is determined for the CSZ rupture area directly offshore each of the three Oregon Coast counties. As presented in **Table 4-1** the scenario moment magnitudes found to match the offshore 2,475-yr offshore wave amplitude threshold tests range from M_W 9.02–9.25, while the maximum slip varies from 38.3–42.4 m. Given estimated convergence rates of ~33 mm/year in northern Oregon (Scholz, 2014; **Figure 1-1**), this equates to ~1,160–1,285 years of accumulated strain. When compared with the original Witter and others (2011) models, the ASCE scenarios present in **Table 4-1** are found to be closer to the more extreme XXL scenario used by Oregon for evacuation purposes. Furthermore, as described previously there are notable differences in the width, shape and estimated subsidence in the latest ASCE source models when compared with the original DOGAMI models.

Table 4-1. CSZ scenarios adopted for the creation of the final 2,475-yr tsunami design zone in Clatsop, Tillamook, and Lincoln Counties.

Scenario	Multiplier	Magnitude (Mw)	Maximum Slip (m)	County	Run Name
DOGAMI Aexp-B-D-UpS-L-U	2.5	9.247	38.3	Clatsop County	Run02c
				Tillamook County	Run01c
DOGAMI Aexp-B-D-UpS-M-U	2.5642	9.172	39.3	Clatsop County	Run02g
				Tillamook County	Run01i
DOGAMI Aexp-B-D-UpS-L-U	2.75	9.274	42.2	Lincoln County	Run01c
Segmented Cs-B-D-UpS-L-U	2.7639	9.019	42.4	Lincoln County	Run02d

Note: Multiplier value used to scale the original Sypus and Wang (2024) deformation and slip models to match the ASCE 2,475-year TDZ.

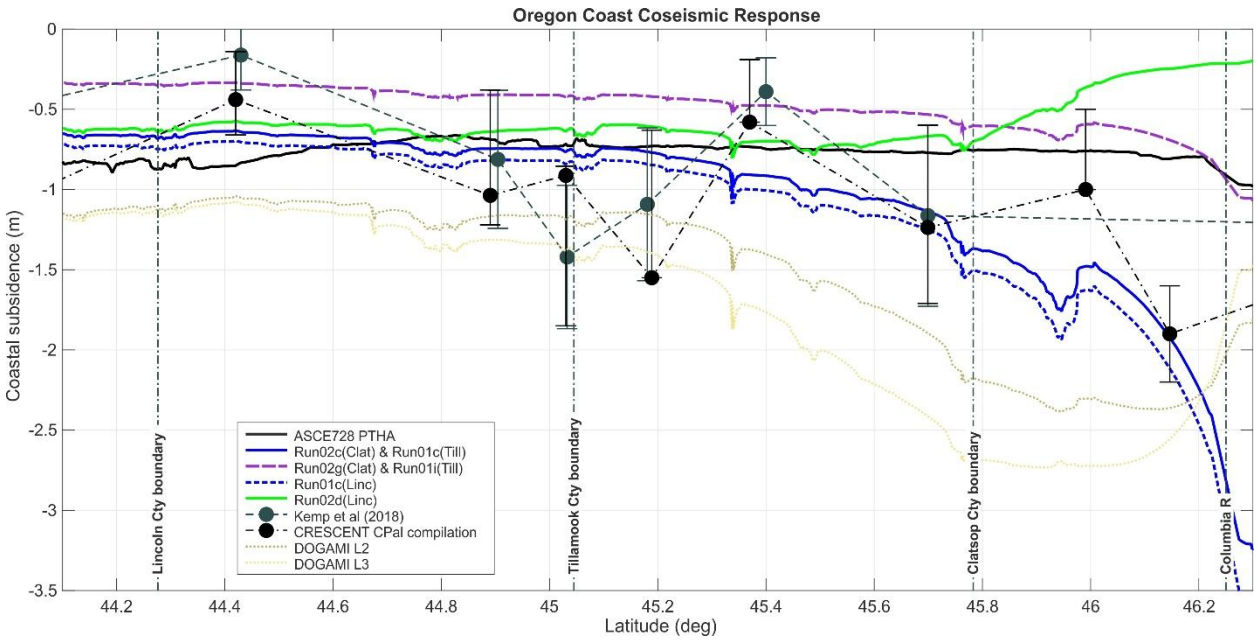
As can be seen in **Table 4-1**, each county is characterized with having two 2,475-yr source models, which are used to construct the final tsunami design zone. Although the DOGAMI Aexp-B-D-UpS-L-U source model was found to dominate tsunami inundation throughout Clatsop and Tillamook County, the authors retained the DOGAMI Aexp-B-D-UpS-M-U source model since it was found to exceed the DOGAMI Aexp-B-D-UpS-L-U inundation mainly around the coastal headlands. Furthermore, the DOGAMI Aexp-B-D-UpS-M-U source model generally produced larger flow depths along the barrier spits in Tillamook County and are therefore important for defining the inundation depth points along those barrier spits that are backed by coastal estuaries.

4.3 Coseismic Responses

Having presented the modeling results for a suite of 2,475-yr CSZ rupture scenarios, this section evaluates the coseismic responses of those simulations that will be used to produce the updated ASCE tsunami design zone maps. Here, the authors compare the amount of subsidence produced by the scenarios presented in **Table 4-1**, with a probabilistic 2,475-yr subsidence model developed by Thio (2026).

Figure 4-14 presents the modeled subsidence defined for all three counties, calculated along the MHW shoreline. Included in the figure is the calculated 2,475-yr subsidence (solid black line) developed by Thio (2026), along with estimates of subsidence derived from the Run02c/01c (solid blue line) and Run02g/01i (purple dash) deformation models used in Clatsop and Tillamook County. **Figure 4-14** also includes estimates of subsidence derived from the Run01c (dark blue dash) and Run02d (green) deformation models used in Lincoln County. Estimates of the measured subsidence values (including uncertainty estimates) derived from two studies are also provided in the figure, including Kemp and others (2018) and the more recent compilation of Bahavar and others (2025). Based on these data, it is evident that the Run02g/01i (purple dash) model consistently underestimates subsidence when compared to the 2,475-yr subsidence, while Run02c/01c (solid blue line) is overestimating subsidence, especially along the Clatsop County shoreline. Nevertheless, the subsidence associated with Run02c falls within the range of the paleoseismic data and is considered to be reasonable. In Lincoln County, both the Run01c (blue dash) and Run02d (solid green line) fall close to the 2,475-yr subsidence, particularly in northern Lincoln County. It is also worth noting the large departure in the coseismic response of Run02d at the Clatsop County southern border, which is at the northern limit of this scenario. In the southern half of the county, both deformation models are found to slightly underestimate subsidence when compared to the 2,475-yr PTHA subsidence. For comparison, the authors also include the subsidence defined for the DOGAMI L2 (shallow buried) and L3 (deep buried) tsunami deformation models, which indicate even larger subsidence; the L1 model (not shown) is characterized with even greater subsidence. However, given recent advances in redefining the CSZ sources and significant improvements in both dating the paleoseismic data and constraining the degree of subsidence, the authors believe the newer deformation models are generally better constrained.

Figure 4-14. Estimates of the 2,475-yr probabilistic subsidence, along with subsidence estimates determined for the various deformation models.



A limitation of **Figure 4-14** is that this figure focuses on subsidence along the MHW shoreline and ignores what may be happening adjacent to the coast. **Figure 4-15**, **Figure 4-16,** and **Figure 4-17** provide maps of differences in the modeled subsidence determined for each of the Counties and for the final suite of model runs used. These differences are calculated relative to the probabilistic 2,475-yr subsidence estimate. For the purposes of these figures, the authors only evaluate those points in the 2,475-yr subsidence model that are located within the inundation zone and include at least one to two grid points in the nearshore. In these figures, the size of the circles provides an indication of the level of agreement, with smaller circles indicating smaller differences relative to the 2,475-yr estimate. Positive values indicate greater subsidence, while negative values indicate less subsidence relative to the probabilistic 2,475-yr estimate.

Figure 4-15 indicates large differences in subsidence between the deformation models and the 2,475-yr probabilistic subsidence across the inundation zone in Clatsop County, consistent with **Figure 4-14** above. In general, **Figure 4-15** (left) confirms that the Run02c deformation model tends to overpredict the amount of subsidence nearer the coast. For example, the largest difference occurs between Tillamook Head and the mouth of the Columbia River, which are on the order of 110% to 225% larger than the 2,475-yr estimate. However, differences between the Run02c model and the 2,475-yr subsidence decrease landward, with subsidence estimates being about 55% to 80% larger at Seaside falling to 30% to 55% in Astoria. However, as noted previously, overestimates in the amount of subsidence predicted by Run02c are considered acceptable because the plausible range in subsidence defined by the paleoseismic data (i.e., the minimum and maximum values of subsidence determined for each discrete record) spans the model data. In contrast, the Run02g deformation model underpredicts subsidence when compared to the 2,475-yr estimate. As can be seen in **Figure 4-15**, the model underpredicts subsidence by -45% to -35% in the Seaside area and in the western half of Astoria. The degree of underprediction increases toward the east.

Figure 4-16 provides a comparison of differences in subsidence calculated for Tillamook County. Overall, the Run01c deformation model (same as used in Clatsop County) now shows relatively good agreement when compared to the 2,475-y PTHA subsidence calculation. As can be seen in **Figure 4-16** (left) the deformation model tends to either over-estimate or under-estimate the amount of subsidence by ∼-30% to +30% along much of the coast. In general, the Run01c model is slightly overpredicting subsidence at the open coast, but with progress inland (e.g., the community of Tillamook) the scaled deformation model underestimates the amount of subsidence relative to 2,475-y PTHA subsidence. Conversely, the Run01i model underestimates subsidence everywhere in **Figure 4-16** (right), with the amount of underestimate increasing eastward away from the coast.

Finally, **Figure 4-17** provides a comparison of differences in the deformation model subsidence and the 2,475-y PTHA subsidence calculated for Lincoln County. Overall, the Run01c deformation model shows good agreement across the length of Lincoln County when compared to the 2,475-y PTHA subsidence calculation. Overall, Run01c both underestimates and overestimates the subsidence by ∼-30% to +33%. Conversely, except for a small area near Depoe Bay where the Run02d model overestimates the subsidence slightly (up to 6%), the Run02d model mostly underestimates subsidence when compared to the PTHA subsidence. In general, the authors see larger separation between the two approaches south of Yaquina Head, with the amount of subsidence underestimated by ∼-45% to -15%.

Figure 4-15. Estimates of coastal subsidence determined for the Run02c and Run02g Clatsop County simulations, calculated as percentage differences relative to the 2,475-yr probabilistic subsidence. Note: positive values indicate greater subsidence relative to the probabilistic 2,475-yr subsidence, while negative values indicate less subsidence.

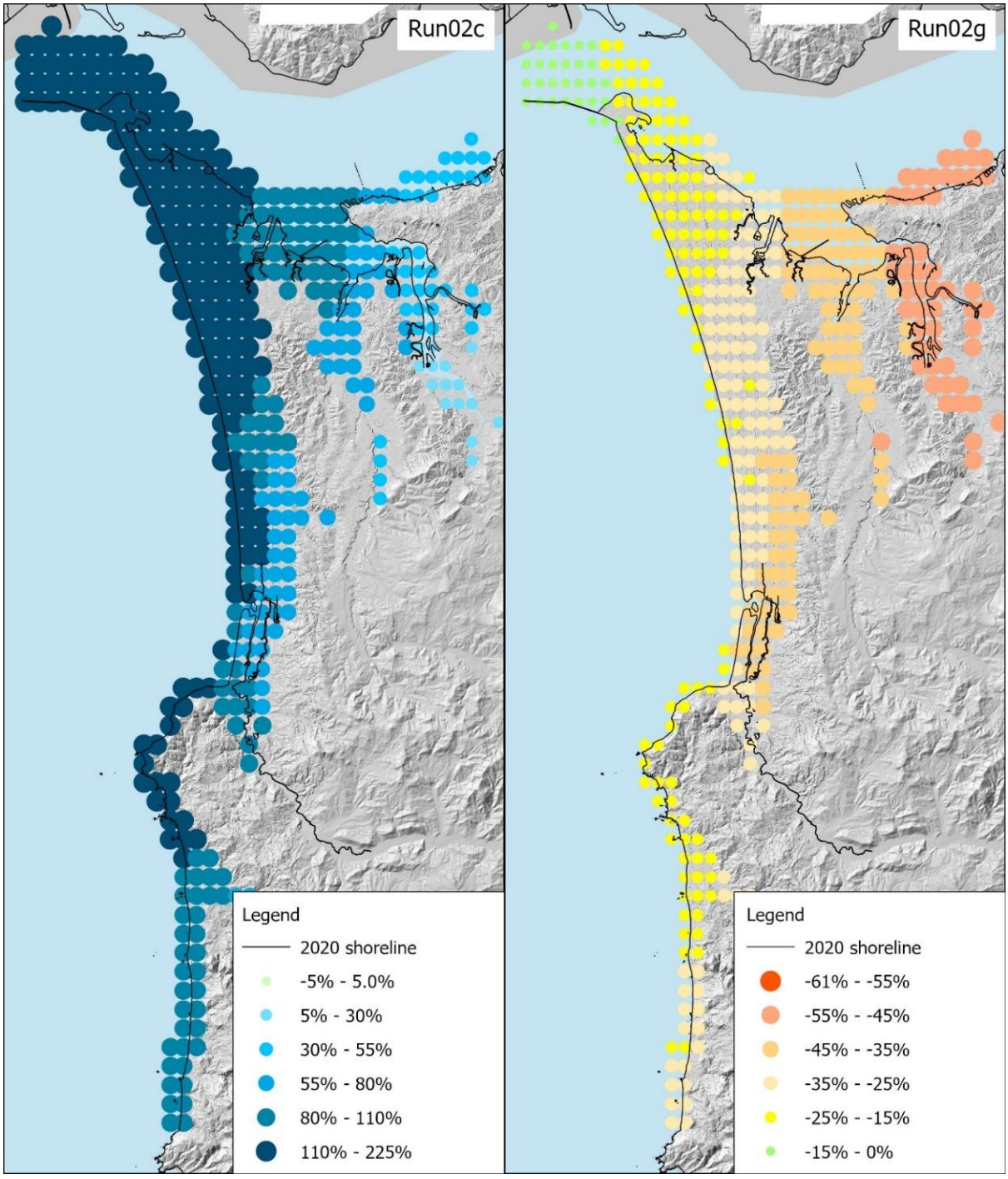


Figure 4-16. Estimates of coastal subsidence determined for the Run01c and Run01i Tillamook County simulations, calculated as percentage differences relative to the 2,475-yr probabilistic subsidence. Note: positive values indicate greater subsidence relative to the probabilistic 2,475-yr subsidence, while negative values indicate less subsidence.

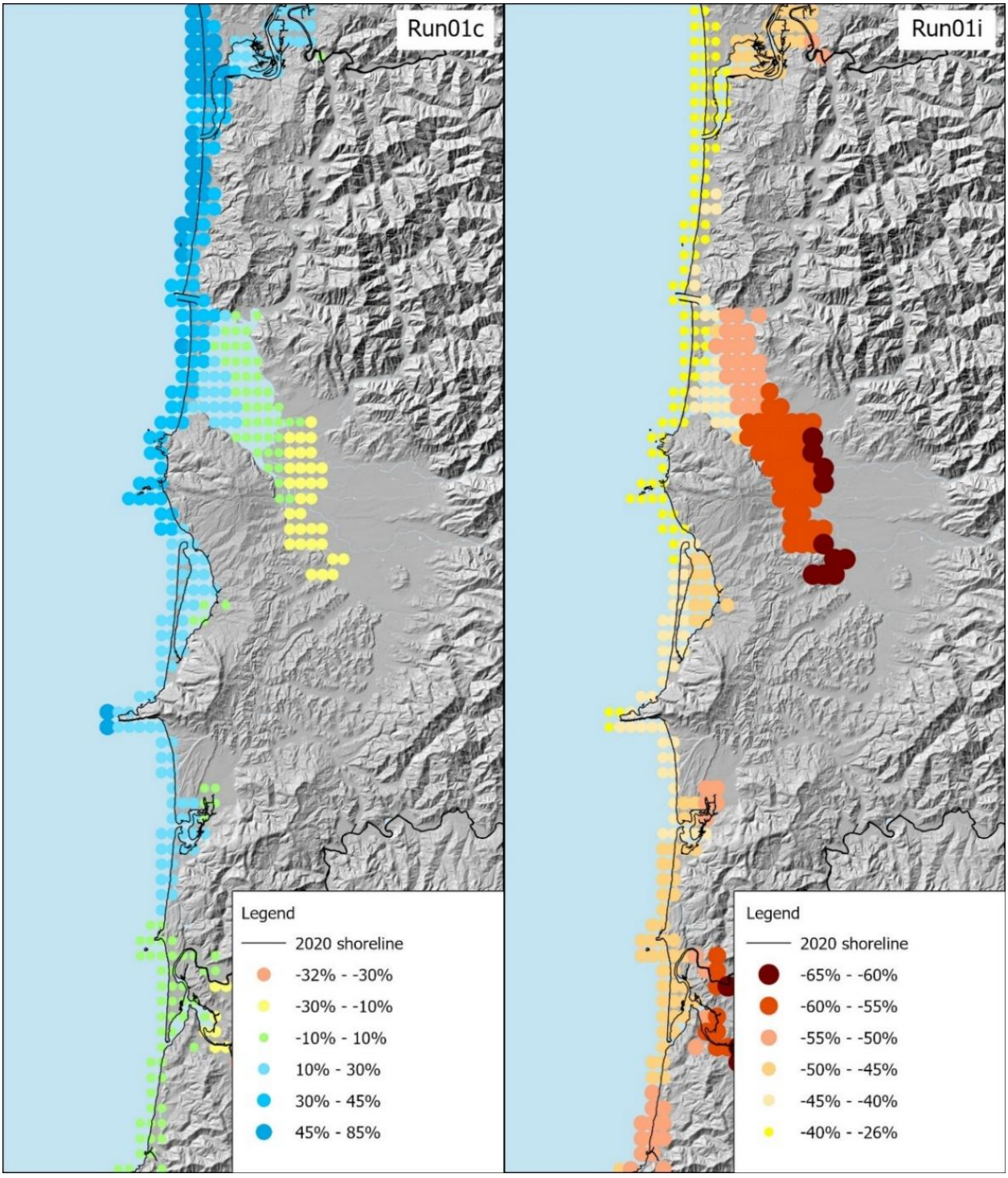
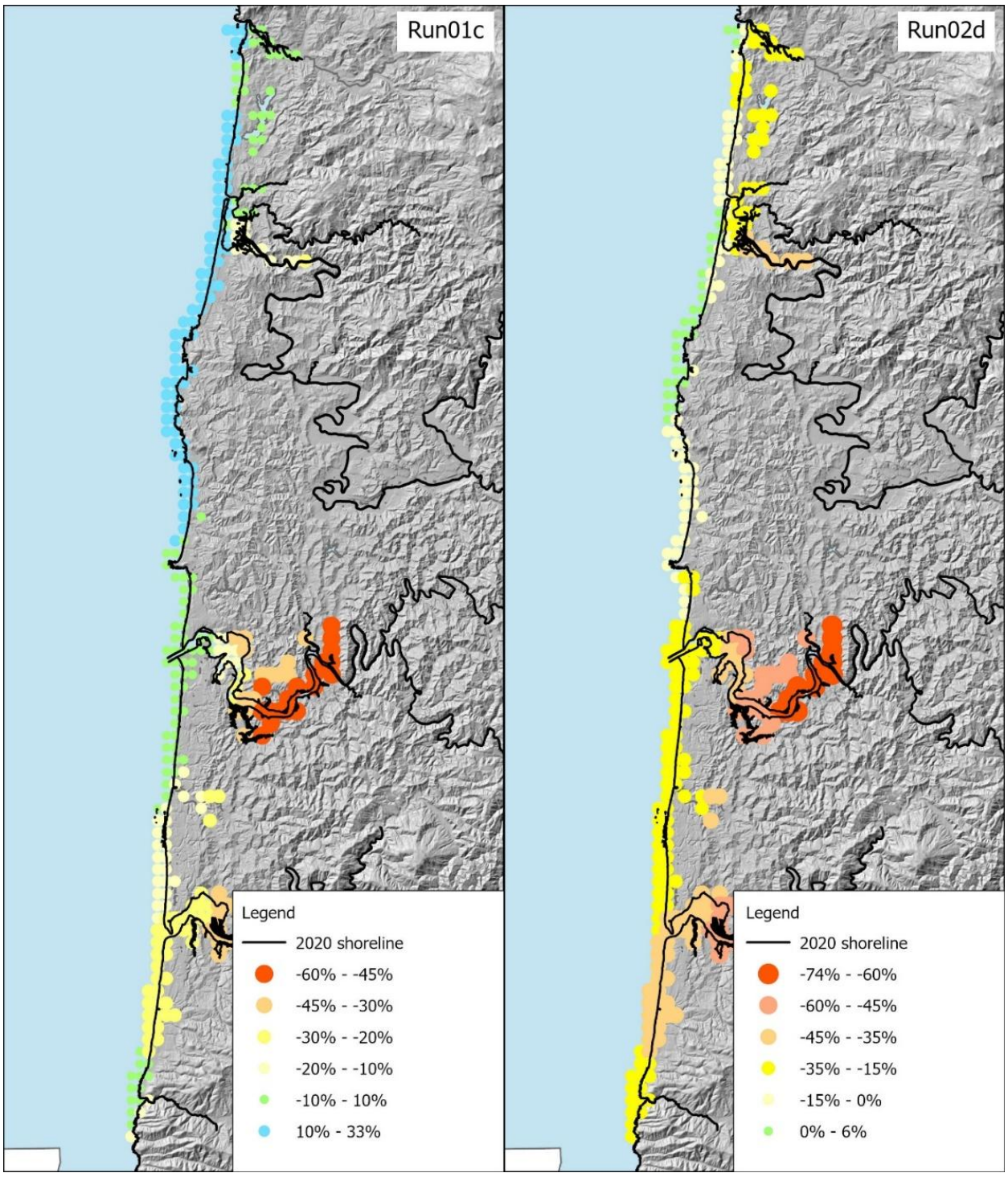


Figure 4-17. Estimates of coastal subsidence determined for the Run01c and Run02d Lincoln County simulations, calculated as percentage differences relative to the 2,475-yr probabilistic subsidence. Note: positive values indicate greater subsidence relative to the probabilistic 2,475-yr subsidence, while negative values indicate less subsidence.



4.4 Revised Central to Northern Oregon Coast 2,475-yr Inundation Maps

Figure 4-18–Figure 4-35 are community-based maps that show the spatial change in the proposed new ASCE7-28 TDZ for Clatsop, Tillamook, and Lincoln Counties, relative to ASCE7-22. For each of the maps, the colored blue zone denotes those areas that are unchanged from the previous mapping, while green areas reflect areas no longer flooded by a 2,475-yr CSZ tsunami. Areas now shown as inundated reflect pink areas (**Figure 4-18–Figure** 4-35). When evaluating the change maps, it is important to be reminded of the very large differences in the resolution of the new maps (5–10 m model grid), when compared to the original ASCE7-22 60-m model grid. The incorporation of both the higher resolution model grids and significant improvements to the CSZ earthquake sources account for the larger differences identified in each of the figures. Consistent with the needs of ASCE, the data accompanying this report may be used to produce rasters of the revised 2,475-yr TDZ, 0.91-m depth contours, inundation depth points along those barrier spits backed by coastal estuaries, and runup elevations calculated along the inundation limit.

Table 4-2 provides a summary of the countywide spatial changes. Based on these updated data, the authors note the following changes for Clatsop County*:*

- There is a significant increase in the area inundated by the revised 2,475-yr CSZ sources (~40.1 km^2). However, some of this change reflects those areas that were never previously modeled in ASCE7-22 (e.g., upriver of Astoria (**Figure 4-18**), or up the Young's River).
- Approximately 12.1 km^2 of the previous TDZ is proposed to be removed (**Table 4-2**). Most of this change occurs in the central to northern Clatsop Plains (**Figure 4-19**).

Changes in Tillamook County indicate the following:

- There is a moderate increase in the area inundated by the revised 2,475-yr CSZ sources (~19.1 km^2). However, as with Clatsop County, part of the increase occurs in areas that were never previously modeled in ASCE7-22 (e.g., upriver of Tillamook [**Figure 4-26**]).
- Approximately 11.3 km^2 of the previous TDZ is proposed to be removed. Most of this change occurs at the distal ends of the major estuaries (e.g., Tillamook Bay and Nestucca Bay).

Changes in Lincoln County indicate the following:

- There is a significant increase in the area inundated by the revised 2,475-yr CSZ sources (~24 km^2). Although part of this change occurs in areas that were never previously modeled in ASCE7-22, the updated modeling indicates an increase in the width of the TDZ in Lincoln City (**Figure 4-29**) and along the Lincoln/Gleneden Beach shore (**Figure 4-30**).
- Approximately 11.5 km^2 of the previous TDZ is proposed to be removed. Most of this change occurs in the more remote areas of the model grid (the distal ends of major estuaries, and up several valley systems).

Table 4-2. Change in probabilistic 2,475-yr tsunami inundation zone area for the central to northern Oregon Coast, relative to the existing ASCE7-22 tsunami design zone.

County	No Change (km^2)	Added (km^2)	Removed (km^2)
Clatsop	288.7	40.1	12.1
Tillamook	214.7	19.1	11.3
Lincoln	159.9	24	11.5

Figure 4-18. Change in the 2,475-yr tsunami design zone proposed for Astoria, Clatsop County.

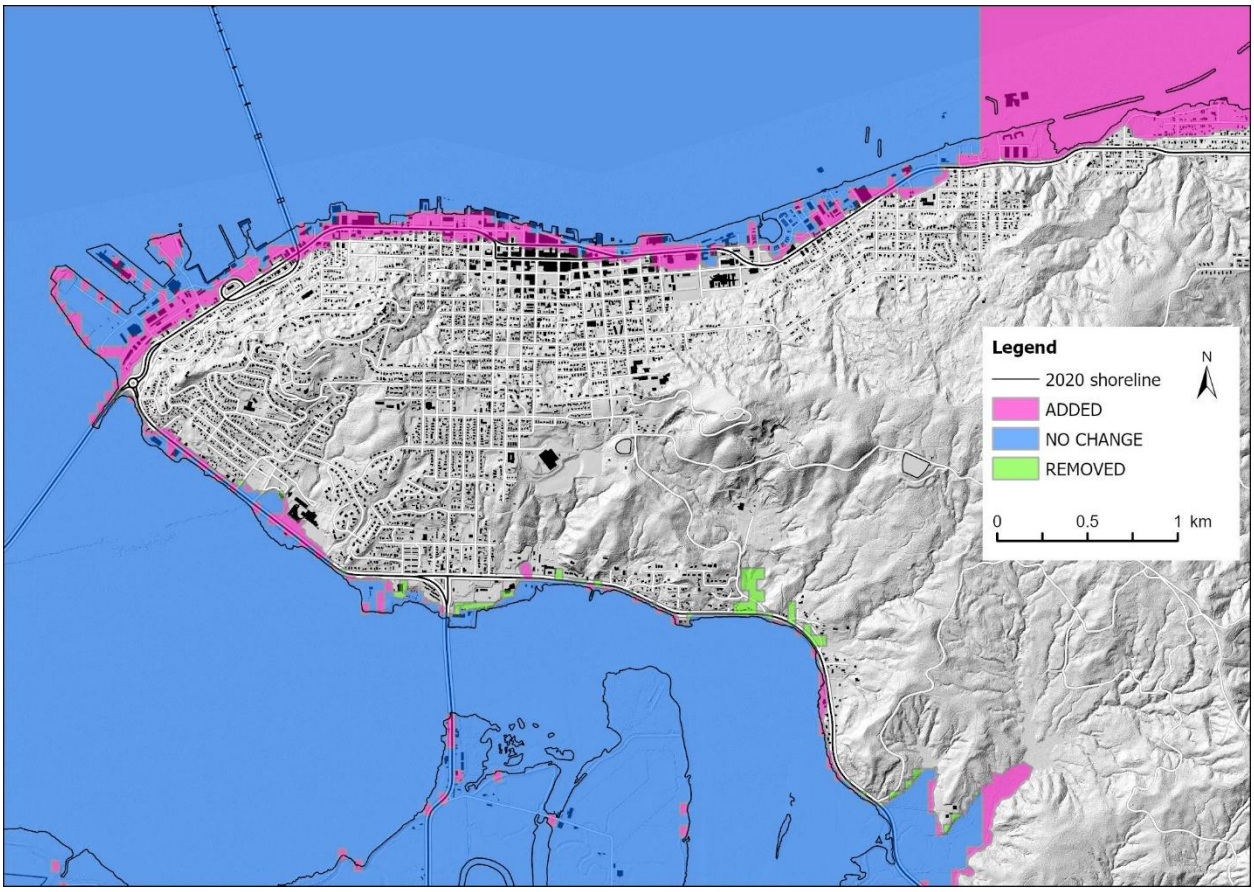


Figure 4-19. Change in the 2,475-yr tsunami design zone proposed for Warrenton, Clatsop County.

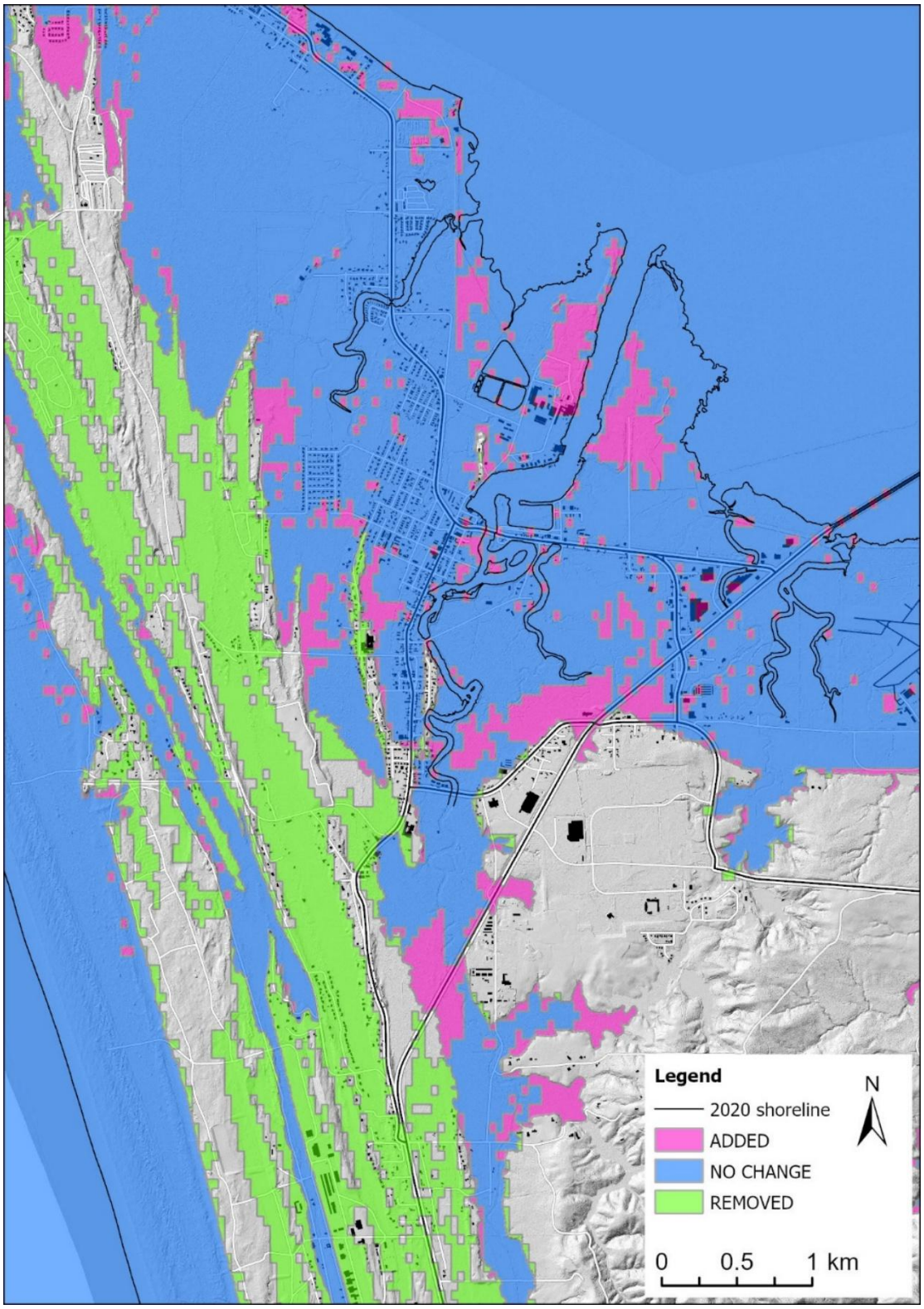


Figure 4-20. Change in the 2,475-yr tsunami design zone proposed for Seaside and Gearhart, Clatsop County.

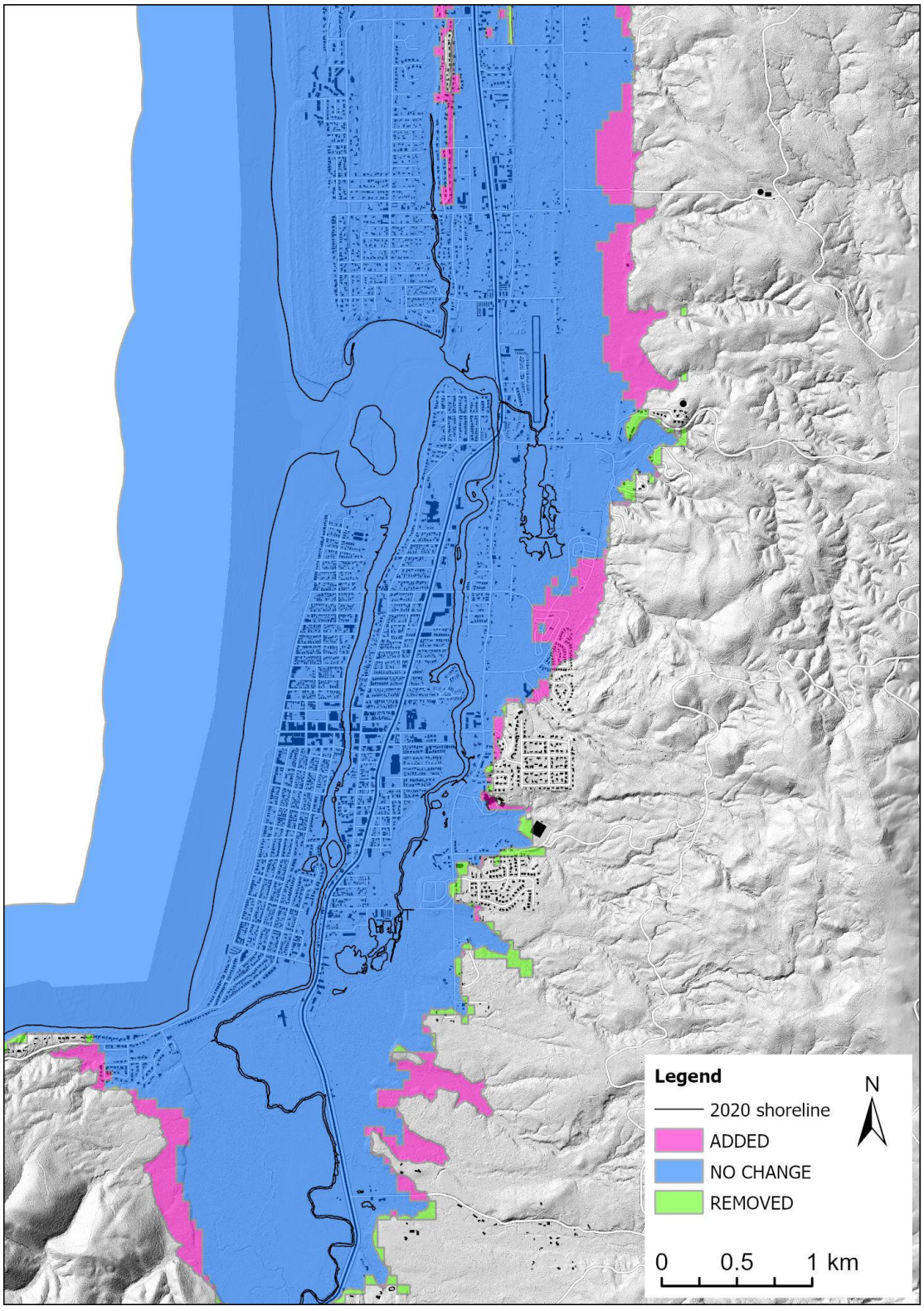


Figure 4-21. Change in the 2,475-yr tsunami design zone proposed for Cannon Beach, Clatsop County.

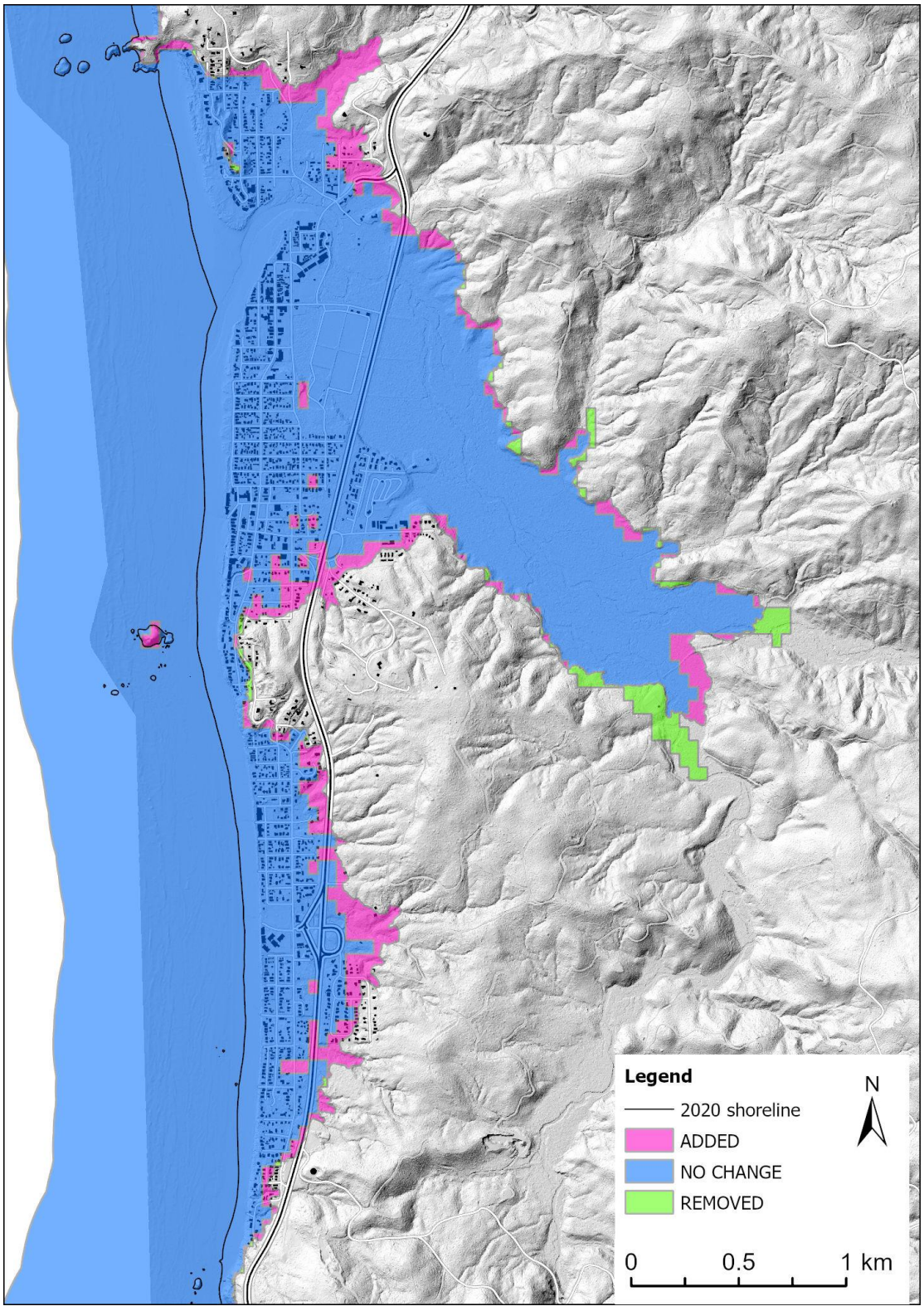


Figure 4-22. Change in the 2,475-yr tsunami design zone proposed for Arch Cape, Clatsop County.

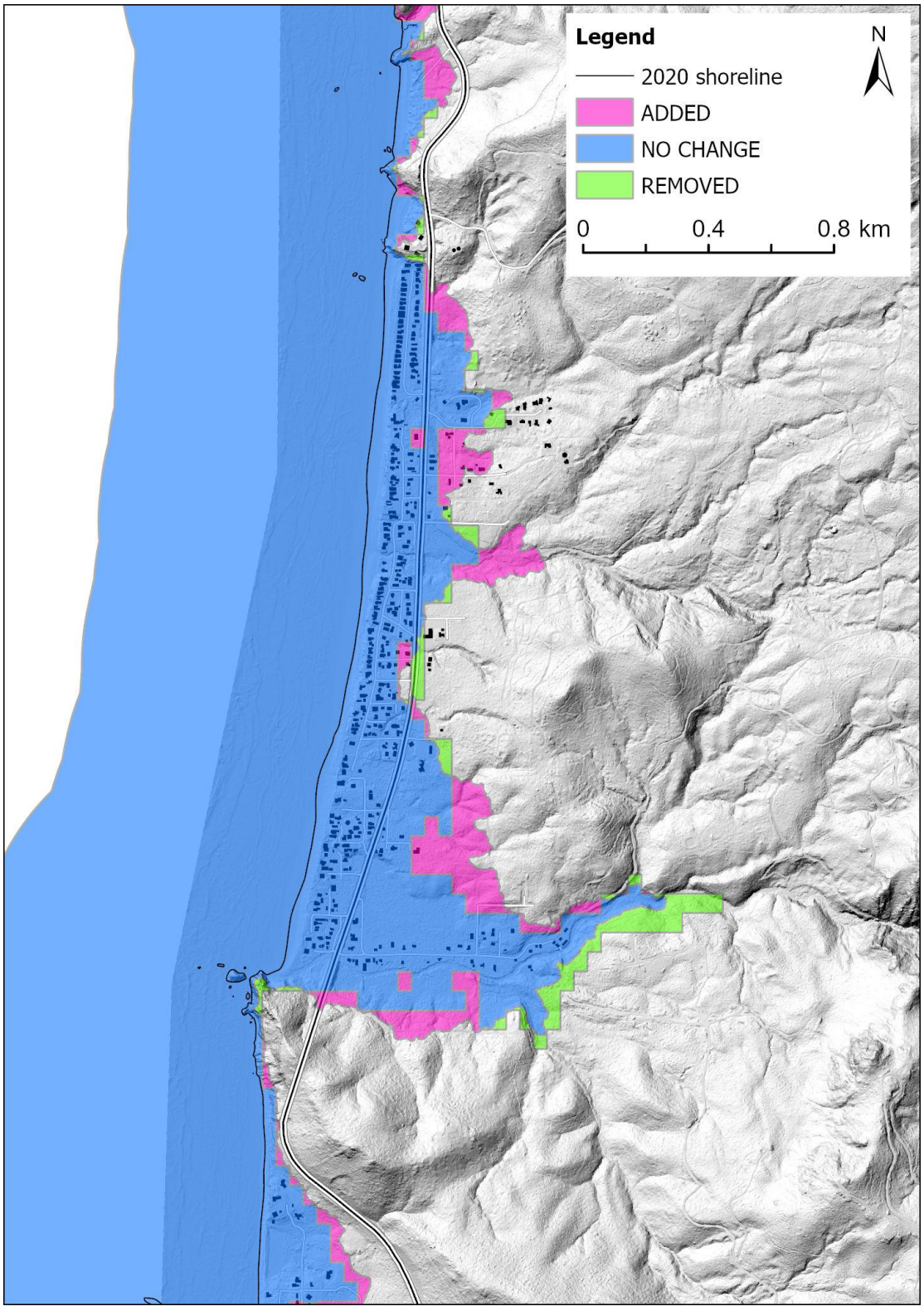


Figure 4-23. Change in the 2,475-yr tsunami design zone proposed for Manzanita, Nehalem, and Wheeler, Tillamook County.

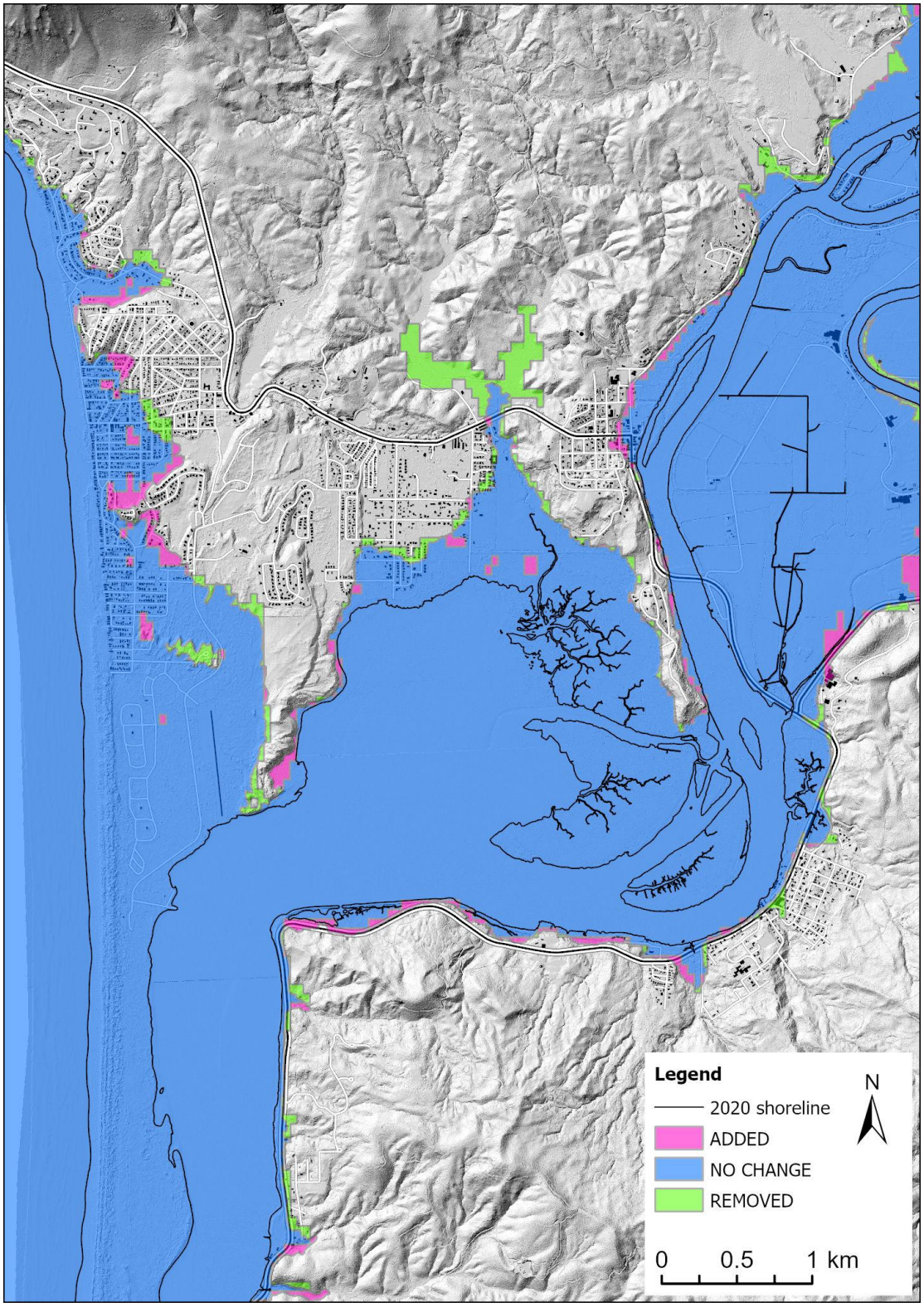


Figure 4-24. Change in the 2,475-yr tsunami design zone proposed for Rockaway Beach, Tillamook County.

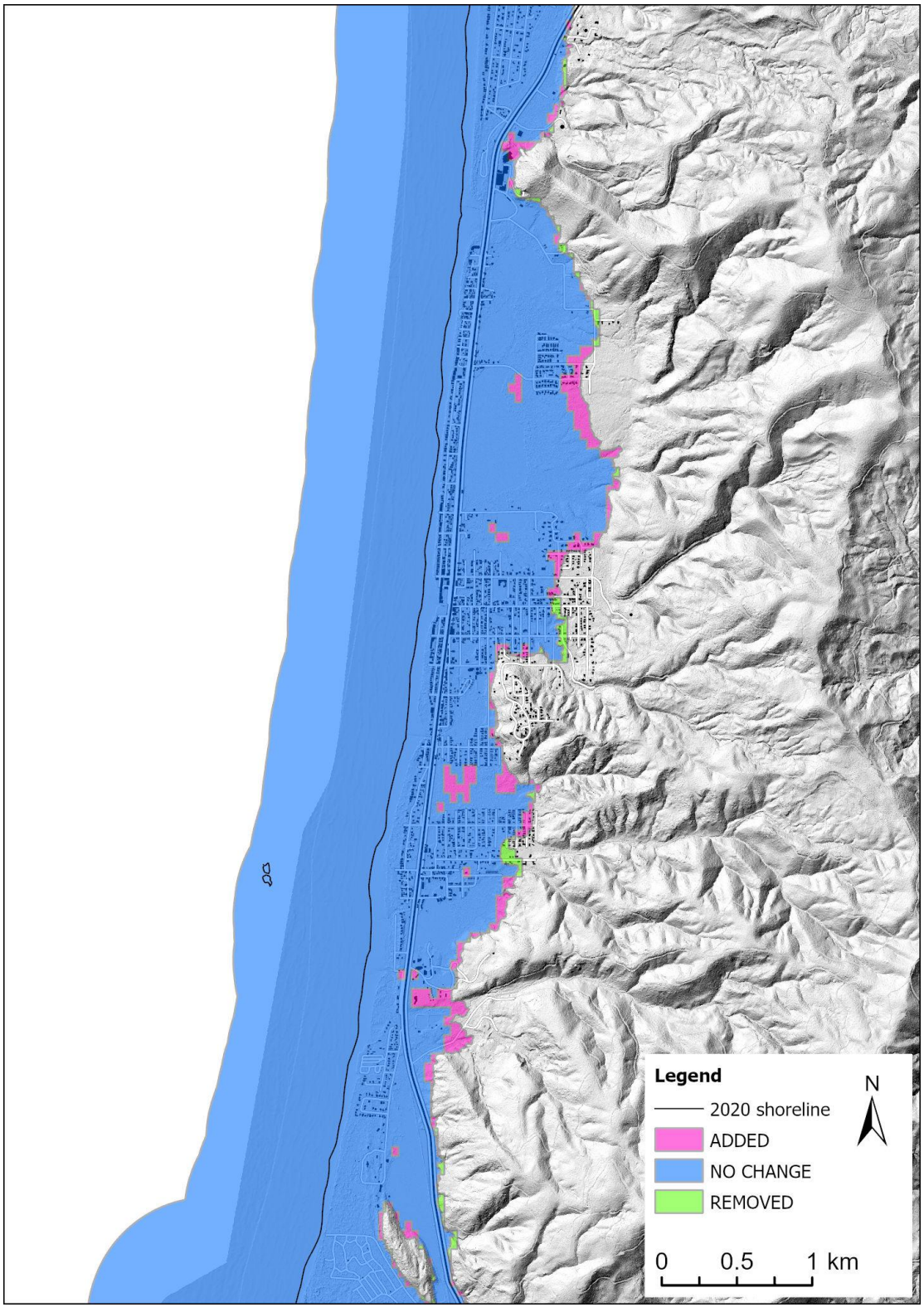


Figure 4-25. Change in the 2,475-yr tsunami design zone proposed for Garibaldi and Bay City, Tillamook County.

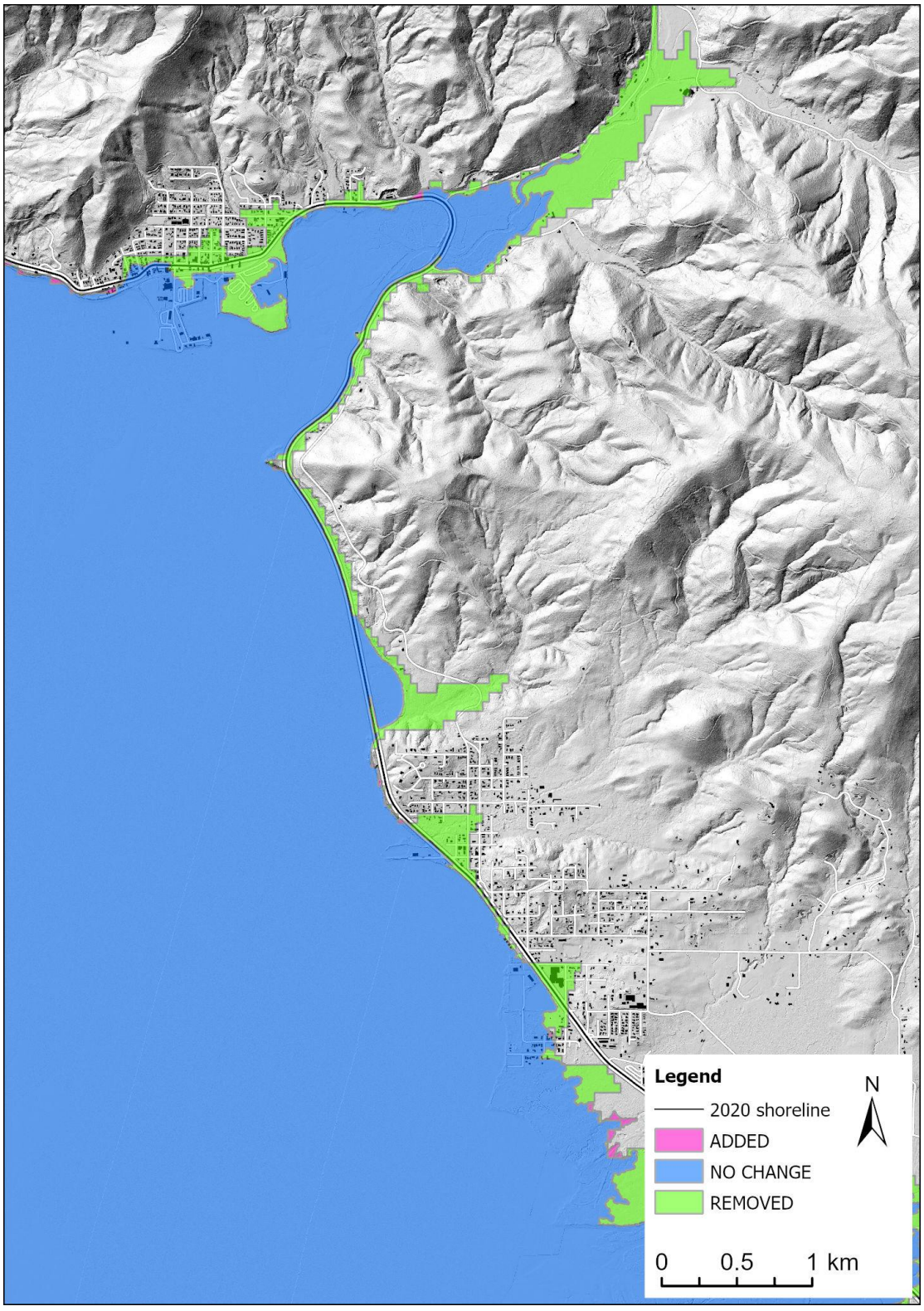


Figure 4-26. Change in the 2,475-yr tsunami design zone proposed for Tillamook, Tillamook County.

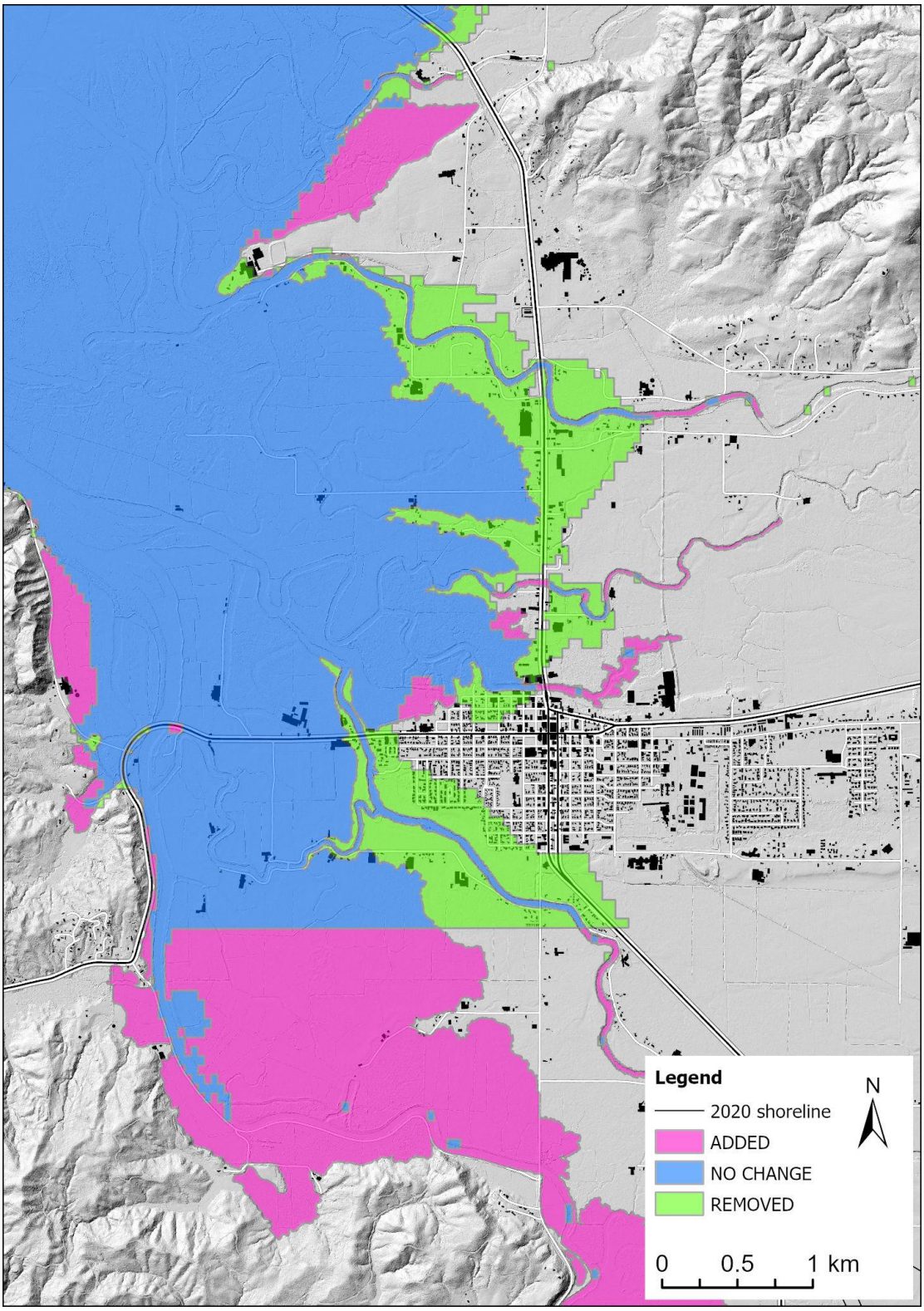


Figure 4-27. Change in the 2,475-yr tsunami design zone proposed for Netarts Bay, Tillamook County.

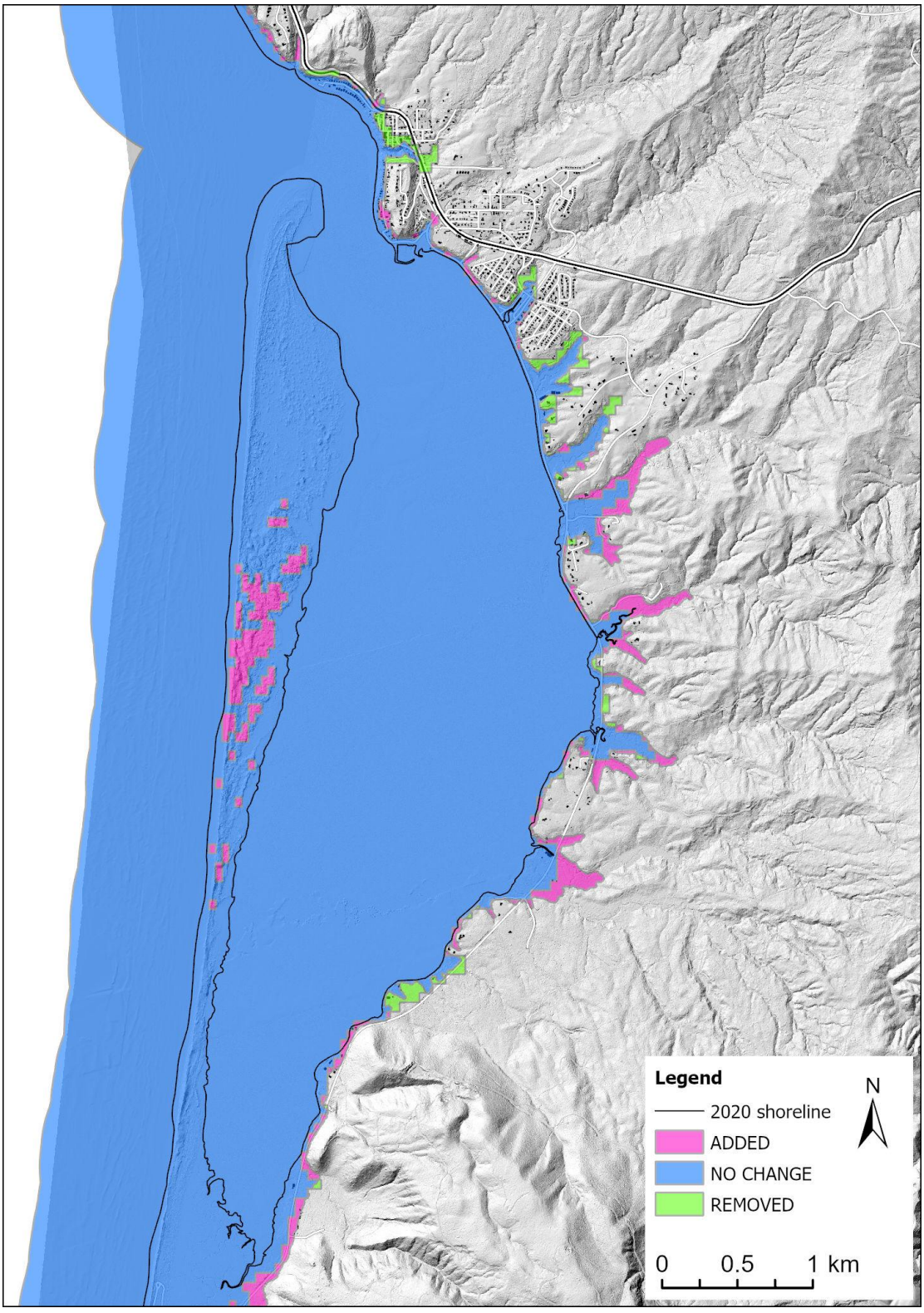


Figure 4-28. Change in the 2,475-yr tsunami design zone proposed for Pacific City, Tillamook County.

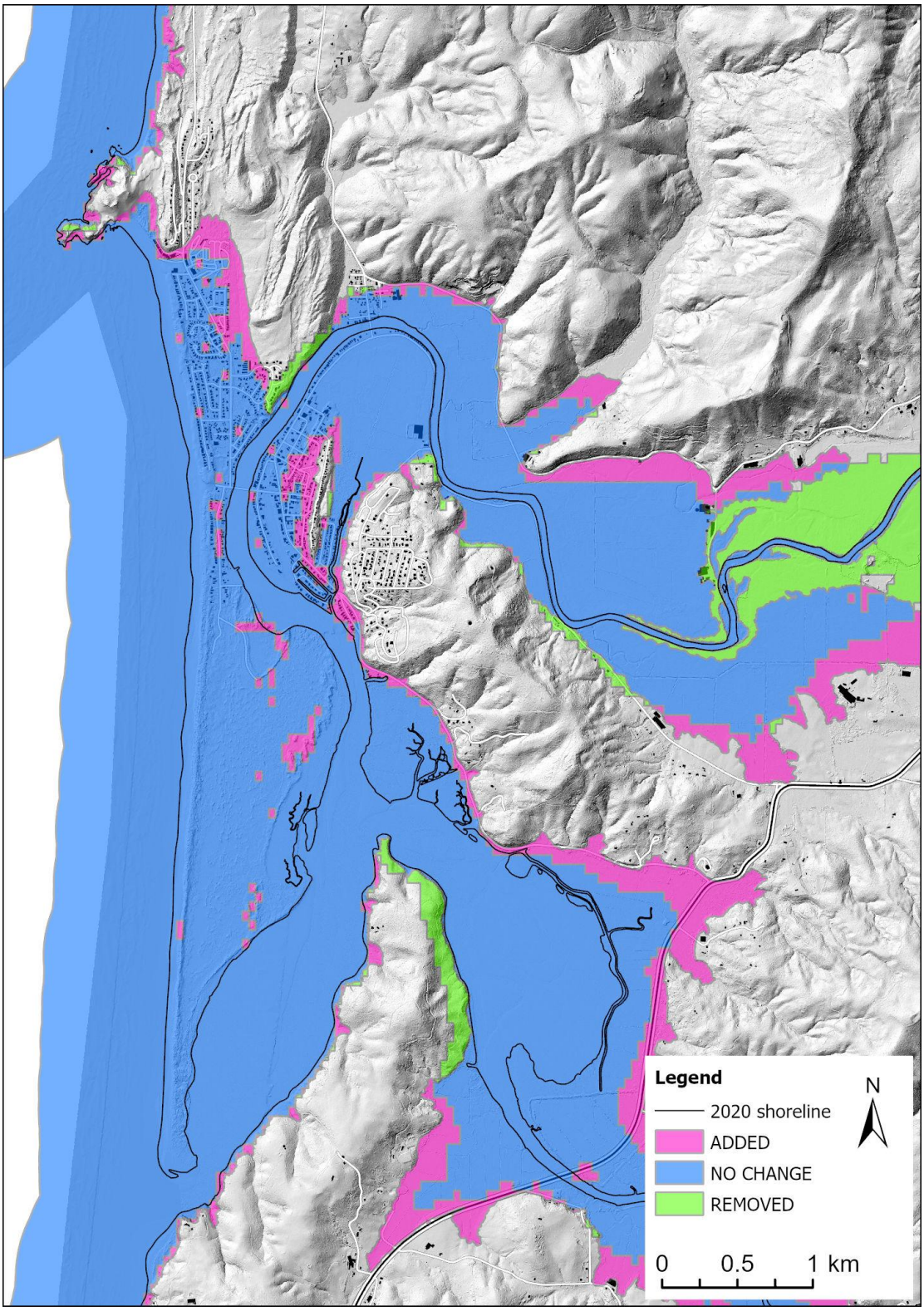


Figure 4-29. Change in the 2,475-yr tsunami design zone proposed for Lincoln City, Lincoln County.

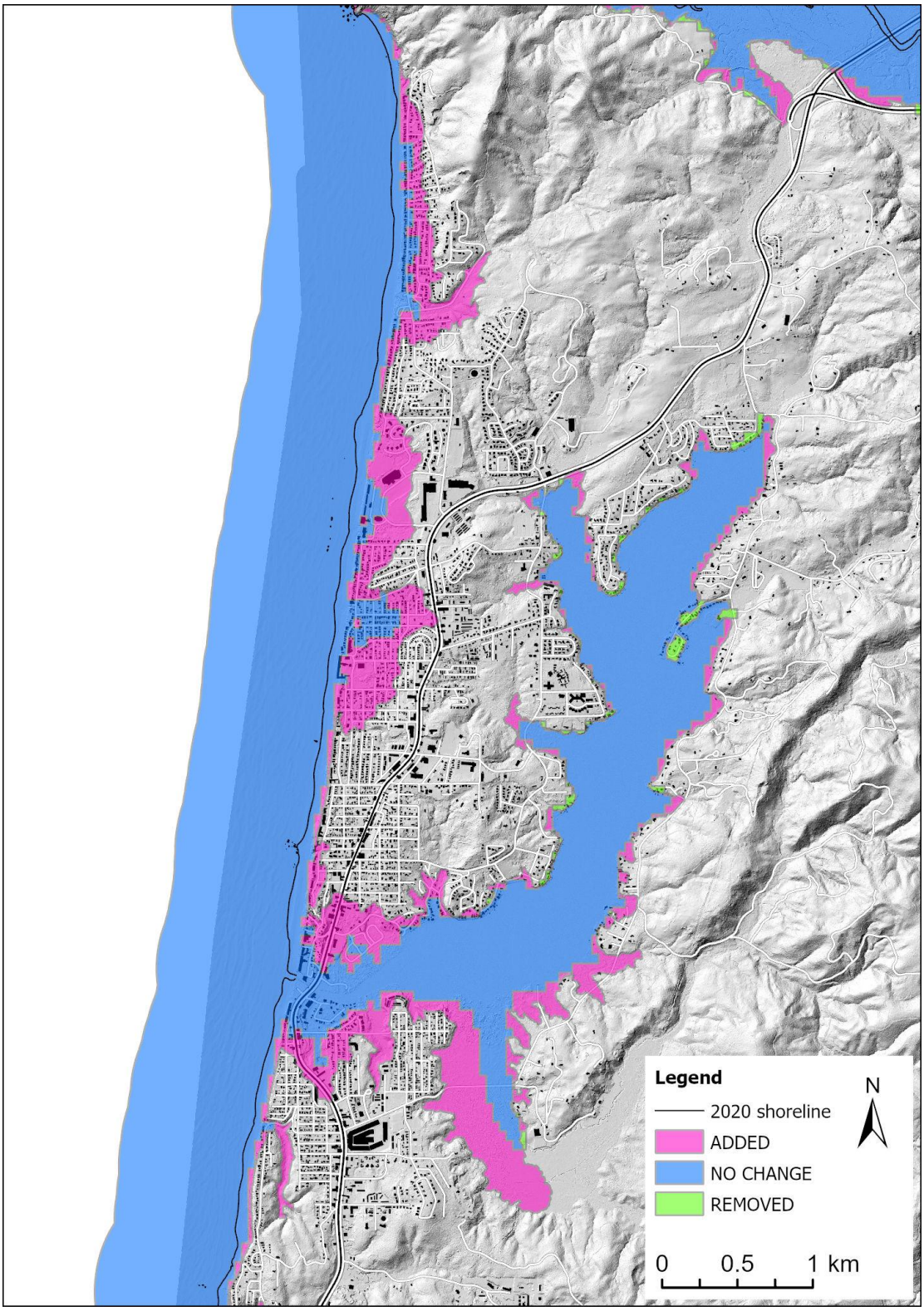


Figure 4-30. Change in the 2,475-yr tsunami design zone proposed for Lincoln Beach and Gleneden Beach, Lincoln County.

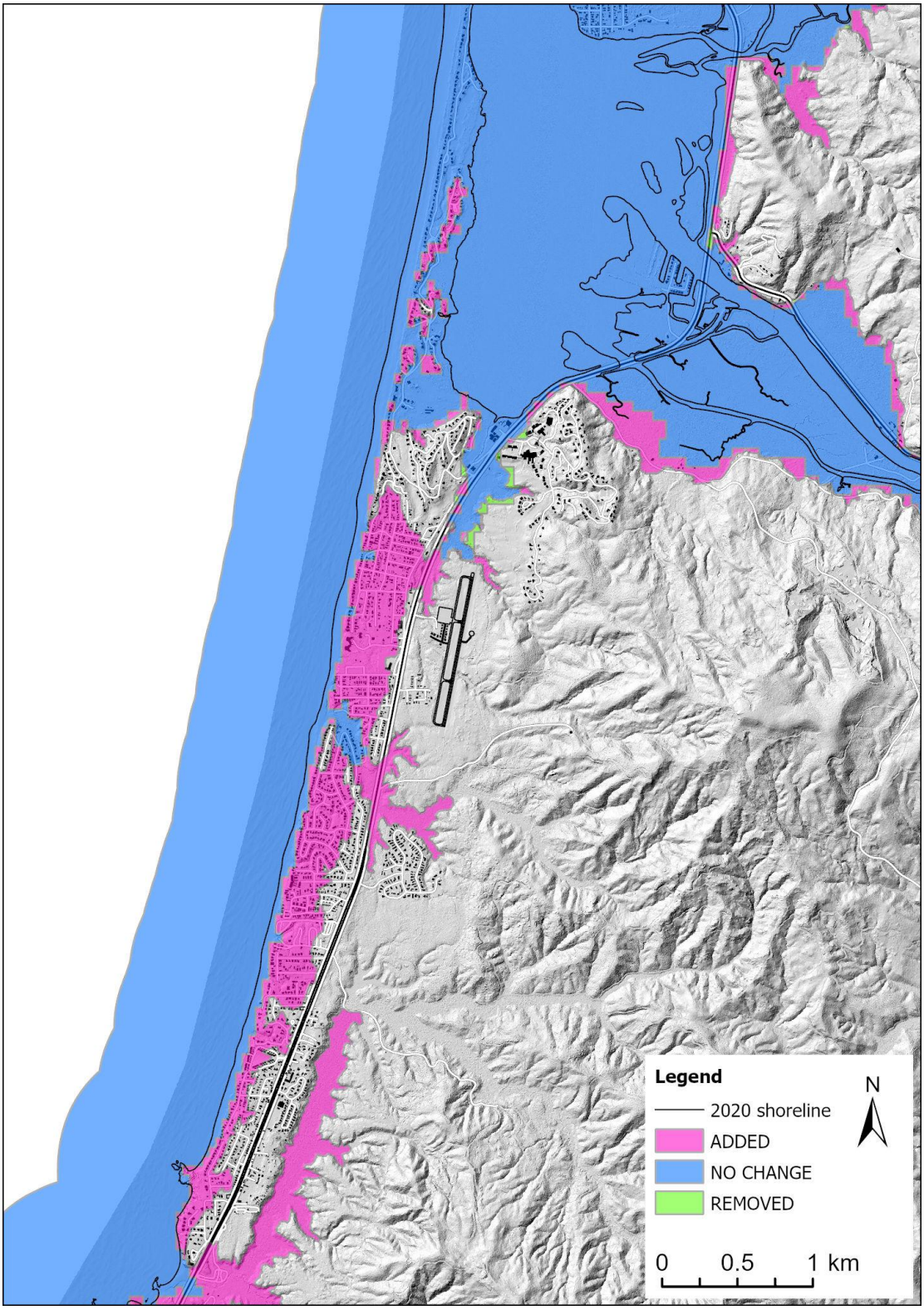


Figure 4-31. Change in the 2,475-yr tsunami design zone proposed for Depoe Bay, Lincoln County.

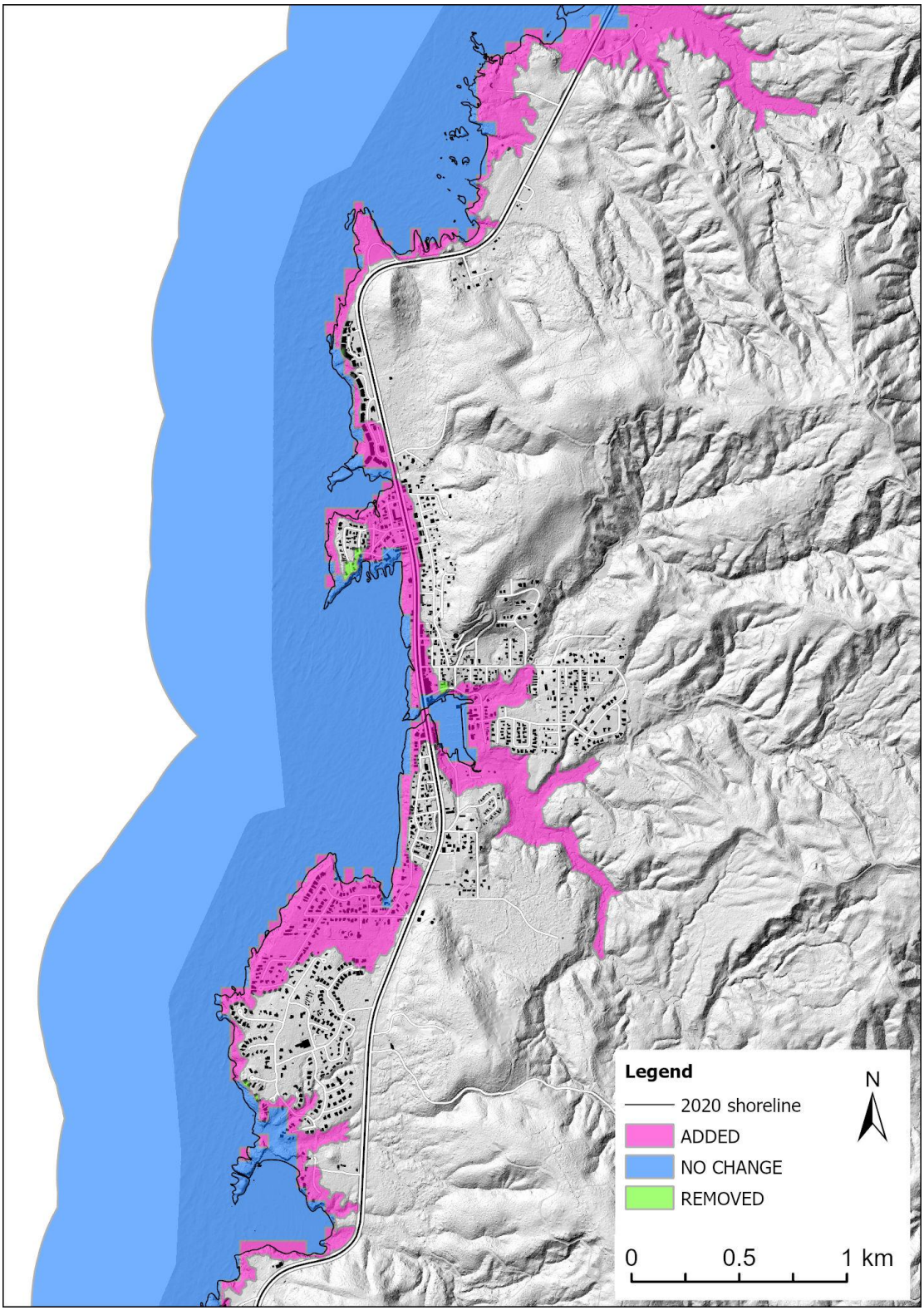


Figure 4-32. Change in the 2,475-yr tsunami design zone proposed for Newport, Lincoln County.

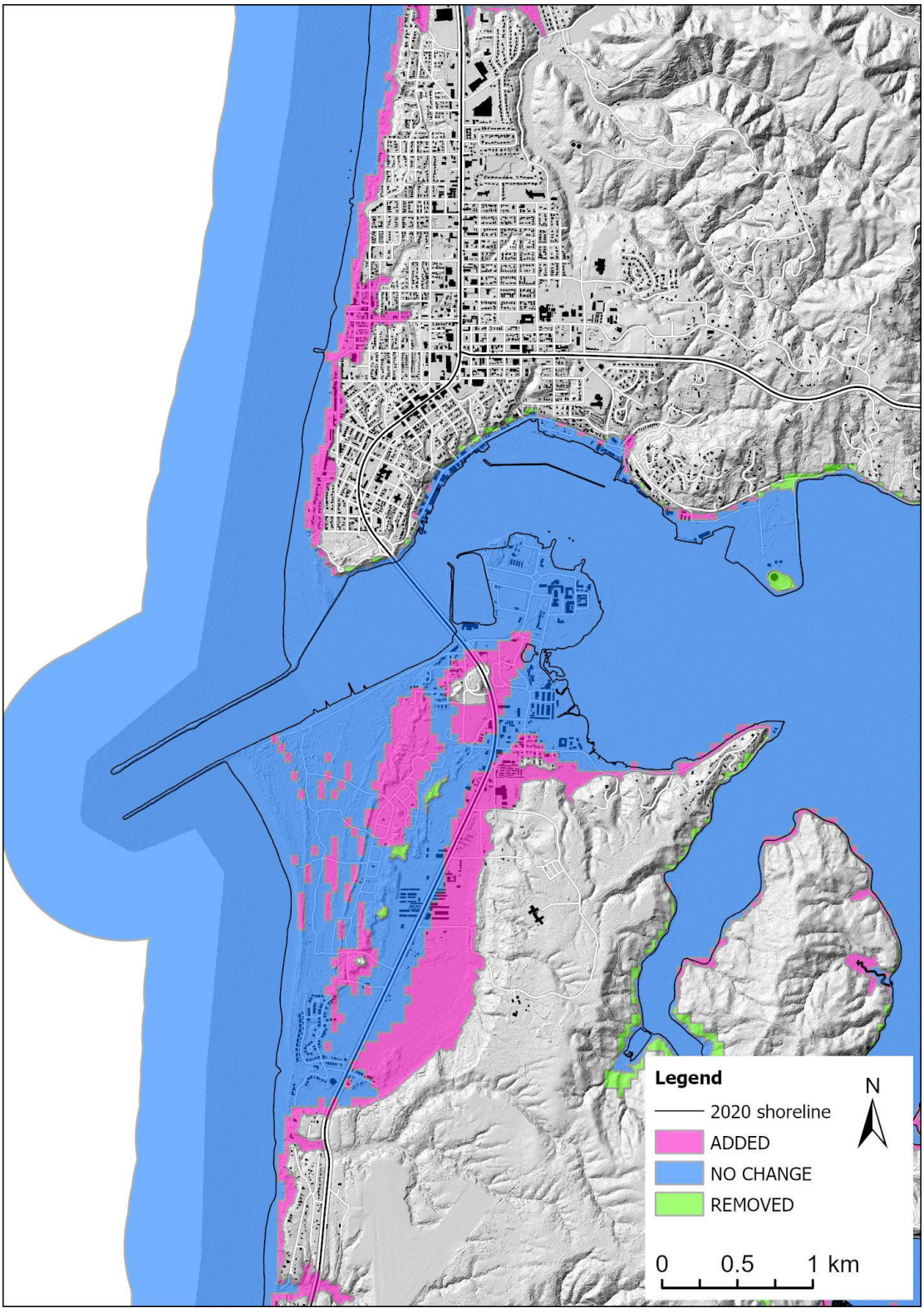


Figure 4-33. Change in the 2,475-yr tsunami design zone proposed for Seal Rock, Lincoln County.

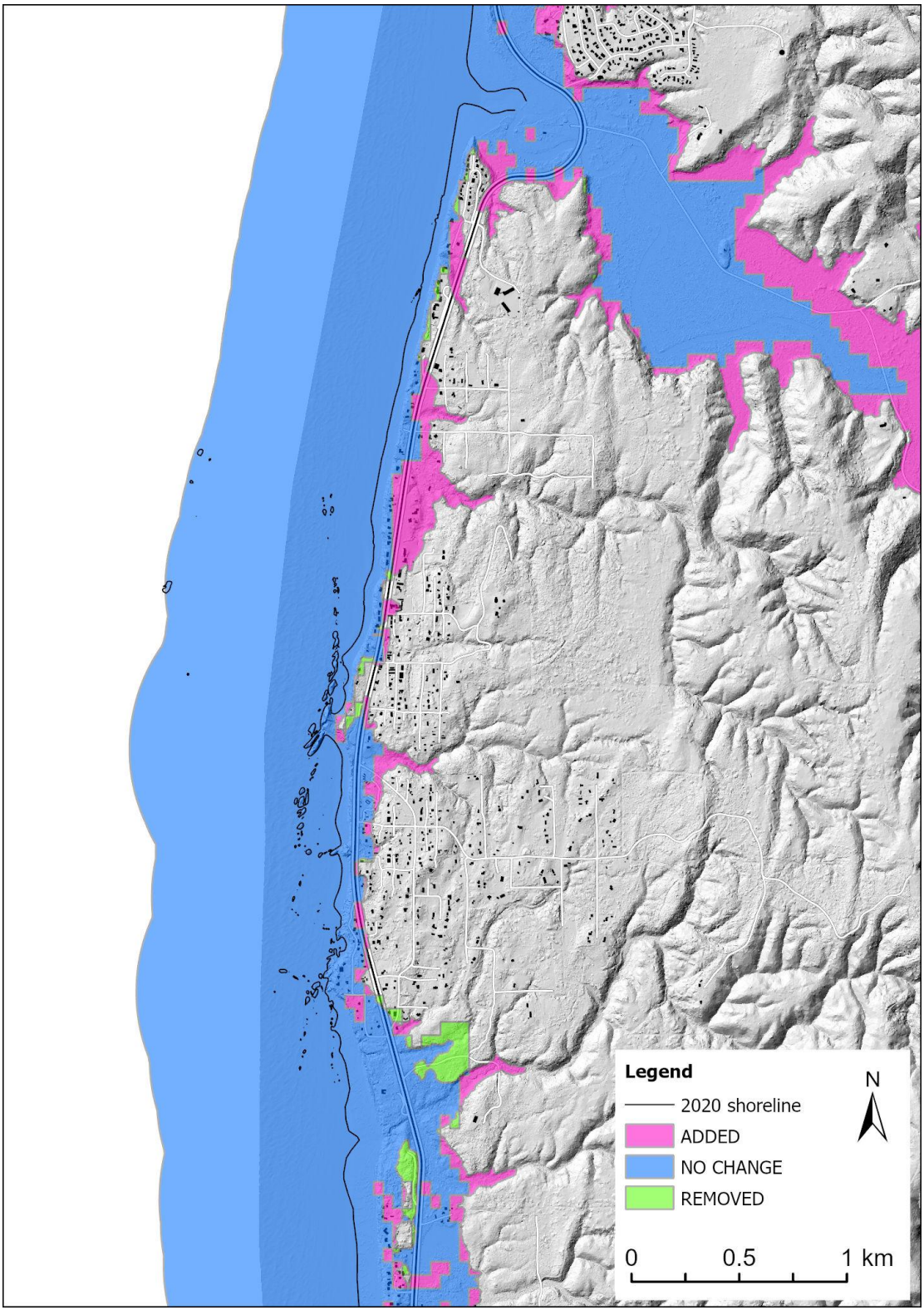


Figure 4-34. Change in the 2,475-yr tsunami design zone proposed for Bayshore and Waldport, Lincoln County.

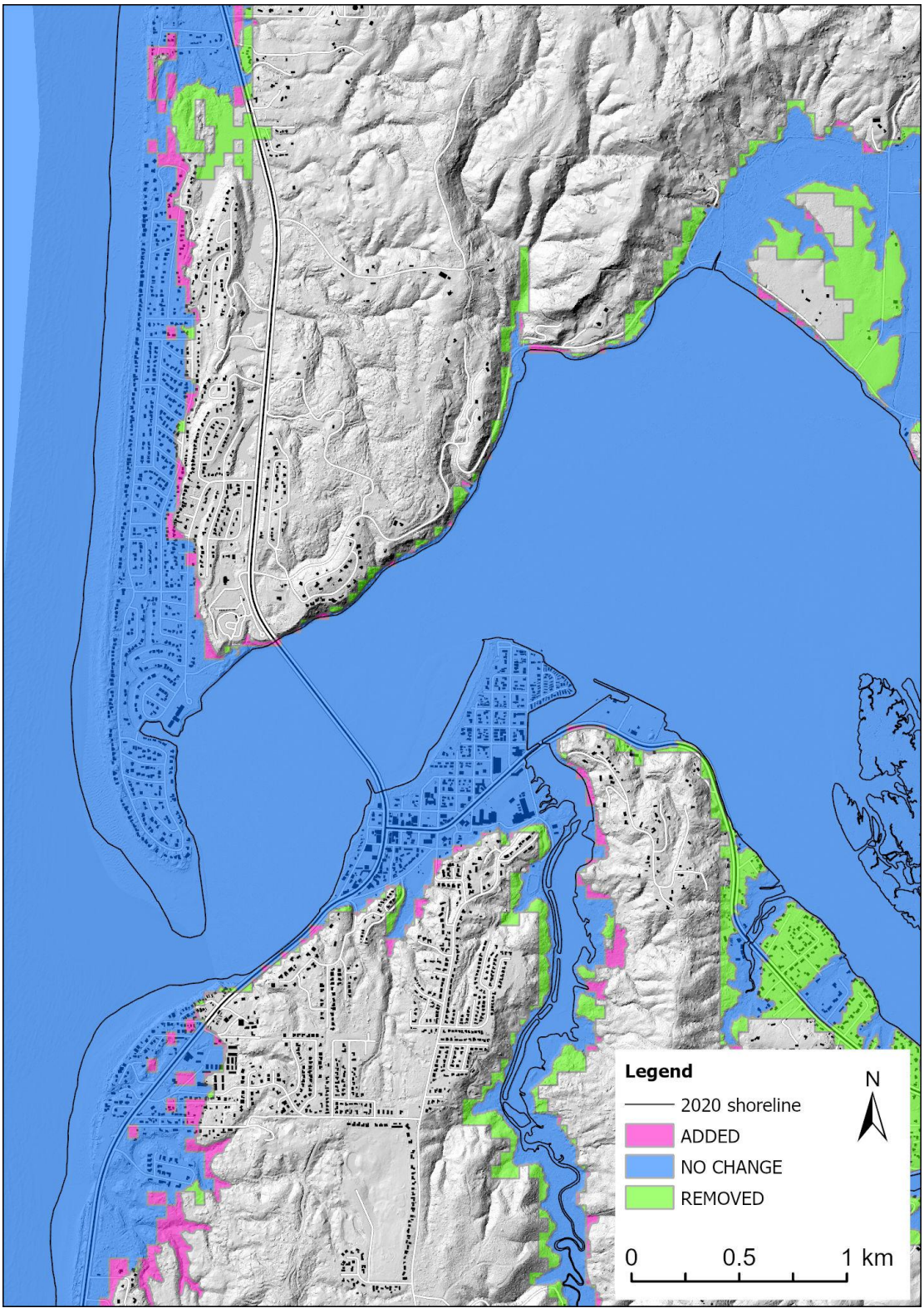
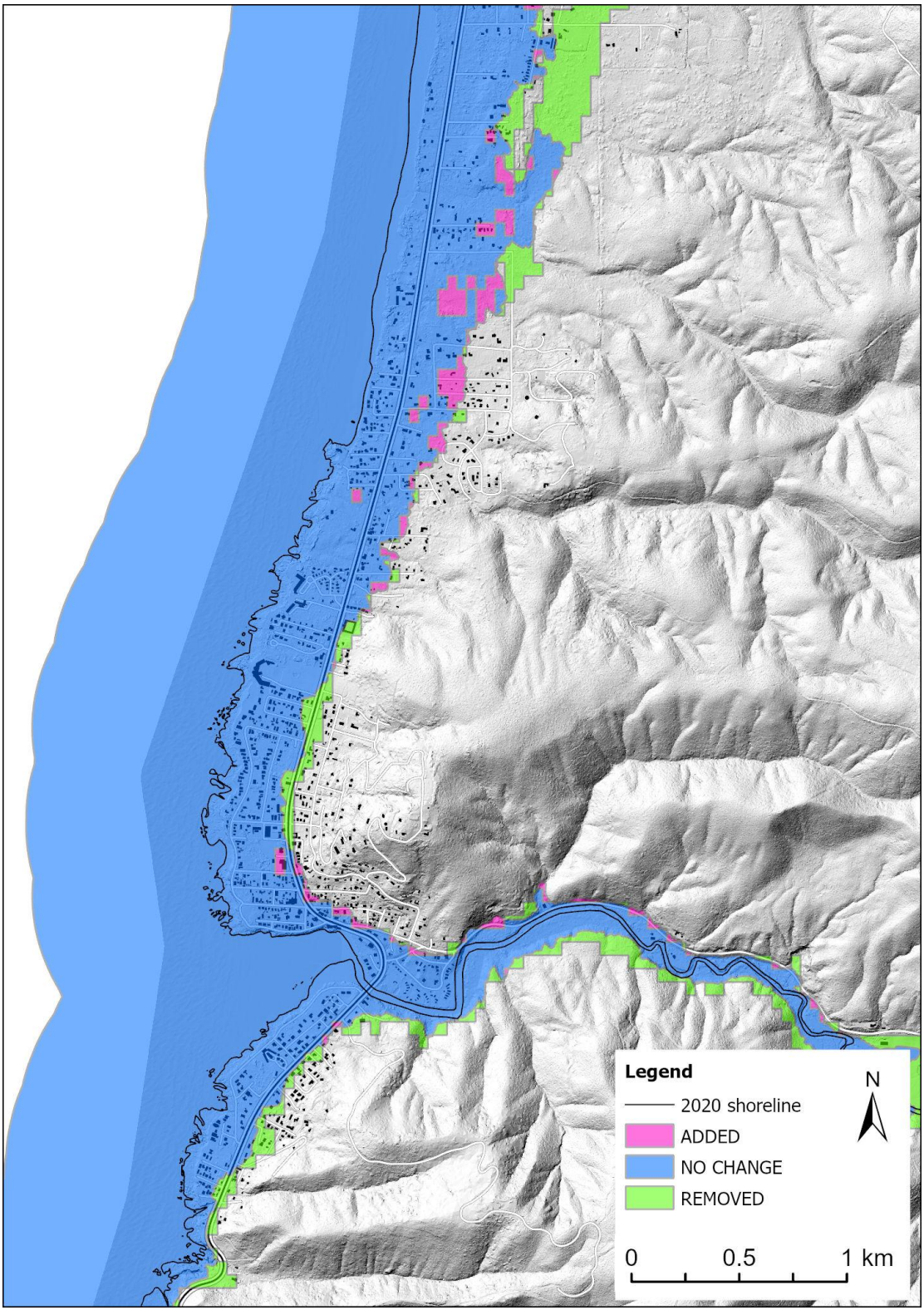


Figure 4-35. Change in the 2,475-yr tsunami design zone proposed for Yachats, Lincoln County.



4.4.1 Modeled Runup Elevations

This section presents a series of empirical cumulative distribution function (ECDF) plots of tsunami runup elevations determined for the latest modeling and compared to the previous ASCE7-22 modeling (**Figure 4-36**). The authors consider only open coast sites in these plots, thereby excluding many of the low runup elevations characteristic of estuaries, rivers and creeks. Similarly, the authors exclude areas around coastal headlands, since those sites skew the tsunami runups to the largest values. Using this approach, the authors note the following statistics for each of the counties:

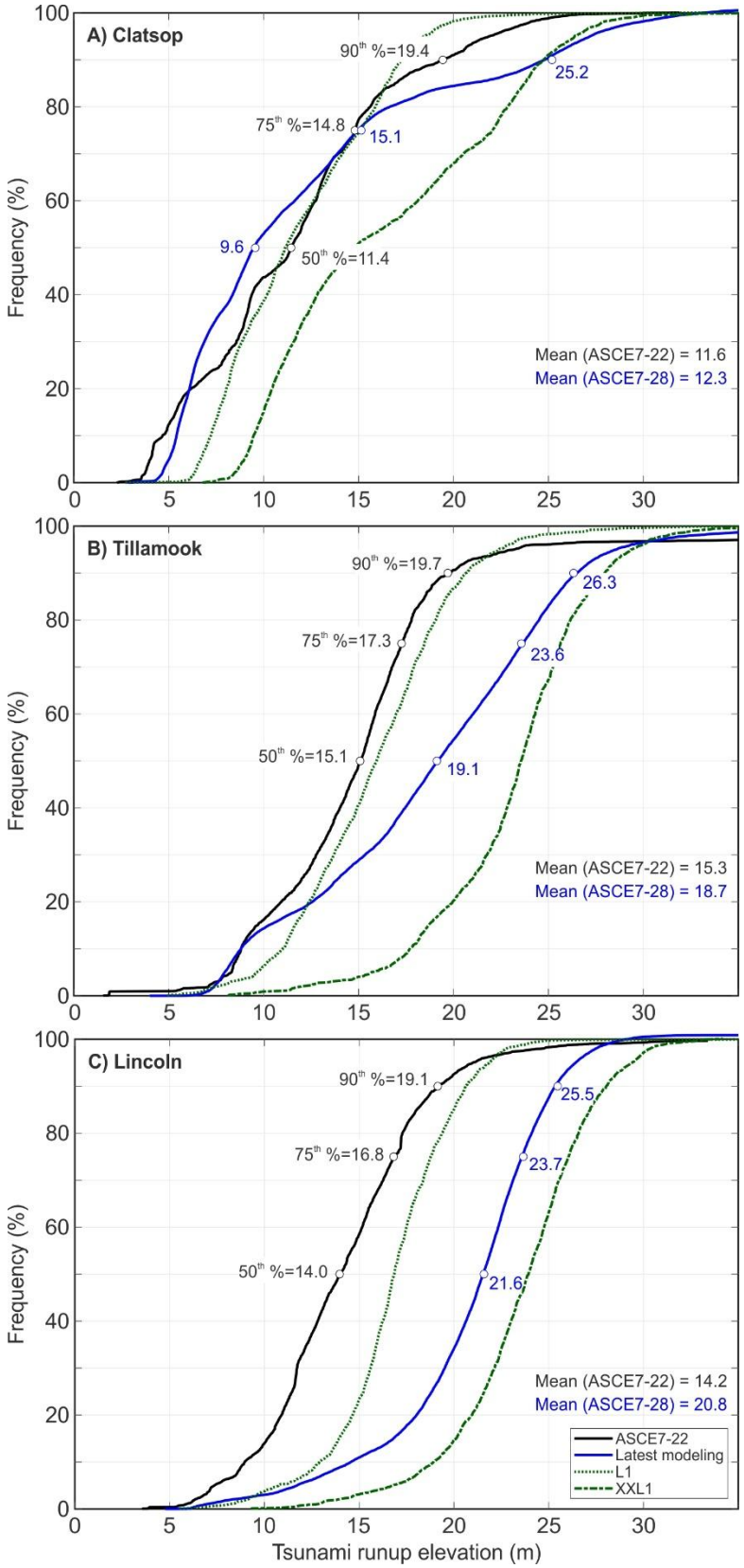
- For Clatsop County (**Figure 4-36A**), the ECDF indicates:
  - 50% of the tsunami runup heights are less than 9.6 m (ASCE7-22 = 11.4 m), and 90% of the tsunami runup heights are less than 25.2 m (ASCE7-22 = 19.4 m).
  - Tsunami runup heights exceed 33.1 m for 1% of all runup (ASCE7-22 = 25.2 m).
- For Tillamook County (**Figure 4-36B**), the ECDF indicates:
  - 50% of the tsunami runup heights are less than 19.1 m (ASCE7-22 = 15.1 m), and 90% of the tsunami runup heights are less than 26.3 m (ASCE7-22 = 19.7 m).
  - Tsunami runup heights exceed 33.8 m for 1% of all the runup (ASCE7-22 = 41.8 m).
- For Lincoln County (**Figure 4-36C**), the ECDF indicates:
  - 50% of the tsunami runup heights are less than 21.6 m (ASCE7-22 = 14 m), and 90% of the tsunami runup heights are less than 25.5 m (ASCE7-22 = 19.1 m).
  - Tsunami runup heights exceed 28.9 m for 1% of all the runup (ASCE7-22 = 25.9 m).

Figure 4-36 also includes ECDF curves for the original DOGAMI L1 and XXL1 runup. In Clatsop County the authors find that the L1 ECDF is slightly more conservative when compared with ASCE7-22 and the latest modeling up to ~85% level. Beyond the 85% level, both ASCE7-22 and the latest modeling indicate higher runup elevations. In contrast, the XXL1 ECDF remains more conservative (i.e., has larger runup) up to the 90% level, above which the latest modeling is exceeding XXL1.

In Tillamook County the authors find that the L1 ECDF is slightly more conservative when compared with ASCE7-22. However, the latest 2,4765-yr modeling exceeds the L1 curve over much of Tillamook County, indicating that the latest model results are consistently producing higher tsunami runup. The XXL1 ECDF remains more conservative (i.e., has larger runup) up to ~96% level, above which the latest modeling and the XXL1 runup are broadly similar to each other. Of note also, these plots point to a slight decrease in the highest runup elevations when compared to ASCE7-22.

In Lincoln County, the L1 ECDF is consistently more conservative when compared with ASCE7-22. However, as with Tillamook County the latest 2,475-yr tsunami modeling exceeds the L1 curve over much of the coast, producing higher tsunami runup overall. The XXL1 ECDF again remains more conservative (i.e., characterized with larger runup) across the entire curve.

Figure 4-36. ECDF plots of tsunami runup elevations determined for Clatsop, Tillamook, and Lincoln Counties.



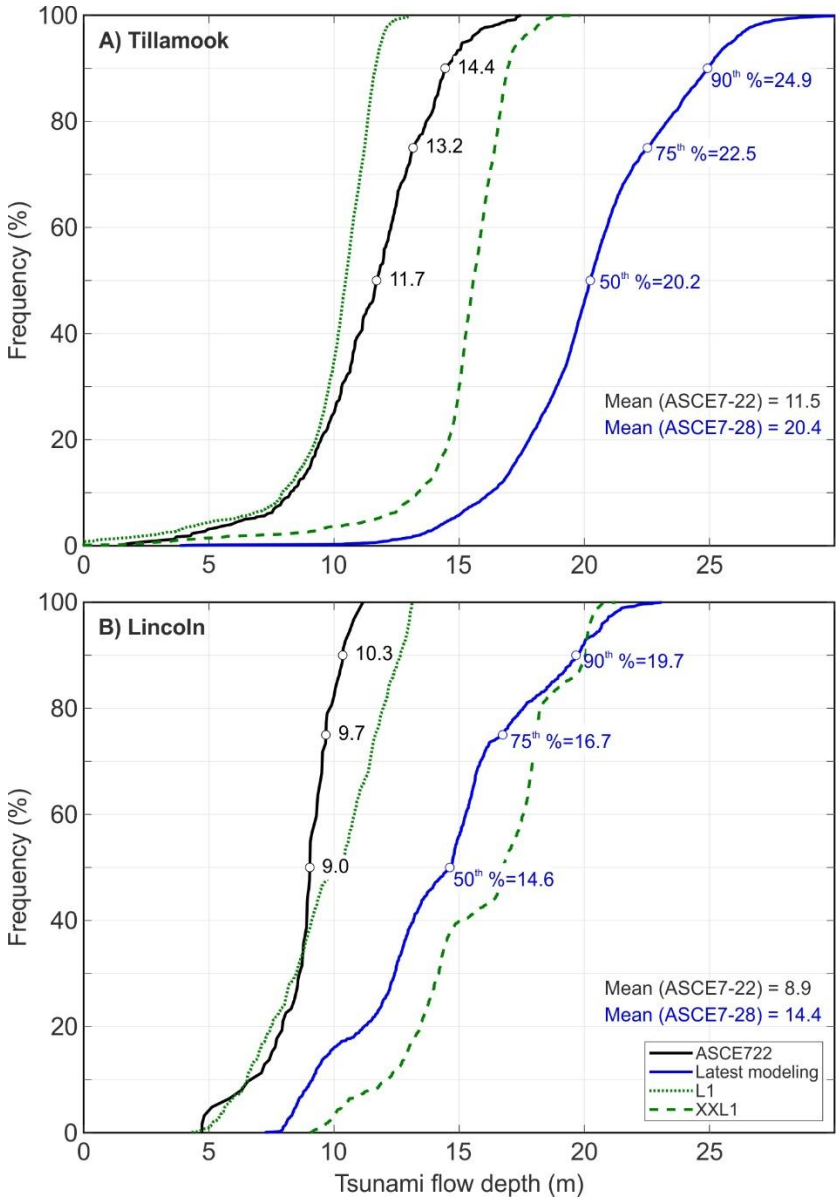
4.4.2 Modeled Flow Depths

Figure 4-37 present empirical cumulative distribution function (ECDF) plots of tsunami flow depths determined adjacent to the 5 m contour elevation along the seaward face of select barrier spits that are backed by coastal estuaries. These data were chosen since they are consistent with similar areas identified in the ASCE Tsunami Hazard Tool. As presented previously for runup, these plots enable us to broadly compare the latest modeling results, with flow depths determined for the previous ASCE7-22 modeling effort, and the DOGAMI L1 and XXL1 scenarios. Using this approach, the authors note the following statistics for Tillamook and Lincoln Counties:

- For Tillamook County (**Figure 4-37A**), the ECDF indicates:
  - 50% of the tsunami flow depths are less than 20.2 m (ASCE7-22 = 11.7 m), 90% of the tsunami flow depths are less than 24.9 m (ASCE7-22 = 14.4 m).
  - Tsunami flow depths exceed 27.8 m for 1% of all the runup (ASCE7-22 = 16.9 m).
- For Lincoln County (**Figure 4-37B**), the ECDF indicates:
  - 50% of the tsunami flow depths are less than 14.6 m (ASCE7-22 = 9 m), and 90% of the tsunami flow depths are less than 19.7 m (ASCE7-22 = 10.3 m).
  - Tsunami flow depths exceed 21.5 m for 1% of all the runup (ASCE7-22 = 11 m).

Overall, these results indicate a substantial increase in tsunami flow depths when compared with ASCE7-22, especially along the coast of Tillamook County. This is further reinforced when comparing the latest modeled flow depths with the L1 and XXL1 scenarios simulated by Witter and others (2011) for Tillamook County. Along the Lincoln County coast, the 2,475-yr modeled flow depths fall mostly below the XXL1 ECDF curve, with ~6% of the flow depths found to exceed XXL1.

Figure 4-37. ECDF plots of tsunami flow depths along barrier spits backed by estuaries in Tillamook and Lincoln Counties.



5.0 DISCUSSION

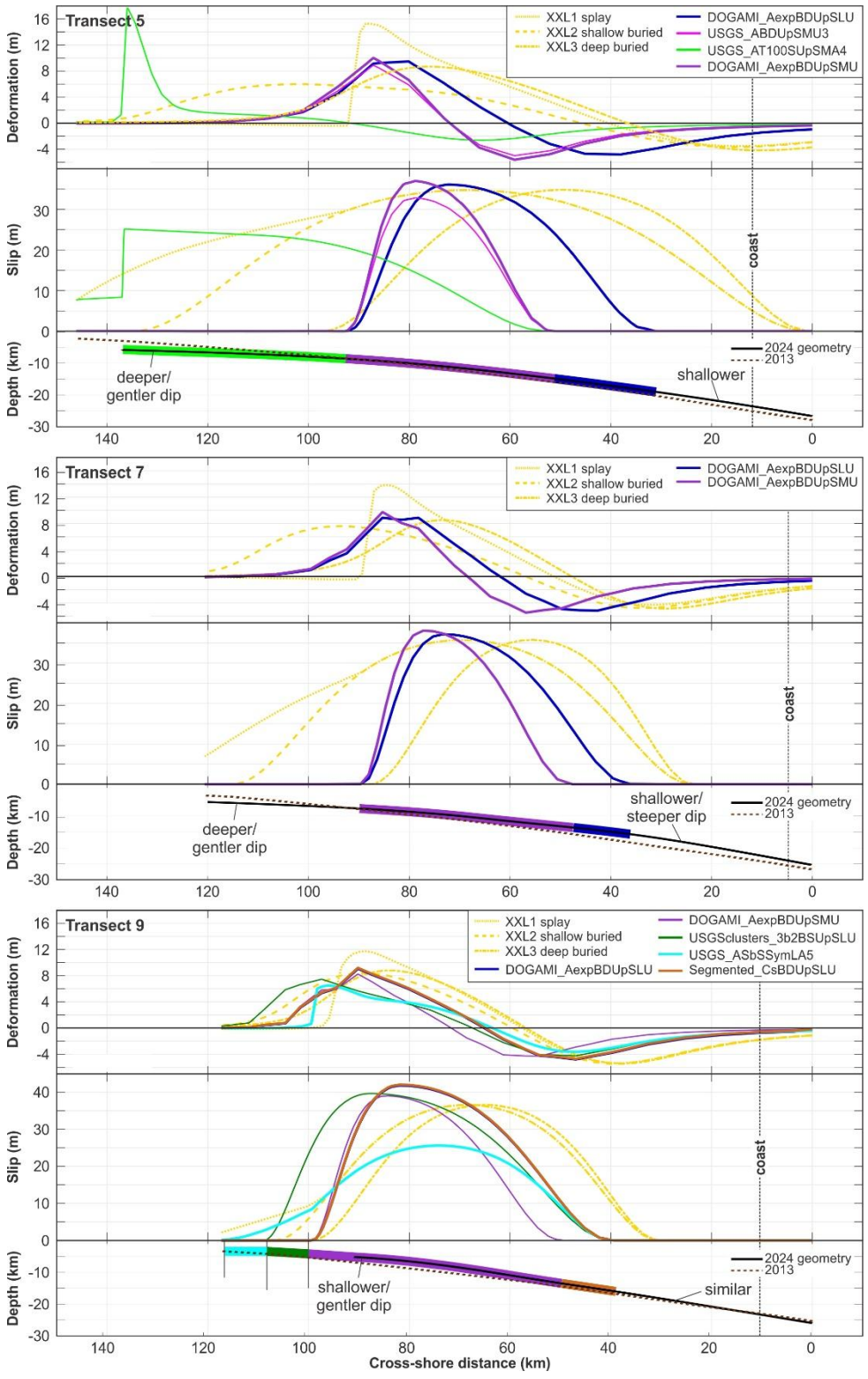
Modeling undertaken as part of this study has raised several issues that should be considered in future ASCE updates. Of greatest concern are the very large flow depths observed in the latest modeling for Tillamook and Clatsop County, which in some cases are likely to preclude the potential adoption of VES in coastal communities such as Seaside (e.g., **Figure 4-6**) or even Rockaway Beach (**Figure 4-9**). Extreme tsunami flow depths of the magnitudes identified in northern Oregon have been observed elsewhere in the world in response to recent tsunami events. For example, Iwai and Goto (2021) identified flow depths that ranged from 15 m to 27.6 m following the 2011 Töhoku, Japan event, and up to 25 m depths in Lohk Nga, Indonesia caused by the 2004 Andaman Ocean megathrust earthquake and tsunami.

The cause of such large flow depths observed in northern Oregon are very much a function of the new CSZ sources, which produce significant asymmetry of the generated tsunami wave (a narrow, steep wave) with large drawdown well offshore the northern Oregon Coast. Together, these processes are effectively displacing a larger volume of water over a narrower source area, when compared with previous source models developed by Witter and others (2011). **Figure 5-1** presents further comparisons of the CSZ source model characteristics for the latest ASCE 2,475-yr scenarios with those developed by Witter and others (2011). In addition to profiles of the modelled deformation, the authors include cross sections of slip and subduction zone geometry used by Witter and others (2011) and the updated geometry developed by Sypus and Wang (2024). These data enable better evaluation of differences in the latest source models with those developed previously.

Of particular importance are the very large differences in the width of modeled slip (and thus deformation), especially in northern Oregon (Transects 5 and 7), which the authors believe is strongly influencing the asymmetry of the modeled tsunami and ultimately the large flow depths described previously at Seaside and Rockaway Beach. Beginning on the northern Oregon Coast at Seaside (Transect 5), it can be seen than the width of modeled slip in the original DOGAMI XXL scenarios ranged from ~95 km (deep buried model) to ~150 km wide (shallow buried model, **Figure 5-1**). In contrast, the new PTHA source models indicate slip widths that are considerably narrower (~40 km to 60 km wide, ~50% less). In northern Tillamook County (Transect 7), the original DOGAMI XXL slip models have decreased to ~63 km (deep buried model) to ~97 km wide (shallow buried model), while the new PTHA source models have widths of ~42 km to 54 km (**Figure 5-1**). At Transect 9 located in central Lincoln County, the original XXL slip models have decreased further to ~63 km to ~85 km wide, while the latest PTHA source models widened slightly to ~50 km to 60 km (**Figure 5-1**). Thus, the XXL models and latest source models appear to converge slightly with distance south along Cascadia.

With respect to the geometry of the subducting plate, all three transect plots indicate that the models exhibit broadly similar plate geometry (**Figure 5-1**). In general, in northern Oregon the Witter and others (2011) geometry model is slightly shallower in the updip sections of the down-going plate, when compared with the latest revised plate geometry. Conversely, the latest geometry model tends to be slightly deeper in the downdip sections of the down-going plate. Broadly speaking, the newer source models indicate a slightly shallower, more gently sloping geometry in the updip section across the northwest Oregon Coast, but a deeper and steeper dip in the downdip portion when compared with Witter and others (2011). On the central Oregon Coast, the geometry of the new CSZ model is broadly similar to Witter and others (2011). Accordingly, given that differences in the overall geometry of the CSZ are relatively minor across this portion of Cascadia, changes in geometry are probably unlikely to have significantly affected the tsunami generated by the latest source models.

Figure 5-1. Profiles of 2,475-yr earthquake vertical deformation, slip, and geometry models used in the latest CSZ tsunami simulations, compared with the original DOGAMI XXL scenarios developed by Witter and others (2011). Solid lines defined for the depth profiles denote the slip patches associated with the various model scenarios and extend to the downdip limit. Note that several of the models overlap in the downdip direction.



Hyndman and Wang (1993) proposed a thermal model, where the downdip limit of seismicity is hypothesized to occur at a transition from velocity-weakening to velocity-strengthening behavior, which occurs at ~350 °C and depths of ~10–5 km. This region is found to occur ~50–90 km offshore the Oregon Coast and is generally consistent with the approximate position of coseismic slip in the latest source models (e.g., **Figure 5-1**). Recall from **Section 2.2.2.1**, downdip limits of slip are specified from shallowest to deepest point (**Figure 2-4**) by three models: halfway between the locked zone defined from a thermal model and the 1 cm/yr locking contour, 1 cm/yr locking contour, and the top of the tremor zone. These limits are specified in the USGS NSHM model for the CSZ (Peterson and others, 2014) and were used by Sypus and Wang (2024). They are depicted in **Figure 5-2** (colored dash lines) along with one of the newer source models used here (left), and the DOGAMI XXL3 buried rupture model (right). Included in **Figure 5-2** is the downdip extent adopted by Gao and others (2018), considered to be a preferred CSZ downdip extent (K. Wang, personal communication, February 2026).

Figure 5-2. A) Comparison of the downdip limits of coseismic slip proposed by the USGS Seismic Hazard Program (Peterson and others, 2014) and adopted by Sypus and Wang (2024) and overlayed on the DOGAMI_AexpBDUpSLU CSZ source model; B) comparing these same downdip limits to the original DOGAMI buried XXL3 model of Witter and others (2011). Note how all compare to the preferred limit (pink dash) of Gao and others (2018).

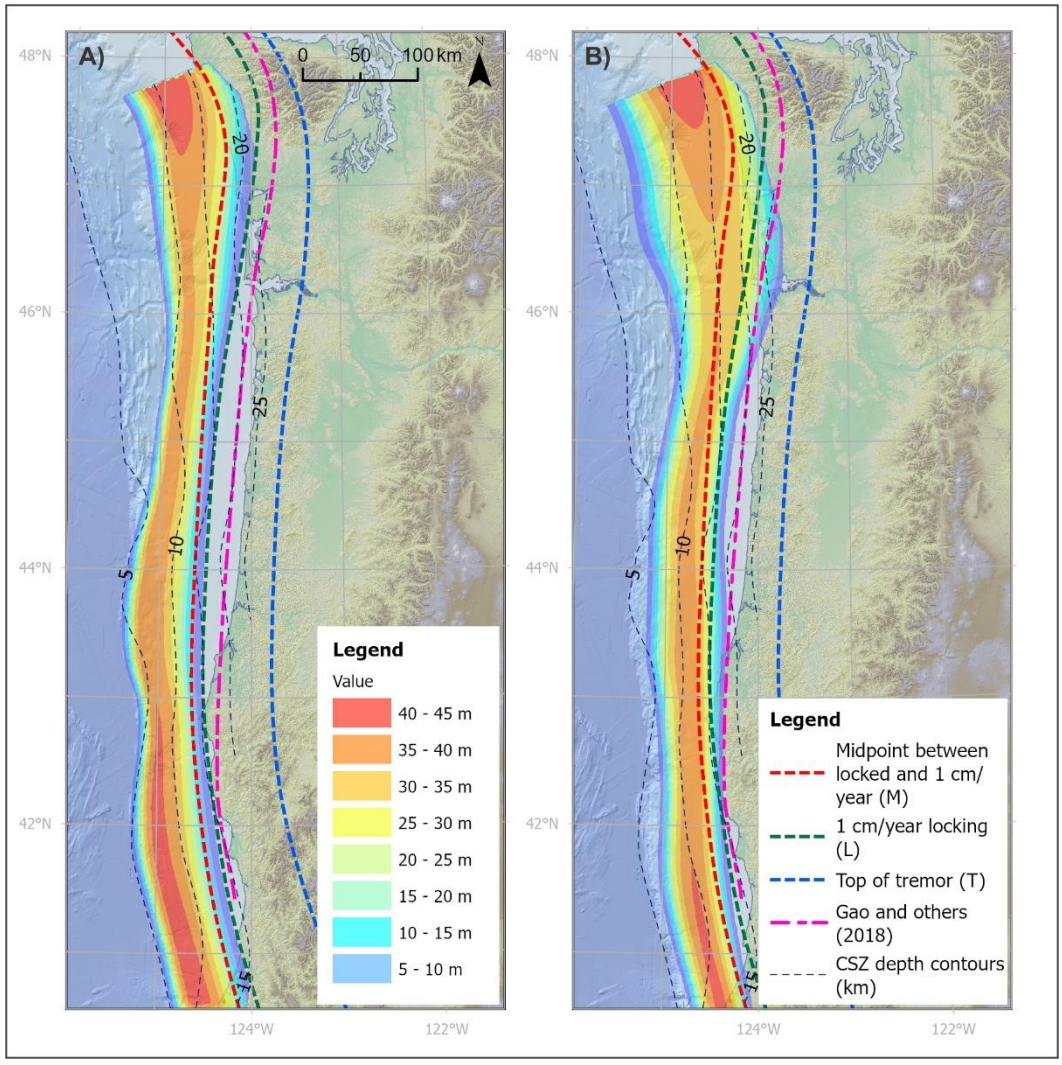


Figure 5-2A indicates that the DOGAMI_Aexp-B-D-UpS-L-U is indeed constrained to the 1 cm/yr locking contour (green dash). Conversely, the XXL3 model exhibits a much wider seismogenic zone in northern Oregon and southern Washington (**Figure 5-2B**) that extends well beyond the Peterson and others (2014) 1 cm/yr locked zone limit, although updip of the top of tremor. As described previously, these differences are more noticeable when viewed in cross-section (**Figure 5-1**).

To better understand differences in the resulting tsunami simulations, the authors completed new tsunami inundation modeling of the original DOGAMI XL2 (shallow buried) and XL3 (deep buried) scenarios for Clatsop County. The authors chose these models since they are broadly similar to the 2,475-yr models (i.e., deep and shallow buried rupture models) and have comparable maximum slip to the 2,475-yr models used here. The main difference in the models is their downdip extents and slip distributions (up skew for the 2,475-yr model in **Figure 5-2A** vs symmetric in XL2 and XL3 in **Figure 5-2B**). In addition to the original DOGAMI source models, the authors also simulated a new source model based on the Gao and others (2018) downdip extent. For this latter scenario, colleagues at the University of Victoria, Canada constructed an up skewed version of the deep buried rupture model, with its downdip limit constrained to match Gao and others (2018). The source model was then scaled by 2.6 to produce a maximum slip comparable to the Clatsop Run02c simulation.

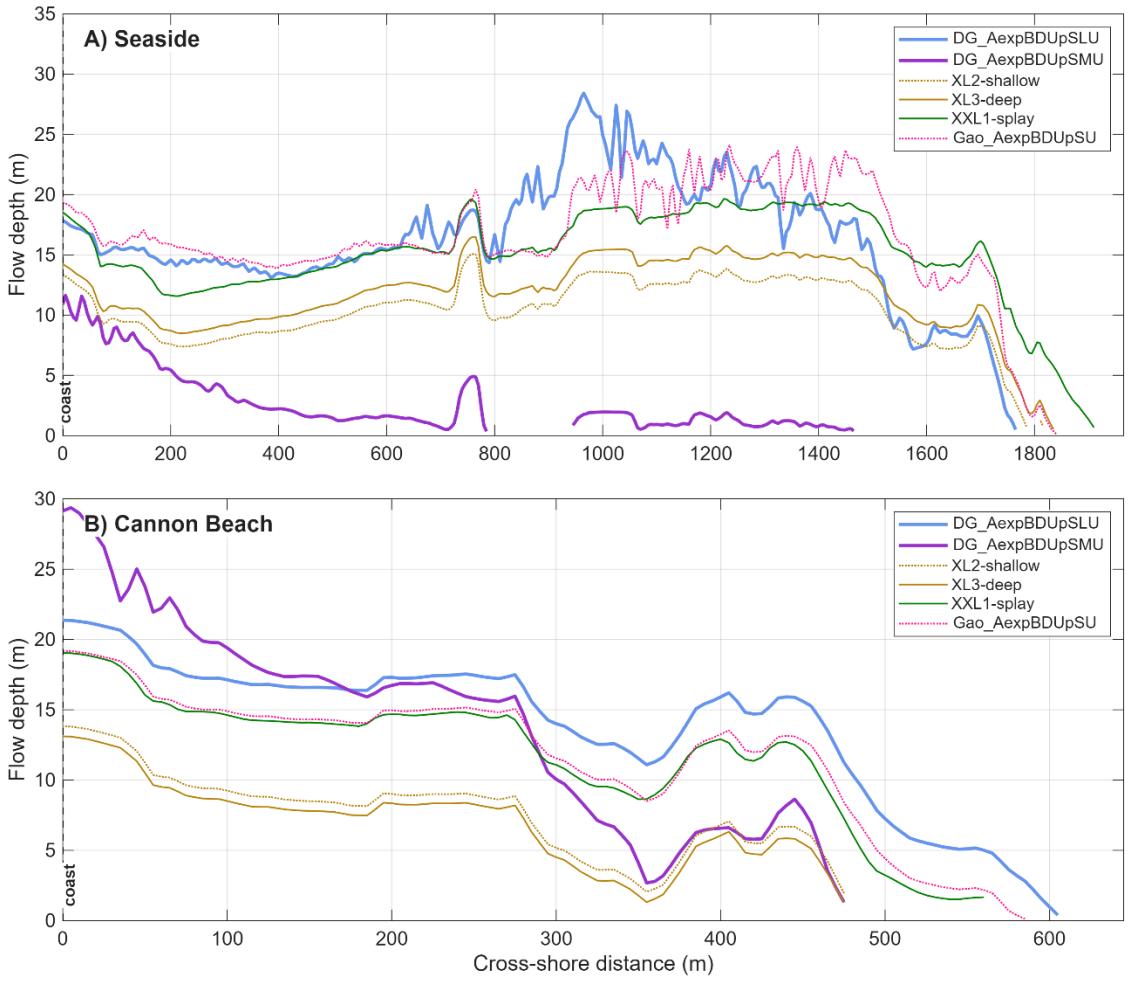
Figure 5-3 presents two cross-sections of the simulated flow depths defined for transects that cross the communities of Seaside and Cannon Beach. As expected, the deep-buried XL3 model indicates larger flow depths (solid gold line) at Seaside when compared with the shallow buried XL2 scenario (dash gold line). However, the XL3 simulated flow depths are ~3–5 m below the 2,475-yr deep buried scenario (solid blue line) within the first 800 m of the coast (**Figure 5-3**). Differences between the XL3 (gold line) and 2,475-yr deep buried scenario (solid blue line) flow depths reach a maximum ~10–12 m at ~1000–1200 m from the coast but then converge ~1500 m from the coast. Again, these differences can be attributed mainly to the steeper and narrower deformation of the new 2,475-yr deep buried scenario when compared to the original DOGAMI models. At Cannon Beach, the XL2 and XL3 rupture models indicate even lower tsunami flow depths (**Figure 5-3**), when compared with the 2,475-yr buried rupture scenarios (blue and purple lines), including the original XXL1 scenario that has large uplift from a splay fault. Interestingly, the shallow buried XL2 model indicates slightly larger flow depths at Cannon Beach when compared with XL3. The new Gao model, which is different only in terms of its downdip extent, produces a comparable tsunami flow depth to the 2,475-yr tsunami (blue line in **Figure 5-3**) within the first 800 m from the beach at Seaside. Further landward, however, the Gao model produces peak flow depths that are ~3–5 m below the 2,475-yr tsunami (blue line in **Figure 5-3**) flow depth. Interestingly, the inundation zone widens slightly for the new Gao model. In contrast, the new Gao model produces flow depths at Cannon Beach that are essentially the same as the DOGAMI XXL1 source model. This very simple comparison highlights how one small adjustment can have a relatively important effect on the simulated flow depths and inundation zones.

Overall, the authors conclude that differences in the tsunami characteristics are probably mainly controlled by the location of the downdip extents; the shape of the slip distributions may be another smaller influence but were unable to assessed here. Finally, the authors note that other effects such as the local bathymetry may also account for some of the more nuanced differences observed at Cannon Beach when compared to Seaside.

The Witter and others (2011) and Priest and others (2009) sources accounted for the landward transition from compressional to extensional upper plate structures inferred from geology and well breakout data to define potential down dip rupture penetration. Gao and others (2018) adopted the downdip CSZ rupture limit proposed by Wang and others (2003) but modified it slightly in southern

Cascadia to better account for complexities in the megathrust geometry. A future PTHA might therefore include tsunami sources that explore these inferences. Lastly, approaches that consider stochastic slip models that vary the rupture depth based on probability distribution functions is another promising area of research (Melgar and others, 2019), which could result in further improvements to existing source models.

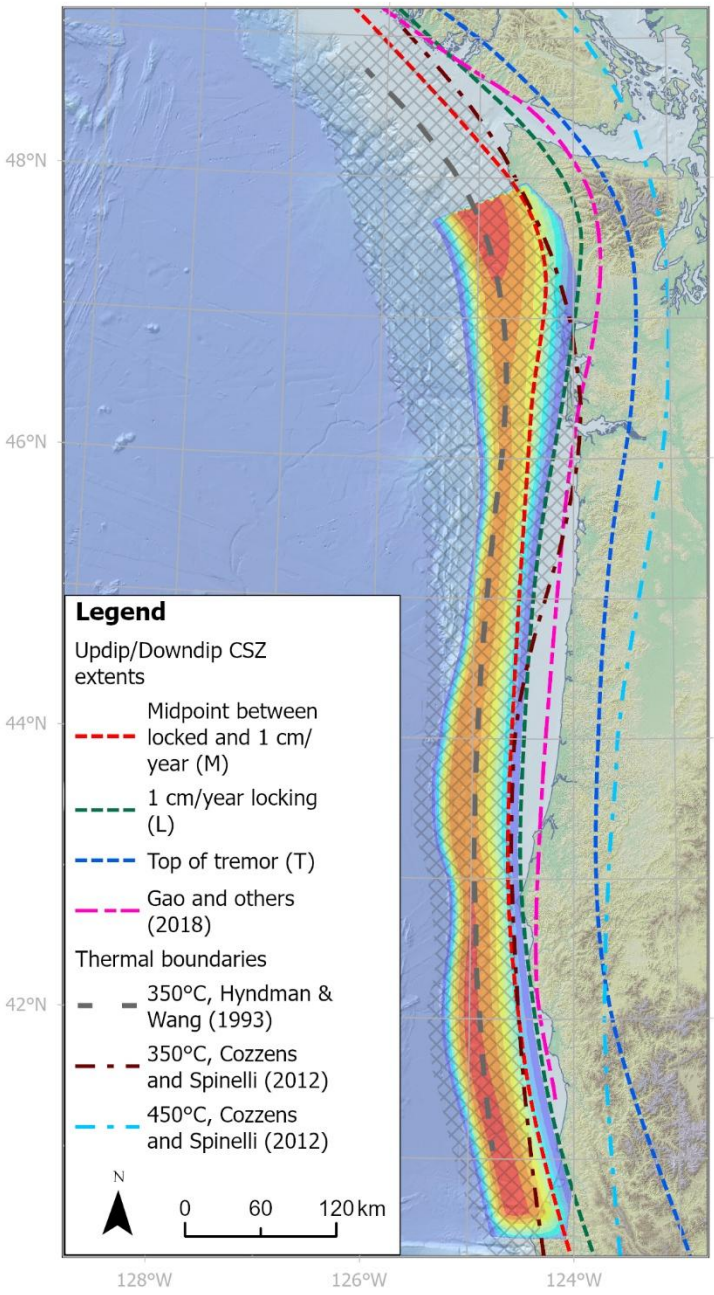
Figure 5-3. Comparison of original DOGAMI XL2 (shallow), XL3 (deep buried), and Gao_AexpBDUpSU rupture models in Clatsop County, compared to the new 2,475-yr rupture models.



Cozzens and Spinelli (2012) evaluated thermal models that included the effects of fluid circulation. They observed that the inclusion of fluid in the thermal model effectively cools the subduction zone, which correspondingly widens the seismogenic zone by ~30 – 55 km (**Figure 5-4**); the latter is accomplished by shifting the ~350 °C boundary downdip, effectively toward the coast. Phrampus and others (2017) evaluated the thermal structure of the CSZ using publicly available seismic lines along with a reinterpretation of bottom simulating reflector (BSR) distributions. They concluded that thermal models that considered fluid circulation were found to match the BSR-derived heat flow boundaries better and were thus an important process affecting the thermal regime of the CSZ. Nevertheless, Phrampus and others (2017) acknowledged that their approach was not necessarily a strict test of existing thermal models and noted that further research was needed. An initial attempt was made to produce a Cozzens

type rupture model. However, having constructed the deformation model, it was found that areas along the Clatsop and Tillamook coastline were now being uplifted, which contradicted the paleoseismic data. Accordingly, this effort was abandoned and remains a topic for future evaluation.

Figure 5-4. Map of Cascadia showing the seismogenic zone of Cozzens and Spinelli (2012, hatched area) based on a thermal model incorporating fluid convection; also shown are their 350°C (dash-dot brown line) and 450°C (dash-dot cyan line) isotherms on the plate boundary. Dashed gray line is the 350°C isotherm of Hyndman and Wang (1993). Colored raster depicts the DOGAMI_ Aexp-B-D-UpS-L-U slip model produced by Sypus and Wang (2024) for the updated 2,475-yr tsunami modeling project. Magenta dashed line is the downdip coseismic rupture limit of Gao and others (2018), while the black dashed line is the limit from Witter and others (2011).



Our overall approach to match various 2,475-yr disaggregated sources with those generated along the 100-m bathymetric contour has also raised several other questions. Fundamentally, the application of Green's functions linear approaches to simplify the PTHA process is generally limited to water depths deeper than ~100 m. The assumption being that at these depths, the propagating tsunami is not influenced by the gradually shallowing bathymetry, nor is it affected by other factors, such as edge waves and reflected waves. However, it is notable that the 100 m isobath offshore the Oregon Coast is located at a wide variety of distances from the shoreline due to large variations in the shelf width, such that some areas are characterized with having a narrow shelf (e.g., Tillamook County), while other areas exhibit a wide shelf (e.g., northern Clatsop County). It is the narrower shelf widths that are especially susceptible to complex reflection from irregularities in the coast. The PTHA modeling strongly indicates that even at depths of 100 m, the authors can see the effects of focusing and defocusing of tsunami energy, reflection of waves away from the coast (areas with narrow shelves or prominent headlands) that are causing tsunami wave amplification, along with the interaction of tsunami with edge waves that become trapped on the shelf. These processes strongly suggest that consideration should be directed at either moving the offshore points to even deeper water depths or explore alternative PTHA approaches, including hybridized approaches. Of note, the rapid expansion of high-power computing systems now allows for potentially running several hundred scenarios (e.g., those local scenarios that dominate the hazard curve between ~475-yr to 5,000-yr) at high resolution on to land, from which a PTHA could be generated for every land-based grid node. This would allow for better accounting for uncertainty and would eliminate the need for amplitude wiggle matching at the offshore domain.

6.0 CONCLUSION

The objective of this study has been to produce new 2,475-yr probabilistic tsunami hazard analysis (PTHA) inundation maps for the central to northern Oregon Coast, including Clatsop County, Tillamook County, and Lincoln County. The new modeling and mapping incorporate significant improvements in Cascadia earthquake rupture models, improved bathymetric and topographic digital elevation models, and high-resolution tsunami inundation modeling.

We modeled seven disaggregated CSZ deformation models that were scaled to meet the minimum requirements of a 2,475-yr earthquake rupture. In total, some 26 tsunami simulations were used for detailed simulations of inundation, including a reevaluation of several rupture scenarios originally produced by DOGAMI between 2010 and 2013. From the simulated results, the authors produced updated GIS data showing tsunami inundation zones for a 2,475-yr tsunami that span multiple scenarios, rasters that depict the simulated flow depths, maximum water levels, and flow depths, as well as other derivative tsunami products. Combined, these data are anticipated to be eventually used by the ASCE Tsunami Loads Committee in order to replace the existing ASCE7-22 TDZ and geodatabases produced for Oregon in 2016. Once adopted, the new 2,475-yr ARP tsunami hazard maps and geodatabase will automatically become part of the Oregon Building Codes 2019 Oregon Structural Specialty Code (OSSC) and will be accessible through the ASCE tsunami hazard tool.

Finally, this study highlighted the sensitivity of tsunami flow depths (and inundation zones) to the down-dip coseismic slip limits, specified in the PTHA. Existing PTHA downdip limits used in the current update are based on the USGS Seismic Hazard Program (Peterson and others, 2014). However, several other downdip extents (e.g., Witter and others, 2011; Gao and others, 2018) should be considered in a future update of the PTHA to better account for aleatory uncertainties of CSZ rupture processes. In addition, since the specified logic tree branch weights were never formerly evaluated by geologists and geophysicists, we recommend that these be carefully reviewed in the next ASCE PTHA update.

7.0 ACKNOWLEDGMENTS

This project was funded under award NA23NWS4670018 and NA24NWSX467G0008 by NOAA through the National Tsunami Hazard Mitigation Program. We thank Dr. Reed Burgette from DOGAMI for his insightful report review and comments. We also thank Dr. Randy LeVeque (University of Washington) and Dr. Elena Troshina (Geophysical Institute, University of Alaska Fairbanks) for providing constructive comments on the technical report. We are also grateful to Daniel Eungard (Washington Geological Survey, Department of Natural Resources) for his collaboration and assistance throughout this project. Finally, we are grateful to Dr. Yijie Zhu at the University of Victoria, Canada, who assisted us with developing deformation models using the Gao and others (2018) downdip limit, along with an initial evaluation of a Cozzens and Spinelli (2012) model. Simulations used in this paper were conducted using the following computational facilities: 1) SciClone at the College of William and Mary, that was provided with assistance from the National Science Foundation, the Virginia Port Authority, Virginia's Commonwealth Technology Research Fund, and the Office of Naval Research; 2) the Extreme Science and Engineering Discovery Environment (XSEDE; grant TG-OCE130032), supported by National Science Foundation grant number OCI-1053575; and 3) NASA's Pleiades supercomputer.

8.0 REFERENCES

Allan, J.C. and O'Brien, F.E., 2025. Earthquake and Tsunami Impact Analysis for the Oregon Coast. Oregon Department of Geology and Mineral Industries Open-File Report O-25-01, Portland, Oregon, 92 p.

Allan, J.C., Zhang, J., O'Brien, F. and Gabel, L., 2018. Columbia River Tsunami Modeling: Towards Improved Maritime Planning Response. Oregon Department of Geology and Mineral Industries Special Paper 51, Portland, Oregon, 83 p.

Allan, J.C., Zhang, J. and O'Brien, F., 2021. Tsunami Inundation Modeling Update for the Northern Oregon Coast: Tillamook and Clatsop Counties. Oregon Department of Geology and Mineral Industries Open-File Report O-21-08, Portland, Oregon, 38 p.

American Society of Civil Engineers (ASCE), 2017. Minimum design loads and associated criteria for buildings and other structures: ASCE/SEI 7-16 Provisions and Commentary, 822 p.

Bahavar, M., Staisch, L., Dura, T., Hawkes, A., Kelsey, H., La Selle, S., Witter, R., Bruce, D., Bachelot, L. and Thomas, A., 2025. The Cascadia Region Earthquake Science Center (CRESCENT) Paleoseismic viewer (1.0.0). CRESCENT Open Documents Library. https://doi.org/10.5281/zenodo.15866115

Behrens, J., Løvholt, F., Jalayer, F., Lorito, S., Salgado-Gálvez, M.A., Sørensen, M., Abadie, S., Aguirre-Ayerbe, I., Aniel-Quiroga, I. and Babeyko, A., 2021. Probabilistic Tsunami Hazard and Risk Analysis: A Review of Research Gaps. *Frontiers in Earth Science*, 9: 114.

Carbotte, S.M., Boston, B., Han, S., Shuck, B., Beeson, J., Canales, J.P., Tobin, H., Miller, N., Nedimovic, M. and Tréhu, A., 2024. Subducting plate structure and megathrust morphology from deep seismic imaging linked to earthquake rupture segmentation at Cascadia. *Science Advances*, 10(23): eadl3198.

Carignan, K.S., Amante, C., Love, M.R. and Stiller, M., 2019. Digital elevation model of Clatsop and Tillamook Counties, Oregon: Procedures, data sources and analysis, NOAA National Center for Environmental Investigation, 10 p.

Carignan, K.S., Amante, C., Love, M.R. and Stiller, M., 2021. Digital Elevation Models of Central Oregon: Procedures, Data Sources and Analysis, NOAA National Center for Environmental Investigation, 11 pp.

Carvajal, M., Sun, T., Wang, K., Luo, H., and Zhu, Y., 2022. Evaluating the tsunamigenic potential of buried versus trench-breaching megathrust slip. *Journal of Geophysical Research: Solid Earth*, 127, e2021JB023722.

Chock, G., Yu, G., Thio, H.K. and Lynett, P.J., 2016. Target structural reliability analysis for tsunami hydrodynamic loads of the ASCE 7 standard. *Journal of Structural Engineering*: 04016092.

Cozzens, B.D. and Spinelli, G.A., 2012. A wider seismogenic zone at Cascadia due to fluid circulation in subducting oceanic crust. *Geology*, 40(10): 899–902.

Flück, P., Hyndman, R.D. and Wang, K., 1997. Three-dimensional dislocation model for great earthquakes of the Cascadia subduction zone. Journal of Geophysical Research, 102(B9): 20539–20550.

Fraser, S., Leonard, G.S., Murakami, H. and Matsuo, I., 2012. Tsunami Vertical Evacuation Buildings – Lessons for International Preparedness Following the 2011 Great East Japan Tsunami. *Journal of Disaster Research*, 7: 446-457.

Gao, D., Wang, K., Insua, T.L., Sypus, M., Riedel, M. and Sun, T., 2018. Defining megathrust tsunami source scenarios for northernmost Cascadia. *Natural Hazards*, 94(1): 445–469.

Goda, K., De Risi, R., Gusman, A. and Nistor, I. (Editors), 2024. Introduction of probabilistic tsunami hazard and risk analysis—toward disaster risk reduction and resilience. In: K. Goda, R. De Risi, A. Gusman and I. Nistor (Editors), *Probabilistic Tsunami Hazard and Risk Analysis: Towards Disaster Risk Reduction and Resilience*. Elsevier, Netherlands, 581 p.

Goldfinger, C., Galer, S., Beeson, J., Hamilton, T., Black, B., Romsos, C., Patton, J., Nelson, C.H., Hausmann, R. and Morey, A., 2017. The importance of site selection, sediment supply, and hydrodynamics: A case study of submarine paleoseismology on the Northern Cascadia margin, Washington USA. *Marine Geology*, 384: 4–46.

Goldfinger, C., Nelson, C.H., Morey, A., Johnson, J.E., Gutierrez-Pastor, J., Eriksson, A.T., Karabanov, E., Patton, J., Gracia, E., Enkin, R., Dallimore, A., Dunhill, G. and Vallier, T., 2012. Turbidite event history: Methods and implications for Holocene paleoseismicity of the Cascadia subduction zone. USGS Professional Paper 1661-F, 178 p.

Hyndman, R.D. and Wang, K., 1993. Thermal constraints on the zone of a major thrust earthquake failure: the Cascadia subduction zone. *Journal of Geophysical Research*, 98(B2): 2039–2060.

Kemp, A.C., Cahill, N., Englehart, S.E., Hawkes, A.D. and Wang, K., 2018. Revising Estimates of Spatially Variable Subsidence during the A.D. 1700 Cascadia Earthquake Using a Bayesian Foraminiferal Transfer Function. *Bulletin of the Seismological Society of America*, 108(2): 654–673.

Ledeczi, A., Lucas, M., Tobin, H., Watt, J. and Miller, N., 2024. Late Quaternary Surface Displacements on Accretionary Wedge Splay Faults in the Cascadia Subduction Zone: Implications for Megathrust Rupture. *Seismica*, 2(4).

Lim, E., Carignan, K.S., Love, M.R., Amante, C. and MacFerrin, M., 2024. Digital Elevation Models of The Lower Columbia River: Procedures, Data Sources, and Analysis, NOAA National Center for Environmental Investigation, 11 p.

Loomis, H.G., 1979. Tsunami prediction using the reciprocal property of green's functions. Marine Geodesy, 2(1): 27–39.

Lucas, M.C., Ledeczi, A.M., Tobin, H.J., Carbotte, S.M., Watt, J.T., Han, S., Boston, B. and Jiang, D., 2025. No evidence for an active margin-spanning megasplay fault at the Cascadia Subduction Zone. *Seismica*, 2.4: 28.

Lynett, P.J., Gately, K., Wilson, R., Montoya, L., Arcas, D., Aytore, B., Bai, Y., Bricker, J.D., Castro, M.J., Cheung, K.F. and David, C.G., 2017. Inter-Model Analysis of Tsunami-Induced Coastal Currents. *Ocean Modelling*, 114: 14–32.

McCrory, P. A., Blair, J. L., Waldhauser, F., and Oppenheimer, D. H., 2012. Juan de Fuca slab geometry and its relation to Wadati-Benioff zone seismicity. *Journal of Geophysical Research: Solid Earth*, 117(9), B09306. doi:10.1029/2012JB009407.

Melgar, D., Williamson, A.L., and Salazar-Monroy, E.F., 2019. Differences between heterogenous and homogenous slip in regional tsunami hazards modelling. *Geophysical Journal International*, 219(1), 553–562.

Miranda, J., Baptista, M., and Omira, R., 2014. On the use of Green's summation for tsunami waveform estimation: a case study. *Geophysical Journal International*, 199(1), 459–464.

Mori, N., Goda, K. and Cox, D., 2018. Recent process in probabilistic tsunami hazard analysis (PTHA) for mega thrust subduction earthquakes. In: V. Santiago-Fandino, S. Sato, N. Maki and K. Luchi (Editors), *The 2011 Japan Earthquake and Tsunami: Reconstruction and Restoration*. Springer Publishing Company, New York, 469–485.

National Police Agency of Japan, 2020. Police countermeasures and damage situation associated with 2011 Tōhoku district—off the Pacific Ocean earthquake, September 10, 2020: Emergency Disaster Countermeasures Headquarters. Retrieved 18 November 2020.

Nelson, A.R., DuRoss, C.B., Witter, R.C., Kelsey, H.M., Engelhart, S.E., Mahan, S.A., Gray, H.J., Hawkes, A.D., Horton, B.P. and Padgett, J.S., 2021. A maximum rupture model for the central and southern Cascadia subduction zone—reassessing ages for coastal evidence of megathrust earthquakes and tsunamis. *Quaternary Science Reviews*, 261: 106922.

Okada Y., 1985. Surface deformation due to shear and tensile faults in a half-space. *Bulletin Seismological Society of America.* 75(4),1135–1154.

Patton, J.R., Eble, M.C., Kyriakopoulos, C., Lynett, P.J., Nicolsky, D., Ross, S., Ryan, K.J., Thio, H.K. and Wilson, R.I., 2022. U.S. Geological Survey Tsunami Sources Powell Center Working Group: Cascadia Probabilistic Tsunami Hazard Assessment Meeting Summary, AGU Fall Meeting. American Geophysical Union, Chicago, Illinois.

Petersen, M.D., Morgan P. Moschetti, Peter M. Powers, Charles S. Mueller, Kathleen M. Haller, Arthur D. Frankel, Yuehua Zeng, Sanaz Rezaeian, Stephen C. Harmsen, Oliver S. Boyd, Ned Field, Rui Chen, Kenneth S. Rukstales, Nico Luco, Russell L. Wheeler, Robert A. Williams and Olsen, A.H., 2014. Documentation for the 2014 Update of the United States National Seismic Hazard Maps. Open-File Report 2014–1091, 243 pp.

Peterson, M.D., Shumway, A.M., Powers, P.M., Field, E.H., Moschetti, M.P., Jaiswal, K.S., Milner, K.R., Rezaeian, S., Frankel, A.D., Llenos, A.L. and Michael, A.J., 2024. The 2023 US 50-state national seismic hazard model: Overview and implications. Earthquake Spectra, 40(1): 5–88.

Priest, G.R. and Allan, J.C., 2019. Comparison of Oregon tsunami hazard scenarios to a probabilistic tsunami hazard analysis (PTHA). Oregon Department of Geology and Mineral Industries Open-File Report O-19-04, Portland, Oregon, 100 p.

Priest, G.R., Goldfinger, C., Wang, K., Witter, R.C., Zhang, Y., and Baptista, A.M., 2009, Tsunami hazard assessment of the northern Oregon coast: A multi-deterministic approach tested at Cannon Beach, Oregon: Oregon Department of Geology and Mineral Industries Special Paper, 41, 47 p. DOI: 10.13140/RG.2.2.25349.47840

Priest, G.R., Goldfinger, C., Wang, K., Witter, R.C., Zhang, Y. and Baptista, A.M., 2010. Confidence levels for tsunami-inundation limits in northern Oregon inferred from a 10,000-year history of great earthquakes at the Cascadia subduction zone. Natural Hazards, 54(1): 27–73.

Priest, G.R., Witter, R.C., Zhang, Y., Wang, K., Goldfinger, C., Stimely, L.L., English, J.T., Pickner, S.G., Hughes, K.L.B., Willie, T.E. and Smith, R.L., 2013. Tsunami inundation scenarios for Oregon. Oregon Department of Geology and Mineral Industries Open-File-Report O-13-19, Portland, Oregon, 14 p.

Satake, K., 1995. Linear and Nonlinear Computations of the 1992 Nicaragua Earthquake Tsunami. Pure and Applied Geophysics, 144, 455–470.

Scholz, C.H., 2014. Holocene Earthquake History of Cascadia: A Quantitative Test. Bulletin of the Seismological Society of America, 104(4): 5.

Shuto, H., 1991. Historical changes in characteristics of tsunami disasters. Proceedings of the International Symposium IDNDR, JSCE Kansai Chapter, 77–86.

Small, D.T., Melgar, D., La Selle, S. and Meigs, A., 2025. Combining Multisite Tsunami and Deformation Modeling to Constrain Slip Distributions for the 1700 CE Cascadia Earthquake. Bulletin of the Seismological Society of America, 115(2): 431–451.

Staisch, L.M., Witter, R.C., Watt, J.T., Grant, A.R., Walton, M.A., Brothers, D., Davis, E., Dura, C., Engelhart, S., Enkin, R., Garrison-Laney, C.E, Goldfinger, C., Hamilton, T., Hawkes, A., Hill, J.C., Hong, I.J., Jaffe, B.E., Kelsey, H., Lahusen, S.R, La Selle, S.M, Nelson, A.R, Nieminski, N.M, Padgett, J.S, Patton, J., Pearl, J.K, Pilarczyk, J., Sherrod, B., and Stanton, K., 2024, Compiled onshore and offshore paleoseismic data along the Cascadia Subduction zone: U.S. Geological Survey data release, https://doi.org/10.5066/P13OJQYW.

Strasser, F.O., Arango, M.C., and Bommer, J.J., 2010. Scaling of the Source Dimensions of Interface and Intraslab Subduction-zone Earthquakes with Moment Magnitude. Seismological Research Letters, 81(6), 941–950.

Sypus, M. and Wang, K., 2024. Improved Cascadia Earthquake Source Models for Tsunami Hazard Assessment. Oregon Department of Geology and Mineral Industries Open-File Report O-24-11, Portland, Oregon, 64 p.

Thio, H.K., 2017. Probabilistic tsunami hazard maps for the State of California (phase 2). Report by AECOM to the California Geological Survey.

Thio, H.K., 2019. Notes on the production of the 1,000 year probabilistic tsunami hazard maps for the Western United States: report by AECOM to the California Geological Survey, AECOM, 21 p.

Thio, H.K., 2026. Update to the ASCE 7-28 Probabilistic Tsunami Hazard Model for Oregon and Washington: report by AECOM.

Thio, H.K., Somerville, P.G. and Polet, J., 2010. Probabilistic tsunami hazard in California. Pacific Earthquake Engineering Research Center Technical Report 2010/108, 331 p.

Thio, H., Wei, Y., Chock, G. and Li, W., 2017. Development of offshore probabilistic tsunami exceedance amplitudes for ASCE 7-16, Proceedings of the Sixteenth World Conference on Earthquake Engineering.

Wang, K., Wells, R., Mazzotti, S., Hyndman, R.D. and Sagiya, T., 2003. A revised dislocation model of interseismic deformation of the Cascadia subduction zone. Journal of Geophysical Research: Solid Earth, 108(B1).

Wang K., and He, J., 2008. Effects of frictional behaviour and geometry of subduction fault on coseismic seafloor deformation. Bull Seismol Soc Am 98(2):571–579.

Wei, Y., Thio, H., Titov, V., Chock, G., Zhou, H., Tang, L. and Moore, C., 2017. Inundation modeling to Create 2,500-year return period tsunami design zone maps for the ASCE 7-16 standard, Proceedings of the Sixteenth World Conference on Earthquake Engineering.

Wirth, E., Frankel, A., Sherrod, B., Grant, A., Dunham, A., Stone, I. and Grossman, J., 2025. Earthquake probabilities and hazards in the U.S. Pacific Northwest, U.S. Geological Survey Fact Sheet 2025–3050, 6 pp.

Witter, R., Zhang, Y., Wang, K., Priest, G.R., Goldfinger, C., Stimely, L.L., English, J.T. and Ferro, P.A., 2011. Simulating tsunami inundation at Bandon, Coos County, Oregon, using hypothetical Cascadia and Alaska earthquake scenarios. Oregon Department of Geology and Mineral Industries Special Paper 43, Portland, Oregon, 57 p.

Witter, R., Zhang, Y., Wang, K., Priest, G.R., Goldfinger, C., Stimely, L.L., English, J.T. and Ferro, P.A., 2013. Simulated tsunami inundation for a range of Cascadia megathrust earthquake scenarios at Bandon, Oregon, USA. Geosphere, 9(6): 1783–1803.

Xu, Z., 2007. The all-source Green's function and its applications to tsunami problems. Science of Tsunami Hazards, 26(1), 59-69.

Zhang, Y.J. and Baptista, A.M., 2008a. A semi-implicit Eulerian-Lagrangian finite-element model for cross-scale ocean circulation. Ocean Modelling, 21(3-4): 71–96.

Zhang, Y.J. and Baptista, A.M., 2008b. An efficient and robust tsunami model on unstructured grids. Part I: Inundation benchmarks. Pure and Applied Geophysics, 165(11-12): 2229–2248.

Zhang, Y.J., Stanev, E.V. and Grashorn, S., 2016a. Seamless cross-scale modelling with SCHISM. Ocean Modelling, 102: 64–81.

Zhang, Y.J., Priest, G.R., Allan, J.C. and Gabel, L., 2016b. Benchmarking an unstructured-grid model for tsunami current modeling. Pure and Applied Geophysics, 173(12): 4075–4087.

Zhang, Y.J., Witter, R.C. and Priest, G.R., 2011. Tsunami–tide interaction in 1964 Prince William Sound tsunami. Ocean Modelling, 40: 246–259.

9.0 APPENDIX A: REPORT ON BENCHMARK RESULTS FROM SCHISM

Required by: NTHMP Model validation workshop (March 30-April 1, 2011)

Prepared by: Y. Joseph Zhang, Ph.D. (VIMS)

Nov 2024

Team: Virginia Institute of Marine Science and Oregon Department of Geology & Mineral Industries

9.1 Introduction

The state of Oregon is part of the US Pacific Northwest (PNW) region with extensive coastline and vibrant coastal communities. The primary tsunami hazards posed to these communities come from the seismic sources including both local (Cascadia Subduction Zone [CSZ]) and distant sources; tsunamis generated by submarine landslides are presently not considered by DOGAMI but could be evaluated as part of future work. Current funding from NTHMP has enabled us to apply state-of-the-art technology, i.e., new geological and computational models, the latter based on unstructured grids, to remap the entire Oregon coast for both local and remote sources (Priest, 2013). Since the authors focused on seismic tsunamis, the tsunami propagation and inundation model (SELFE) was carefully benchmarked for this purpose (NTHMP, 2012; Horillo and others, 2014).

The author has been working in partnership with DOGAMI in the preparation and dissemination of inundation maps since the 1990s, first under Oregon Senate Bill379, when the author (Zhang) was with OHSU, and then later after the author moved to Virginia Institute of Marine Science (VIMS). In 2011, the original model (SELFE) was benchmarked and approved by NTHMP via an NTHMP sponsored tsunami benchmarking workshop. Since then, the model has been renamed SCHISM due to license issues and has also been improved. Although SCHISM has not been formally benchmarked for inundation, SCHISM was evaluated as part of the NTHMP tsunami currents benchmarking workshop held in Portland, Oregon in 2015 and successfully passed those tests (Zhang and others, 2016; Lynett and others, 2017). Since then, SCHISM has been used by the State of Oregon to simulate tsunami inundation in select Oregon ports and harbors for the purposes of developing maritime guidance (e.g., Allan and others, 2018, 2020, 2024). Of note, these studies evaluated the interaction of fluctuating (dynamic) tides, river discharge, tsunami and variable bottom friction in order to simulate conditions that are probably closer to reality. The model was also used to remap tsunami inundation in two Oregon coast counties in order to correct for errors identified in the source DEMs (Allan and others, 2021).

This report documents the re-benchmark results using SCHISM. Since the inundation scheme of SCHISM is the same as in SELFE, and other parts of the model have been improved, it's not surprising that similar (or better) results are obtained with SCHISM, as shown below. Nevertheless, there are differences and these are not unexpected since the author is not using the exact same unstructured grids as was used originally when benchmarking SELFE, because most of those files have been lost due to disk failure.

9.2 Model Description

The fault dislocation model the authors use for the CSZ earthquakes is based on Okada's point source model but with extensive geophysical constraints (Priest and others, 2009; Witter and others, 2011). In modeling Oregon Coast tsunami inundation, Witter and others (2011) developed 15 megathrust rupture models for Cascadia subduction zone earthquakes that define vertical seafloor deformation used to

simulate tsunami inundation. All the rupture models reflected full-margin scenarios, where the entire 1,000 km long (along-strike) megathrust is considered to fail. The types of rupture models (down-dip) considered included slip partitioned to a splay fault in the accretionary wedge and models that varied the updip limit of slip on a buried (deep and shallow scenarios) megathrust fault. Coseismic slip was estimated from turbidite paleoseismic records (Goldfinger et al., 2010) and constrained from tsunami simulations at Bradley Lake (Witter et al., 2012). Alternative earthquake source scenarios were evaluated using a logic tree that ranked model performance based on geophysical and geological data. Scenario weights at the branch ends of the logic tree are the products of the weights of the two parameters, earthquake size and fault geometry, and represent the relative confidence that a particular model represents a reasonable rupture scenario based on geological and geophysical data, theoretical models and the judgment of the scientific team (Witter and others, 2011). The basal (and most important) branch of the logic tree, estimated fault slip from recurrence interval, is based on the frequency of turbidite interevent times over the last 10,000 years. The second branch of the logic tree developed for Oregon considered three rupture geometries that vary the distribution of slip on the updip end of the locked zone: (1) activation of a shallow splay fault in the accretionary wedge; (2) shallow buried rupture that tapers slip to zero at the deformation front; and (3) a deeper buried rupture that tapers slip to zero beneath a sharp break in the slope of the accretionary wedge offshore Washington and northern Oregon.

For remote sources the scientific team limited themselves to the Alaska-Aleutian subduction zone as historically it poses the most severe threat to the Oregon coast. Witter and others (2011) considered two scenarios: the 1964 Great Alaska earthquake and a hypothetical worst-case scenario. The source model for the 1964 event came from Johnson and others (1996) while the source model for the worst-case scenario was originally used in a pilot study at Seaside, Oregon (TPSWG, 2006). Both scenarios involve M_w ~9.2 earthquakes near the eastern end of the Aleutian Islands. Results of simulations for the 1964 tsunami were checked against historical observations of water levels and wave runup along the Oregon coast, allowing verification of the hydrodynamic model (Zhang et al., 2011a).

The worst-case Gulf of Alaska earthquake scenario, identified as "Source 3" in Table 1 of Gonzalez and others (2009), has uniform slip on 12 subfaults with each subfault assigned an individual slip value of 15, 20, 25 or 30 m. These extreme parameters result in maximum seafloor uplift nearly twice as large as uplift produced by the 1964 earthquake estimated by Johnson and others (1996). Analyses of the maximum tsunami amplitude simulated for this source indicate beams of high energy directed toward the Oregon coast compared with other Alaska-Aleutian subduction zone sources (TPSWG, 2006). Because of its precedent use for the Seaside tsunami study by TPSWG (2006), Witter and others (2011) adopted the hypothetical Gulf of Alaska scenario as a maximum distant tsunami source for Oregon. Testing the geological plausibility of this scenario was beyond the scope of this study and remains an option for future probabilistic tsunami hazard analysis work underway for Oregon, Washington and Northern California.

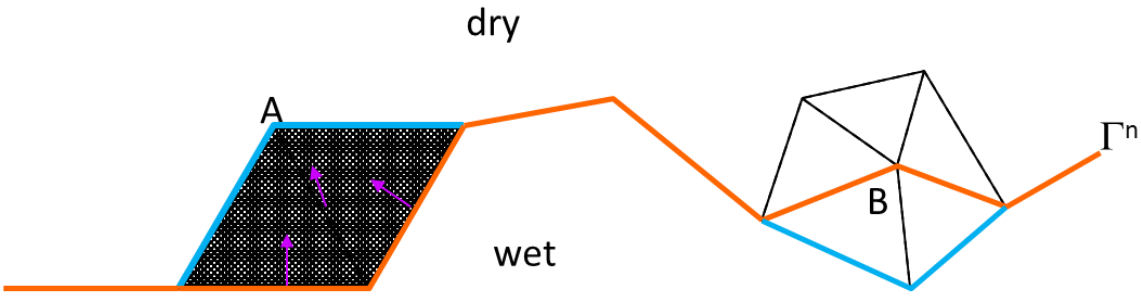
The tsunami propagation and inundation model the author tested in this report is SCHISM (Zhang and Baptista 2008a; Zhang and others, 2016), which was envisioned at its inception to be an open-source community-supported 3D hydrodynamic/hydraulic model. This philosophy has been the cornerstone of the model to this day. Originally developed as SELFE to address the challenging 3D baroclinic circulation in the Columba River estuary, it has since been adopted by 400+ groups around the world and evolved into a major modeling system encompassing such physical/biological processes as general circulation (Burla et al., 2010), tsunami- and hurricane-induced compound flooding (Ye and others, 2020), ecology and water quality (Rodrigues and others, 2009a, b), sediment transport (Pinto and others, 2011), wave-current interaction (Roland and others, 2011), and oil spill (Azvedo and others, 2009). Currently, the author maintains a central website dedicated to this model, a user mailing list, and mail archive system,

and also have organized annual user group meetings since 2004 and conducted several online and in-person training courses for users.

The rapid growth of the SELFE/SCHISM user community owes a great deal to the numerical scheme used, which combines numerical accuracy with efficiency and robustness; the last two model traits are indispensable for large-scale practical applications as commonly found in tsunami hazard mitigation studies. The time stepping is done *semi-implicitly* for the momentum and continuity equations, and together with the Eulerian-Lagrangian method (ELM) for the treatment of the advection, the most stringent stability conditions for the shallow-water equations (e.g., CFL) are bypassed. The remaining stability conditions are related to the horizontal viscosity and baroclinic gradient terms, which contribution is insignificant (in the case of tsunami applications, these conditions are absent). The use of unstructured (hybrid triangular-quadrangular) grids in the horizontal dimension further enhances the model efficiency and flexibility due to their superior capability in fitting complex coastal boundary and resolving bathymetric and topographic features as well coastal structures. The vertical grid used in SCHISM (for 3D model) uses a hybridized system called LSC^2, which has been well demonstrated to be superior to either Z- or s-coordinates (Zhang and others, 2016). The model can be configured in multiple ways: 2D or 3D or even partially 2D/3D; Cartesian (i.e., map projection) or spherical (latitude/longitude). In tsunami applications, modelers typically apply the 2D hydrostatic (nondispersive) configuration for maximum efficiency. For seismic tsunamis, the author explicitly models the earthquake stage (i.e., with moving bed) in order to obtain accurate initial acceleration (Zhang and Baptista, 2008b).

The inundation algorithm in SCHISM is the same as in SELFE and uses a simple iterative procedure to capture the moving shoreline as shown in **Figure 9-1**. Because a semi-implicit scheme is used, which enables exceptionally large time step, the iterative procedure allows wetting and drying over multiple layers of elements over a single time step (i.e., with local CFL number >1). This simple procedure has led to accurate and stable results even near the wet/dry front where supercritical flow is not uncommon.

Figure 9-1. Inundation algorithm in SCHISM. The orange line is the shoreline from the previous time step, and the cyan lines are corrections made to obtain the shoreline at the new time step because point A is inundated, and B is dried.



The version used in this study (v5.11.0) does not explicitly model wave breaking effects, and therefore breaking waves are often represented as shock fronts in the model results. This approach is consistent with the conservative approach the author applies in inundation mapping.

Since 2007 all components of the SELFE/SCHISM modeling system have been fully parallelized using domain decomposition and Message Passing Interface (MPI). This has further enhanced efficiency. For example, in the simulation of the impact of 1964 Alaska event on US west coast, Zhang and others (2011a) used a large grid (with 2.9 million nodes and 6 million elements) to resolve 12 major estuaries and rivers

in the PNW. With 256 CPUs on NASA's Pleiades cluster, the 6-hour simulation took only 2.25 hours of wall-clock time. This performance has since been improved by ~10-fold on newer clusters.

9.3 Benchmark Results

As mentioned previously, the author only report here the results for those benchmark problems relevant to seismic sources. A few additional cases are omitted that were originally presented for SELFE benchmarking in Zhang and others (2011b) since they are not required by NTHMP. The benchmark tests re-examined here are fully described in the NTHMP (2012) report and summarized in Horillo and others (2014). Following the procedures described in NTHMP (2012) and in the NTHMP MMS guidance on model benchmarking, the author evaluated five main tests adopted by NTHMP modeling participants. These included the following:

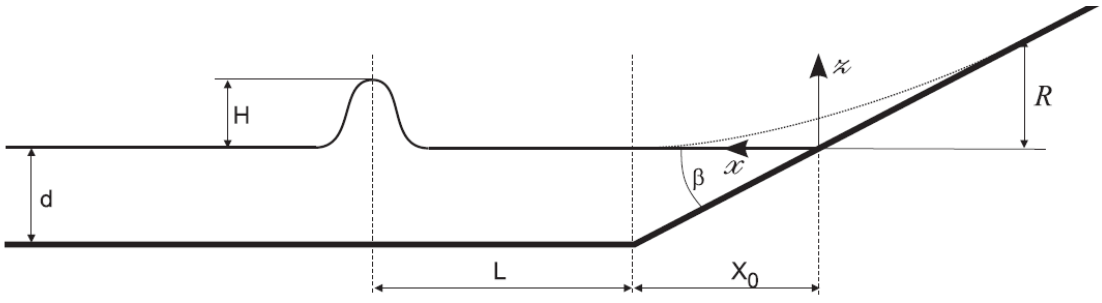
- BP1: single wave on a simple beach
- BP4: solitary wave on a simple beach
- BP6: solitary wave on a conical island
- BP7: for tsunami runup onto a complex 3-dimensional beach at Monai Valley in lab scale
- BP9: Okushiri Island Tsunami

In addition to the four NTHMP tests, the author also simulated BP2 (analytical solution for solitary wave on a composite beach). More detailed descriptions of the various benchmark tests and allowable errors are fully described in Sections 1.5–1.9 in NTHMP (2012).

9.3.1 BP1: Solitary Wave on Simple Beach – Analytical Solution

This canonical problem deals with a single solitary wave propagating along a constant depth and then over a sloping beach (**Figure 9-2**). The problem is completely defined by 3 parameters: d (offshore depth), β (beach slope) and H (height of the solitary wave over constant depth), and all variables are nondimensional with respect to d. The goal is to validate the model for both propagation and inundation on the beach.

Figure 9-2. Domain sketch for BP1.



For convenience, the author chose d = 9.81 m in the model simulations. The model grid covers $-98\,m \le x \le 686.7m$, with 2-element wide in the y direction. A "uniform" grid with $\Delta x = \Delta y = 0.1*d$ was used with each square divided into 2 triangular elements, and therefore there are altogether 2403 nodes in the grid. The time step was set at Δt = 0.05 s, and the implicitness factor (in the implicit scheme) at 0.6 (the maximum runup is somewhat sensitive to this factor; as explained in Zhang and Baptista (2008b),

the best accuracy is achieved near 0.5). On the left boundary a Flather type open boundary condition was imposed to minimize reflection there. The author used frictionless bottom and nonlinear shallow-water equation (SWE) to be consistent with the assumptions made in the analytical solution.

The comparisons were made in several ways. First the surface profiles at multiple times are compared in **Figure 9-3**. The model can accurately simulate the entire runup and run-down process, and the performance is similar to SELFE (**Table 9-1**).

Figure 9-3. Comparison of surface profiles at various times for the non-breaking wave, case A (H/d = 0.0185) of BP1. All variables are nondimensional. The RMSE at t = 60 (near the maximum runup) is 0.001 and the Willmott skill is 0.998 (we have restricted the calculation of errors to x<2 to remove the uninteresting part of the solution offshore).

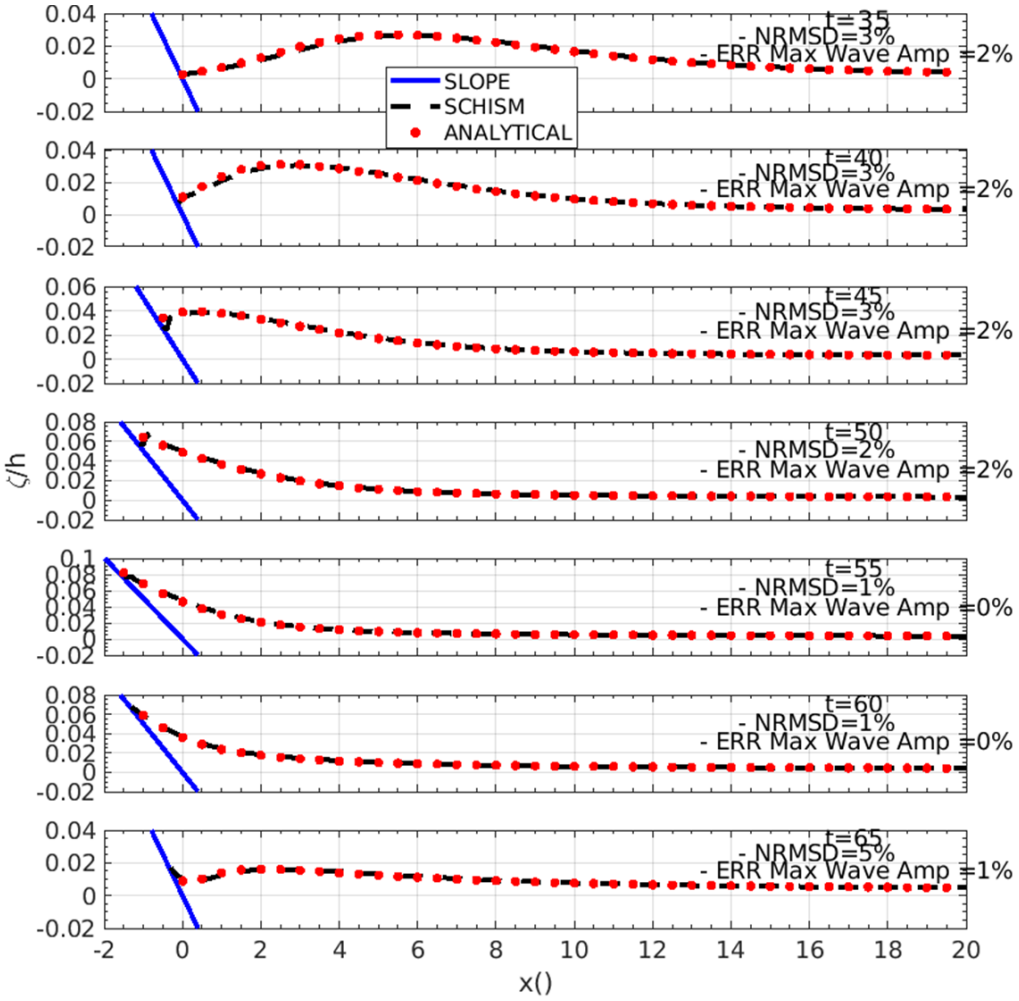


Table 9-1. BP1 model errors for surface profiles at t = [35, 40, 45, 50, 55, 60, 65], with respect to the analytical solution for H/d = 0.0185, as simulated by SELFE and SCHISM. "RMS" is the RMSE normalized by the data range; "Max" refers to the % error at the maximum runup.

Model	t = 35 RMS %	t = 35 Max %	t = 40 RMS %	t = 40 Max %	t = 45 RMS %	t = 45 Max %	t = 50 RMS %	t = 50 Max %	t = 55 RMS %	t = 55 Max %	t = 60 RMS %	t = 60 Max %	t = 65 RMS %	t = 65 Max %	Mean RMS %	Mean Max %
SELFE	3	4	3	4	2	3	1	2	1	0	1	0	5	1	2	2
SCHISM	3	2	3	2	3	2	2	2	1	0	1	0	5	1	3	1

In addition to the conventional root-mean-square error (RMSE) the author also used the Willmott skill number which is defined as (Willmott et al. 1985):

$$W = 1 - \frac{\sum(m-o)^2}{\sum[|m-\bar{o}| + |o-\bar{o}|]^2} \quad (1)$$

where m and o are model and data respectively and $\bar{o}$ is the data mean. This number combines the contributions from both RMSE and the correlation; a Wilmot number of 1 indicates perfect skill and the model is more skilled with a higher W.

Secondly, the time series at two stations were compared (**Figure 9-4**). Note that at one station (x = 0.25) wetting and drying occurred as indicated in both the model results and the analytical solution. Again, the model skill is high in this aspect (**Table 9-2**).

Figure 9-4. Comparison of elevation time series at two locations for BP1. The RMSEs at the two stations are 0.001 and 0.0008, and the Willmott skills are 0.995 and 0.999, respectively.

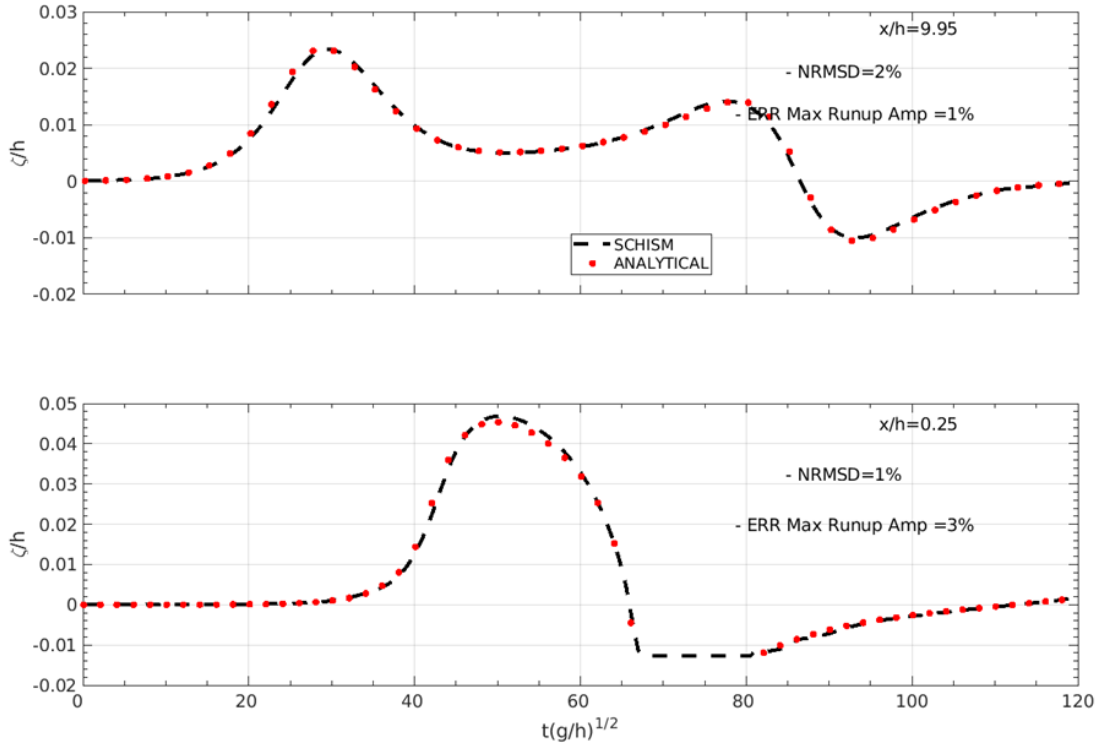
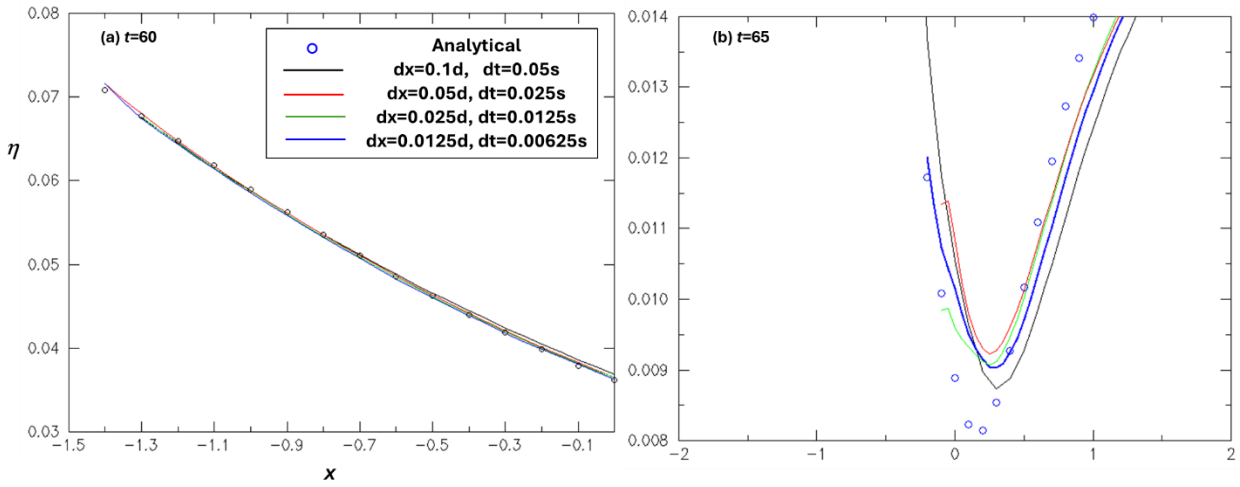


Table 9-2. BP1 model errors at two stations (x = 9.95 and x = 0.25) with respect to the analytical solution for H/d = 0.0185, as simulated by SELFE and SCHISM. "RMS" is the RMSE normalized by the data range; "Max" refers to the % error at the maximum runup.

Model	x = 9.95 RMS %	x = 9.95 Max %	x = 0.25 RMS %	x = 0.25 Max %	Mean RMS %	Mean Max %
SELFE	2	2	1	1	2	2
SCHISM	2	1	1	3	2	2

The convergence of the model is illustrated by using successively finer grid size and time step; the grid size and time step were varied in such a way that the CFL number remains constant as required by the model (Zhang and Baptista, 2008a). As shown in **Figure 9-5a**, the modeled maximum runup indeed converges to the analytical value; at the finest resolution the error for the runup value is 1%. The convergence for the rundown is less good (**Figure 9-5b**), with the error for the t = 65 of 10% at the finest resolution (at the request and help from a reviewer, the author managed to recover the analytical data at the maximum rundown at t = 70, and the maximum rundown error is 6.6%).

Figure 9-5. Convergence test for case A of BP1 at a time near (a) the maximum runup (t = 60); (b) rundown (t = 65).

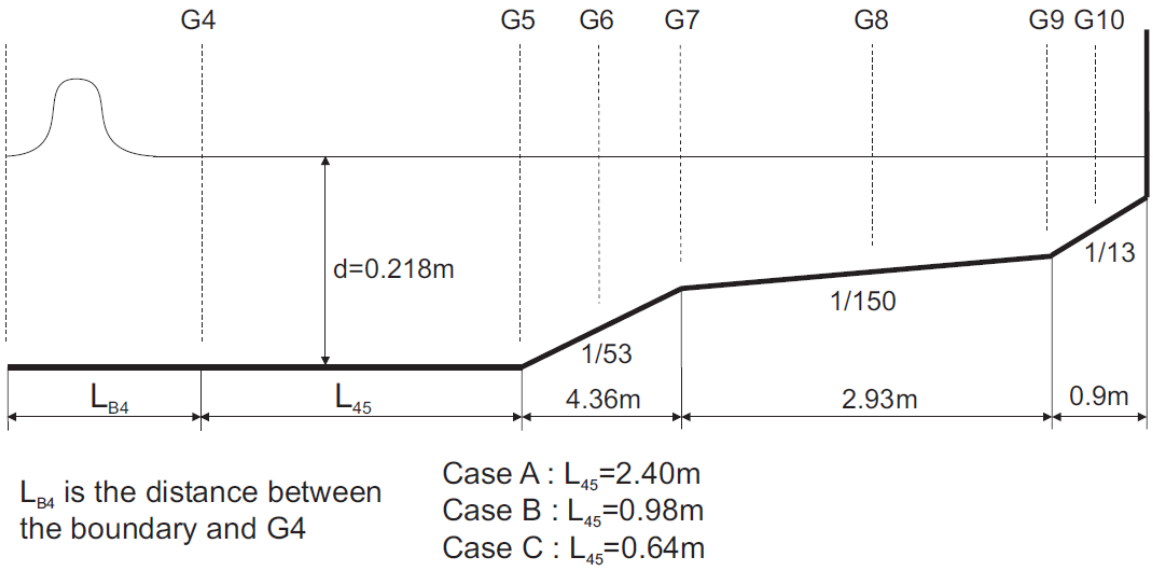


Due to the small grid size used in this benchmark problem, the CPU time is modest. For example, the 120–time-unit run shown in **Figure 9-4** took less than 1 min of wall-clock time to complete with 1 CPU (all tests shown in this report, unless otherwise noted, were conducted on an Intel Gold 6130 cluster with CPU clock speed of 3.0 GHz and gigabit EDR infiniband connection).

9.3.2 BP2: Solitary Wave on Composite Beach – Analytical Solution

This problem was modeled against Revere Beach located approximately 6 miles northeast of Boston in the City of Revere, Massachusetts. A physical model was constructed at the Coastal Engineering Laboratory of the U.S. Army Corps of Engineers, Vicksburg, Mississippi facility. The model beach consists of three piecewise-linear slopes of 1:53, 1:150, and 1:13 from seaward to shoreward with a vertical wall at the shoreline (**Figure 9-6**). In the experiments the wave maker was moved to different locations for each of the 3 cases: A, B, and C. Here the author simply used the measured time series at gauge 4 as the boundary condition for the model. For comparison with the analytical solution, which was derived from the linearized SWE, the author will only consider case A for the reason stated below.

Figure 9-6. Schematics of the composite beach and locations of gauges used in BP2.

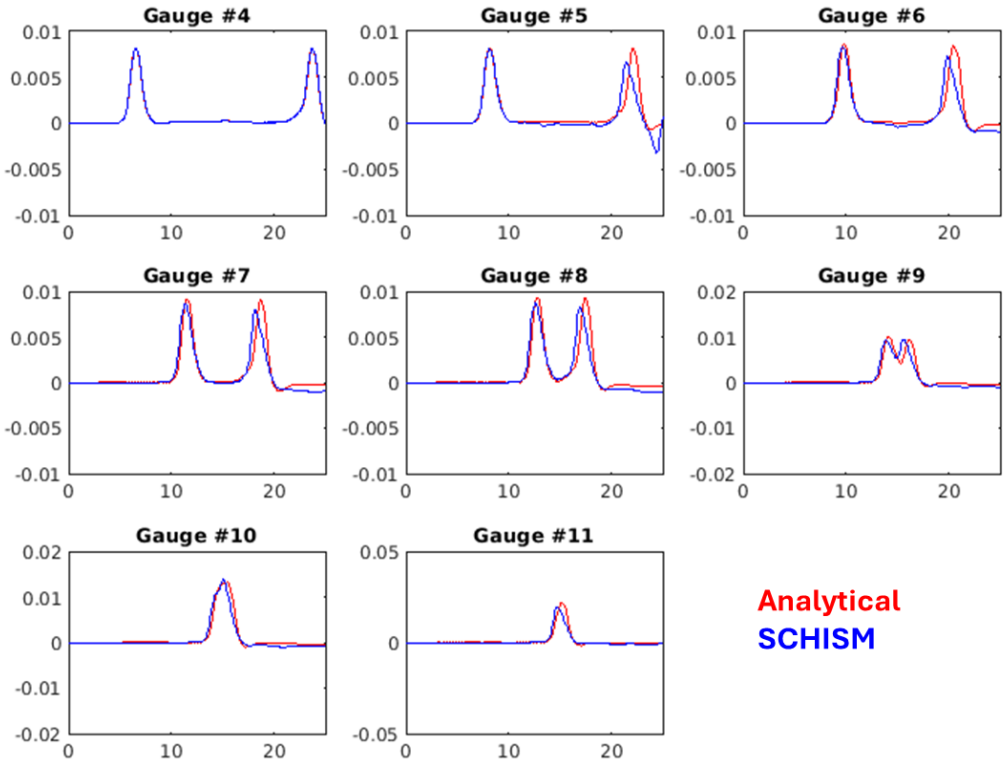


In the model, a rectangular domain with variable grid size (Δy = 2.5mm and Δx varies from 1cm at the left boundary to 1mm at the vertical wall, in order to capture the large runup there) was used to cover $12.64m \leq x \leq 23.23m$ (case A), $14.06m \leq x \leq 23.23m$ (case B) and $14.4m \leq x \leq 23.23m$ (case C). Note that the author did not use dimensionless variables in this test. The time step was set at 0.05s and the total run time was 30s. The grid for case A was the largest with 11115 nodes, and it took 1 min of wall-clock time to complete the 30-s simulation with 2 CPUs.

Figure 9-7 shows the comparison at various gauges along the flume. Good agreement is observed in general. The "errors" in the numerical solution can be partly attributed to the different assumptions used in the analytical and numerical solutions; in SCHISM a strict "linear" solution of the SWE is not possible as the flux term in the integrated continuity equation can only be treated nonlinearly.

For the other two cases (B&C), the amplitude of the incident wave is not small as compared to the water depth, and therefore the analytical solution, which linearizes the SWE around η = 0, is definitely not valid even as a 1st-order approximation of the SWE. Consequently, the author excluded these in this section. Comparison with the lab data will be presented in **Section 9.3.4**.

Figure 9-7. Comparison of elevation time history at 8 stations for case A of BP2. Gauge 4 is located at the domain boundary and serves as a check for the imposed boundary condition; gauge 11 is at the vertical wall, where the RMSE is 1.7mm and the Wilmot skill is 0.95.



9.3.3 BP4: Solitary Wave on Simple Beach – Lab Experiments

The description of the problem can be found in **Section 9.3.1**. Here the author compares the results for cases A and C, as well as for the runup as a function of the incident wave height. The model parameters are the same as in **Section 9.3.1**, except that non-zero bottom friction based on the Manning formulation was used. **Figure 9-8** shows surface profiles at various times for the non-breaking case A. The model is able to capture the runup and rundown process well. The model performance for the results in **Figure 9-8** is included in Table 3 and is mostly comparable to SELFE.

For wave breaking case C, the SWE is no longer appropriate, and therefore the hydrostatic version of SCHISM initially gave larger errors (**Figure 9-9**). The steepening of the crest as seen in the model results is typical of any hydrostatic model due to lack of energy dissipation. After wave breaking occurs, however, the SWE can reasonably simulate the runup process (last panel of **Figure 9-9**). The modeled maximum runup is also slightly sensitive to the choice of the bottom friction, and a smaller friction leads to a larger runup.

The repeated experiments using different wave heights provided the runups as a function of the wave height, and the comparison is presented in **Figure 9-10**. The experiments indicated that wave breaking initiates when H/d >0.045. The modeled runups are accurate up to this limit and are less accurate beyond it (**Figure 9-10**).

Figure 9-8. Comparison of surface profiles for case A of BP4. The Manning friction coefficient is n0 = 0.016. The error for the maximum elevation at t = 60 (near the maximum runup) is 2%.

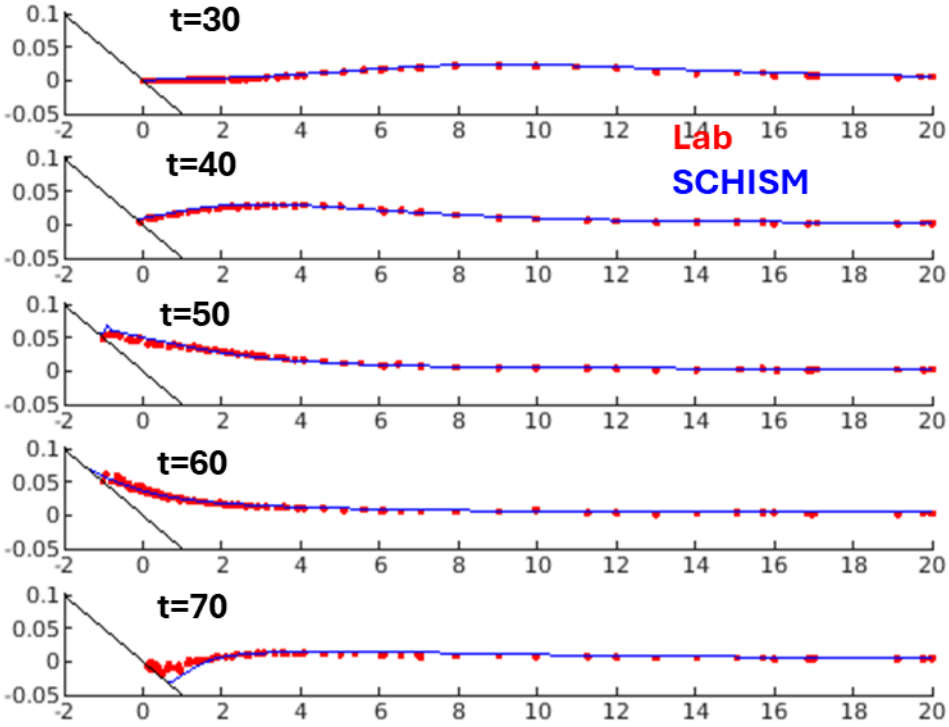


Table 9-3. BP4 model errors with respect to the lab experiment data a) surface profile for Case A, H/d = 0.0185 as simulated by SELFE and SCHISM. "RMS" is the RMSE normalized by the data range. "Max" refers to the error for runup error.

Model	t = 30 RMS %	t = 30 Max %	t = 40 RMS %	t = 40 Max %	t = 50 RMS %	t = 50 Max %	t = 60 RMS %	t = 60 Max %	t = 70 RMS %	t = 70 Max %	Mean RMS %	Mean Max %
SELFE	10	3	9	1	5	3	4	3	14	2	8	2
SCHISM	9	6	8	3	6	12	4	2	14	6	8	6

Figure 9-9. Comparison of surface profiles for breaking-wave case C (H/d = 0.3) of BP4. Model results with two choices of bottom friction are shown.

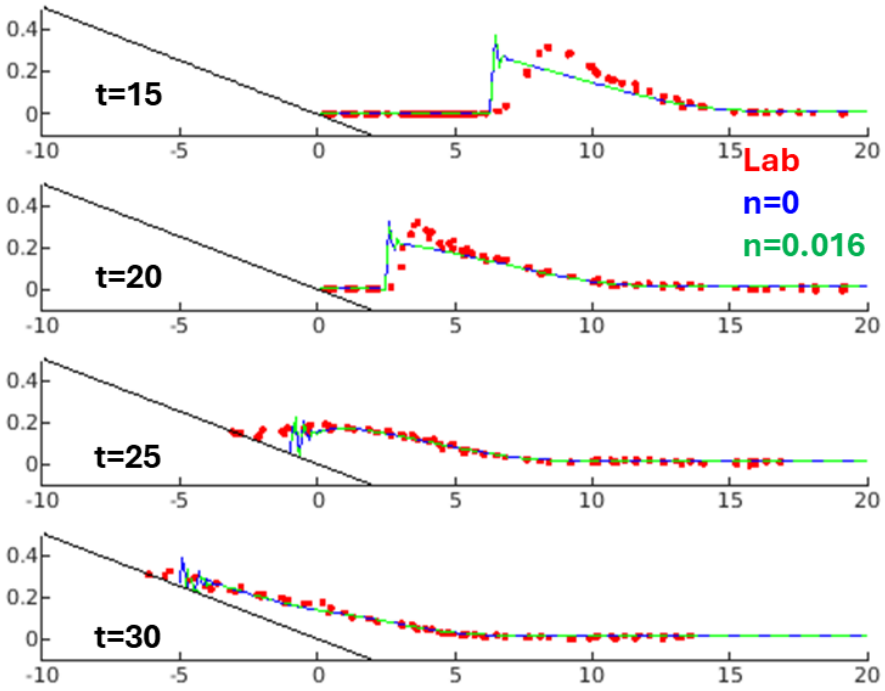
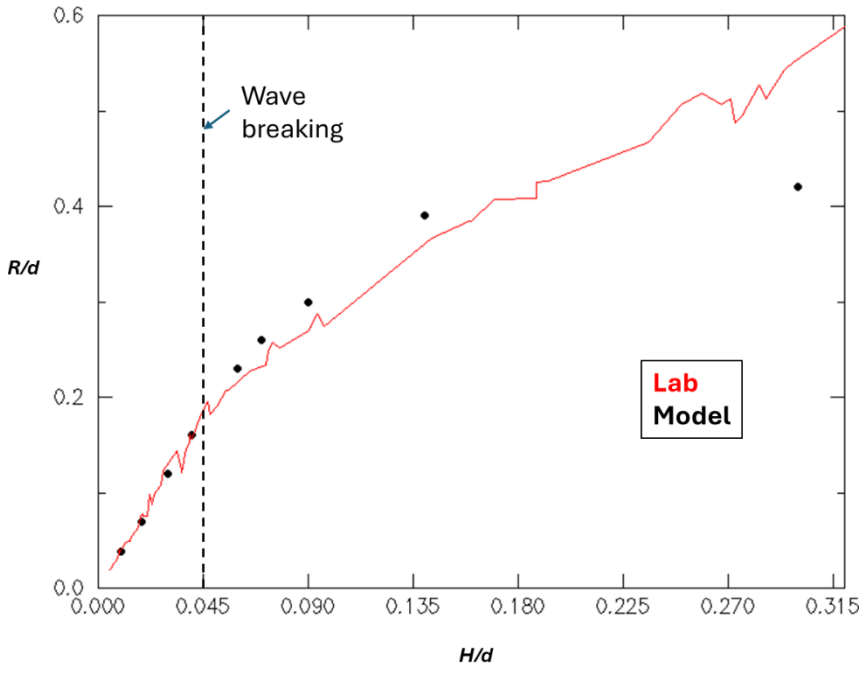


Figure 9-10. Runups as a function of the incident wave height for BP4. The maximum runup error for non-breaking waves is 5%.



9.3.4 BP5: Solitary Wave on Composite Beach – Lab Experiments

The set-up of the experiments has been described in **Section 9.3.2**. The model uses the nonlinear SWE instead of the linear SWE as in **Section 9.3.2**. The author has also explored variation of the Manning coefficient (n_0) but found little sensitivity in the results to this parameter. The results presented below were obtained using $n_0 = 0$.

The elevation time series for all 3 cases (A, B and C) are presented in **Figure 9-11**–**Figure** 9-13. The mismatches in the mean water level at gauge 7 in **Figure 9-11,** etc., suggest a problem in the lab data. In general, the model results compare reasonably well with the lab data, except for the largest wave of case C (**Figure 9-13**).

Furthermore, the modeled runups at the vertical wall are also in reasonable agreement with the data for cases A and C. For case A, the modeled and lab measured runups are 2.5 cm and 2.7 cm, respectively. For case C, they are 24 cm and 27.4 cm, respectively. For case B, the large waves colliding with the wall generated very high splash, which explains the largest runup measured among the 3 cases (45.7 cm). Since the model does not explicitly simulate this process, the modeled runup was substantially lower (19 cm). The runup results from SCHISM are similar to that from SELFE. In all three cases, the model runs were stable with no sign of instability.

Figure 9-11. Comparison of elevation time series for case A (L45 = 2.40 m) of BP5.

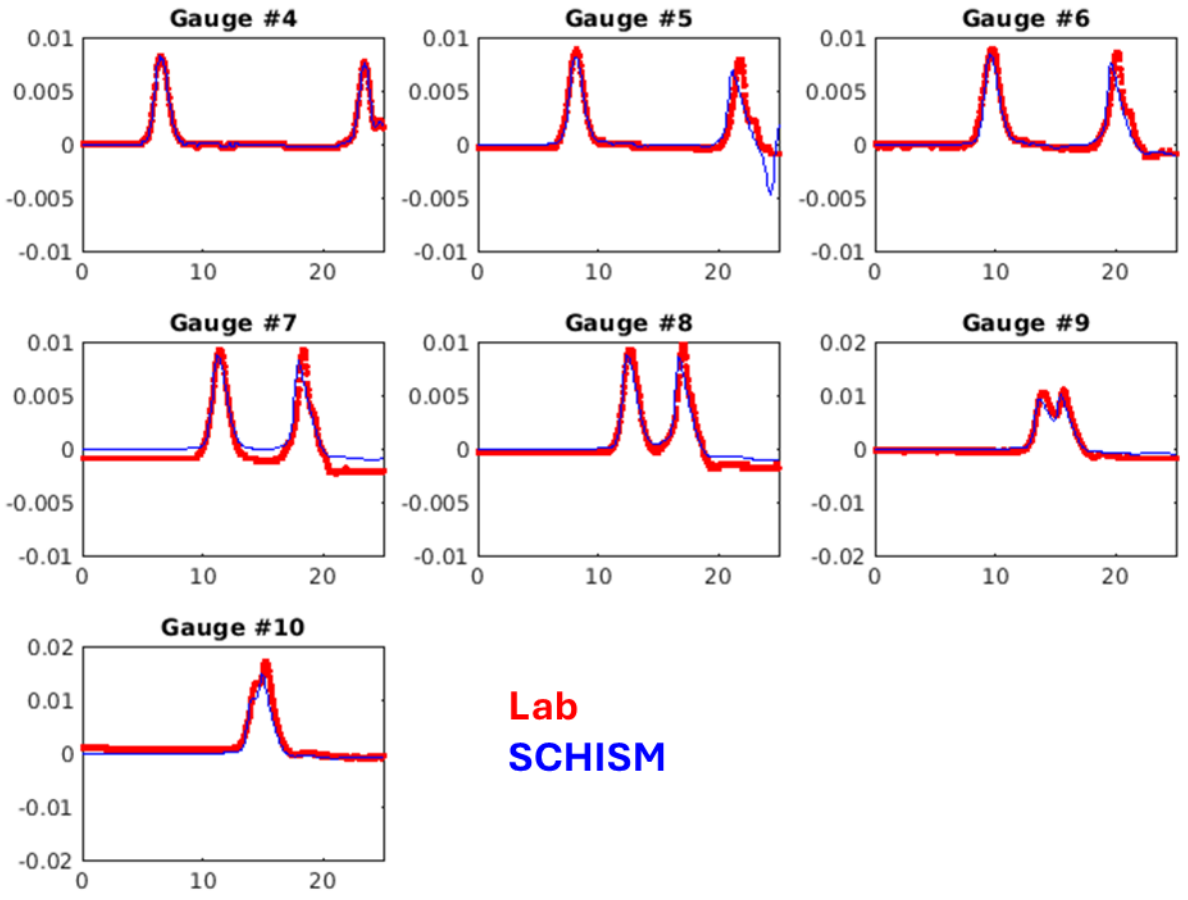


Figure 9-12. Comparison of elevation time series for case B (L45 = 0.98 m) of BP5.

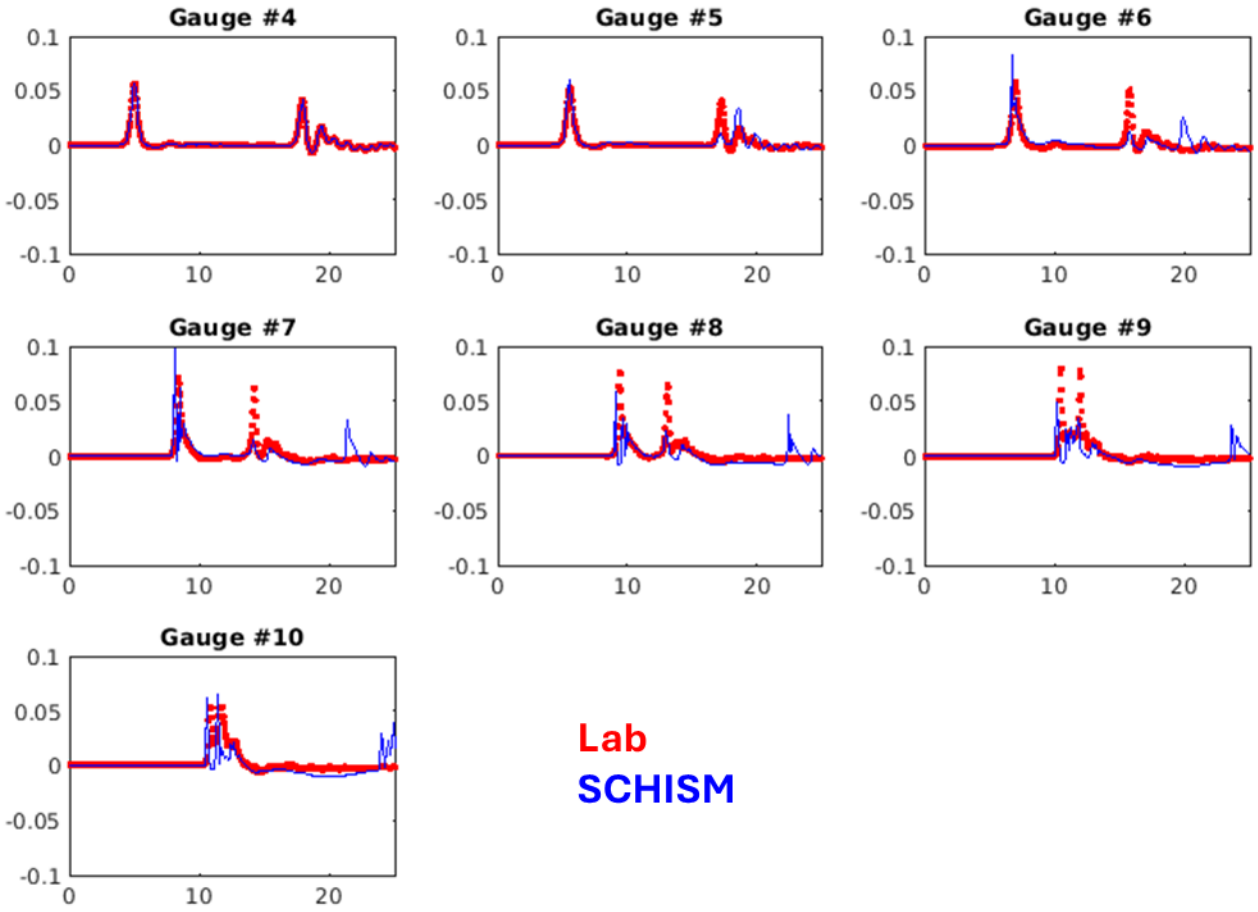
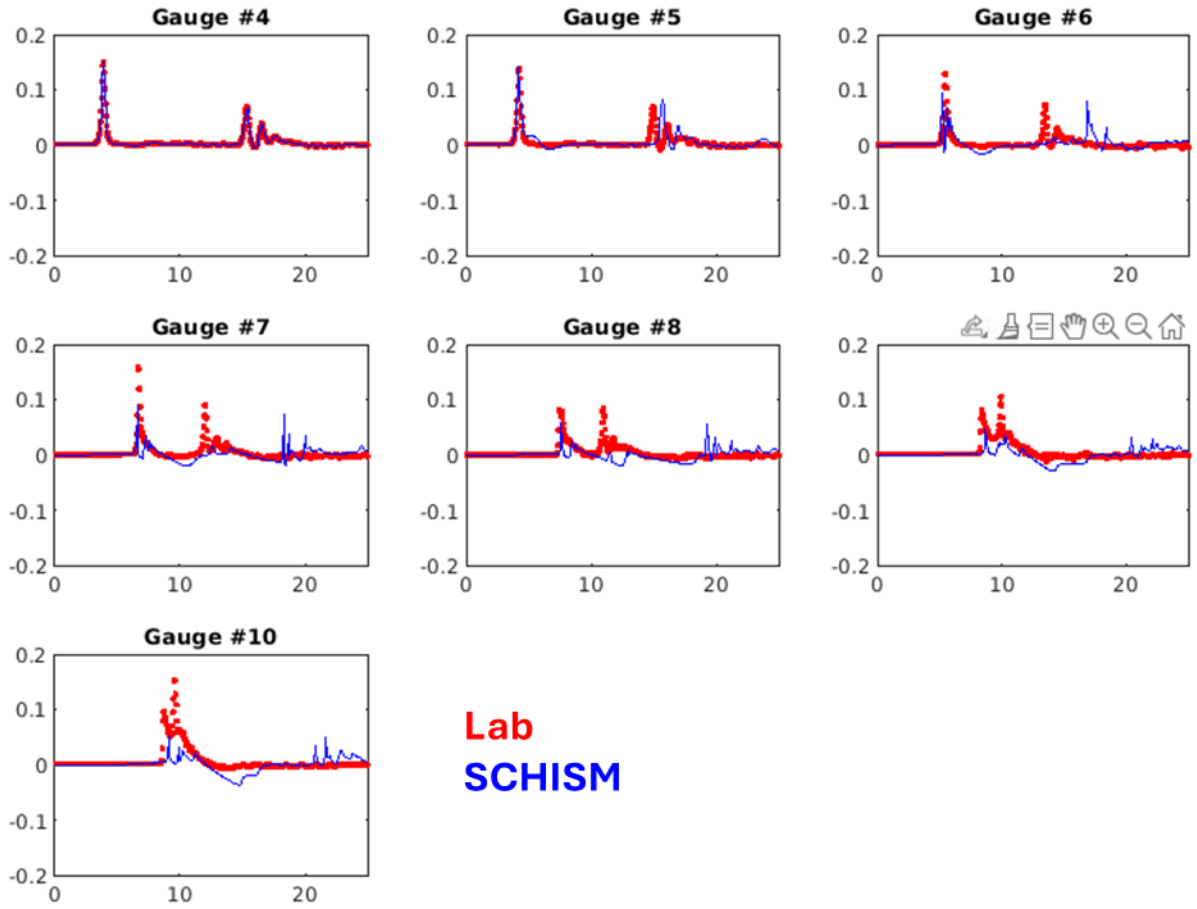


Figure 9-13. Comparison of elevation time series for case C (L45 = 0.64 m) of BP5.



9.3.5 BP6: Solitary Wave on a Conical Island

To examine the model performance in more than one dimension, the experiment of solitary wave around a conical island (**Figure 9-14a**) is simulated numerically here. The lab data includes time series at various gauges in the tank as well as run-up measurements around the perimeter of the conical island.

We did not model the wave maker in the experiment but instead used the time series at a gauge close to the wave maker as the boundary condition. An unstructured grid was generated for this problem to better resolve the downwave side of the island where large runups due to collision of two waves were expected. A 10 cm grid size was used at the outer tank boundaries, 1cm at the boundary of the flat top of the cone (which has a diameter of 2.2 m), and 5 cm in the upwave half of the circle that defines the toe of the conical island, and 2 cm for the downwave half (**Figure 9-15**). The total number of the nodes was 256494 for case A (the largest grid). The time step was set at 0.02 s, and the Manning's coefficient n_0 = 0.01. The total simulation time was 60 s, which took 4 min of wall-clock time on 32 CPUs.

Figure 9-14 shows the comparison of elevation time series at 4 gauges (#6, #9, #16, and #22) for 3 cases (H = 0.045, H = 0.096, H = 0.181), with progressively larger incident wave amplitude. The modeled elevations are in good agreement with the lab data, and the model was stable for all cases. A summary of error statistics is shown in **Table 9-4**.

Figure 9-14. Comparison of elevation time series at 4 gauges for 3 cases of BP6. (a) shows the experimental setup.

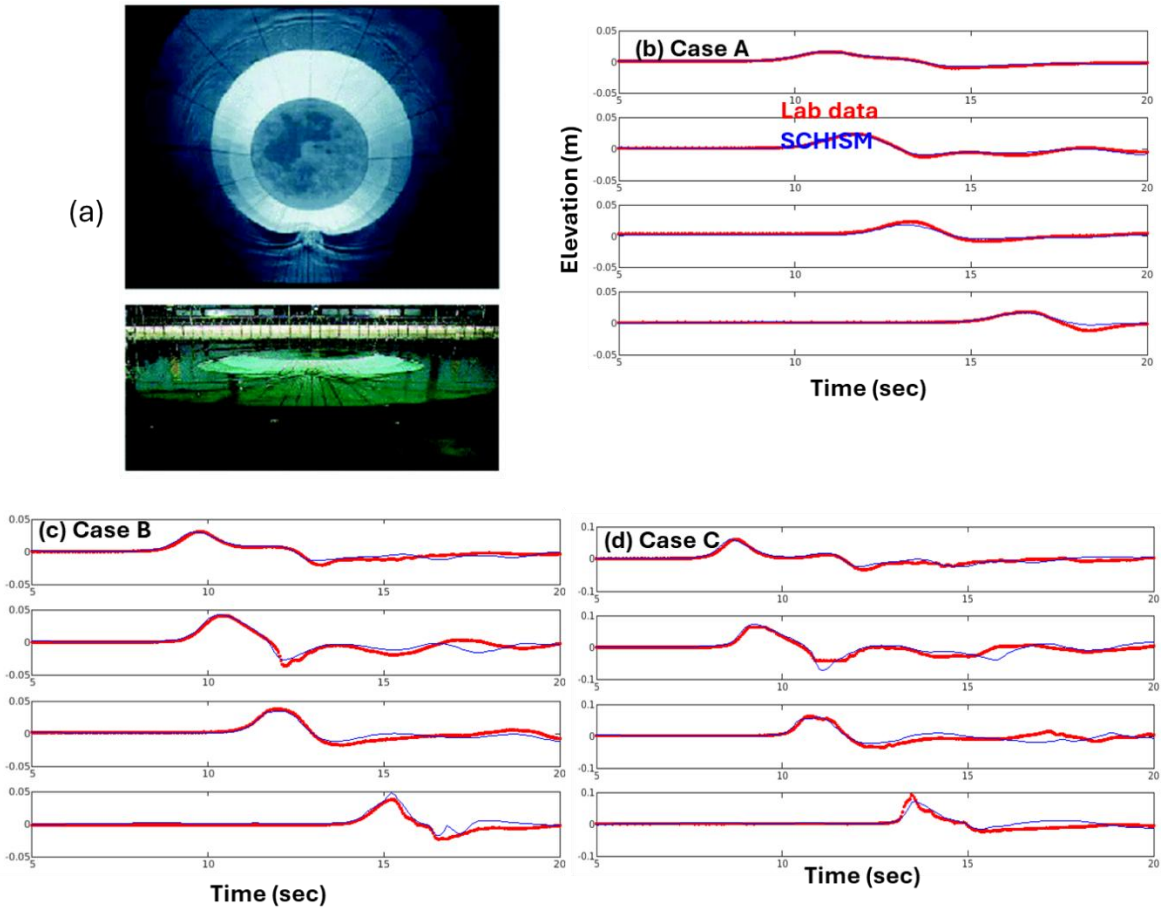


Figure 9-15. Nodes in the unstructured grid used in BP6.

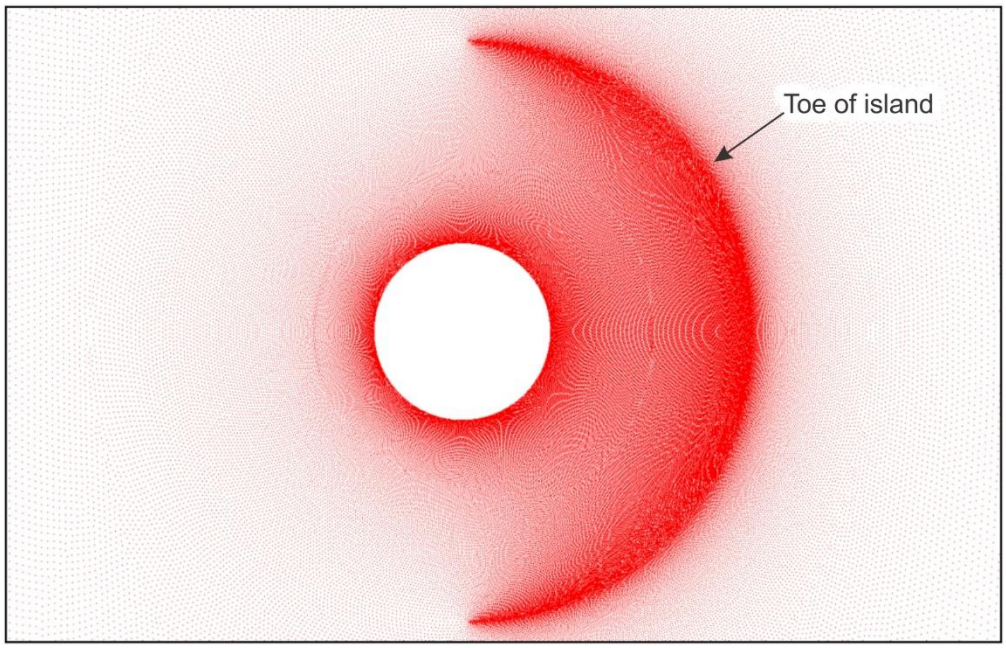


Table 9-4. Error statistics for the 3 cases of BP6. RMS is the RMSE normalized by the data range; MAX is the relative error for the maximum runup.

Case Studies and Model	Gauge 6 RMS %	Gauge 6 Max %	Gauge 9 RMS %	Gauge 9 Max %	Gauge 16 RMS %	Gauge 16 Max %	Gauge 22 RMS %	Gauge 22 Max %	Mean RMS %	Mean Max %
Case A SELFE	6	2	5	4	8	18	8	7	7	8
Case A SCHISM	5	3	5	1	8	19	8	9	7	8
Case B SELFE	6	1	7	3	7	10	9	28	7	11
Case B SCHISM	6	0	7	4	7	9	9	27	7	10
Case C SELFE	6	3	12	13	8	5	8	22	9	11
Case C SCHISM	6	2	10	15	11	3	8	21	9	10

The modeled runup distribution around the island is compared to the measured values in **Figure 9-16**, while **Figure 9-17** is a spatial representation of the same information as in **Figure 9-16**. The agreement is good for cases A and B; the maximum errors were below 6%. For case C, both lab data and model results exhibit a slight asymmetry (**Figure 9-17**) and the model has an underestimation of the maximum runup at the back of the island. The wave breaking that occurred in this case cannot be accurately modeled by SCHISM, but the error still falls below the 20% allowable error specified in Table 1-5 (NTHMP, 2012). Comparison of error statistics against SELFE is shown in **Table 9-5**.

Figure 9-16. Comparison of runups around the conical island for the 3 cases of BP6.

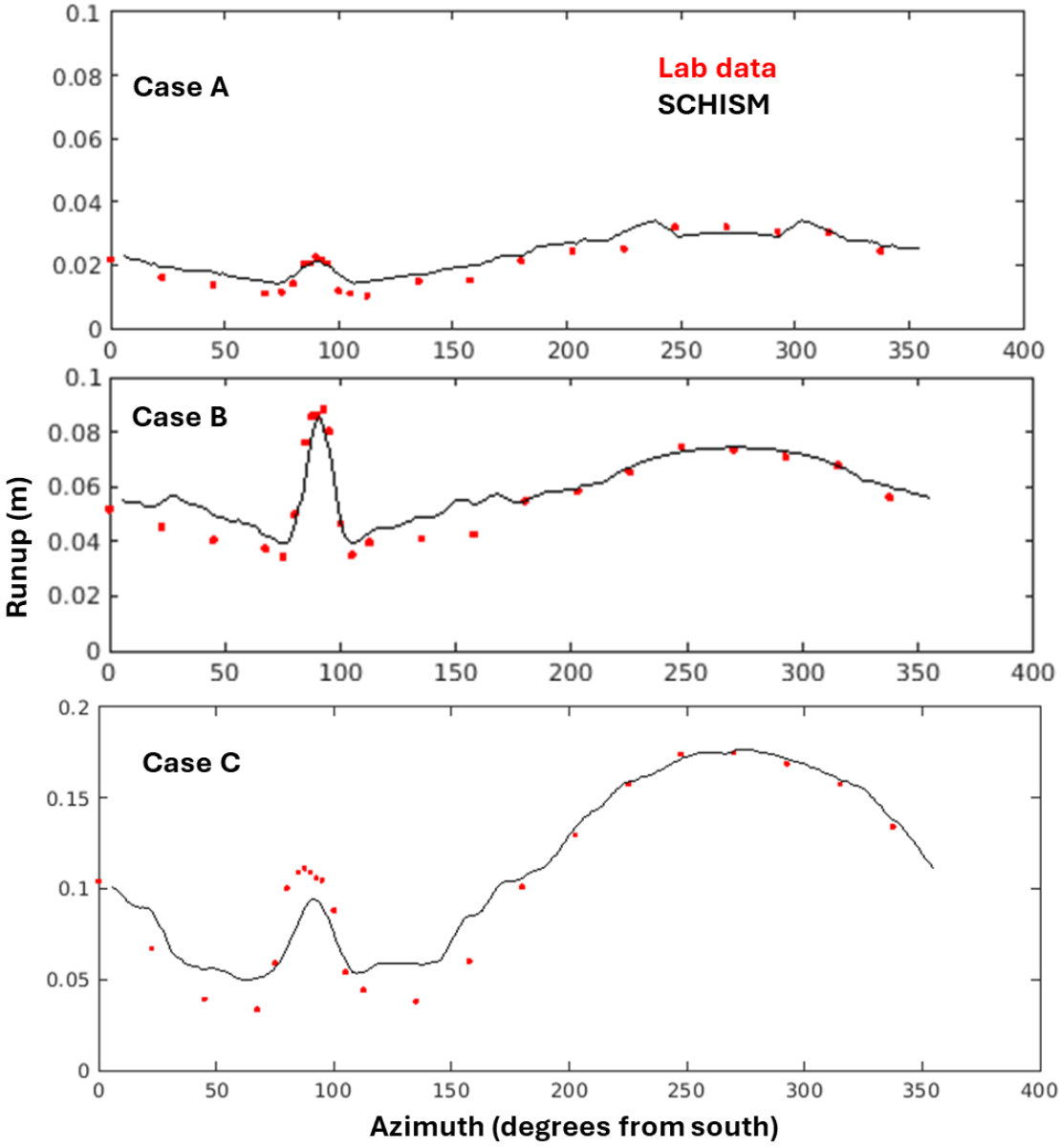


Figure 9-17. Comparison of runups around the conical island for the 3 cases of BP6, in spatial form.

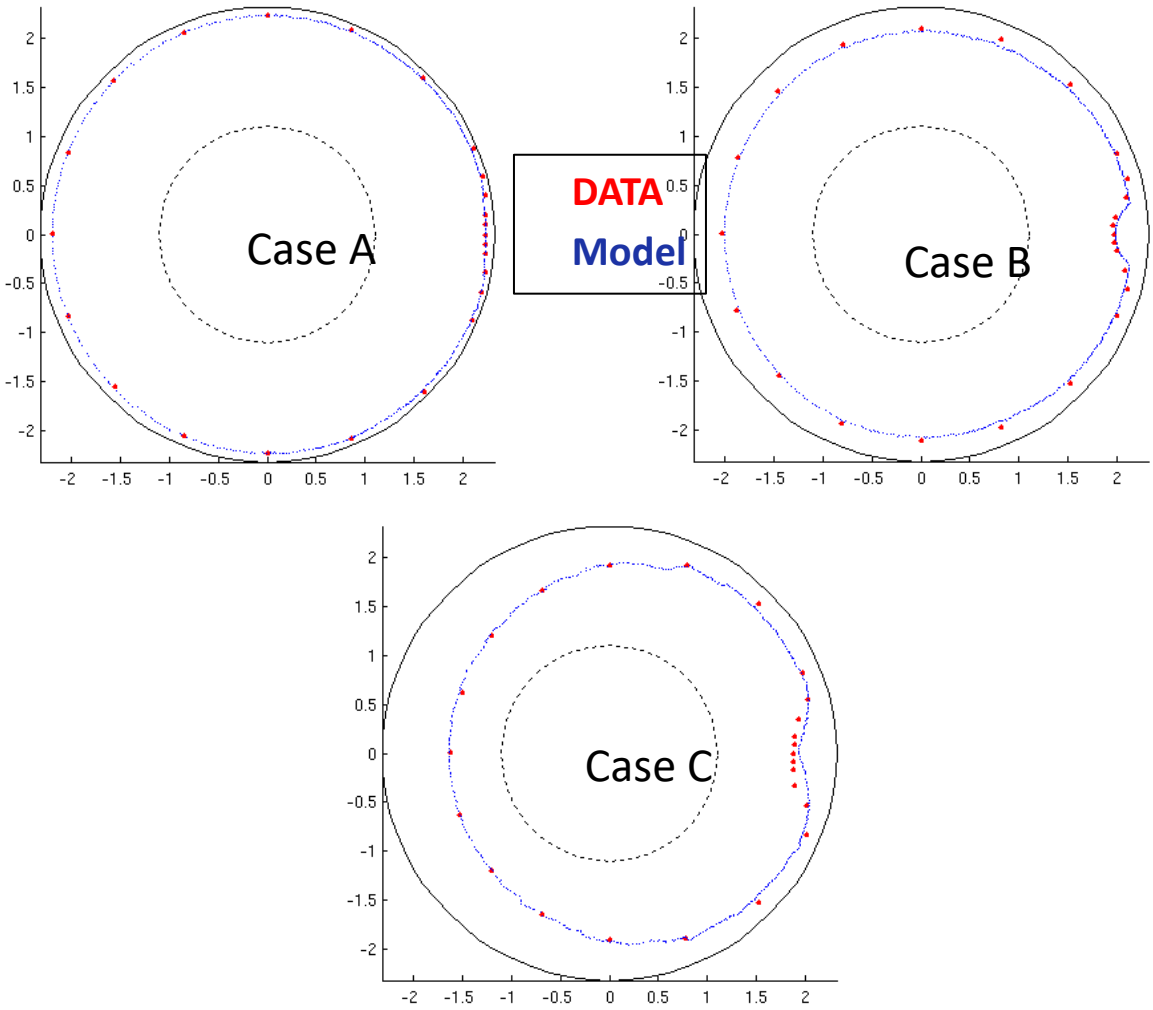


Table 9-5. Error statistics for runups for the 3 cases of BP6. RMS is the RMSE normalized by the data range; MAX is the relative error for the maximum.

Model	Case A RMS %	Case A Max %	Case B RMS %	Case B Max %	Case C RMS %	Case C Max %	Mean RMS %	Mean Max %
SELFE	14	4	11	4	10	2	12	3
SCHISM	13	3	10	4	10	0	11	2

9.3.6 BP7: Wave Runup on Monai Valley

This test considers the wave tank experiment that models the 1993 Okushiri Island tsunami. The lab data includes time series at 3 gauges (**Figure 9-18a**) as well as video images that illustrate the runup sequence in a narrow valley near Monai.

The model used a uniform grid resolution of 1.4 cm and a time step of 0.01 s. Therefore, there were altogether 95892 nodes in the grid. The author has tested the sensitivity to Manning's n_0 and found little influence from this parameter. The results below were obtained using n_0 = 0. The total simulation time was 22.5s, which took 1 min of wall-clock time with 20 CPUs.

The comparison of time series at the 3 gauges in front of the valley is shown in **Figure 9-18**. The model was able to capture the arrival time and the amplitude of the first waves well. The inundation sequence in the narrow valley is shown in **Figure 9-19**, which agrees qualitatively with the lab observation: the modeled maximum runup of 10 cm matches the observed mean value of 10 cm (and therefore the maximum runup error is 0%).

Figure 9-18. Comparison of elevations at 3 gauges in front of the valley as shown in (a), from BP7. RMSEs for the 3 gauges are 4.2, 3.8 and 4.6 mm, respectively.

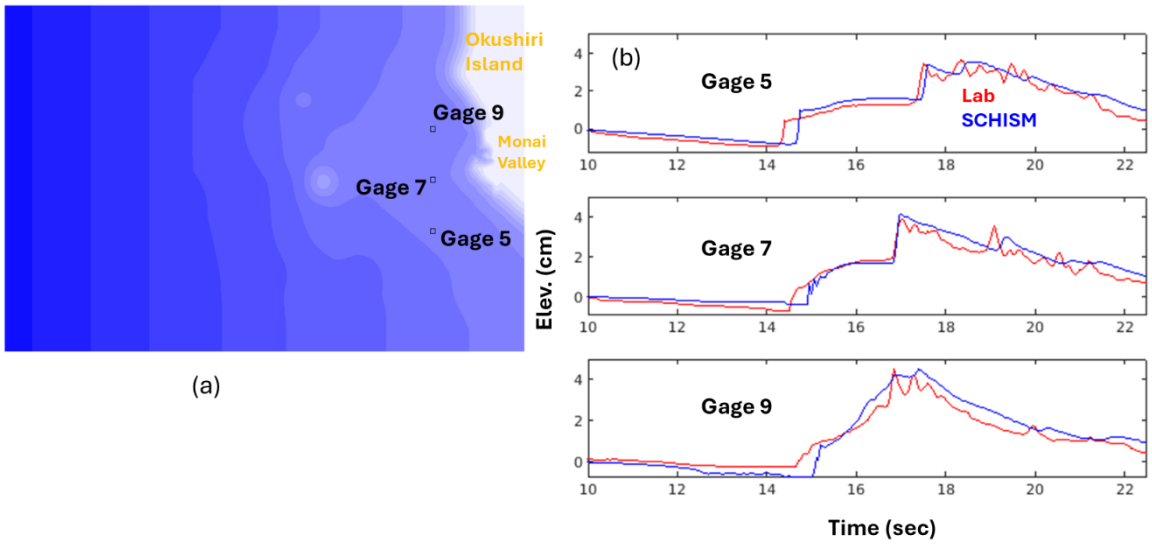
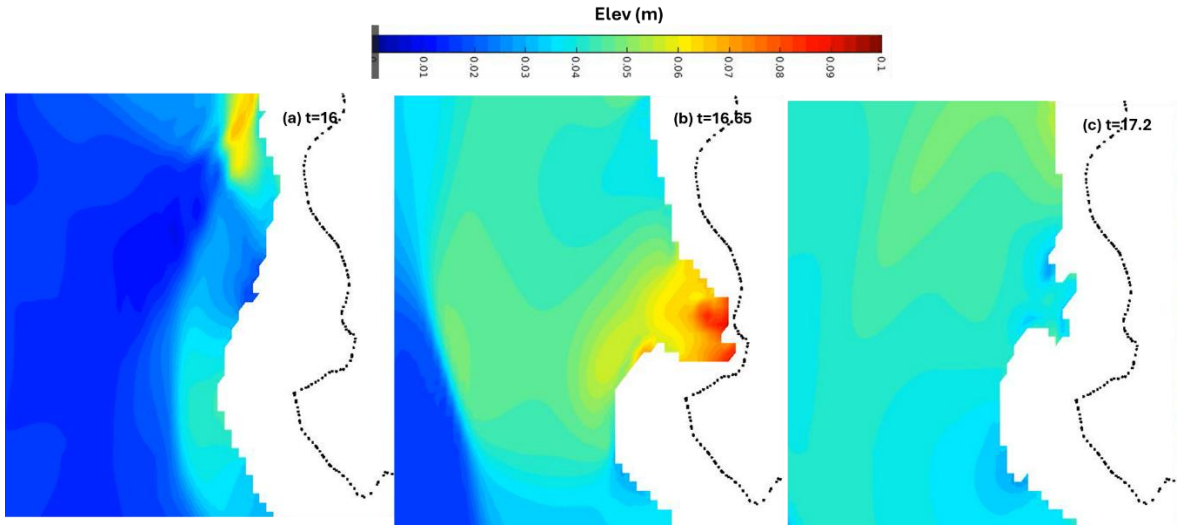


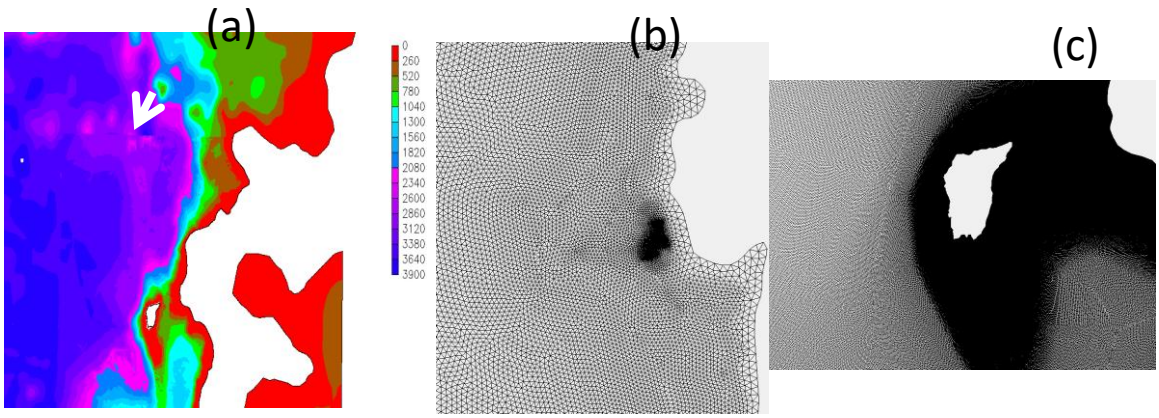
Figure 9-19. Inundation sequence near the narrow valley in BP7; t = 16.65 is close to the maximum runup, which is ~10 cm. Dash line represents 11cm isobath.



9.3.7 BP9: Field – Okushiri Island

The first field test conducted was the simulation of the 1993 Hokkaido-Nansei-Oki tsunami that impacted the Japanese island of Okushiri. The historical data were originally collected by the post-tsunami survey group and passed onto the author by Dr. Tomo Takahashi; they include the pre- and post-event bathymetry survey data, the estimated source information, tide gauge records at 2 gauges, and estimated runup distribution around the island. However, the horizontal datum used in the files was later found to contain errors when overlaid with modern maps. The files used in this study were corrected by Dr. Dmitry Nicolsky (University of Alaska Fairbanks). As shown in **Figure 9-20a**, there still appear to be mismatches (offset, indicated by the white arrow) among various files that define the DEMs.

Figure 9-20. (A) Bathymetry as embedded in DEMs used in BP9; (B) unstructured grid and (C) zoom-in around Okushiri Island. The white arrow in (A) indicates a mismatch of bathymetry from multiple DEM sources.



To better capture the runup distribution around the island, the author used variable resolution around the island, with 30 m resolution at the shoreline, and ~5 m around the narrow Tsuji Valley where the maximum runup (~31 m) was observed (**Figure 9-20**). At the outer ocean boundary, the author used a coarse resolution of 7 km. The total number of nodes in the grid was 2,544,177 with over 95% spent around the island. Note that the original grid used by SELFE was lost, and the author had to re-create the grid here for SCHISM. A time step of 0.5 s was used to carry out the 1-hour simulation, which took 20 min on 320 CPUs.

The comparison at the two tide gauges is shown in **Figure 9-21**. While the modeled arrival time approximately matched the gauge record at Esashi, it was too early at Iwanai, suggesting errors in the source information; note that a similar mismatch was also observed by Kato and Tsuji (1994).

On the other hand, the agreement between the model and data for the distribution of the runups around the island was much more reasonable (**Figure 9-22**, **Table 9-6**). Note that the data were digitized from a figure in Kato and Tsuji (1994) and therefore the precise locations of observation were unknown. Nevertheless, the model seemed to have captured well the variation along the west, north and south coast, with large errors along the east coast (**Figure 9-22**, **Table 9-6**), where the errors in the source information may be more pronounced. The model adequately simulated the large runups around the Tsuji Valley (with 20% error) on the west coast, and around Aonae-Hamatsumae on the south coast. The two waves reported in various post-tsunami surveys as arriving ~10min apart devastated the town of Aonae; these were correctly simulated by the model (**Figure 9-23**). Overall, the SCHISM modeling indicates slight improvements, when compared with the SELFE model runup elevations. The author believes the difference is most likely due to the different grids used.

Figure 9-21. Comparison of elevations at 2 tide gauges in BP9.

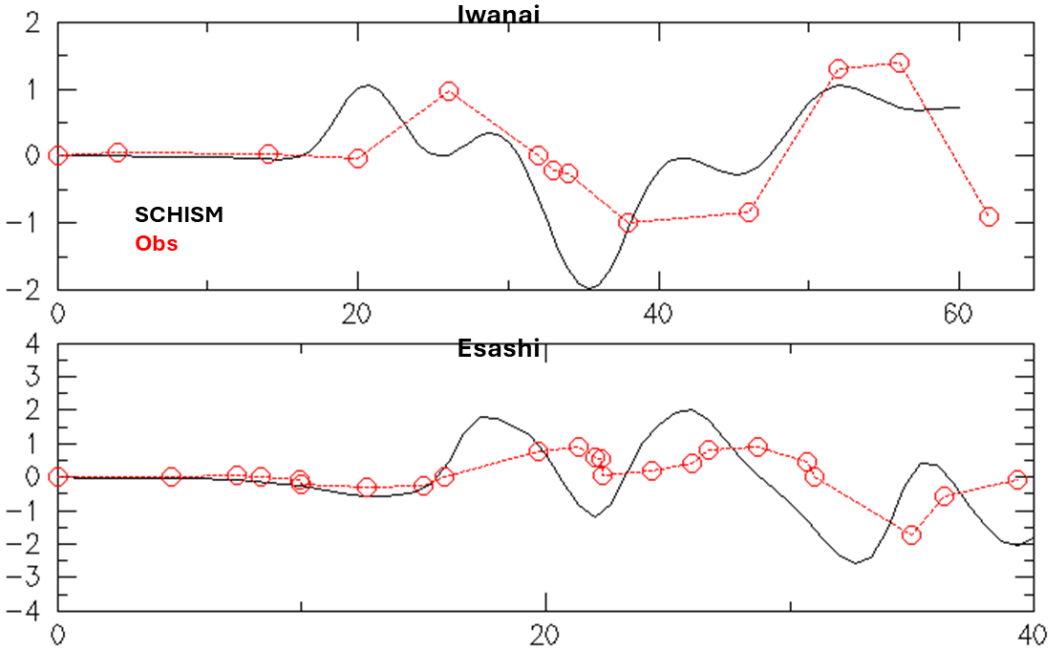


Figure 9-22. (A) Comparison of runups around the island in BP9. Red numbers are from the model. (B) Model predicted runups around the island. The coordinates given by the file provided by the Workshop have a datum shift so the coordinates used in this plot are from the Workshop final report.

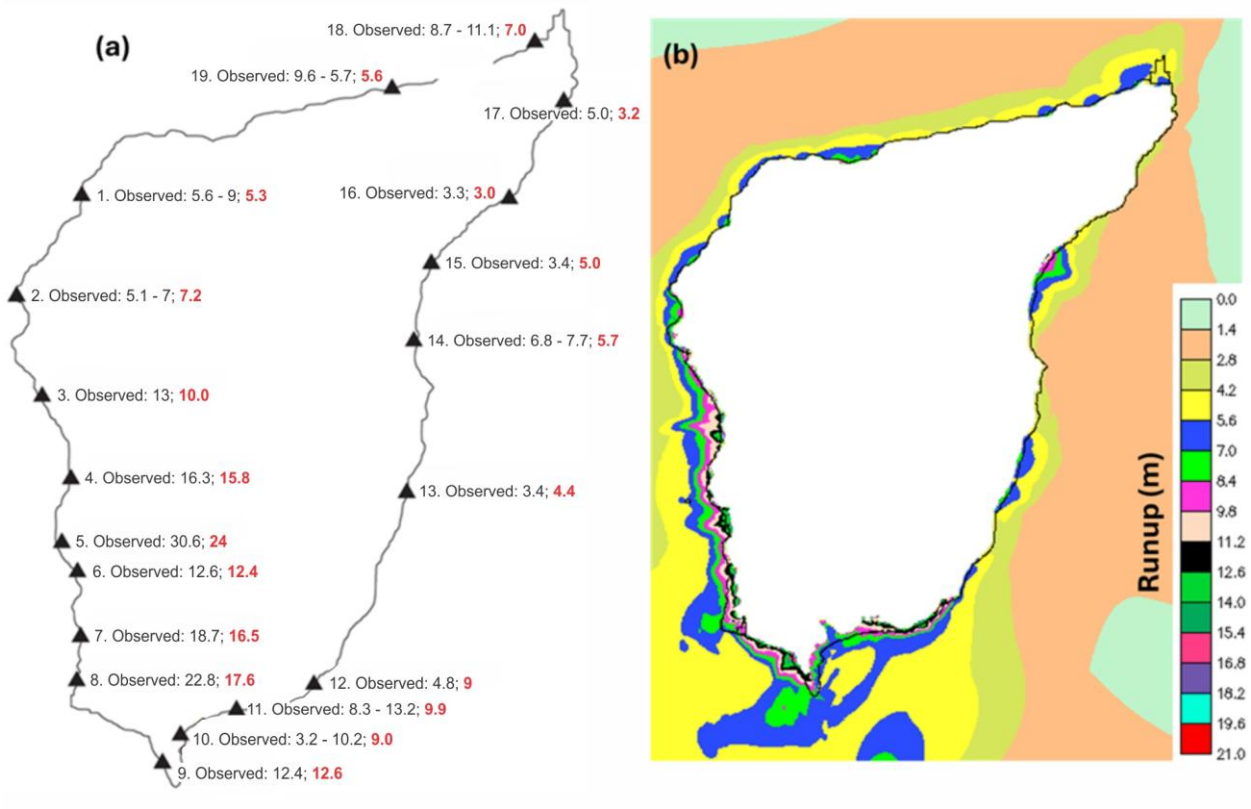
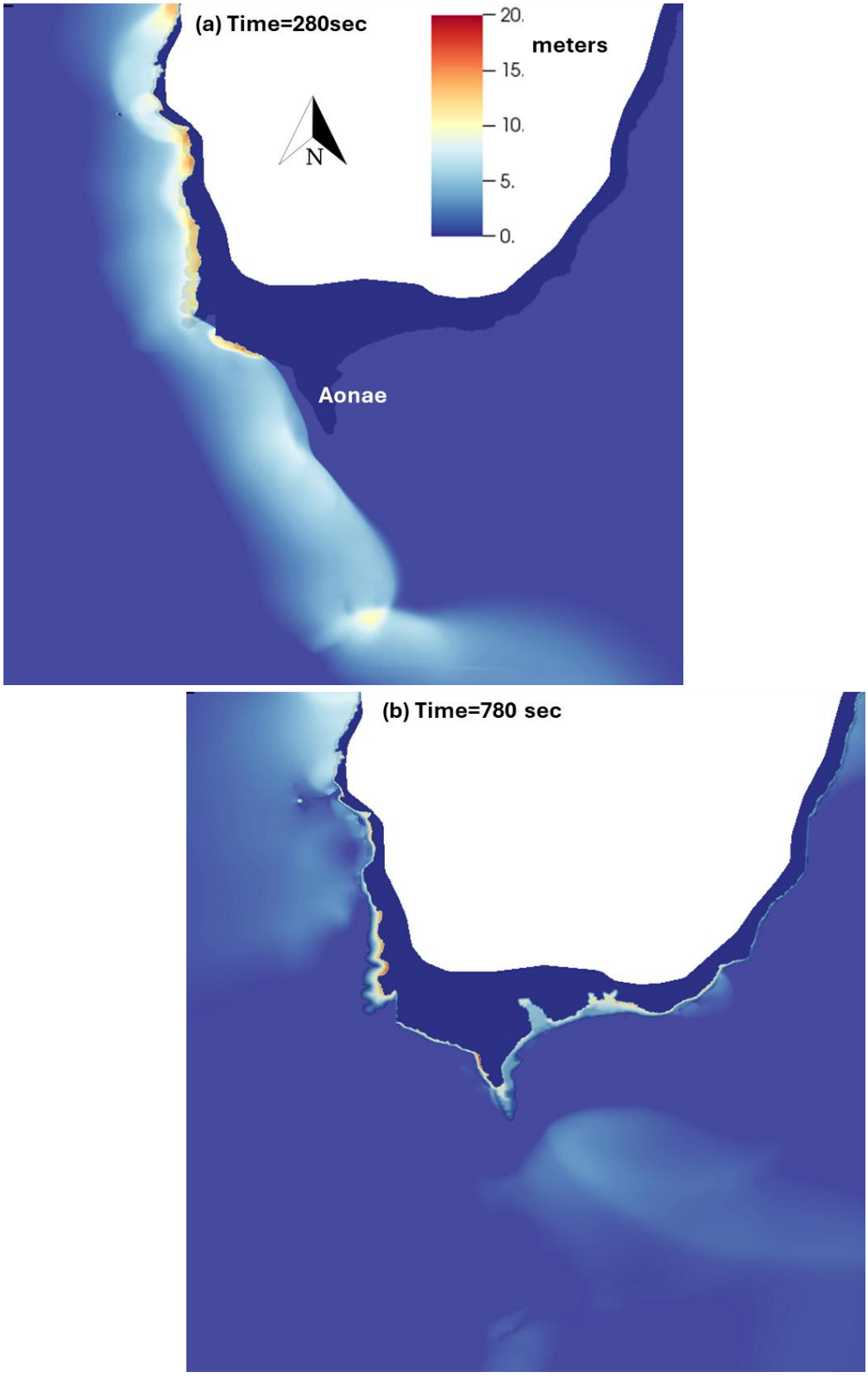


Table 9-6. Runup errors from SCHISM and SELFE (the latter from NTHMP 2012 report) for BP9. The errors were calculated using the best match if the observation is specified in a range. SCHISM errors show two numbers (error in meters and % error in parentheses). The mean SCHISM error is 17% and the mean SELFE error is 17%.

ID	Longitude	Latitude	Observed (m)	SCHISM errors m (%)	SELFE errors (%)
1	139.4292	42.18818	5.6–9.0	-0.3 (5%)	0
2	139.4112	42.16276	5.1–7.0	0.2 (3%)	11
3	139.4183	42.1374	13.0	-3.0 (23%)	58
4	139.4262	42.11655	16.3	-0.5 (3%)	0
5	139.4237	42.10041	30.6	-6.6 (22%)	14
6	139.428	42.09301	12.6	-0.2 (2%)	12
7	139.4289	42.07664	18.7	-2.2 (12%)	5
8	139.4279	42.06546	22.8	-5.2 (22%)	0
9	139.4515	42.0447	12.4	0.2 (1%)	0
10	139.4565	42.05169	3.2–10.2	0	0
11	139.472	42.05809	8.3–13.2	0	0
12	139.4934	42.0645	4.8	4.2 (87%)	71
13	139.5191	42.11306	3.4	1.0 (29%)	20
14	139.5211	42.15138	6.8–7.7	-1.1 (13%)	58
15	139.5259	42.17101	3.4	1.6 (47%)	13
16	139.5475	42.18745	3.3	-0.3 (6%)	10
17	139.5625	42.21198	5.0	-1.8 (36%)	41
18	139.5546	42.22698	8.7–11.1	-1.7 (19%)	0
19	139.5151	42.21525	5.7–9.6	-0.1 (2%)	14

Figure 9-23. Arrival of two waves at Aonae in BP9. The first wave came from the west while the second wave attacked from the east.



9.4 Lessons Learned

During the benchmarking exercise one of the most perplexing problems the author encountered was related to the incomplete information regarding those tests. The author had to spend considerable amount of time gleaning files from various sources. For the field tests (e.g., Okushiri) some critical pieces of information (such as the horizontal datums of the DEMs) are still missing. Perhaps the most serious problem with field tests is uncertainty about the geometry of the earthquake source. This issue causes serious errors in simulations for areas proximal to the source (e.g., poor match of simulated runup on the east coast of Okushiri Island).

The set of benchmark problems proposed in OAR-PMEL-135 was found to be mostly appropriate except for a few extreme cases (e.g., the larger wave breaking case C in the composite beach case). The combination of analytical, lab, and field tests adequately tests the performance of models.

Additional field tests have been done using SCHISM for the 1964 Great Alaska tsunami, with focus on its impact on the Oregon coast for select ports and harbors, and the results are found in various DOGAMI reports (e.g., Allan and others, 2018, 2020, 2024).

9.5 Acknowledgements

We are grateful for review comments provided by Dr. Elena Sulimani (University of Alaska), Dr. Juan Horillo (Texas A&M), and Dr. Randy LeVeque (University of Washington).

9.6 References

Allan, J.C., Zhang, J., O'Brien, F. and Gabel, L., 2018. Columbia River Tsunami Modeling: Towards Improved Maritime Planning Response. Special Paper 51, Portland, Oregon, 83 pp.

Allan, J.C., Zhang, J., O'Brien, F. and Gabel, L., 2020. Coos Bay tsunami modeling: Toward improved maritime planning response. O-20-08, Portland, Oregon, 78 pp.

Allan, J.C., Zhang, J. and O'Brien, F., 2021. Tsunami Inundation Modeling Update for the Northern Oregon Coast: Tillamook and Clatsop Counties. O-21-08, Portland, Oregon, 38 pp.

Allan, J.C., Zhang, J., O'Brien, F. and Gabel, L., 2024. Brookings tsunami modeling: Toward improved maritime planning response. O-24-03, Portland, Oregon, 79 pp.

Azvedo, A., Oliveira, A., Fortunato, A.B. and Bertin, X. (2009) Application of an Eulerian-Lagrangian oil spill modeling system to the Prestige accident: trajectory analysis*. J. Coastal. Res.*, 56, 777–781.

Burla, M., Baptista, A.M. Zhang, Y., and Frolov, S. 2010 Seasonal and inter-annual variability of the Columbia River plume: a perspective enabled by multi-year simulation databases. Journal of Geophysical *Research*, 115, C00B16.

Goldfinger, C., Nelson, C.H., Johnson, J.E., Morey, A.E., Gutiérrez-Pastor, J., Karabanov, E., Eriksson, A.T., Gràcia, E., Dunhill, G., Patton, J., Enkin, R., Dallimore, A., and Vallier, T., and the Shipboard Scientific Parties, 2010, Turbidite Event History: Methods and Implications for Holocene Paleoseismicity of the Cascadia Subduction Zone: U.S. Geological Survey Professional Paper 1661-F.

Gonzalez F, Geist EL, Jaffe B, Kaˆnogˇlu U, Mofjeld H, Synolakis C, Titov VV, Arcas D, Bellomo D, Carlto, D (2009) Probabilistic tsunami hazard assessment at seaside, Oregon, for near-and far-field seismic sources. J Geophys Res Oceans 114: C11023

Hanks, T.C., and Kanamori, H., (1979) A moment magnitude scale. Journal of Geophysical Research 84, 2348–2350.

Horrillo, H., Grilli, S.T., Nicolsky, D., Roeber, V. and Zhang, Y. (2014) Performance Benchmarking Tsunami Models for NTHMP's Inundation Mapping Activities, *Pure and Applied Geophysics*, DOI 10.1007/s00024-014-0891-y.

Hyndman, R.D., 2013. Downdip landward limit of Cascadia great earthquake rupture. *Journal of Geophysical Research: Solid Earth*, 118(10): 5530–5549.

Johnson, J., Satake, K., Holdahl, S., Sauber, J. (1996) The 1964 Prince William Sound earthquake: joint inversion of tsunami and geodetic data. *J. Geophys. Res.,* 101(B1), 523–532.

Kato, K., and Tsuji, Y. (1995) Estimation of fault parameters of the 1993 Hokkaido-Nansei-Oki earthquake and tsunami characteristics. *Bull. Earthq. Res. Inst*., Univ. of Tokyo, vol. 69, 39–66.

Lynett, P.J., Gately, K., Wilson, R., Montoya, L., Adams, L., Arcas, D., Aytore, B., Bai, Y., Bricker, J.D., Castro, M.J., Cheung, K., David, C., Dogan, G., Escalante, C., Gonzalez, F.I., Gonzalez-Vida, J., Grilli, S.T., Heitmann, T.W., Horrillo, J., Kaˆnogˇlu, U., Kian, R., Kirby, J.T., Li, W., Macaas, J., Nicolsky, D.J., Ortega, S., Pampell-Manis, A., Park, Y., Roeber, V., Sharghivand, N., Shelby, M., Shi, F., Tehranir, B., Tolkova, E., Thio, H., Velioglu, D., Yalciner, A., Yamazaki, Y., Zaytsev, A., Zhang, Y. (2017) Inter-Model Analysis of Tsunami-Induced Coastal Currents, Ocean Modelling, 114, 14–32 (http://dx.doi.org/10.1016/j.ocemod.2017.04.003).

Melgar, D., (2021) Was the January 26th, 1700 Cascadia earthquake part of a rupture sequence? Journal of Geophysical Research: Solid Earth, 126(10): e2021JB021822.

NTHMP (2012) Proceedings and results of the 2011 NTHMP (National Tsunami Hazard Mitigation Program) model benchmarking workshop. Boulder: US Depart. of Commerce/NOAA/NTHMP, NOAA Special Report 436p.

Patton, J.R., Eble, M.C., Kyriakopoulos, C., Lynett, P.J., Nicolsky, D., Ross, S., Ryan, K.J., Thio, H.K. and Wilson, R.I., 2022. U.S. Geological Survey Tsunami Sources Powell Center Working Group: Cascadia Probabilistic Tsunami Hazard Assessment Meeting Summary, AGU Fall Meeting. American Geophysical Union, Chicago, Illinois.

Patton, J.R., Ross, S.L., Eble, M.C., Kyriakopoulos, C., Lynett, P.J., Nicolsky, D.J., Ryan, K., Thio, H.K., Wilson, R.I. and Wu, B., 2025. Developing a Probabilistic Tsunami Hazard Assessment Framework for Pacific Sources: USGS Powell Center Meeting Summary. *Environmental & Engineering Geoscience*, 31(1): 67–76.

Pinto, L., Fortunato, A.B., Zhang, Y., Oliveira, A. and Sancho, F.E.P. Development and validation of a three-dimensional morphodynamic modelling system, *Ocean Modelling* (submitted).

Priest, G.R., Goldfinger, C., Wang, K., Witter, R.C., Zhang, Y.J., and Baptista, A.M., (2009) Confidence levels for tsunami-inundation limits in northern Oregon inferred from a 10,000-year history of great earthquakes at the Cascadia subduction zone: *Natural Hazards*, DOI 10.1007/s11069-009-9453-5.

Priest, G.R., Witter, R.C., Zhang, Y., Wang, K., Goldfinger, C., Stimely, L.L., English, J.T., Pickner, S.G., Hughes, K.L.B., Willie, T.E. and Smith, R.L., 2013. Tsunami inundation scenarios for Oregon. Open file report O-13-19, Oregon Department of Geology and Mineral Industries, Portland, Oregon.

Rodrigues, M., Oliveira, A., Queiroga, H., Fortunato, A.B., and Zhang**,** Y. 2009a Three-Dimensional Modeling of the Lower Trophic Levels in the Ria de Aveiro (Portugal), *Ecological Modelling,* **220**(9–10), 1274–1290.

Rodrigues, M., Oliveira, A., Costa, M., Fortunato, A.B. and Zhang, Y. 2009b Sensitivity analysis of an ecological model applied to the Ria de Aveiro. *Journal of Coastal Research*, SI**56**, 448–452.

Roland, A., Zhang, Y., Wang, H.V., Maderich, V. and Brovchenko, I. 2011 A fully coupled wave-current model on unstructured grids, *Compt. & Geosciences* (submitted).

Staisch, L.M., Witter, R.C., Watt, J.T., Grant, A.R., Walton, M.A., Brothers, D., Davis, E., Dura, C., Engelhart, S., Enkin, R., Garrison-Laney, C.E, Goldfinger, C., Hamilton, T., Hawkes, A., Hill, J.C., Hong, I.J., Jaffe, B.E., Kelsey, H., Lahusen, S.R, La Selle, S.M, Nelson, A.R, Nieminski, N.M, Padgett, J.S, Patton, J., Pearl, J.K, Pilarczyk, J., Sherrod, B., and Stanton, K., (2024) Compiled onshore and offshore paleoseismic data along the Cascadia Subduction zone, U.S. Geological Survey data release, https://doi.org/10.5066/P13OJQYW.

TPSWG (Tsunami Pilot Study Working Group) (2006) Seaside, Oregon tsunami pilot study—modernization of FEMA flood hazard maps. National Oceanic and Atmospheric Administration OAR Special Report, NOAA/OAR/PMEL, Seattle, WA.

Wang, K., 2025. Thermal control on the updip and downdip extents of megathrust earthquake rupture: revisiting Dr. Roy Hyndman's seminal contributions 30 years later. Canadian Journal of Earth Sciences, 62(4): 710–724.

Watt, J.T. and Brothers, D.S., (2021) Systematic characterization of morphotectonic variability along the Cascadia convergent margin, Implications for shallow megathrust behavior and tsunami hazards. Geosphere, 17(1): 95–117.

Willmott, Cort J.; Ackleson, Steven G.; Davis, Robert E.; Feddema, Johannes J.; Klink, Katherine M.; Legates, David R.; O'Donnell, James; Rowe, Clinton M. (1985) Statistics for the Evaluation and Comparison of Models, J. Geophys. Res., Vol. 90, No. C5, pp. 8995–9005

Witter, R.C. (2008) Prehistoric Cascadia tsunami inundation and runup at Cannon Beach, Clatsop County, Oregon, Oregon Department of Geology and Mineral Industries, Open-File Report O-08-12, 36 p., appendices.

Witter, R.C., Jaffe, B., Zhang, Y. and Priest, G.R. (2011) Reconstructing hydrodynamic flow parameters of the 1700 tsunami at Cannon Beach, Oregon, USA., Natural Hazards, DOI 10.1007/s11069-011-9912-7.

Witter, R.C, Zhang, Y., Wang, K., Goldfinger, C., Priest, G.R., Allan, J.C. (2012) Coseismic slip on the Cascadia megathrust implied by tsunami deposits in an Oregon lake. Journal of Geophysical Research-Solid Earth, 117, B10303, doi:10.1029/2012JB009404.

Witter, R.C., Y. Zhang, Wang, K., Priest, G.R., Goldfinger, C., Stimely, L., English, J.T. and Ferro, P.A. (2013) Simulated tsunami inundation for a range of Cascadia megathrust earthquake scenarios at Bandon, Oregon, USA, Geosphere, 9, 1783–1803.

Ye, F., Zhang, Y., Yu, H., Sun, W., Moghimi, S., Myers, E.P., Nunez, K., Zhang, R., Wang, H.V., Roland, A., Martins, K., Bertin, X., Du, J., and Liu, Z. (2020) Simulating storm surge and compound flooding events with a creek-to-ocean model: importance of baroclinic effects, Ocean Modelling, 145. https://doi.org/10.1016/j.ocemod.2019.101526

Zhang, Y., and Baptista, A.M. 2008a SELFE: A semi-implicit Eulerian-Lagrangian finite-element model for cross-scale ocean circulation. *Ocean Modelling*, 21(3-4), 71–96.

Zhang, Y., and Baptista, A.M. 2008b An Efficient and Robust Tsunami Model on Unstructured Grids. Part I: Inundation Benchmarks. *Pure and Applied Geophysics*, **165**, 2229–2248.

Zhang, Y., Witter, R.W. and Priest, G.P. (2011a) Nonlinear Tsunami-Tide Interaction in 1964 Prince William Sound Tsunami, *Ocean Modelling* 40, 246–259.

Zhang, Y. (2011b) Report on benchmark results from SELFE, NTHMP Workshop, Boulder, CO.

Zhang, Y., Ye, F., Stanev, E.V., Grashorn, S. (2016). Seamless cross-scale modeling with SCHISM, Ocean Modelling, 102, 64-81. doi:10.1016/j.ocemod.2016.05.002

10.0 APPENDIX B: PROCEDURES USED TO PRODUCE THE UPDATED GIS

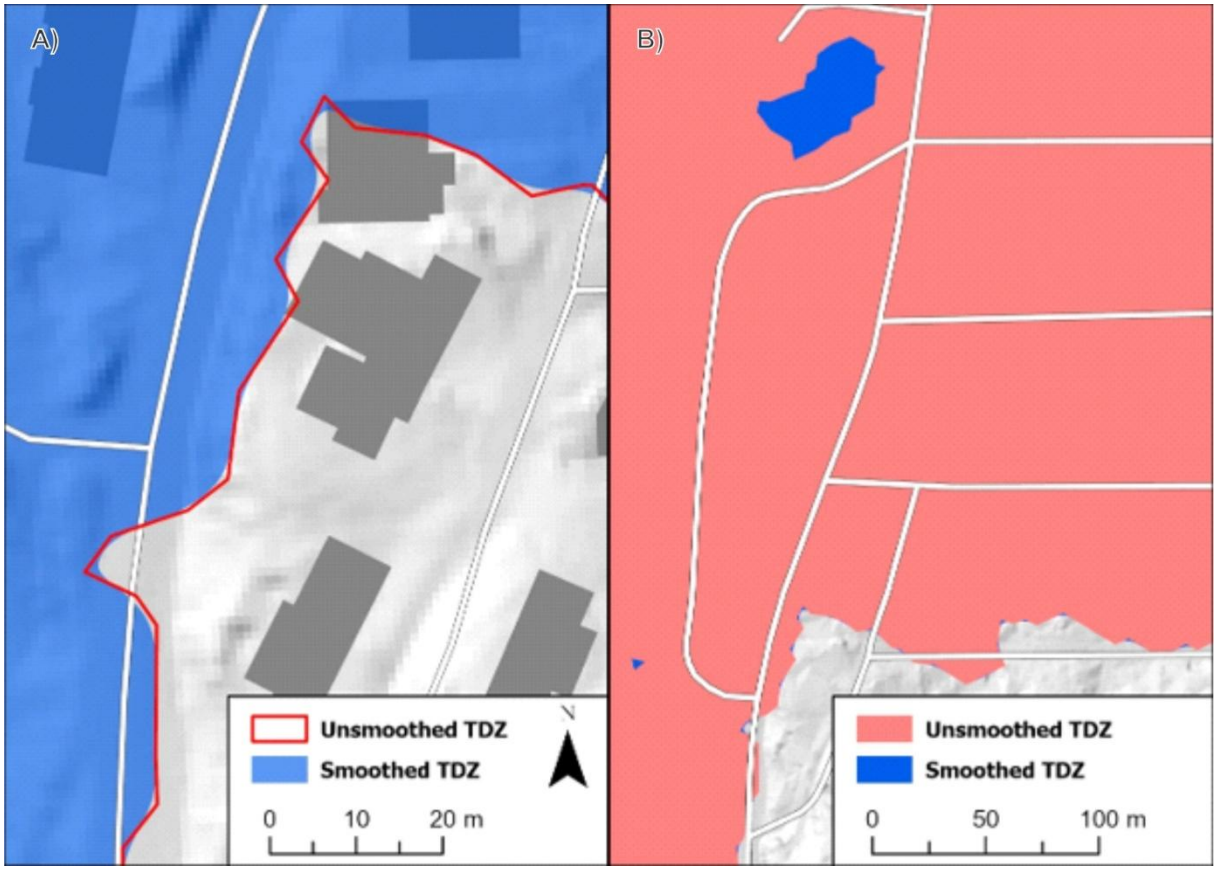
This section describes the step-by-step GIS procedures DOGAMI used for generating the final TDZ inundation zone, runup elevations, and overwash inundation depth points along those barrier spits backed by coastal estuaries. The overall approach follows Wilson and others (2021), with a few minor modifications.

10.1 Approach Used to Generate the Oregon Coast TDZ

The following steps were followed to generate the Oregon Coast TDZ:

1. Convert the model simulation data (i.e., ASCII files) to raster (gridded) GIS data.
2. Convert the raster to a vector polygon feature.
3. Automatically fill all polygon holes less than 2,800 m^2.
4. Automatically remove all disconnected polygons less than 2,800 m^2.
5. Smooth the edges of the polygon using Polynomial Approximation with Exponential Kernel (PAEK; Bodansky and others, 2002) smoothing algorithm and using a tolerance value of 10 (**Figure 9-1**).

Figure 10-1. A) Example maps comparing the unmodified "raw" TDZ (red outline) to the smoothed TDZ (blue area), producing a more realistic looking inundation boundary. B) Figure on the right is scaled from the left and shows the same smoothing applied to the final TDZ (blue area). Holes smaller than 2,800 m^2 in size are automatically removed, while larger holes (>2,800 m^2 <60,000 m^2) are manually evaluated.



6. Manually review all polygon holes between 2,800 m^2 and 60,000 m^2.
    a. The holes were typically filled if one of the following criteria was true:
        i. They were in a remote area with no human development and adjacent to a more significant area of high ground.
        ii. The high ground responsible for the hole was based on undesirable or temporary features such as wood piles.
        iii. The underlying lidar bare earth fails to show a strongly distinct topographic high ground feature. For example, sometimes holes occur on the edge of a flat farm field where slightly higher points along a berm/levee exist.
    b. The holes were preserved if the following criteria were true:
        i. It was in an inhabited area, and alternative better high ground locations were not adjacent.
        ii. The underlying lidar bare earth displays a very strong topographic higher ground feature. If the feature was strong, the hole was pretty much always persevered regardless of other criteria.
7. Manually review disconnected polygons. Disconnected polygons were removed unless:
    a. It was caused by significant flooding occurring behind a hydraulic connection such as a culvert.
    b. It was in a major stream channel with a clear water connection between the disconnected feature and the main inundation polygon.
    c. In these cases, the disconnected polygon was manually connected and merged into the main inundation polygon.
8. Merge and dissolve inundation for applicable runs for each county.
    a. Clatsop: Run02c and Run02g
    b. Tillamook: Run01c and Run01i
    c. Lincoln: Run01c and Run 02d
9. Modify the TDZ polygon (i.e., the new model inundation zone) at the southern end of the Lincoln County boundary so that it merged with the nearest or most appropriate ASCE7-22 (previous modeling) TDZ and runup elevation.
10. Convert the polygon format to an inundation raster format. This is accomplished using a 3 m cell size.

A special note: the process to generate the DOGAMI TDZ with inundation depths less than three feet used the same approach, except the ArcGIS function “Raster Calculator” was used to subtract three feet from the PTHA flow-depth model results before converting to polygons.

10.2 NOAA-NCEI Tsunami Model Bathymetry/Topography Source DEM for Oregon

Over the past decade, the lead Author has worked closely with scientists at NOAA-NCEI to produce updated high resolution tsunami digital elevation models for the Cascadia region. Those efforts are summarized in several publications introduced in **Section 3.1**. The following is the approach used to compile those data for Oregon:

1. Download all 1/9 arc-second (~3 m) bathymetry/topography DEM datasets (Ascii file format) for the northern to central Oregon coast from NCEI (e.g., Carignan and others, 2019; Carignan and others, 2021; Linn and others, 2024), relative to the North America Vertical Datum 1988 (NAVD88). These DEMs are the same as those used in the numerical tsunami modeling.
2. Convert the Ascii (*.asc) files to a raster format using ArcGIS Pro.

3. Export the raster layer as a geotiff (*.tif), 32-bit float, and "-9999" no data value

10.3 Process to Generate the Overwash Inundation Depth Points

The ASCE tsunami loads committee has identified certain areas along the seaward face of select barrier spits that are backed by coastal estuaries, where the flow depths are explicitly defined. These data can be found in the ASCE Tsunami Hazard Tool. Consistent with this need, we revised and updated the overwash depth points for select areas along the central to northern Oregon Coast:

1. Identify Inundation Depth points at overwash areas, in the same locations as identified in ASCE 7-22. Inundation Depth points were either added or modified in the following areas:
    a. Added points along Bayshore (Alsea Bay).
    b. Revised the Inundation Depth points along Siletz Spit due to the spit having experienced substantial erosion since ASCE7-22.
    c. Revised Inundation Depth points near Pacific City to remove a few points not backed directly by the Nestucca estuary.
    d. Revised Inundation Depth points near Sand Lake to address recent changes in the configuration of the barrier spit.
2. Generate points along the line with a minimum spacing of 40 m.
3. Extract flow-depth values at each point using the DOGAMI PTHA flow-depth model raster. This was accomplished for those runs used to create the final inundation zone. For each depth point location, the highest flow depth of the runs was used.
4. Generate coordinates at each point (latitude and longitude) in decimal degrees.

10.4 Process to Generate the Runup Elevation Points

The ASCE Tsunami Hazard Tool contains runup elevations produced by a 2,475-yr tsunami, which are specified for the TDZ. Consistent with this need, we defined new runup elevations based on our final inundation modeling results, which are specified for each County examined. We used the following approach to specify the runup elevations:

1. We converted the TDZ polygon to an ESRI polyline Shapefile and generated points along the lines every 10 m.
2. Generated coordinates at each point (latitude and longitude) in decimal degrees.
3. We then extracted runup elevation values from the appropriate DEM in NAVD88. To also provide MHW elevation values, the authors took the following steps:
    a. Ran the boundary points (as csv) through the online NOAA VDatum tool to get the MHW conversion where it exists for those points. Only a relatively small number of boundary points received a MHW conversion from the tool, these mostly being on the open coast near the shoreline.
    b. Ran normal shoreline points through the online NOAA tool. This provided conversion values everywhere on the shoreline. This was produced to help fill in the gaps in MHW conversion, where applicable.
    c. Manually reviewed the boundary points and identified locations where they were not assigned MHW conversion values from the NOAA VDatum tool. At these locations, the authors either used adjacent runup point MHW conversion values to interpolate/choose an appropriate value used the MHW conversion from the most relevant shoreline points.

In this way, the MHW conversion was determined for all runup points, and the MHW value was calculated based on the NAVD88 value.